Visualising cellular interactions underpinning T-cell activation



Mateusz Kotowski

St John's College

University of Oxford

A thesis submitted for the degree of

Doctor of Philosophy

Hilary 2024

Acknowledgements

First, I would like to thank Simon for admitting me to his lab almost five years ago and for providing me with opportunities to grow as a scientist and T-cell enthusiast. Presenting at multiple conferences and imaging at Janelia were among the highlights of my DPhil. I am grateful to Mafalda for all the scientific and non-scientific advice, as well as for her encouragement to pursue challenging experiments. Simon and Mafalda, thank you for the guidance and discussions that helped me complete this thesis. I would also like to thank Dave and Steve for welcoming me into their labs during my visits to Cambridge and for sharing their expertise which enabled the progress of this work.

To the Davis Lab – thank you for fostering a creative and supportive environment for doing science. Thank you for all the cakes, especially Mai's Guinness cake and Mafalda's Biscoff cake, and for the countless coffees that led to many valuable discussions. Thank you to Mai for teaching me her cloning and protein purification tricks. Sumana – I am glad we embarked on the primary-T-cell journey and the many quests to edit T cells. Also, thank you for the opportunity to co-author a review in the first year of my DPhil, which inspired my scientific thinking. A special mention goes to Oliver for his computational wizardry and the regular provision of late-evening chocolate bars.

To my fellow kids, I would like to thank João for always finding the bright side and making the lab feel busy from midday till midnight. Ed, for sharing his ideas, always being excited about my data, and being an unofficial mentor. Janina, for being my tissue culture buddy. Martin, for sharing the SPR trade secrets, always finding time for an early coffee break, for many swims and bike rides, and for sharing an affinity (pun intended) for Italian bitters – but most importantly, for introducing me to Lilli and Jesús! Markus and Dan – thank you for spending many hours in dark rooms imaging my T cells. I cannot thank Markus enough for proposing the visit to the AIC and for two very exciting weeks on the Janelia farm.

Patryk, thank you for the continued support, for the long discussions during our walks, and for braving the Edinburgh-Oxford, Cambridge-Oxford, and then London-Oxford train journeys for over four years. And, very importantly, for your patience when reading through many pages of science and for bearing with my aversion to articles.

Dla Rodziców, którzy wspierali moje pomysły, od wyjazdu na północ Anglii przez krótki rok w Londynie do prawie dziewięcioletniego życia w Oksfordzie. Dla Julii, która sprawiła, że Oksford stał się bardziej domowy i dbała o mój dobrostan zapewniając chlebem bananowy i coroczne mazurki. I oczywiście za wspólną przygodę wprowadzki do mieszkania numer 16. Dla Babci i Dziadka za umożliwienie mojego rozowju akademickiego i za oczekiwanie na moje powroty do domu.

Authorship and Funding

I hereby declare that except where specific reference is made to the work of others, the contents of this dissertation are original and have not been submitted in whole or in part for consideration for any other degree or qualification in this, or any other university. This dissertation is my own work and contains nothing which is the outcome of work done in collaboration with others, except as specified in the text and in the following:

- ImmTACs and biotinylated CD3$\epsilon\gamma$ were provided by Ben de Wet at Immunocore Ltd.
- 2xHis_6-tagged GP100-HLA-A2 was purified by Mai Vuong from the Davis Laboratory, University of Oxford
- Epi-illumination selective plane illumination microscopy was performed in collaboration with Dr. Ziwei Zhang and Dr. Bing Li from the Klenerman Laboratory, University of Cambridge.
- Epifluorescence widefield microscopy, spinning disk confocal microscopy and total internal reflection fluorescence microscopy were performed in collaboration with Daniel Heraghty and Dr. Debasis Banik from the Klenerman Laboratory, University of Cambridge.
- resPAINT microscopy was performed by Dr. Debasis Banik and Dr. Bing Li from the Klenerman Laboratory, University of Cambridge.
- Laser scanning confocal microscopy of monocyte-derived dendritic cells was performed by Dr. Edward Jenkins from the Davis Laboratory, University of Oxford
- Quantitative analysis of the epifluorescence widefield microscopy data was performed by Daniel Heraghty from the Klenerman Laboratory, University of Cambridge
- Python code for the quantitative analysis of the epifluorescence widefield microscopy data was written by Dr. Markus Koerbel from the Klenerman Laboratory, University of Cambridge

- MATLAB code for the analysis of calcium signalling was written by Dr. Jane Humphrey from the Klenerman Laboratory, University of Cambridge
- Three-dimensional structured illumination microscopy was performed in collaboration with Dr. Jesse Aaron from the Advanced Imaging Centre, Janelia Research Campus (HHMI) and Markus Koerbel from the Klenerman Laboratory, University of Cambridge
- Sample processing for FIB-SEM imaging and FIB-SEM imaging were performed by Dr. Jesse Aaron from the Advanced Imaging Centre, Janelia Research Campus (HHMI)

The work presented in this thesis was supported by:

- Medical Research Council

Approximate word count: 48,000
Mateusz Kotowski (19/04/24)

Abstract

Cell-cell contact is fundamental to the immune response. The contact sites are likely to be dynamic environments where short-lived receptor/ligand interactions occurring on timescales of seconds drive critical decision-making processes. T cells use finger-like membrane protrusions, known as microvilli, to interrogate their targets by forming 'close contacts' at the cellular interface. These initial T cell/target cell interactions have been predominantly studied in reductionist systems. While informative, such systems fail to recapitulate the complexity of authentic cellular interfaces.

In this study, a cellular system was developed to visualise the early interactions between cytotoxic T cells and model cancer cells. To engage T cells, ImmTACs, clinically relevant bispecific molecules, were adopted as universal T-cell receptor (TCR) ligands. ImmTACs were shown to mimic the native TCR ligands, maintaining compatibility with co-receptor recruitment and the dimensions of close contacts.

At the interface with cancer cells, T cells formed sub-micron-sized close contacts stabilised by small adhesion molecules, CD2/CD58, but the interactions were transient and spatially limited. Inclusion of the LFA-1 ligand, ICAM-1, on the cancer cell dramatically increased the efficiency of close contact formation and their stability. The dimensions of close contacts were independent of the presence of the TCR ligand or ICAM-1 on the target cells. In contrast, overexpression of CD58 increased the close contact size, leading to T-cell activation in the absence of the TCR ligands. The microvilli-created contacts were shown to be the sites of TCR triggering, and a single close contact was sufficient for T-cell activation. The close contacts were depleted of the CD45 phosphatase, supporting the kinetic-segregation model of TCR triggering. Finally, exploration of the T cell/cancer cell interface ultrastructure was initiated to map and correlate structural features of microvilli and close contacts. These findings establish the cellular basis of antigen detection by T cells.

Contents

List of Figures xiii

List of Tables xvi

List of Abbreviations xvii

1 Introduction 1

1.1 How we live and how we die, the secret life of T cells 2

1.1.1 Overview of the immune system 2

1.1.1.1 Historical perspective on T lymphocytes 2

1.1.1.2 Innate system 3

1.1.1.3 Adaptive system 3

1.1.2 Development of T cells 4

1.1.3 T-cell trafficking 6

1.1.4 Antigen presentation 7

1.2 Molecular and cellular determinants of T-cell interactions 10

1.2.1 Antigen recognition apparatus 10

1.2.1.1 T-cell receptor complex 10

1.2.1.2 Lck kinase 12

1.2.1.3 CD45 phosphatase 13

1.2.1.4 Co-receptors 15

1.2.1.5 ZAP70 kinase 16

1.2.2 T-cell adhesion system 17

1.2.2.1 LFA-1/ICAM-1 17

1.2.2.2 CD2/CD58 20

1.2.3 Glycocalyx 21

1.2.4 T-cell surface 22

1.2.4.1 T-cell membrane topology 22

1.2.4.2 Distribution of key receptors at the resting T-cell surface 24

1.3 T-cell activation 25

1.3.1 TCR signalling pathways 25

1.3.2 Early T cell/target cell interactions . . . 28
1.3.2.1 TCR microclusters . . . 28
1.3.2.2 Microvillar contacts . . . 30
1.3.3 Immune synapse . . . 31
1.4 Models of T-cell receptor triggering . . . 33
1.4.1 Oligomerisation . . . 33
1.4.2 Conformational change . . . 34
1.4.2.1 Allosteric control . . . 35
1.4.2.2 Mechanotransduction . . . 37
1.4.3 Kinetic segregation . . . 38
1.4.4 TCR triggering models, antigen discrimination and sensitivity 40
1.5 T cell-redirecting immunotherapies . . . 43
1.5.1 Immunotherapy targets . . . 43
1.5.1.1 Tumour-associated antigens . . . 43
1.5.1.2 Tumour-specific antigens . . . 44
1.5.2 Adoptive cell transfer . . . 44
1.5.3 T-cell engagers . . . 45
1.6 Methods for imaging of T-cell activation . . . 47
1.6.1 Cellular substrates . . . 47
1.6.2 APC and target cell surrogates . . . 48
1.7 Aims of this thesis . . . 50

2 Materials and Methods **51**
2.1 Methods . . . 51
2.1.1 Molecular gene cloning . . . 51
2.1.1.1 General . . . 51
2.1.1.2 Restriction enzyme DNA digestion . . . 51
2.1.1.3 Agarose gel electrophoresis . . . 52
2.1.1.4 DNA ligation . . . 52
2.1.1.5 Transformation of *E. coli* . . . 52
2.1.1.6 Purification of DNA from *E. coli* liquid cultures . 53
2.1.2 Tissue culture . . . 54
2.1.2.1 Cell culture media and buffers . . . 54
2.1.2.2 Maintenance of cell lines . . . 55
2.1.2.3 Cryopreservation of cell lines and primary $CD8^+$ T cells . . . 56
2.1.2.4 Isolation of primary $CD8^+$ T cells . . . 56
2.1.2.5 Lentivirus production . . . 57
2.1.2.6 Transduction of cell lines . . . 57

2.1.2.7 Preparation of lentivirus-coated retronectin plates for transduction of primary CD8$^+$ T cells 58
2.1.2.8 Rapid expansion mix 58
2.1.2.9 Transduction of primary CD8$^+$ T cells with ZAP70-HaloTag construct 59
2.1.2.10 Electroporation of U-2 OS cells with RNP 60
2.1.3 Protein expression and purification 60
2.1.3.1 C-tag affinity purification 60
2.1.3.2 Size exclusion chromatography 61
2.1.3.3 Polyacrylamide gel electrophoresis 61
2.1.3.4 Western blotting 62
2.1.3.5 Surface Plasmon Resonance 62
2.1.4 Flow cytometry 64
2.1.4.1 General flow cytometry 64
2.1.4.2 Fluorescence-activated cell sorting 65
2.1.4.3 Co-culture assays of T cells with U-2 OS cells . . 65
2.1.4.4 Analysis of monocyte-derived dendritic cells . . . 66
2.1.5 Live-cell imaging 68
2.1.5.1 Calcium release assays 68
2.1.5.2 Preparation of primary T cells and U-2 OS cells for multi-colour imaging 69
2.1.5.3 Epifluorescence widefield microscopy 70
2.1.5.4 Epi-illumination selective-plane illumination microscopy 71
2.1.5.5 Spinning disk confocal microscopy 73
2.1.6 Fixed-cell imaging 73
2.1.6.1 Scanning electron microscopy 73
2.1.6.2 Confocal imaging of U-2 OS cells 74
2.1.6.3 3D-SIM imaging of cryo-fixed T cell/U-2 OS cell conjugates 75
2.1.6.4 FIB-SEM imaging of cryo-fixed T cell/U-2 OS cell conjugates 78

3 A cellular system for study of primary CD8$^+$ T-cell activation 79
3.1 Introduction 80
3.2 Results 81
3.2.1 Biophysical characterisation of an ImmTAC panel 81
3.2.2 Characterisation of U-2 OS cells and their modification for T-cell activation assays 83

3.2.3 Isolation and characterisation of primary human CD8$^+$ T cells . . . 91
3.2.4 Optimisation and analysis framework for co-culture assays 92
3.2.5 Relationship between ImmTAC potency and affinity 94
3.2.6 Relationship between ImmTAC potency and topology . . . 95
3.3 Discussion . . . 96
3.3.1 Biophysical characterisation of an ImmTAC panel 96
3.3.2 Characterisation of U-2 OS cells and their modification for T-cell activation assays . . . 100
3.3.3 Isolation and characterisation of primary human CD8$^+$ T cells . . . 102
3.3.4 Measurements of ImmTAC potency with respect to affinity and size . . . 102

4 Mechanistic correlates of TCR triggering by ImmTAC ligands 105
4.1 Introduction . . . 106
4.2 Results . . . 107
4.2.1 Role of small adhesion molecules in ImmTAC-induced T-cell activation . . . 107
4.2.2 Effect of engineered extension of pMHC on ImmTAC potency 113
4.2.3 Interactions of the CD8αβ co-receptor with the ternary TCR/ImmTAC/pMHC complex . . . 115
4.2.4 Truncation of CD45 phosphatase attenuates ImmTAC-induced T-cell activation . . . 121
4.3 Discussion . . . 124
4.3.1 Role of small adhesion molecules in ImmTAC-induced TCR triggering . . . 125
4.3.2 Effect of engineered extension of pMHC in ImmTAC potency 126
4.3.3 Interactions of CDαβ co-receptor with ternary TCR-ImmTAC-pMHC complex . . . 127
4.3.4 Truncation of CD45 phosphatase attenuates ImmTAC-induced T-cell activation . . . 128

5 Topography of the T-cell surface and the receptor organisation therein during interactions with cancer cells 130
5.1 Introduction . . . 131
5.2 Results . . . 133
5.2.1 Generation of ZAP70-HaloTag primary CD8$^+$ T cells . . . 133
5.2.2 Morphology of the primary CD8$^+$ T-cell surface . . . 133

5.2.3 Proximal signalling of CD8$^+$ T cells in response to the N-MED ImmTAC . . . 134
5.2.4 Generation and characterisation of U-2 OS cell lines for imaging of T cell/target cell interactions . . . 136
5.2.5 ICAM-1 alters the dynamics of the T cell/U-2 OS cell interaction . . . 141
5.2.6 Primary CD8$^+$ T cells form discrete contacts at the interface with target cells . . . 143
5.2.7 A single close contact is sufficient for T-cell activation . . . 153
5.2.8 Scanning behaviour of T cells in the absence of the TCR ligand . . . 154
5.2.9 Hallmarks of KS-based signalling within close contacts . . . 158
5.2.10 Overexpression of CD58 increases the dimensions of close contacts . . . 165
5.3 Discussion . . . 167
5.3.1 Model T cell/target cell system for imaging of cellular interactions . . . 169
5.3.2 CD58 as a close-contact marker . . . 170
5.3.3 Visualisation of the T cell/cancer cell interactions . . . 171

6 Ultrastructure of CD8$^+$ T cell/U-2 OS cell conjugates imaged using correlative light and electron microscopy 174
6.1 Introduction . . . 174
6.2 Results . . . 176
6.2.1 Purification and validation of the N-MED ImmTAC . . . 176
6.2.2 Cryogenic 3D-SIM imaging of primary CD8$^+$ T cell/U-2 OS cell conjugates . . . 178
6.2.3 FIB-SEM imaging of the primary CD8$^+$ T cell/U-2 OS cell conjugates . . . 187
6.3 Discussion . . . 191
6.3.1 Production and validation of the N-MED ImmTAC . . . 191
6.3.2 CLEM imaging of the T cell/U-2 OS cell interactions . . . 192

7 General discussion 194
7.1 ImmTACs as synthetic TCR ligands and immunotherapeutics . . . 195
7.1.1 ImmTAC potency rivals that of native TCR ligands . . . 195
7.1.2 Topological requirements of synthetic TCR ligands . . . 196
7.1.3 Geometrical requirements of CD8 recruitment . . . 197
7.2 Interactions of T cells with genuine cellular surfaces . . . 198
7.2.1 How are the microvilli stabilised on the cancer cell surface? 199

7.2.2 How do T cells scan the target cell surface? 200
7.2.3 Effects of signalling on the T cell/U-2 OS cell interface . . 201
7.2.4 Formation of synapse-like structures at the T cell/cancer cell interface 202
7.3 Mechanisms of TCR triggering 203
7.3.1 CD45 exclusion from close contacts 203
7.3.2 Close-contact size 205
7.3.3 Insights into other models of TCR triggering 207
7.4 Concluding remarks 208

References **210**

Appendices

A Appendix 1 **238**

List of Figures

1.1 Pathways of antigen presentation. 8
1.2 Structure of the T-cell receptor complex. 12
1.3 TCR triggering apparatus. 18
1.4 Cancer cell surface 21
1.5 T-cell surface. 23
1.6 TCR downstream signalling network. 26
1.7 Interactions of T cells with surrogates of target cells. 29
1.8 Evolution of T cell/target cell interactions. 31
1.9 Mechanisms of TCR triggering. 36
1.10 Formats of bispecific T-cell engagers. 46

2.1 Layout of the epifluorescence widefield microscope. 71
2.2 Layout of the epi-illumination selective-plane illumination microscope. 72
2.3 Layout of the cryogenic three-dimensional structured illumination microscope. 77

3.1 Architecture of TCR-targeted bispecifics 82
3.2 SPR measurements of ImmTAC/GP100-MHC binding 85
3.3 SPR measurements of ImmTAC/CD3$\epsilon\gamma$ binding 85
3.4 Topography of an individual U-2 OS cell and a U-2 OS cell monolayer. 86
3.5 Characterisation of the U-2 OS cell surface. 88
3.6 Characterisation of the mature monocyte-derived DC surface . . . 90
3.7 Generation and quantification of GP100-MHC antigen on the surface of U-2 OS cells. 91
3.8 Preparation and testing of primary human $CD8^+$ T cells 93
3.9 Framework for analysis of flow cytometry data from co-culture assays 95
3.10 Relationship between the potency of N-terminal ImmTACs and the ImmTAC/CD3ϵ affinity. 97
3.11 Relationship between the potency of ImmTACs and their topology. 99

4.1 Panel of U-2 OS cell lines expressing a ~7000-fold range of CD58 and their effect on T-cell activation in the absence of ligand. . . . 109

4.2 Relationship between CD58 expression levels and T-cell activation by ImmTACs. . . . 112
4.3 Extension of the GP100-MHC antigen and its effect on T-cell activation in the absence of TCR ligand. . . . 114
4.4 Relationship between the size of the ImmTAC/GP100-MHC ligand and T-cell activation. . . . 117
4.5 U-2 OS cell lines expressing A2-K^B, WT and KA variants of GP100-SCT and their effect on T-cell activation in the absence of TCR ligand. . . . 118
4.6 Relationship between the CD8αβ/MHC-I affinity and T-cell activation by ImmTACs. . . . 120
4.7 Jurkat T cell lines expressing truncated CD45 and its effect on T-cell activation in the absence of TCR ligand. . . . 122
4.8 Impact of CD45 truncation on T-cell activation by ImmTACs. . . . 123

5.1 Preparation of ZAP70-HaloTag primary $CD8^+$ T cells. . . . 134
5.2 Scanning electron microscopy of primary $CD8^+$ T cells. . . . 135
5.3 Calcium release assays of primary $CD8^+$ T cell responses to the N-MED ImmTAC. . . . 137
5.4 Generation of U-2 OS cell lines for imaging of interactions with primary $CD8^+$ T cells. . . . 139
5.5 Co-culture assays of primary $CD8^+$ T cell with CD58LO and CD58LO+ICAM-1 U-2 OS cell lines. . . . 141
5.6 eSPIM imaging of interaction between primary $CD8^+$ T cells and CD58LO ImmTAC-labelled U-2 OS cells. . . . 144
5.7 eSPIM imaging of interaction between primary $CD8^+$ T cells and CD58LO+ICAM-1 ImmTAC-labelled U-2 OS cells. . . . 145
5.8 eSPIM imaging of interaction between primary $CD8^+$ T cells and CD58LO U-2 OS cells in the absence of TCR ligand. . . . 146
5.9 eSPIM imaging of interaction between primary $CD8^+$ T cells and CD58LO+ICAM-1 U-2 OS cells in the absence of TCR ligand. . . . 147
5.10 eWM imaging of interaction between primary $CD8^+$ T cells and ImmTAC-labelled CD58LO or CD58LO+ICAM-1 U-2 OS cells. . . . 149
5.11 eWM imaging of interaction between a single primary $CD8^+$ T cells and ImmTAC-labelled CD58LO or CD58LO+ICAM-1 U-2 OS cells. . . . 151
5.12 Analysis of the topography and the dynamics of close contacts at the interface of T cells and U-2 OS cells. . . . 152
5.13 eWM imaging of calcium flux during interactions of single primary $CD8^+$ T cells and CD58LO+ICAM-1 U-2 OS cells. . . . 155

5.14 eWM imaging of calcium flux during interactions of single primary CD8$^+$ T cells and CD58LO U-2 OS cells. 156
5.15 eWM imaging of interaction between primary CD8$^+$ T cells and CD58LO U-2 OS cells in the absence of TCR ligand. 158
5.16 eWM imaging of interaction between primary CD8$^+$ T cells and CD58LO+ICAM-1 U-2 OS cells in the absence of TCR ligand. . . 159
5.17 eWM imaging of the TCR ligand at the interface between a single primary CD8$^+$ T cells and hGP100-pulsed U-2 OS cells. 161
5.18 eWM imaging of TCR ligand at the interface between a single primary CD8$^+$ T cells and GP100-SCT U-2 OS cells. 163
5.19 eWM imaging of ZAP70 recruitment to the close contacts at the interface between a single ZAP70-HaloTag primary CD8$^+$ T cell and CD58LO+ICAM-1+GP100-SCT U-2 OS cells. 164
5.20 eWM imaging of CD45 segregation from the close contacts at the interface between a single primary CD8$^+$ T cell and CD58LO+ICAM-1 U-2 OS cells. 165
5.21 SDCM imaging of CD45 segregation from the close contacts at the interface between primary CD8$^+$ T cells and CD58LO+ICAM-1 U-2 OS cells. 167
5.22 eWM imaging of interaction between a single primary CD8$^+$ T cells and CD58HI U-2 OS cells. 168

6.1 Expression and purification of the N-MED ImmTAC. 176
6.2 Biophysical validation of the N-MED ImmTAC. 180
6.3 Functional validation of the N-MED ImmTAC. 180
6.4 Cryo-fluorescence widefield montage of a coverslip containing primary CD8$^+$ T cell/CD58LO U-2 OS cell conjugates. 182
6.5 Cryo-fluorescence widefield montage of a coverslip containing ZAP70-HaloTag primary CD8$^+$ T cell/WT U-2 OS cell conjugates. 183
6.6 Cryo-fluorescence widefield microscopy images of primary CD8$^+$ T cell/CD58LO U-2 OS cell conjugates. 186
6.7 Cryo-fluorescence widefield microscopy images of ZAP70-HaloTag primary CD8$^+$ T cell/WT U-2 OS cell conjugates. 186
6.8 Cryo 3D-SIM images of primary CD8$^+$ T cell/CD58LO U-2 OS cell conjugates. 188
6.9 X-ray tomography images of resin-embedded primary CD8$^+$ T cell/CD58LO U-2 OS cell conjugates. 189
6.10 FIB-SEM images of primary CD8$^+$ T cell/CD58LO U-2 OS cell conjugates. 190

A.1 Primary CD8$^+$ T cells can activate in response to a *bona fide* single ImmTAC. 239

List of Tables

2.1 Tissue culture media and supplements 54
2.2 Antibodies and staining reagents for flow cytometry 64
2.3 Antibodies and staining reagents for microscopy 68

List of Abbreviations

3D-SIM . . . . Three-dimensional structured illumination microscopy

ACT . . . . . Adoptive Cell Therapy

AF . . . . . Alexa Fluor

aMDM . . . . Activating monocyte-derived dendritic cell medium

ANOVA . . . . Analysis of variance

APC . . . . . Antigen presenting cell

BCR . . . . . B-cell receptor

BiTE . . . . . Bispecific T-cell engager

B2M . . . . . β_2-microglobulin

BRS . . . . . Basic rich sequence

BSA . . . . . Bovine serum albumin

CAR . . . . . Chimeric antigen receptor

CC . . . . . Close contacts

CDR . . . . . Complementarity-determining region

CLEM . . . . . Correlative light and electron microscopy

CLP . . . . . Common lymphoid progenitor

Csk . . . . . C-terminal Srk kinase

cSMAC . . . . Central supramolecular activation cluster

CTLA-4 . . . . Cytotoxic T-lymphocyte associated protein 4

DAG . . . . . Diacylglycerol

DART . . . . . Dual-affinity re-targeting molecules

DC . . . . . Dendritic cells

dSMAC . . . . Distal supramolecular activation cluster

EC_{50} . . . . . Half-maximal effective concentration

ECD . . . . . Extracellular domain

eSPIM . . . . . Epi-illumination selective plane illumination microscopy

eWM . . . . . Epifluorescence widefield microscopy

EM . . . . . Electron microscopy

ERM . . . . . Ezrin/radixin/moesin

Fab . . . . . Fragment antigen-binding

FACS . . . . . Fluorescence-activated cell sorting

FBS . . . . . Fetal bovine serum

FS . . . . . Freeze substitution

FWHM . . . . Full width at half maximum

GADS . . . . . Grb2-related adapter protein 2

HKM . . . . . HEK 293T medium

hGP100 . . . . Heteroclitic GP100 peptide

ImmTAC . . . Immune-mobilizing Monoclonal TCR against Cancer

IgSF . . . . . Immunoglobulin superfamily

iRPMI . . . . Imaging T cell medium

ITAM . . . . . Immunoreceptor tyrosine-based activating motif

ITK . . . . . IL-2 inducible tyrosine kinase

JF . . . . . Janelia Fluor

JTM . . . . . Jurkat T cell medium

$\mathbf{K_D}$ . . . . . Equilibrium dissociation constant

$\mathbf{k_{off}}$ . . . . . Dissociation rate constant

$\mathbf{k_{on}}$ . . . . . Association rate constant

KS . . . . . Kinetic segregation

LAT . . . . . Linker for the activation of T cells

Lck . . . . . Lymphocyte-specific protein tyrosine kinase

$\mathbf{LN_2}$ . . . . . Liquid nitrogen

LPS . . . . . Lipopolysaccharide

LSCM . . . . . Laser scanning confocal microscopy

LLSM . . . . . Lattice light sheeting microscopy

LM . . . . . Light microscopy

MACS . . . . . Magnetic-activated cell sorting

MDM . . . . . Monocyte-derived dendritic cell medium

MHC . . . . . Major histocompatibility complex

MIP . . . . . Maximum intensity projection

moDC . . . . . Monocyte-derived dendritic cell

PAGE . . . . . Polyacrylamide gel electrophoresis

PBMC . . . . Peripheral Blood Mononuclear Cells

PBS . . . . . Phosphate-buffered saline

PD-1 . . . . . Programmed Death 1

PE . . . . . Phycoerythrin

PHA . . . . . Phytohemagglutinin

PIP_3 . . . . . Phosphatidylinositol triphosphate

PLC . . . . . Peptide loading complex

PLCγ . . . . . Phospholipase C γ 1

pMHC . . . . . Peptide-major histocompatibility complex

PLC . . . . . Peptide loading complex

PRR . . . . . Pattern recognition receptor

PTCM . . . . Primary T cell medium

pSMAC . . . . Peripheral supramolecular activation cluster

RPMI . . . . . Roswell Park Memorial Institute

RPTP . . . . . Receptor-like protein tyrosine phosphatase

ROI . . . . . Region of interest

RT . . . . . Room temperature

scFv . . . . . Single-chain fragment variable

SCT . . . . . Single chain trimer

SDCM . . . . . Spinning disk confocal microscopy

SDS . . . . . Sodium dodecyl sulfate

SEC . . . . . Size exclusion chromatography

SEM . . . . . Standard error of the mean

SHP2 . . . . . Src-homology phosphatase-2

SIGLEC . . . . Sialic acid-binding immunoglobulin-like lectins

SiR . . . . . Silicon Rhodamine

SLB . . . . . Supported lipid bilayer

SLP-76 . . . . SH2 domain-containing leukocyte protein 76 kDa

SMAC . . . . . Supramolecular activation cluster

SMLM . . . . Single-molecule localisation microscopy

SPR . . . . . Surface plasmon resonance

S1P Sphingosine-1-phosphate

TAA . . . . . Tumour-associated antigens

TCR . . . . . T-cell receptor

TEM . . . . . Transmission electron microscopy

TIL . . . . . Tumour infiltrating lymphocytes

TIRFM . . . . Total internal reflection fluorescence microscopy

TM . . . . . Transmembrane

TSA . . . . . Tumour-specific antigens

U2M . . . . . U-2 OS cell medium

WGA . . . . . Wheat germ agglutinin

WT . . . . . Wild type

ZAP-70 . . . . Zeta-chain-associated protein kinase 70

1 Introduction

Contents

1.1 How we live and how we die, the secret life of T cells 2
1.1.1 Overview of the immune system . . . 2
1.1.2 Development of T cells . . . 4
1.1.3 T-cell trafficking . . . 6
1.1.4 Antigen presentation . . . 7
1.2 Molecular and cellular determinants of T-cell interactions . . . 10
1.2.1 Antigen recognition apparatus . . . 10
1.2.2 T-cell adhesion system . . . 17
1.2.3 Glycocalyx . . . 21
1.2.4 T-cell surface . . . 22
1.3 T-cell activation . . . 25
1.3.1 TCR signalling pathways . . . 25
1.3.2 Early T cell/target cell interactions . . . 28
1.3.3 Immune synapse . . . 31
1.4 Models of T-cell receptor triggering . . . 33
1.4.1 Oligomerisation . . . 33
1.4.2 Conformational change . . . 34
1.4.3 Kinetic segregation . . . 38
1.4.4 TCR triggering models, antigen discrimination and sensitivity . . . 40
1.5 T cell-redirecting immunotherapies . . . 43
1.5.1 Immunotherapy targets . . . 43
1.5.2 Adoptive cell transfer . . . 44
1.5.3 T-cell engagers . . . 45
1.6 Methods for imaging of T-cell activation . . . 47
1.6.1 Cellular substrates . . . 47
1.6.2 APC and target cell surrogates . . . 48

1.7 Aims of this thesis 50

1.1 How we live and how we die, the secret life of T cells

1.1.1 Overview of the immune system

1.1.1.1 Historical perspective on T lymphocytes

Over 100 years have passed since Paul Ehrlich formulated the 'side chain' theory conceptualising the recognition of non-self by host-produced factors before the discovery of antibodies and the complement system[1]. The initial focus on humoral responses has shifted to lymphocytes originating in the thymus following seminal work by Jacques Miller showing that neonatal thymectomy abrogates immune responses. Later came the discovery of the histocompatibility genes which were identified as potential ligands for T lymphocytes by Doherty and Zinkernagel. The functional relevance of T lymphocytes was revealed in experiments showing that the depletion of cells originating from the thymus abolishes cytotoxic responses against allogeneic tissues. The curative potential of T cells in the context of cancer, which has defined T-cell biology over the last two decades, was illustrated in a series of pioneering studies whereby prior exposure to cancer cells conferred protection against the tumour[2,3]. These studies culminated in the first demonstration by Rosenberg et al. that cancer-reactive T cells can be manipulated *ex vivo* and mediate tumour regression in humans upon re-infusion[4]. As the study of the immune system evolved from a largely cellular to a molecular science, it has become clear that the antigen receptor expressed by T lymphocytes, the T cell receptor (TCR) is central to these 'magic-bullet-like' responses. Nevertheless, the inner workings of the T lymphocytes which allow the TCR to recognise antigens with unparalleled discriminative power and sensitivity remain unclear.

1.1.1.2 Innate system

The innate immune system represents an ancient form of immunity found across domains of life[5]. The immune cells that constitute the innate arm of the immune system arise from the differentiation of the common myeloid progenitor and include macrophages, granulocytes, mast cells and dendritic cells (DCs). It needs to be noted that some subsets of dendritic cells can also develop from the common lymphoid progenitor (CLP). The recognition of non-self by innate immune cells involves several families of germline-encoded pattern recognition receptors (PRR)[6]. PRRs are specific for highly conserved pathogen-associated molecular patterns or damage-associated molecular patterns. These PRR families include Toll-like receptors, NOD-like receptors, RIG-like receptors and DNA sensors exemplified by the cGAS-STING pathway. The innate immune system also has a humoral component known as the complement system. The complement system directly recognises pathogen-associated molecular patterns by soluble oligomeric lectin receptors binding to glycans that are not terminated by a sialic acid residue, but it can also indirectly bind to protein antigens via antibodies[7]. Activation of the complements results in the production of inflammatory mediators and lysis of the pathogen through the formation of a so-called membrane attack complex.

1.1.1.3 Adaptive system

The adaptive immune system is restricted to jawed vertebrates and several species of jawless fish[8]. The adaptive system is primarily distinguished from the innate system by the expression of antigen receptors that are not germline-encoded but are generated through somatic recombination of gene segments. The gene segments that give rise to the variable regions of the Gnathostomata antigen receptors are known as variable (V), diversity (D), and joining (J). The VDJ rearrangements are mediated by an array of proteins, the most important of which are RAG1/2 recombinases[9]. V(D)J recombination results in a repertoire of genetically rearranged, clonally distributed antigen receptors.

Differentiation of the CLP gives rise to multiple lineages including Natural Killer cells and innate lymphoid cells, but only B and T lymphocytes express the rearranged antigen receptors arising from V(D)J recombination. The B cell receptor (BCR) is a bivalent molecule which predominantly recognises conformational epitopes on proteins in their native state. The TCR is a monovalent molecule composed of two chains, α and β or γ and δ; however, T cells expressing the $\alpha\beta$ constitute the majority of T lymphocytes (~95%). Predominantly, $\alpha\beta$TCRs recognise linear epitopes in the form of short peptides presented on the cell surface by highly polymorphic major histocompatibility (MHC) molecules. The TCR is composed of two polypeptide chains, α and β, both of which are type I transmembrane proteins with their extracellular domains composed of two immunoglobulin superfamily (IgSF) domains. The structure of the TCR can be divided into a variable region and a constant region, both of which are composed of two IgSF domains. Vα and Vβ domains, comprising the variable region, both have three flexible loops known as complementarity-determining regions (CDR) which come together to form a binding site, also known as the paratope, for the peptide-MHC (pMHC) complex. The constant region is composed of Cα and Cβ domains which are directly linked to the transmembrane (TM) region and do not participate in antigen recognition. The assembly of TCRs from the V(D)J segments is highly controlled and takes place during T-cell development in the thymus.

1.1.2 Development of T cells

Development of T cells from the CLP is initiated through Notch1 signalling which leads to the expression of T-cell specific combination of transcription factors such as TCF-1 and GATA-3[10,11]. The thymocytes progress through several stages marked by changes in the expression of surface receptors, crucially the two co-receptors CD4 and CD8 (see section 1.2.1.4)[12]. As a result, developing T cells can be divided into three groups: double-negative ($CD4^-CD8^-$), double-positive ($CD4^+CD8^+$) and single-positive ($CD4^+CD8^-$ or $CD4^-CD8^+$)[12]. The key events of the T-cell development are as follows.

First, the recombination of V(D)J gene segments to assemble a functional TCR (see section 1.2.1.1). The β chain is assembled from three segments V, D, and J with the junction between the three segments located within the CDR3, and a constant (C) segment. The C segments are not subject to recombination but rather are joined to the V(D)J segment through alternative splicing. Due to a phenomenon of junctional diversity whereby random nucleotides are inserted into the junctions between the V(D)J segments, the CDR3 loops are highly diverse. Whether a stable β chain was assembled is tested by its association with pre-T-cell α chain to form a pre-TCR[13]. If the pre-TCR cannot signal, another round of recombination takes place involving the set of DJ segments located directly upstream from the TRBC2 locus or the β-chain locus on the other chromosome. Allelic exclusion ensures that only one β chain chain is expressed as thymocytes progress to the double-positive stage. Next, V and J segments corresponding to the α chain are rearranged. Similar to the CDR3 of the β chains, the CDR3 of the α chains contains the junction between V and J segments. The α chain loci do not undergo allelic exclusion, thus mature T cells can express two α chains; however, the probability of both chains being functional is low and most T cells express a single TCR on their surface[14].

Second, positive selection ensures that the assembled TCR can bind to one of the MHC molecules encoded by the MHC loci of the given individual. Double-positive thymocytes enter positive selection while the α chain loci are still undergoing rearrangements. Positive selection takes place in the cortex of the thymus where thymocytes interact with cortical thymic epithelial cells which abundantly express MHC class I and class II molecules[15,16]. T cells expressing a TCR capable of interacting with MHC class I and class II are committed to $CD4^+$ and $CD8^+$ lineage, respectively[17]. T cells that cannot interact with either of the MHC molecules undergo death by neglect. Hereafter, thymocytes are referred to as single-positive. The $CD4^+$ versus $CD8^+$ lineage commitment endows T cells with a set of functional properties. In the periphery, the $CD4^+$ T cells primarily act by releasing immunomodulatory cytokines and regulate the behaviour of other

leukocytes e.g. macrophages. Crucially, $CD4^+$ T cells provide 'help' to B cells to improve humoral responses. In contrast, the primary function of $CD8^+$ T cells is cytotoxicity – killing of infected or transformed cells.

Third, negative selection to ensure that T cells whose TCRs display high reactivity to self pMHC complexes are eliminated. This process takes place in the region of the thymus known as the medulla where thymocytes interact with medullary thymic epithelial cells (mTEC). The expression of tissue-restricted antigens by mTEC is achieved through the expression of a promiscuous transcription factor known as an autoimmune regulator[18]. According to the affinity model of thymic selection, T cells expressing a TCR interacting with self pMHC with high affinity undergo clonal deletion, whereas intermediate affinity induces the T cells to adopt a regulatory phenotype[19]. Following successful progression through negative and positive selection, naïve T cells egress from the thymus and migrate to secondary lymphoid organs[20].

1.1.3 T-cell trafficking

Following egress from the thymus, naïve T cells circulate through the secondary lymphoid organs and blood to maximise the chances of an antigen encounter[21–23]. T cells extravasate from the bloodstream via high endothelial venules into the lymph nodes, where they survey the DCs therein for 6-12 hours before they exit through the efferent lymphatic vessels and migrate into another lymph node[21,24]. Within the lymph nodes, T cell migration is regulated by interactions of a chemokine receptor CCR7 with its ligands CCL19 and CCL21, both of which are abundantly expressed by lymph-node resident fibroblastic reticular cells[21,25]. The exit from the lymph nodes back into the bloodstream via the efferent lymphatic vessels is regulated by a gradient of sphingosine-1-phosphate (S1P), which is maintained at a higher concentration in the blood and lymph than the secondary lymphoid organs[26,27]. T cells detect the S1P gradient via a G-protein coupled receptor, $S1P_1$, whose expression is upregulated upon entry into the lymph nodes[27]. Thus, modulation of the $S1P_1$ receptor is vital to retaining

the naïve T cells in the lymph node following recognition of cognate pMHC. Expression of a C-type lectin CD69 on the T cell surface in response to TCR signalling promotes internalisation and degradation of $S1P_1$ preventing migration out of the secondary lymphoid organs[28]. However, CD69 expression is transient and following activation and expansion, T cells re-enter the bloodstream[20,21].

In the context of cancer immunity, to mount an effective antitumour response, the naïve T cells need to be primed by cross-presenting DCs (see next section) in the secondary lymphoid tissues[29]. This step is highly dependent on the ability of the DCs to capture fragments of cancer-cell debris and present them to T cells in the presence of pro-inflammatory cytokines so as not to induce tolerogenic responses. Under optimal conditions, following egress from the secondary lymphoid organs, the T cells will traffic to the site of the tumour, recognise the cancer antigens and eliminate them. The $CD8^+$ T cells are the primary effectors in the antitumour responses, but $CD4^+$ T cells also have been shown to have role[30,31]. T cells face multiple barriers which prevent them from efficient recognition of tumour cells and execution of effector mechanisms[29]. Some of those with relevance to this thesis include loss of MHC expression, downregulation of adhesion molecules required for interactions with T cells, and upregulation of physical glycoprotein barriers on their surface[32–36].

1.1.4 Antigen presentation

$CD8^+$ and $CD4^+$ T cells interact with peptides associated MHC class I (MHC-I) and class II (MHC-II), respectively (Figure 1.1A)[37]. MHC-I is composed of a heavy chain associated with β_2-microglobulin (β_2M)[37]. The heavy chain is composed of three domains (α1-3) and has a single-pass transmembrane region. MHC-II is composed of two chains, α and β, each with a distinct transmembrane region. For both types of MHC, the peptide binds in a so-called peptide binding groove located at the top of the MHC molecules where it is flanked by two long α helices and sits on a β-sheet 'saddle'. The K_D values for the peptide-MHC interaction are below 500 nM. There are structural differences in how the peptides

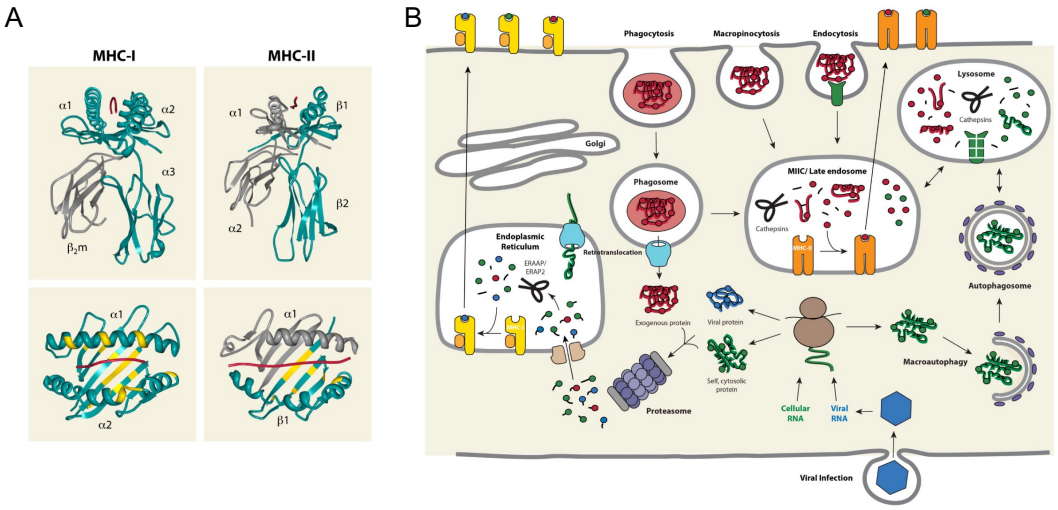


Figure 1.1: Pathways of antigen presentation. A. Structures of MHC molecules class I (left) and class II (right). MHC class I molecules are composed of a heavy chain and a non-covalently associated β_2-microglobulin. The heavy chain is composed of the α1-3 domains and a transmembrane region. The α1 and α2 domains constitute the peptide-bindind groove. The α3 domain contains a CD8 co-receptor binding site. **B**. MHC class II molecules are composed of two chains α and β each containing a transmembrane region. The α1 and β domains form the peptide-binding groove. The binding site of the CD4 co-receptor is located at the interface of the α2 and β2 domains. **B**. Pathways of antigen presentation. For presentation on MHC class I molecules, ubiquitinated intracellular proteins are degraded by the proteasome and translocated into the endoplasmic reticulum (ER) by the TAP transporter. Within the ER, peptides are edited by ERAPP aminopeptidases and peptide loading is regulated by the peptide-loading complex composed of calreticulin, ERp57 and tapasin. Stably associated peptide-MHC class I complexes are then trafficked from the ER to the plasma membrane. Cross-presenting antigen-presenting cells such as dendritic cells can also direct extracellular material ingested through phagocytosis and micropinocytosis into the MHC class I processing pathway. For presentation on MHC class II molecules by antigen-presenting cells, ingested material is degraded within lysosomes which fuse with endosomes containing MHC class II molecules. Within the endosomes, the loading of peptides onto the MHC is regulated by HLA-DM and HLA-DO. Figure was adapted from Blum et al.[37]

are bound by the two MHC classes. In MHC-I, the termini of the peptide are enclosed by the binding groove, while in MHC II the peptide can extend beyond its confines. As a result, the peptides bound to MHC-I and MHC-II are 8-10 and 13-17 residues in length, respectively. The membrane-proximal regions of both MHC molecules are composed of IgSF domains.

While MHC-I is expressed on all nucleated cells, MHC-II is exclusively expressed on antigen-presenting cells (APC) such as DCs, B cells or macrophages.

The processes that underlie the loading of peptides onto MHC-I and MHC-II rely on different pathways relying on proteolysis of either the endogenous or exogenous proteins, respectively[37].

The peptides destined for presentation on MHC-I complexes arise from proteins degraded by the proteasome in the cytoplasm (Figure 1.1B). Subsequently, the peptides are translocated into the endoplasmic reticulum (ER) by a transporter associated with antigen processing (TAP), which is associated with the peptide-loading complex (PLC)[38–40]. The components of the PLC: calreticulin, ERp57 and tapasin, facilitate the loading of the peptides onto empty MHC-I complexes[37]. Additionally, in the ER lumen, the N-terminal of the peptide is trimmed by ER aminopeptidases (ERAPP and ERAP1) to adjust its length and expose a preferred N-terminal anchor residue for the MHC-I binding[41] . The ERp57-tapasin complex promotes the exchange of peptides until a high-affinity peptide binds to the groove of MHC-I[37,42] . Following the formation of a stable peptide-MHC (pMHC) complex, the PLC dissociates and the pMHC is transported to the cell surface. The MHC class I loaded with peptides from foreign or mutated proteins can be recognised by $CD8^+$ T cells in the periphery which then eliminate the infected or transformed cells. However, such $CD8^+$ T cells need to be first primed in the secondary lymphoid organs before they can exert effector functions. Cross-presentation is a mechanism whereby professional APCs, predominantly DCs, can present peptides derived from intracellular proteins of other cells on MHC-I molecules (Figure 1.1B)[43]. To this end, APCs ingest extracellular material through phagocytosis and macropinocytosis and this allows them to acquire material from dying or dead cells[43,44,45]. Additionally, DCs may also absorb exosomes containing cytoplasmic proteins[46]. There are two main pathways for loading exogenous onto MHC-I molecules[43,47]. First, the cytosolic pathway which requires a release of the exogenous material from phagosomes into the cytoplasm and these proteins then enter the classical MHC-I processing pathway[48]. Second, the vacuolar pathway which involves degradation of the exogenous proteins and MHC-I loading within the phagosome followed by trafficking of the pMHC-I

to the cell surface[47]. The cytosolic pathway appears to be the predominant mechanism of cross-presentation[49,50].

The proteins for presentation on MHC-II molecules are internalised by APCs through a combination of endocytosis, phagocytosis and micropinocytosis (Figure 1.1B)[37]. The vesicles containing the exogenous proteins then enter the lysosomal pathway leading to degradation of the external material by cathepsins. MHC-II molecules are assembled in the ER where they are prevented from associating with peptides by an invariant chain that blocks their binding groove (Figure 1.1B). Through the association of three invariant chains, MHC-II molecules in the ER assemble into trimers[51,52]. As the MHC-II trimer is trafficked from the ER into the endocytic pathway, the MHC-II are released from the association with the invariant chain through proteolysis and assume a monomeric form. However, a fragment of the invariant chain known as CLIP remains bound to the peptide binding groove[53]. The late endosomes containing CLIP-MHC-II complex fuse with lysosomes and early endosomes carrying the peptides derived from exogenous proteins[54]. The exchange of CLIP for other peptides is facilitated by a HLA-DM/HLA-DO complex which acts in a manner analogous to PLC leading to the formation of MHC-II complexes bound to high-affinity peptides[55]. Presentation of peptides on MHC-II molecules by DCs in the lymph nodes is necessary for priming of naïve $CD4^+$ T cells.

1.2 Molecular and cellular determinants of T-cell interactions

1.2.1 Antigen recognition apparatus

1.2.1.1 T-cell receptor complex

The TCR/CD3 complex is an octameric membrane-embedded receptor composed of four heterodimers (Figure 1.2) The TCR heterodimer is composed of α and β chains, non-covalently associated with two invariant heterodimers CD3$\gamma\epsilon$, CD3$\gamma\delta$, and two disulphide-linked CD247 ζ-chains[56,57] All four heterodimers are type I transmembrane proteins with their α-helical TM domains arranged

into two-helix bundles held together in the membrane environment through a network of hydrophobic and ionic interactions[56].

The main differences in the structure of the four heterodimers come from their distinct ECDs and cytoplasmic regions. The ECDs of TCRα and TCRβ chains are composed of two IgSF domains per chain with the membrane-proximal, constant domains (Cβ and Cα) encoded by the constant TRBC1/2 and TRAC genes and the membrane-distal variable domains (Vβ and Vα) encoded by the V(D)J re-arranged variable loci . The TCR$\alpha\beta$ engages the pMHC complexes via six complementary determining regions (CDR) located at the top of the variable domains with each of the domains contributing three CDR loops. The three CD3 heterodimers have similar ECDs, with each of the constituent chains (γ, δ, 2xϵ) having only one IgSF domain. Uniquely, the ECD of CD3ζ chains are very short being composed of just nine amino acid residues.

Despite being directly responsible for the recognition of pMHC, the cytoplasmic tails of TCR$\alpha\beta$ do not contain signalling motifs. In turn, the three heterodimers collectively bear 10 immunoreceptor tyrosine-based activation motifs (ITAM) with a consensus sequence of Yxx(L/I)$x_{6\text{-}8}$Yxx(L/I)[58]. Each of the CD3γ, δ, ϵ chains contains a single ITAM, whereas the ζ chains contain three ITAMs each. The tyrosine (Y) residues within ITAMs become phosphorylated by Lck kinase upon binding of the TCR to a cognate pMHC (Figure 1.3A).

The conformational arrangement of the ITAMs in the cytoplasmic space is a matter of active debate, as it has been suggested that TCR triggering may involve their rearrangement upon pMHC binding (see section 1.4.2). In the most recent, cryoEM structure of the unligated TCR/CD3 complex the electron densities corresponding to the cytoplasmic tails couldn't be resolved suggesting them to be intrinsically disordered[56].

For a time, the TCR/CD3 complex was proposed to form higher-order assemblies which were invoked to explain the single-pMHC T-cell sensitivity[59–62]. Formation of TCR clusters or multivalent TCR/CD3 complexes on the resting T cell surface was primarily supported by biochemical experiments and electron

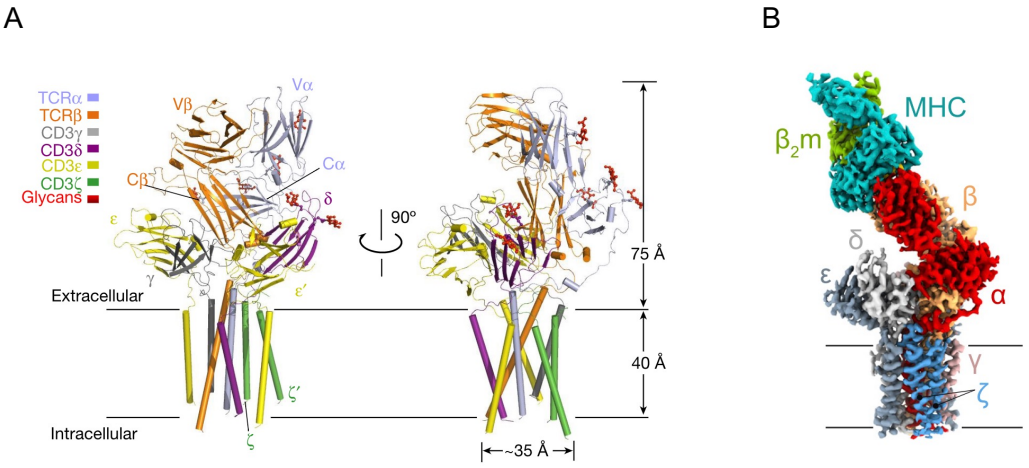


Figure 1.2: Structure of the T-cell receptor complex. Cryo-EM structures of the T-cell receptor complex in **A**. apo and **B**. holo states. The T-cell receptor complex is composed of eight chains arranged in four dimers: TCR$\alpha\beta$, CD3$\epsilon\gamma$, CD3$\epsilon\delta$, and CD3$\zeta\zeta$. The TCR$\alpha\beta$ dimer binds to the native TCR ligand, pMHC via CDR loops, but has very short cytoplasmic domains and does not have an intrinsic signalling capacity. The remaining subunits of the T-cell receptor complex contain a total of ten immunoreceptor tyrosine-based activation motifs which are phosphorylated upon binding of an agonist pMHC to the TCR$\alpha\beta$ dimer. The TCR$\alpha\beta$ is tilted by 59° relative to the plasma membrane. The structure of the cytoplasmic domains has not been resolved to date. Figures were adapted from Dong et al.[56] and Susac et al.[57]

microscopy[63,64]. However, spectroscopic studies of TCR/CD3 complex on an intact resting T-cell surface argue against the existence of multivalent TCR/CD3 complexes[65,66]. The recent cryo-EM structures further support this data and so, it is highly likely that the TCR/CD3 complex exclusively exists in a monomeric state[56,57,67,68].

1.2.1.2 Lck kinase

While different mechanisms have been proposed to explain how ligand binding induces TCR triggering (see section 1.4.2), all agree that the phosphorylation of its cytoplasmic tails is performed by a lymphocyte-specific protein tyrosine kinase (Lck), an enzyme belonging to the Src kinase family[69]. Lck is composed of an SH3, SH2 and tyrosine kinase (SH1) domains. The activity of Lck is largely restricted to the plasma membrane, where it is anchored through myristoylation and palmitoylation of two residues near its N-terminus[70,71]. A fraction of total Lck associates with the co-receptors CD4 and CD8 via its N-terminal, thus, there are

two populations of Lck, free and co-receptor-bound[72]. Additionally, Lck was shown to interact with the proline-rich motifs in the cytoplasmic domains of CD2[73].

Lck has a non-trivial regulatory mechanism with implications for the TCR triggering mechanism (Figure 1.3B). The key elements of Lck regulation are the SH2 domain and two regulatory residues, Y349 and Y505 located within the activation loop and the C-terminal tail, respectively. Both tyrosine residues can be dephosphorylated by CD45 phosphatase, but Y505 is phosphorylated by a C-terminal Srk kinase (Csk) and Y394 is subject to autophosphorylation.

Upon phosphorylation, the Y505 residue can interact with the SH2 domain forcing Lck to adopt an auto-inhibited state. On the other hand, phosphorylation of the Y394 residue enhances the kinase activity[74,75]. The double-phosphorylated and dephosphorylated states also exist, but only the former has a significant catalytic activity[76–78]. The proportions of active Lck in a resting T cell are consequential for the TCR triggering mechanism – are sufficient amounts of active Lck constitutively present in a resting T cell or is prior Lck activation required for TCR triggering? The former scenario, known as the stand-by model, is supported by a study by Nika et al. who found that 40% of the total Lck was in the active p-Y349 state[77]. Furthermore, the amount of active Lck was found not to change following T-cell activation[77,79]. However, more recent measurements in live T cells relying on FRET-based sensors indicate that the Lck undergoes *de novo* activation corresponding to phosphorylation of the Y349 residue in response to TCR stimulation[78,80]

1.2.1.3 CD45 phosphatase

CD45 is a large transmembrane glycoprotein that belongs to the family of receptor-like protein tyrosine phosphatases (RPTP) expressed on all nucleated leukocytes. The ECD of CD45 has multiple isoforms and their expression is regulated through alternative splicing mechanisms[81]. All isoforms of CD45 contain a membrane-proximal core composed of a cysteine-rich domain (d1) and fibronectin domains (d2–d4), but some isoforms additionally contain highly glycosylated mucin-like

domains (A, B, C) at the membrane-distal N-terminus. Naïve T cells express CD45RA and memory T cells express the shortest isoform CD45RO. There is conflicting evidence regarding the functional relevance of the differential expression of CD45 isoforms across T cell subsets[82,83]. Regardless of the isoform, CD45 is highly expressed[84].

All isoforms of CD45 were shown to be rigid and extend between 25 nm (CD45RO) to 40 nm (CD45ABC) beyond the T-cell membrane[85,86]. The size mismatch between the dimensions of CD45 isoforms, TCR/pMHC complex (14 nm) and CD58/CD2 adhesion pair suggests that CD45 would be excluded from the sites of close cellular interaction stabilised by either of these two small complexes. The propensity of various CD45 isoforms to segregate from such sites purely on the basis of their size was studied in an *in vitro* reconstituted system[87]. Both the shortest and the longest isoforms were found to be excluded from the sites of TCR/pMHC accumulation, albeit the longer CD45RABC form segregates faster. Segregation of CD45 from cellular interfaces is a basis of the kinetic segregation model of TCR triggering (see section 1.4.2).

CD45 acts on the two main components of the antigen recognition apparatus, ITAMs within the cytoplasmic tails of the TCR/CD3 complex and the Lck kinase (Figure 1.3). While the dephosphorylation of the ITAMs has a clear-cut negative effect on T cell activation, dephosphorylation of Lck is less straightforward. Dephosphorylation of the residue Y505 prevents Lck from adopting the impaired auto-inhibited conformation and thus has an activating effect, but dephosphorylation of Y394 leads to full activation of the kinase domain[69]. *In vitro* studies show that CD45 has a greater preference for the ζ ITAMs over either of the sites on the Lck kinase[88].

Due to the dual CD45/Lck regulatory axis, a series of experiments were conducted to dissect the relationship between CD45 activity and the T-cell activation threshold. Ablation of CD45 from T cells renders them unresponsive to stimulation with pMHC antigens or TCR/CD3 cross-linking antibodies[89–91],

whereas hypophysiological levels of CD45 were shown to induce hyperresponsiveness, likely due to increased phosphorylation of the Lck on the Y394 residue[90,91] At physiological levels CD45 suppresses Y394 phosphorylation and restores the native threshold[90]. Nonetheless, in peripheral T cells, there is a substantial pool of active Lck (~40%)[77]. Under such conditions, inhibition of the CD45 using a tyrosine phosphatase inhibitor, pervanadate results in T-cell activation[92].

1.2.1.4 Co-receptors

CD4 and CD8 co-receptors came to denote the two major subsets of αβ T cells. Despite both having related interaction partners, the ECD of the two co-receptors are structurally distinct. The ECD of CD4 is composed of four concatenated IgSF domains stabilised through interdomain interactions and linked to a TM region[93]. The most membrane-distal IgSF domain of CD4 can bind to the non-polymorphic region of MHC class II antigens (Figure 1.3A). In contrast, CD8 is composed of two chains α and β, which can associate through an interchain disulphide to form either CD8αβ or CD8αα heterodimers, with the latter found in a small subset of T cells. Both of the chains have a single IgSF domain, each residing on the top of a heavily glycosylated extended stalk, which does not assume a secondary structure[94–96]. Both co-receptors can associate with the membrane-anchored Lck via a 'zinc clasp' whereby di-cysteine motifs in the cytoplasmic region of the co-receptor coordinate a single Zn^{2+} ion[72,97–99] The relevant cysteine residues are located in the cytoplasmic tails of the CD8α chain and CD4. Binding to the non-polymorphic region of the MHC class I and class II is mediated exclusively by the IgSF domain of the CD8α chain and the most membrane-distal IgSF domain of the CD4 co-receptor, respectively[94].

The binding of the CD8 co-receptor to MHC class I has estimated 3D K_D values of ~200 μM and ~135 μM for the human CD8αα and murine CD8αβ heterodimers, respectively[100,101]. Due to the extremely weak interactions of CD4 and MHC class II molecules in solution, to date, their binding affinity has

only been estimated through 2D measurements placing the K_D value at 5000 molecules/μm^2 equivalent to a 3D K_D value of 5.1 mM[102].

Although initially described as intercellular adhesion molecules, the current view is that co-receptors augment the TCR signalling principally through two mechanisms[103,104]. First, recruitment of the Lck-associated co-receptors to the TCR/pMHC complex would increase the local kinase activity thus increasing the probability of TCR triggering. The second mechanism, independent of the kinase activity of Lck, involves stabilisation of the TCR/pMHC complex through binding of SH2 domain of the Lck to ITAMs pre-phosphorylated by the free Lck[105–109]. This would result in the formation of a ternary complex where TCR and pMHC interact both directly and indirectly through the co-receptor.

Co-receptor recruitment was also implicated in enhancing antigen discrimination by providing a mechanistic basis for kinetic proofreading (see section 1.4.4). This mechanism assumes that a low proportion of co-receptors exist in an Lck-bound state, and TCR triggering can only occur solely after the recruitment of co-receptors bearing an active Lck kinase[110]. Consequently, multiple co-receptors need to associate with the TCR/pMHC complex before triggering, favouring long-lived TCR/pMHC interactions. However, this mechanism is disputed as the CD4 co-receptor was recently found to exist primarily in Lck-bound form, whereas the occupancy of the CD8 co-receptor is ~60%[111]. Furthermore, TCR is more dependent on co-receptors for recognition of low-affinity, rather than high-affinity ligands arguing against their proposed role in antigen discrimination[112]. Several models of TCR triggering based on co-receptor recruitment were proposed (see section 1.4.1).

1.2.1.5 ZAP70 kinase

ZAP70 is a tyrosine kinase with a unique domain architecture, it is composed of tandem SH2 domains and a tyrosine kinase domain (SH1)[113]. Only the Syk kinase which has an analogous function in B cells has a similar domain arrangement. The tandem domains reflect the binding mode of ZAP70 to the

two neighbouring phosphorylated tyrosine residues in the ITAMs. The bidentate interaction increases its affinity for cytoplasmic tails of TCR/CD3 complex up by 100-fold[9,114,115]. ZAP70 also contains two interdomain regions, A and B, one located between the two SH2 domains and one between the SH2 and the SH1 domains, respectively.

As ZAP70 binds to the phosphorylated ITAMs, it becomes phosphorylated by Lck on Y493 within the kinase activation loop which allows it to adopt an active conformation (Figure 1.3A). Subsequently, Y315 and Y319 residues within interdomain B are phosphorylated by Lck increasing the dwell-time of ZAP70 at the membrane[116] . Thereafter, phosphorylation on Y126 residue located in interdomain A and binding of ATP leads to a reduction in the affinity of ZAP70 for the phosphorylated ITAMs and facilitates its dissociation from the TCR. The delayed dissociation of the active ZAP70 kinase from the TCR was dubbed a 'catch-and-release' model and was hypothesised to lead to the dispersal of the TCR signal[116]. The release of ZAP70 from the TCR is also facilitated by CD45-driven dephosphorylation of ITAMs permitted by the cyclic unbinding and rebinding of the tandem SH2 domains[115] . The active ZAP70 initiates the downstream signalling by phosphorylation of the TM protein, linker for the activation of T cells (LAT) and SH2-domain-containing leukocyte protein of 76 kDa (SLP-76)[117].

1.2.2 T-cell adhesion system

1.2.2.1 LFA-1/ICAM-1

LFA-1 is an adhesion molecule belonging to the family of heterodimeric integrin receptors, universally expressed in leukocytes. LFA-1 is composed of non-covalently associated α_L (CD11a) and β_2 (CD18) chains[120]. Both of the chains have multidomain ECDs (a total of 13 domains) connected to short cytoplasmic domains via a single-pass TM region. Since LFA-1 is an αI integrin, its α_L chain contains an additional apical domain involved in binding to its ligand, ICAM-1. The structure of LFA-1 can be divided into the headpiece and legs. The headpiece contains the ICAM-1 binding site and can adopt either a closed conformation,

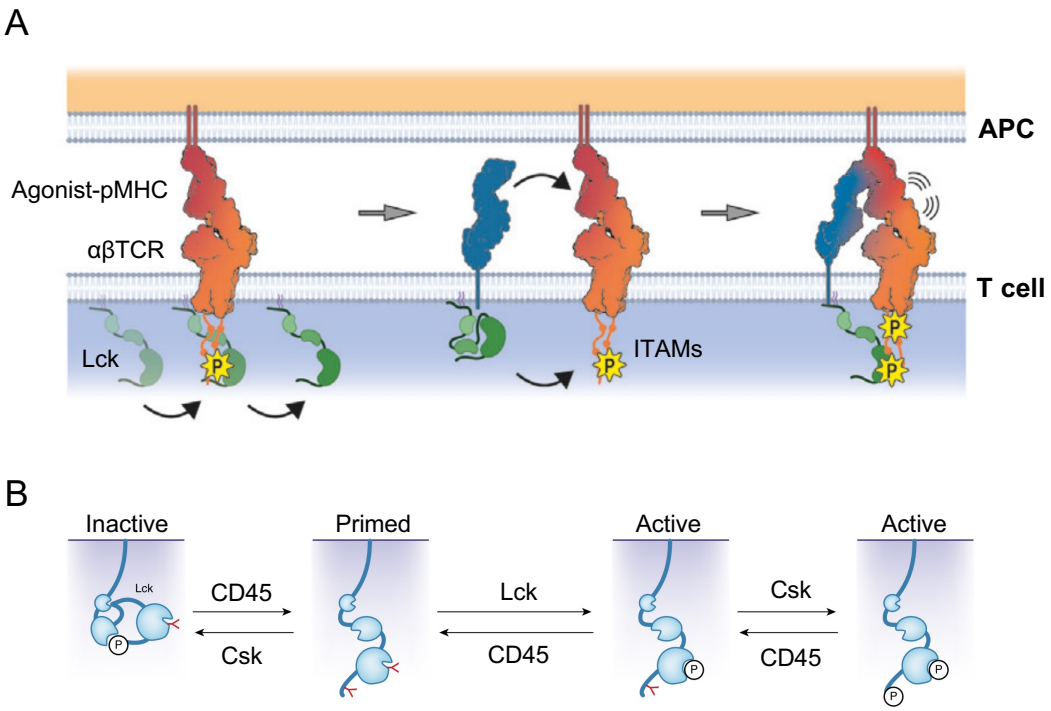


Figure 1.3: TCR triggering apparatus. A. In a resting state, the TCR/CD3 complex is kept unphosphorylated by ubiquitous CD45 phosphatase (not shown). Upon binding of the agonist pMHC to the TCR/CD3 complex, the immunoreceptor tyrosine-based activation motifs (ITAM) are phosphorylated by the Lck kinase. The Lck kinase is attached to the inner leaflet of the plasma membrane. A proportion of Lck is associated with one of the co-receptors (CD4 and CD8). The free Lck kinase mediates the initial phosphorylation of the ITAMs followed by the co-receptor-bound Lck. Additionally, the recruitment of the co-receptor the the pMHC-TCR/CD3 complex increases its stability through ternary complex formation whereby the extracellular domain of the co-receptor binds to the pMHC and the associated Lck to the phosphorylated ITAMs. Subsequently, ZAP70 kinase is recruited to the phosphorylated ITAM and it becomes phosphorylated itself by the Lck kinase. ZAP70 initiates the downstream TCR signalling. **B**. Regulation of Lck kinase activity. The activity of the Lck kinase is regulated through phosphorylation of two tyrosine residues, Y394 and Y505. Phosphorylation of the Y349, located within the kinase domain, is required for full activation of Lck. This residue is phosphorylated by Lck through trans-phosphorylation. Y505 is phosphorylated by the Csk kinase. Phosphorylated Y505 interacts with the constituent SH2 domain of Lck resulting in the adoption of an auto-inhibited conformation. Both Y394 and Y505 are dephosphorylated by the CD45 phosphatase. Figure adapted from Morch et al.[118] and Chakraborty and Weiss[119]

unfavourable to ICAM-1 binding or a binding-permissive open conformation. The legs similarly can adopt two conformations, bent or extended[121]. Collectively, through the conformational changes in these two regions, LFA-1 has three distinct conformational states: bent-closed, extended-closed and extended-open[120]. The shift from the bent-closed to the extended-open conformations of LFA-1 on the T-cell surface is associated with a 6,000-fold increase in affinity[122–124]. However, the affinity of the extended-closed conformation for its ligand has been more controversial, with an intermediate affinity being proposed[125–127]. This question was addressed by a study by Springer and colleagues where Fabs were used to selectively induce various conformations of a model αI integrin (LFA-1/2) followed by affinities measurements[125]. Only two affinity states were found to exist, defined by the conformation of the headpiece. Therefore, the intermediate affinity can be attributed to the simultaneous presence of both open and closed states on the cell surface. Indeed, some studies suggest that a small proportion of LFA-1 adopts the open conformation in resting T cells[128]. However, the extended conformation may increase the accessibility of LFA-1 for ICAM-1 binding[123].

The closed-to-open transition is regulated by the TCR and chemokines signalling[122,126,129,130]. The process via which the extracellular stimuli promote ICAM-1/LFA-1 adhesion is known as inside-out signalling. The chemokine and antigenic stimulation induce the binding of talin to the cytoplasmic domains LFA-1 which disrupts the 'clasp' between the cytoplasmic domains of the two chains allowing transition into the extended conformation[131]. Additionally, binding of ICAM-1 to the headpiece is required to complete the transition of LFA-1 into the high-affinity open state[132]. Since the stabilisation of the open state can only be achieved by a membrane-bound, but not soluble form of ICAM-1, the involvement of traction forces was suggested. It was proposed that force could be applied through the cytoskeleton linked to LFA-1 via intracellular proteins such as kindlin and paxillin[123]

LFA-1 can bind to multiple ligands of the ICAM family (1, 2, 3, 5) expressed on APCs, but ICAM-1 is its highest affinity partner[133]. ICAM-1 is composed

of five IgSF domains and extends 19 nm beyond the membrane, thus forming a complex spanning 40 nm across two membranes when bound to LFA-1 (20-25 nm) in the 'extended' conformations. The LFA-1/ICAM-1-mediated adhesion enhances the antigen sensitivity of T cells by up to 100-fold[134].

1.2.2.2 CD2/CD58

CD2/CD58 pair is an archetypic heterophilic adhesive interaction. Both CD2 and CD58 are type I membrane proteins with their ECDs composed of two IgSF domains. The two adhesion molecules measure ~7 nm in the axial direction and bind via their membrane-distal IgSF domains thus forming a complex spanning ~14 nm across the membranes. The 3D and 2D K_D values for the CD2-CD58 interaction were measured to be 9-22 μM and 21 molecules/μm^2, respectively[135,136]. Unlike LFA-1, neither CD2 nor CD58 can undergo conformational changes in response to cellular stimuli, and thus, their binding affinity is fixed. The fast kinetics of the interaction allow it to respond to the rapid remodelling of the intercellular interfaces during antigen search of T cells[137]. CD2/CD58 adhesion increases T-cell antigen sensitivity by up to 10-fold and it can synergise with the LFA-1/ICAM-1 pair[138].

The cytoplasmic domain of CD2 contains proline-rich sequences which contain five putative SH3-binding motifs, thus providing an opportunity for multiple interactions with cytoplasmic signalling proteins[73]. The potential interaction partners include kinases including Lck and Fyn, and cytoskeletal adaptors such as CIN85, CD2BP1 and CD2AP[139–144]. Recruitment of kinases to the cytoplasmic domain of CD2 accounts for its co-stimulatory properties and the observations that CD2 cross-linking can induce T-cell activation without TCR stimulation[145–147] On the other hand, recruitment of CD2AP allows CD2 to locally reshape the actin cytoskeleton in response to ligand binding allowing the T cell to alter its morphology while surveying its environment[143,148].

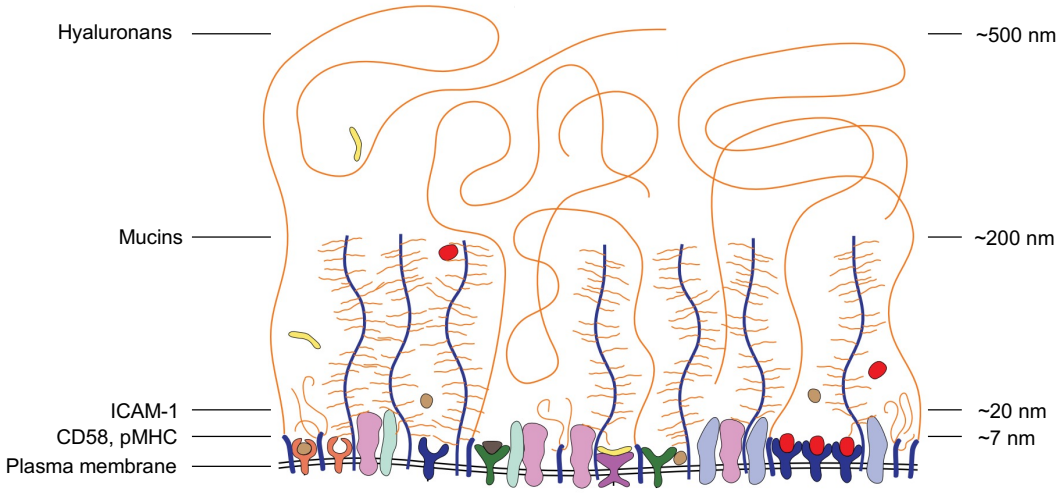


Figure 1.4: Cancer cell surface The surface of cancer cells is typically covered in a thick layer of glycocalyx whose components such as mucins and a network of hyaluronan anchored to the plasma membrane by CD44 can extend up to 500 nm beyond the cell surface. The key adhesion molecules for interactions with T cells, ICAM-1 and CD58 measure up to 20 nm and 7 nm beyond the plasma membrane. Similarly, the axial size of pMHC complex is only 7 nm. The glycocalyx creates a physical barrier that T cells need to penetrate to scan the cancer cell surface. The figure was adapted from Kuo et al.[149].

1.2.3 Glycocalyx

Cellular surfaces are typically covered in a glycocalyx layer composed of cross-linked oligosaccharised, glycoproteins and glycolipids (Figure 1.4)[32]. Since the glycocalyx often extends beyond the adhesion molecules and receptors, it determines the first intercellular interactions and regulates the access to the shorter signalling molecules[137,149,150]. Forces up to 500 pN may be needed to part the glycocalyx and engage the adhesion molecules such as ICAM-1 and CD58[151]. In addition to acting as a physical barrier, glycocalyx displays ligands of inhibitory receptors. For instance, sialic acid located at the termini of glycan chains can induce inhibitory signalling through Siglec family receptors expressed on leukocytes including T cells[152,153]. In healthy cells, the glycocalyx limits non-specific interactions and immune responses, but transformed cells harness these properties as an immune evasion mechanism[32].

The common components of cancer cell glycocalyx include glycosaminoglycans such as hyaluronan and glycoproteins, particularly mucin family proteins. Hyaluronan is a polymer composed of repeating disaccharide units produced by hyaluronan synthases, TM enzymes which simultaneously extrude into the extracellular space[32]. It can be synthesised by cancer cells which upregulate the synthase expression, but also cancer-associated stromal cells. The hyaluronan polymers are anchored to the cell surface via a transmembrane glycoprotein CD44 which itself is linked to the cortical cytoskeleton via ezrin/radixin/moesin proteins[154].

Mucin family proteins are large glycoproteins overexpressed by a wide range of cancers[32]. Mucins display a high degree of glycosylation which leads to their cross-linking by galectin-3. Such mucin/galectin-3 mesh poses an additional barrier to penetration by immune cells[155]. Some mucins, such as Muc1 can extend up to 200 nm beyond the cell membrane[151]. Additionally, Muc1 can be hypersialylated thus potentially inducing more inhibitory signalling through Siglecs-7 and Siglec-9 expressed by T cells and NK cells[153,156–158]. Partial removal of the glycocalyx layer through ablation of the Mucin-encoding genes and enzymes involved in glycosylation from cancer cells have all been shown to increase their propensity for interactions with cytotoxic lymphocytes[159–161]

1.2.4 T-cell surface

1.2.4.1 T-cell membrane topology

The surface of T lymphocytes is covered by finger-like microvillar protrusions. Analysis of early TEM and SEM images indicated that these projections measure ~100 nm in diameter and extend 300-400 nm on average beyond the cell body, but can be as long as 1 μm (Figure 1.5A and B)[163,165]. Microvilli densely cover the T cell surface with ~4 microvilli/μm^2[163]. The microvilli, as seen on the resting T-cell surface, are primarily involved in scanning the target cell surface, but upon TCR signalling the microvilli collapse and the T-cell membrane becomes flattened against the target cell[166,167].

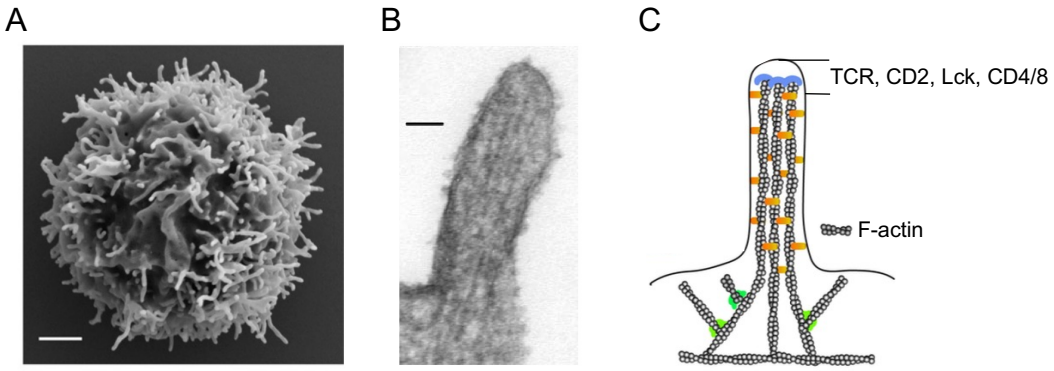


Figure 1.5: T-cell surface. A. Scanning electron microscopy image of a resting human T cell. The T-cell surface is covered with finger-like microvillar protrusions measuring up to ~400 nm and ~100 nm in length and diameter, respectively. Scale bar = 1 µm **B**. Transmission electron microscopy image of an individual T-cell microvillus showing the f-actin filaments running through the centre of the protrusion. Scale bar = 50 nm **C**. Diagram of a microvillus showing the f-actin filaments and the distribution of key T-cell surface molecules. TCR/CD3 complex, CD2, co-receptor and Lck kinase accumulate at the microvillar tip. In contrast, LFA-1 is predominantly found at the cell body and CD45 is uniformly distributed across the T-cell surface. Figures were adapted from Jung et al.[162], Majstoravich et al.[163], Kim and Jun[164].

While the EM studies of the T cell surface provided useful insights, they are prone to fixation artefacts and only offer a snapshot of dynamic events. Due to the proximity of the microvillar dimensions to the light diffraction limit and few instruments affording a sufficient temporal and spatial resolution, microvilli in live T cells had eluded detection. The development of lattice-light sheet microscopy (LLSM) allowed for these challenges to be circumvented. Using this method, microvilli were demonstrated to be highly mobile, undergo cycles of adsorption and projection from the T-cell body as well as infrequent merging[168]. In contrast to the EM studies, the thickness of microvilli was estimated to be ~540 nm using the LLSM. However, the real dimensions of microvilli are not straightforward to measure as the diffraction limit means that they likely appear larger than in reality.

The microvillar architecture and movement are orchestrated by remodelling of the actin cytoskeleton. Their tubular structure is imposed by a column of f-actin running through the centre of the microvillus (Figure 1.5B and C)[165,169]. During T-cell migration, the microvilli are primarily located at the actin-rich leading edge also referred to as the lamellipodium[165]. During scanning, T-cell microvilli can

exert sufficient force to invade tissues and deform the apposed cell membrane[165]. For that reason, microvilli have also been hypothesised to be instrumental to part of the glycocalyx layer (50-500 nm thick) on the target cell surface to access adhesion molecules and pMHC antigens[32,137,149,165,170]. Treatment of T-cells with actin depolymerising and arresting drugs demonstrated that the force produced by the cytoskeletal rearrangements is necessary for the active probing of the target cell[137,165,171] Furthermore, atomic force microscopy experiments show that pushing and pulling forces exerted by the T cell are intensified upon TCR stimulation, presumably to increase the number of cellular contacts[171]

1.2.4.2 Distribution of key receptors at the resting T-cell surface

The complex topography of the T-cell surface poses a challenge to the study of receptor distribution. For instance, the enrichment of receptors on the microvillar tips could be interpreted as clusters, protein islands or multivalent structures if the membrane morphology is not taken into account[172,173]. Currently, molecular organisation on the resting T-cell surface is primarily studied by single-molecule localisation microscopy (SMLM) and more recently LLSM.

The location of the TCR/CD3 complex on the T-cell surface is the best studied among the T-cell surface receptors. Jung et al. were the first to show that TCR/CD3 complex is enriched at the microvillar tips and this was supported by subsequent studies (Figure 1.5C)[162,169,174]. Similar distribution displayed by other surface molecules critical for antigen recognition such as CD4, CD2 and CD8, as well as some intracellular signalling molecules like Lck, presumably through its association with the co-receptors or CD2 (Figure 1.5C)[169]. In contrast to CD2, the other fundamental adhesion molecule LFA-1 is found predominantly on the cell body with only a fraction found on the microvillar tips (<5%)[175,176]. While the recent studies of T-cell surface are unequivocal regarding the microvillar localisation of the TCR/CD3 complex, the distribution of CD45 is more controversial. Using SMLM, Jung et al. found that CD45 is evenly distributed across the T-cell surface and these findings were later corroborated

by LLSM performed by Krummel and colleagues[162,168]. However, imaging of artificially expanded T cells with a laser scanning confocal microscope (LSCM) suggested that CD45 is pre-excluded from the microvillar tips[174].

Several mechanisms were proposed for the maintenance of the distribution of surface molecules, particularly in terms of enrichment and depletion at microvillar tips. Some studies suggest that the composition of the lipid membrane differs across the various membrane compartments. For instance, cholesterol is enriched in membrane areas at negative curvature such as microvillar tips[174]. Based on the biochemical properties of their TM regions, the surface molecules would selectively partition into different areas of the membrane[174,177,178]. Alternatively, direct attachment of the cytoplasmic tails of surface receptors to the cortical cytoskeleton was also suggested to determine T-cell surface organisation. Ezrin/radixin/moesin proteins mediate the enrichment of TCR/CD3 complex in the microvillar tips through simultaneous binding of its constituent chains and f-actin[169,179,180]

1.3 T-cell activation

1.3.1 TCR signalling pathways

In a resting T-cell, the TCR/CD3 complex is kept non-signalling through the activity of the CD45 phosphatase[92]. Upon binding to a cognate pMHC on the target cell, the ITAM motifs of the TCR/CD3 complex become phosphorylated by the Lck kinase[99]. Recruitment of the co-receptors to the pMHC-TCR complex occurs in concert with its phosphorylation by Lck. The phosphorylation of the TCR/CD3 complex generates docking sites for binding of the ZAP70 kinase which is also phosphorylated by Lck[181]. The key substrates of ZAP70 are LAT and SLP76 (Figure 1.6)[182,183]. Phosphorylation of LAT creates docking sites for SH2 signalling proteins, crucially Grb2-related adapter protein 2 (GADS), which mediates the formation of a LAT/GAD/SLP76 ternary complex essential for further signal propagation[184–186]. Until this point, the pathway is linear, but it becomes more complex downstream[117]. Therefore, for this thesis, only

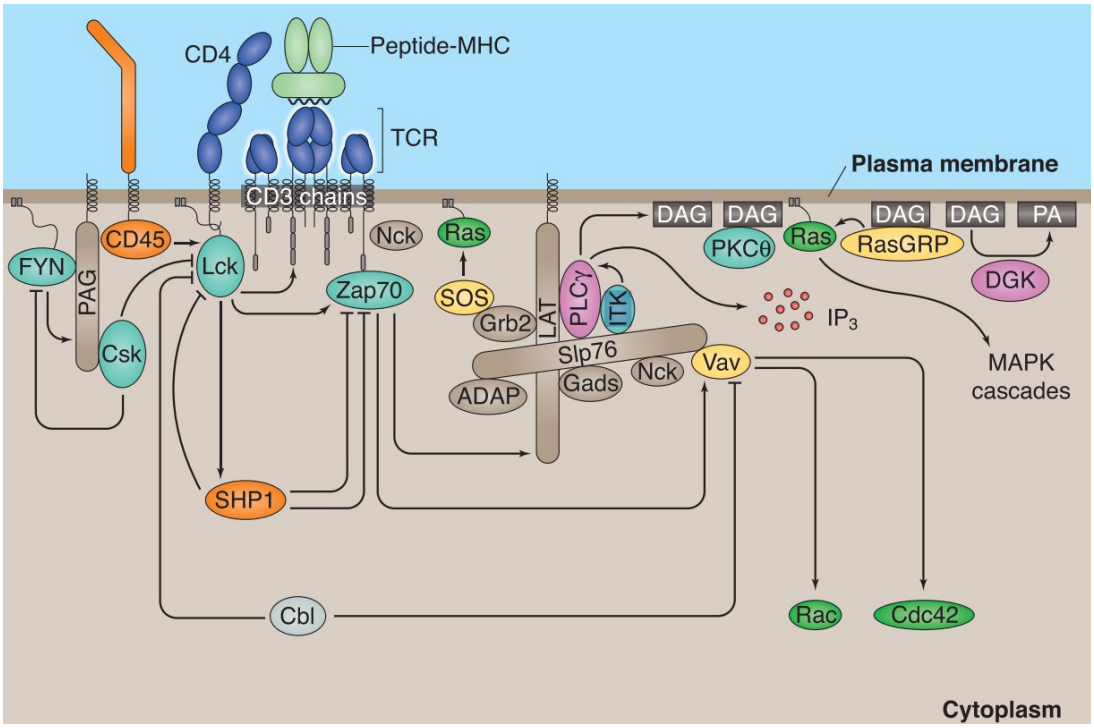


Figure 1.6: TCR downstream signalling network. Following phosphorylation of the TCR/CD3 complex by Lck. The ZAP70 kinase recruited to the phosphorylated immunoreceptor tyrosine-based activation motifs phosphorylates Lat and SLP-76 which become linked through GADS. Both IL-2 inducible T-cell kinase (ITK) and phospholipase C γ 1 (PLCγ) are recruited to the Lat-GADS-SLP-76 complex and PLCγ becomes phosphorylated by ITK resulting in its activation. PLCγ cleaves, phosphatidylinositol triphosphate (PIP_3) into diacylglycerol (DAG) and inositol trisphosphate (IP_3). The former activates mitogenic pathways involving PKCθ and Ras. The latter acts as a secondary messenger to release Ca^{2+} ions from the endoplasmic reticulum. Vav is another molecule recruited to the Lat-GADS-SLP-76 complex which induces reorganisation of the actin cytoskeleton. Adapted from Huse[117].

the signalling modules involved in the release of calcium ions from the ER and remodelling of the actin cytoskeleton will be described.

Remodelling of cytoskeleton in response to TCR signalling is initiated by recruitment of a guanine exchange factor Vav1 to SLP76 which activates GTPases Rac and Cdc42[117]. In turn, these two GTPases indirectly activate Arp2/3 which simulates the growth of branched actin filaments. These events also lead to the recruitment of talin which activates integrins (see section 1.2.2.1).

The first step leading to calcium release from the ER is the recruitment of phospholipase C γ 1 (PLCγ1) to the LAT/GAD/SLP76 complex[117]. PLCγ1 cleaves phosphatidylinositol triphosphate (PIP_3) located in the inner leaflet of the

membrane to generate two secondary messengers diacylglycerol (DAG) and inositol trisphosphate (IP_3). Full activation of PLCγ1 requires prior phosphorylation by IL-2-inducible T-cell kinase (ITK) which is recruited to SLP76. DAG activates multiple signalling modules leading to mitogenic signalling. Soluble IP_3 binds to IP_3-gated calcium ion channels in the ER membrane resulting in a sharp increase in the cytoplasmic calcium ion levels from 50 nM to 300-1000 μM[187]. The spike in calcium acts through a calmodulin/calcineurin module to dephosphorylate a transcription factor NFAT promoting its translocation to the nucleus. Other transcription factors critical to T-cell activation are NF-κB and AP-1.

T-cell responses are modulated by pathways originating from co-stimulatory and inhibitory receptors. The most prominent of the former group is CD28 which binds to CD80 and CD86 on the target cell[188,189]. Classically, during T cell priming by DCs in the primary lymphoid organs, CD28 and TCR needs to be stimulated in concert to prevent T cells from entering an anergic state[190,191]. These observations led CD28 signalling to be known as 'signal two' along 'signal one' originating from the TCR. The binding of CD28 to either of its partners results in phosphorylation of its cytoplasmic tails and downstream signalling involving PI3K, Grb2, Vav and ITK.

One of the best characterised inhibitory receptors is the cytotoxic T-lymphocyte associated protein (CTLA-4) expressed on the T cell surface. CTLA-4 competes with CD28 for binding to both CD80 and CD86 and can remove both of them from the APC surface through trans-endocytosis[192]. Another example is programmed cell death protein 1 (PD-1) which in contrast to CTLA-4, predominantly acts in the periphery where its ligands, PD-L1 and PD-L2 are expressed. To date, no signalling pathways unique to PD-1 have been identified and it is thought that it primarily acts by attenuating TCR signalling via a following mechanism. Upon binding to its ligands, the immunoreceptor tyrosine inhibitory motif located within the cytoplasmic tail of PD1 becomes phosphorylated creating a docking site for Src-homology phosphatase-2 (SHP2). In turn, SHP2 dephosphorylates

the ITAMs of the neighbouring TCR/CD3 complex, thus reducing the probability of successful TCR triggering[193].

1.3.2 Early T cell/target cell interactions

The nature of the earliest interaction between T cells and target cells was established through an amalgam of imaging techniques. Imaging of T cells on supported lipid bilayers (SLB) presenting ICAM-1 and agonist pMHC led to the discovery of TCR microclusters which were considered to be the sites of antigen recognition and signal amplification (Figure 1.7A)[194–197]. With the advances in the understanding of T-cell surface topography came the idea that tips of T-cell microvilli may in fact be the sites of the first interactions[137,162,168,172,198]. Microvillar contacts would form size-restricted intermembrane areas referred to as close contacts (CC) where antigens can be effectively scanned.

1.3.2.1 TCR microclusters

Bunnel et al. visualised the formation of discrete clusters of TCR co-localising with ZAP70 at the interface of T cells with antibody-coated glass[197]. Development of SLB system containing mobile agonist pMHC and ICAM-1 allowed more detailed characterisation of TCR microclusters estimated to contain 40-150 TCRs and were ~500 nm in diameter (Figure 1.7A)[194–196]. Observations that TCR microclusters form before calcium signalling and that they co-localise with signalling proteins such as ZAP70, SLP70, PLCγ1 and LAT suggested that they might be the *bona fide* sites of antigen recognition[194–196]. Additionally, TCR microclusters were found to be depleted of CD45[194]. Formation of the TCR microclusters was found to be dependent on the remodelling of the actin cytoskeleton as shown by the treatment of T cells with actin arresting and depolymerising agents. Hashimoto-Tane et al. demonstrated that TCR microclusters are stabilised by micro-adhesion rings containing LFA-1 linked to cytoskeletal adapters[199,200]. Both PD-1 and CD28 were found to accumulate within the TCR microclusters, suggesting that they also may be the site of signal integration[199]. In later stages of the interaction,

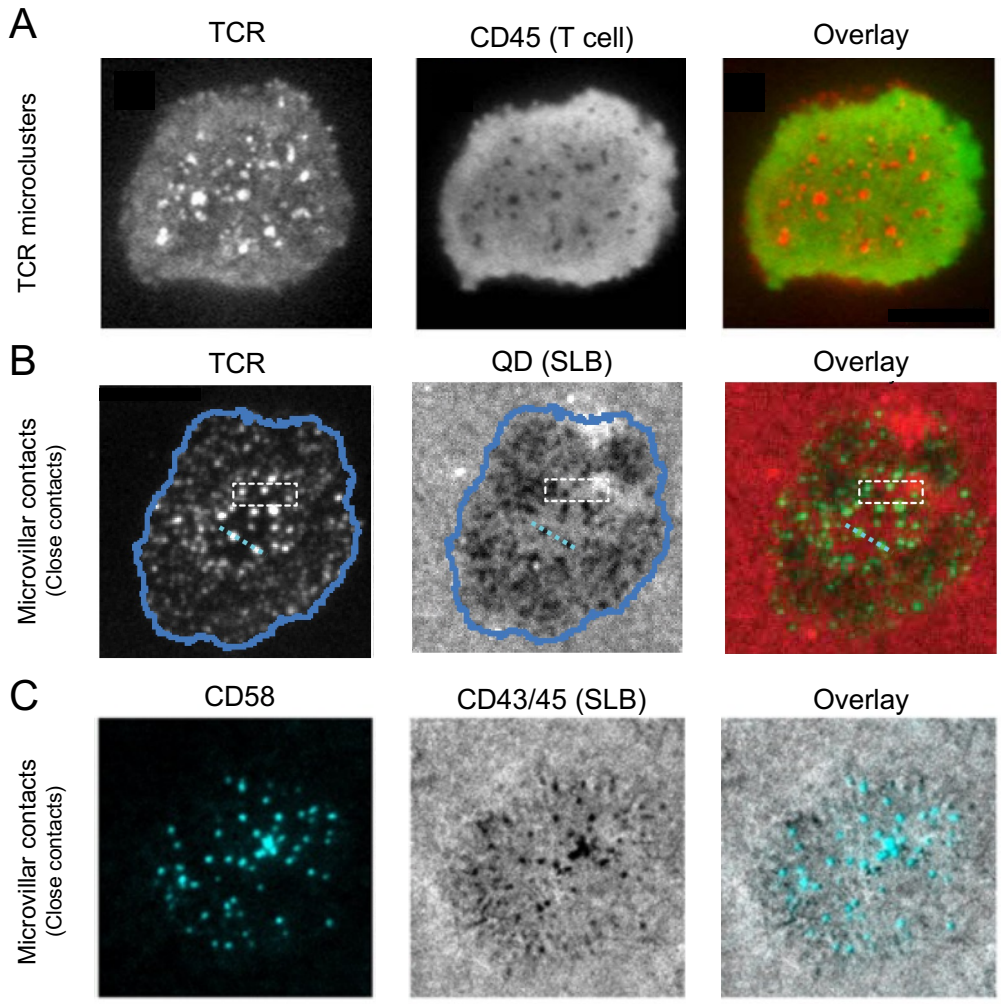


Figure 1.7: Interactions of T cells with surrogates of target cells. A. TCR microclusters as imaged by Varma et al.[194] on a supported-lipid bilayer (SLB) containing agonist pMHC and ICAM-1. From the left, the image panel shows TCR, CD45 and the overlayed images. **B**. Microvillar contacts as imaged by Cai et al.[168] on SLBs containing agonist pMHC, ICAM-1 and quantum dots (QD). From the left, the image panel shows TCR, QDs and the overlayed images. The black 'holes' in the QD SLB fluorescence correspond to individual microvillar contacts. **C**. Microvillar contacts as imaged by Jenkins et al.[137] on SLBs containing agonist pMHC, ICAM-1, CD58, CD43 and CD45. From the left, the image panel shows CD58, combined CD43 and CD45, and the overlayed images. The black 'holes' in the CD43/CD45 SLB fluorescence correspond to individual microvillar contacts.

TCR microclusters migrate to the centre of the T cell/SLB interface to form a central supermolecular activation cluster (cSMAC) where signalling is terminated, while signalling is sustained in peripheral TCR microclusters[194–196].

1.3.2.2 Microvillar contacts

The role of microvilli in forming the initial contacts with target cells was hypothesised following visualization of submicron membrane puncta on glass surfaces prior to T-cell spreading[198,201]. The case for microvillar contacts was strengthened by SMLM studies showing enrichment of the key receptors and adhesion molecules at their tips[162,169,172]. In a landmark study, Krummel and colleagues visualized the microvilli during scanning of a model APC[168]. In the same study, the microvillar contacts were imaged on SLBs containing quantum dots (QD) alongside the standard agonist pMHC and ICAM-1, a method that authors referred to as 'synaptic contact mapping' (Figure 1.7B). Upon interaction of microvilli with the SLB, the QDs were segregated resulting in the formation of 'holes' at the contact site. It was found that microvilli form ~500 nm contacts, some of which were found to accumulate TCR and ZAP70. Jenkins et al. further characterised microvillar contacts using an SLB system that, in addition to agonist pMHC and ICAM-1, contained CD58 and ECDs CD45 phosphatase and a large glycoprotein CD43[137]. Segregation of the two glycoproteins, akin to QDs, permitted tracking of the microvillar contacts (Figure 1.7C). These contacts were found to be strikingly similar in size to those characterised by Krummel and colleagues and formed in the absence of TCR ligand. Additionally, it was found that the contacts were depleted of the CD45 phosphatase and accumulated both CD58 and the TCR ligand pMHC. In both studies, following T-cell triggering the contacts displayed centripetal movement leading to synapse formation.

In summary, microvillar contacts and TCR microclusters share multiple similarities including dimensions and molecular composition e.g. TCR accumulation. However, not every microvillar contact is a site of active signalling and thus does not assume TCR-microcluster-like appearance. Thus, it is likely that TCR

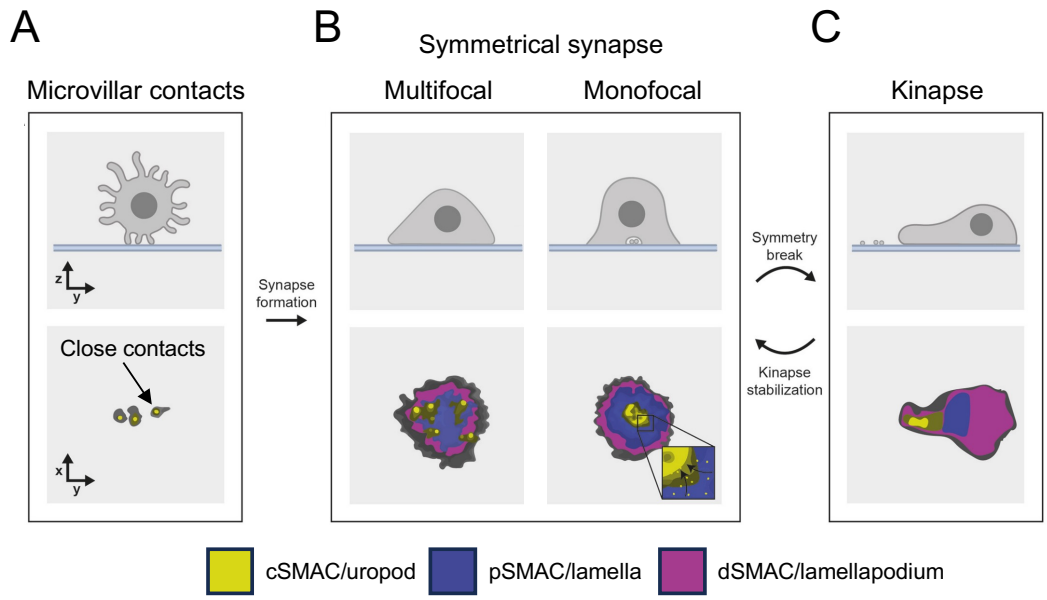


Figure 1.8: Evolution of T cell/target cell interactions. A. The interactions between T cells and target cells are initiated by T-cell microvilli forming close contacts at the cellular interface. **B**. Following TCR triggering the T cell forms a synaptic structure which can either multifocal with multiple sites of TCR accumulation (left) or a monofocal synapse (right) where TCR is centrally accumulated in a structure known as central supramolecular activation cluster (cSMAC). In the multifocal synapse, the individual foci are surrounded by dispersed ICAM-1/LFA-1 adhesion pair. The cSMAC is surrounded by peripheral and distal SMACs containing ICAM-1/LFA-1 pair and CD45, respectively. The secretory apparatus is assembled at the cSMAC of $CD8^+$ T cells. **C**. *In vivo*, T cells balance the signalling of the TCR with that of chemokine receptors. If the latter dominates, the synapse can transition into its mobile equivalent known as a kinapse. In the kinapse, the cSMAC is located within the uropod and the pSMAC and dSMAC are located toward the leading edge. T cells can switch between the kinapse and synapse architecture depending on the relative strength of the chemokine and antigenic stimuli. The figure panel shows the yz (top) and xy (bottom) planes of the interaction. Figure adapted from Morch et al.[118]

microclusters represent a subset of microvillar contacts that have successfully accumulated the ligand rather than a distinct structure.

1.3.3 Immune synapse

T cell signalling leads to the assembly of an immunological synapse, first defined by Kupfer and colleagues, composed of concentric ring-shaped regions known as supramolecular activation cluster (SMAC)[202]. Central SMAC (cSMAC) is a site of TCR/pMHC and CD2/CD58 acumulation[202–205]. cSMAC surrounded by a

peripheral SMAC (pSMAC) composed of LFA-1/ICAM-1. CD45 was found to be located in the outermost region of the synapse referred to as distal SMAC (dSMAC) (Figure 1.8B)[204,206,207]. A fraction of CD45 also translocates to the cSMAC at a later time point where it was hypothesised to halt TCR signalling[194,206]. However, it was also shown that CD45 may be centrally located before segregation into the dSMAC[207]. A further layer of complexity was added by recent findings showing the accumulation of the CD2/CD58 pair in the dSMAC region of a mature synapse. These so-called CD2 corollas were found to be depleted of CD45 and facilitate signalling of co-stimulatory receptors[208] The assembly of the mature synapse is accompanied by a centripetal flow of TCR microclusters to form the cSMAC where the phosphorylated TCR is internalised and degraded[194]. Continued signalling in the periphery and formation of new contacts is necessary for the maintenance of the mature synapse[194–196,209]. Such monofocal, symmetrical synapse, described as having a 'bull's-eye' pattern was characterised first at the interfaces of $CD4^+$ T cells and either B cell or ICAM-1-presenting SLBs. Similar molecular assemblies also form at the interface of cytotoxic $CD8^+$ T cells and cancer cells[205,210]. In $CD8^+$ T cells, the cSMAC is the site of actin depolymerisation and formation of a secretory apparatus through which cytotoxic granules are released[210,211]. It was postulated that the ring of LFA-1/ICAM-1 surrounding cSMAC also acts as a gasket to limit damage to neighbouring tissues[210,212]. There are several lines of evidence suggesting that other types of synapses can form depending on the T cell state, the density of TCR ligand and environmental cues[213] Multifocal synapses which are devoid of cSMAC and instead contain several foci accumulating TCR/pMHC complex were found to form at interfaces of naïve $CD8^+$ T cell and Th2-polarised $CD4^+$ T cell with DCs and APC surrogates, respectively (Figure 1.8B)[214,215]. Similar to cSMAC these foci were surrounded by LFA-1/ICAM-1 pair which was distributed throughout the interface. While interacting with target cells in tissues, T cells are exposed to chemokine gradients that promote migration and oppose immobilisation, necessary for the assembly of the symmetrical synapse[216–220]. As a result, mobile, asymmetric synaptic structures known as kinapses may form

which allow the T cells to integrate and amplify signals during migration (Figure 1.8C)[221]. In the kinapse, a cSMAC-equivalent structure forms at the uropod and microvilli scan the surface of the apposed cells at the leading edge analogous to dSMAC[221,222]. During migration T cells can switch between the two modes of interaction depending on the relative magnitude of the chemokine and antigenic stimuli[221–223]. More specifically, the synapse-kinapse switch is regulated by the activities of protein kinase Cθ and Wiskott–Aldrich syndrome protein[222]. Kinapse formation was observed for both $CD8^+$ and $CD4^+$ T cells[223].

1.4 Models of T-cell receptor triggering

The nature of the TCR trigger – the mechanistic basis for transduction of ligand binding across the membrane to convert TCR from the resting to the signalling state, remains unclear[224,225]. Multiple models have been proposed invoking interactions with co-receptors, conformational changes and size-driven segregation of CD45. These models are not mutually exclusive and could act in concert to drive TCR phosphorylation.

1.4.1 Oligomerisation

The first one of the oligomerisation models is the heterodimerisation model which describes the recruitment of the co-receptors, CD4 and CD8, to the TCR/CD3-pMHC complex as the event driving TCR triggering (Figure 1.9A). Lck kinase associated with the co-receptor phosphorylates the pMHC-TCR complex and initiates downstream signalling[225]. This model was modified by Davis and colleagues into a so-called pseudodimer model (Figure 1.9B)[61,226,227]. The premise of the pseudodimer model is that the co-receptor bridges two TCR-pMHC complexes, the first one involving an agonist pMHC and the second a self pMHC. In the first iteration of this model, it was proposed that the ECD of the co-receptor would bind to the self pMHC while the associated Lck kinase would interact with the cytoplasmic tails of the TCR/CD3 complex bound to the agonist pMHC[61]. It was suggested that pseudodimerisation would position

the co-receptor in an orientation favourable to ITAM phosphorylation, more so than heterodimerisation. Another iteration of the model was followed by the work of Krogsgaard et al. who found that soluble heterodimers of agonist and self-pMHC can trigger T cells unlike monomeric agonist pMHC molecules[226]. Mutation of the CD4 binding site on the agonist pMHC within the dimer, but not the self-pMHC abolished signalling, indicating that formation of the pseudodimer would involve association of the CD4 ECD with the self-pMHC rather than the agonist pMHC as initially proposed by Irvine et al.[61,226] Applicability of this mechanism to pMHC class I was shown in experiments where agonist/self pMHC heterodimers induced negative selection of OT-I $CD8^+$ T cells in fetal thymic organ cultures[227]. The main disadvantage of the co-receptor-based models is their inability to account for T-cell activation in the absence of the co-receptors owing to a considerable amount of free Lck kinase[62,112,228,229]. Other oligomerisation-based TCR triggering models were proposed based on the observations that tetrameric agonist pMHC and antibodies that cluster the TCR/CD3 complex activate T cells[230–233]. However, these mechanisms were largely discounted by findings that a single agonist pMHC is sufficient to trigger the TCR[59,61,62,234].

1.4.2 Conformational change

Conformational change models posit that binding of the cognate pMHC to the TCR/CD3 complex is transduced through the ECDs of the octamer to induce reorganisation of the cytoplasmic tails increasing their accessibility to the Lck kinase (Figure 1.9C)[224]. The model can be further subdivided into two types. First, the allosteric model stipulates that binding of the pMHC to the TCR$\alpha\beta$ is sufficient to trigger conformational changes in the TCR/CD3 complex. Second, the mechanotransduction model, similar to the allostery-based model, invokes conformational changes in the TCR/CD3 complex, but it stipulates that a piconewton shear forces need to be applied to the TCR/CD3 complex for triggering to occur.

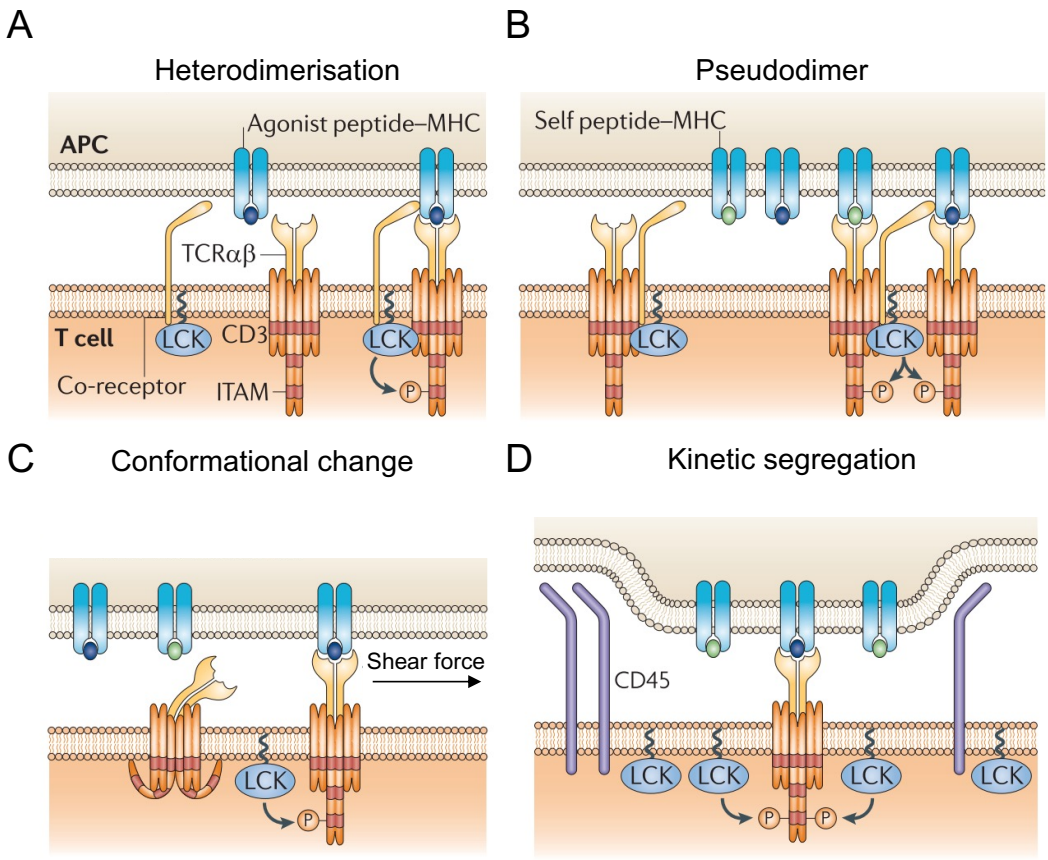


Figure 1.9: (Following page)

1.4.2.1 Allosteric control

The potential conformational changes in the ECD of the TCR$\alpha\beta$ were first proposed based on X-ray crystallography of the constituent chains of the TCR/CD3 complex. One of the regions that was proposed to be involved in signal transmission was an unusually long Cβ FG loop protruding from the side of the Cβ domain[235]. The Cβ FG loop was proposed to transmit the conformational change in the $\alpha\beta$TCR dimer to the neighbouring CD3$\epsilon\gamma$ signalling subunit[235–237]. The Cβ FG loop was a particularly attractive candidate as it is unique to the Cβ domain of the TCR and is absent from equivalent domains of antibodies. With developments in structural biology, NMR, better suited than X-ray crystallography to study signalling dynamics, was used to elucidate structures of two pMHC-TCR complexes: murine TCR bound to an HIV GP120 peptide-H2-D^{d} complex and human A6 TCR bound to HIV Tax-HLA-A2 complex[238,239]. Together, these

Figure 1.9: Mechanisms of TCR triggering. **A**. Heterodimerisation model. According to this model, TCR triggering is driven by the binding of the co-receptor (CD8/CD4) to the side of the pMHC molecule bound to the TCR. The Lck kinase associated with the cytoplasmic tail of the co-receptor then phosphorylates the adjacent immunoreceptor tyrosin-based activation motifs (ITAM) of the TCR/CD3 complex **B**. Pseudodimerisation model. Similar to the heterodimerisation model it invokes co-receptor recruitment as a driver of TCR triggering, but involves two pMHC/TCR/CD3 complexes, one containing an agonist pMHC and the other a self pMHC. The extracellular domain of the co-receptor binds to the agonist pMHC, but it phosphorylates the TCR/CD3 complex bound to the self pMHC. The binding of the co-receptor across two pMHC/TCR/CD3 complexes positions in an orientation that increases the probability of phosphorylation. **C**. Conformational change models can be divided into two subtypes: allosteric and mechanotransduction models. Both models posit that in a resting state, the ITAMs of the TCR/CD3 complex are sequestered in the plasma membrane which reduces their accessibility to the Lck kinase. Upon binding of the agonist pMHC the TCR/CD3 complex undergoes a series of conformational changes that results in a release of ITAMs from the plasma membrane and phosphorylation by the Lck kinase. The allosteric model assumes that simply binding the agonist pMHC to the TCR/CD3 complex is sufficient to induce the conformational change, whereas the mechanotransduction model dictates that tangential forces need to be applied to the TCR/CD3 complex for triggering to occur. **D**. Kinetic segregation model. According to the kinetic segregation model, the formation of the pMHC/TCR/CD3 complex requires the formation of so-called close contacts between the two apposed cells. The close contacts are only ~14 nm across resulting in the exclusion of CD45 phosphatase whose extracellular domain is >20 nm. As the Lck kinase is not subject to exclusion, close contact formation is concomitant with a local increase of the net kinase activity and ITAM phosphorylation. Figure was adapted from Van der Merwe and Dushek[225]

studies found that allosteric changes occurred in the previously favoured Cβ FG loop and other regions, such as the Cα AB loop and Cβ A helix. However, in functional studies where the Cβ FG loop was removed, TCR signalling is unaffected or reduced, but not completely abolished[240,241]. Comparison of the cryo-EM structures of the TCR/CD3 complex in a holo and ano apo state so far found no conformational changes in the ECD of the complex, including the Cβ FG loop[56,57,68].

The conformational changes in the ECDs of the TCR/CD3 complex would need to alter the properties of the signalling chains to promote phosphorylation. ITAMs are interspersed with so-called basic rich sequence (BRS) motifs which, due to their net positive charge, associate with the negatively charged phospholipids in the membrane[242–248]. One of the mechanisms proposes that in the resting state,

the ITAMs would be sequestered in the inner leaflet of the plasma membrane. Following ligand binding, the cytoplasmic tails would be released, and their increased accessibility would lead to phosphorylation by Lck. This mechanism is supported by *in vitro* experiments by Aivazian et al. where changes in the structure and phosphorylation of CD3ζ could be detected upon the addition of anionic lipid vesicles[242]. Further *in vivo* experiments using FRET demonstrated that the cytoplasmic tails of CD3ϵ are membrane-associated in resting T cells, and their dissociation can be induced by TCR stimulation[243,245]. However, whether the release of the cytoplasmic tails from the plasma membrane leads to ITAM phosphorylation or vice versa is not clear. Zhang et al. found that while CD3ζ dissociation occurs upon TCR stimulation, it was dependent on the activity of the Lck kinase indicating that the latter may be true[244] Furthermore, the functional relevance of the ITAM sequestration through the BRS motifs is contentious as mutations of the positively charged residues of the CD3ϵ chain does not result in spontaneous phosphorylation[246].

It needs to be noted that the conformational changes initially associated with the allosteric model were incorporated into the mechanotransduction model. This includes the conformational changes of the Cβ FG loop and the ITAM-release mechanism.

1.4.2.2 Mechanotransduction

The evidence for mechano-sensing properties of the TCR comes from single-molecule assays whereby a pulling force is exerted on the TCR/CD3 complex on a T-cell. Through these assays, it was found that TCR phosphorylation occurs only upon application of force and that binding of a static pMHC is insufficient to induce TCR signalling[249,250]. As the force needs to be applied tangentially, the TCR/CD3 complex was dubbed to be an 'anisotropic force sensor'.

Selective formation of slip-bonds and catch-bonds between the TCR/CD3 and agonist and non-agonistic pMHC complexes is invoked as a basis for antigen discrimination within the mechanotransduction model[251–253] . The catch bonds

are defined as interactions whose lifetime increases under force and the opposite effect applies to slip bonds. Due to the short-lived nature of the structural states under forces, so far catch bond formation was only modelled through molecular dynamics simulations suggesting that catch bond formation may involve changes in the hydrogen bond network at the TCR/pMHC interface[251,254] . The structural basis for the long-range transduction to the cytoplasmic tails in response to force has not been experimentally elucidated. However, some studies point out that it could involve the extension of the TCR/CD3 complex as well as conformational changes in the Cβ FG loop. In experiments where force was applied to the pMHC-TCR/CD3 complex using either optical traps or biomembrane force probes, ~15 nm deformations of the complex were detected and interpreted as conformational changes involving lengthening of the TCR/CD3 complex[253,254]. Deletion of the Cβ FG loop was shown to interfere with this structural transition implying that it might confer the mechano-sensing properties[253]. Due to the static nature of the cryo-EM structures of the TCR/CD3 complex effects of force on the receptor cannot be inferred[56,57,68]. However, a recent cryoEM structure of an unligated 1G4 TCR/CD3 complex reconstituted in lipid nanodisks mimicking the native T-cell membrane environment demonstrated that the TCR/CD3 complex can adopt compact and extended conformations[67]. The latter confirmation was favoured by addition of a cognate pMHC ligand. Thus, the transition from the compact to the extended state could correspond to the extension observed in the single-molecule force assays. While the compact confirmation appears to represent the genuine resting state of the TCR/CD3 complex, curiously the transition to the extended confirmation is not required for T-cell activation.

1.4.3 Kinetic segregation

The kinetic segregation (KS) model was formulated based on structural data showing a mismatch in the sizes of T-cell surface molecules involved in antigen recognition[255] Namely, TCR/pMHC complex whose height was estimated to be 14 nm is significantly shorter than any of the isoforms of the CD45 phosphatase.

Additionally, the complex of ubiquitously expressed CD58 and CD2 is identical in size to the TCR/pMHC complex. Therefore, CD45 would be excluded from intercellular contact stabilised by the CD58/CD2 pair and hence permissive to TCR/pMHC binding (Figure 1.9D). Due to the strict topographical requirements, these cellular spaces came to be known as close contacts (CC). Since the Lck kinase is freely diffusing in the inner leaflet of the plasma membrane or associates with co-receptors similar in size to the TCR/pMHC complex, it is not subject to segregation. Thus, the net kinase activity in the CC would increase creating an area favourable to TCR phosphorylation. The probability of TCR triggering is determined by its dwell time within the CCs[256,257]. As the TCR binds to the cognate pMHC its diffusion rate is reduced and it is more likely to trigger. Similarly, if the CCs were large enough, even the freely diffusing, unligated TCR would be phosphorylated due to extended dwell time in the CD45-depleted area[86,137,256,258]. Therefore, implicit in the KS model is that the CC should be size-constrained to limit non-specific activation[256,259]. The KS model was initially challenged due to the complicated regulatory relationship of CD45 phosphatase and Lck kinase – it was speculated that a local reduction in CD45 activity could lead to deactivation of Lck and thus prohibit TCR phosphorylation (see section 1.2.1.2)[260]. However, this issue was settled by findings showing that ~40% of Lck is in an active state in a resting T cell[77,79] . Additionally, treatment of T cells with the potent phosphatase inhibitor, pervanadate, led to T-cell activation showing that a sudden increase in the net kinase activity can drive TCR phosphorylation[92]. The fundamental evidence for the KS model comes from experiments involving the manipulation of the antigen recognition apparatus. Truncation of CD45 ECD and artificial extension of the native and artificial TCR ligands reduces T-cell activation[86,256,261–268]. Extension of the small adhesion molecules has the same effect, presumably by increasing the CD45 levels in the CCs and reducing the likelihood of TCR/pMHC engagement[269]. Another line of evidence is provided by reconstitution of the antigen triggering apparatus

both *in vitro* and *in vivo* demonstrating that CD45 segregation is independent of secondary cellular mechanisms[87,270].

Large-scale exclusion of CD45 was readily imaged at interfaces of T cells with APCs and APC surrogates, but it did not align with the requirements of the KS model[204,206,207]. Firstly, the exclusion was only visible following TCR triggering so a causal relationship could not be established. Secondly, these exclusion zones were too large to ensure the specificity of antigen recognition – mathematical models of the KS model indicate that the CCs cannot exceed 500 nm in diameter[256,259]. Evidence supporting the existence of submicron CD45-depleted areas was provided by Varma et al., who observed that CD45 is segregated from TCR microclusters (<500 nm in diameter)[194]. Chang et al. visualised the formation of *bone fide* CCs on SLB presenting solely small adhesion molecules[86]. Also, large CD45-depleted CCs were found to drive T-cell triggering in a ligand-independent manner consistent with the theoretical predictions. Furthermore, increasing the dwell time of the TCR/CD3 complex within unperturbed CCs by slowing its diffusion is sufficient to produce low amounts of signalling[258]. Both of these observations can be uniquely explained by the KS model. The structural basis for the CCs was not clear until the recognition that microvillar tips might be the site of CC formation[172]. Whilst CD45 segregation from CCs was readily observed in advanced T cell/SLB systems (~40% exclusion), imaging of microvilli interacting with a genuine APC surface revealed no exclusion[137,168]. While it was hypothesised that the greater deformability of the plasma membrane compared to SLBs could be responsible for the absence of CD45 exclusion, imaging of T cells on 'soft' SLBs increased the observable exclusion levels[271,272].

1.4.4 TCR triggering models, antigen discrimination and sensitivity

All of these models need to be able to account for the following features of antigen recognition. First, T cells respond to single pMHC molecules, a testament to the remarkable sensitivity of the antigen recognition machinery[59,61,234,273,274]. Second,

T cell can discriminate between pMHC molecules differing by a single amino acid residue showing that the TCR can distinguish self from non-self on a basis of minute structural differences[275–277]. Several mechanisms, agnostic of the molecular aspects of TCR triggering, were proposed to explain these observations.

Serial triggering was proposed by Valitutti et al., who hypothesised that multiple TCRs are triggered by a single pMHC following an observation that more TCRs are downregulated from the T-cell surface than the number of available pMHCs on the partner APC[278]. The lifetimes of TCR/pMHC interaction (0.1-10 s) are shorter than the average dwell-time of a microvillus stabilised at the APC surface (>10 s) thus creating a time window for serial triggering to occur within a single CC[168,279]. Based on serial triggering alone, TCR/pMHC affinity and potency should be negatively correlated – high affinity should result in low potency. However, experimental data show that the affinity/potency relationship adopts a bell-shaped curve with the affinity optimum determined by the ligand dose[280–282]. This suggests that there is a countervailing effect favouring long-lived interactions. Kinetic proofreading posits that the TCR/pMHC interaction needs to achieve a minimum temporal threshold before TCR is triggered[119,283]. If the complex dissociates before the threshold is reached, the TCR returns to its ground state. Therefore, frequent but short-lived interactions of a single pMHC with multiple TCRs are not sufficient for triggering to occur. The mechanistic basis for kinetic proofreading is not clear, but it was suggested that it may correspond to the reversible proximal signalling events leading to the formation of the Lat-GADS-SLP76 complex. Pettman et al. recently estimated that there may be between 2 and 3 kinetic proofreading steps collectively lasting 3 s[284]. These could correspond to ITAM phosphorylation, co-receptor or ZAP70 recruitment, and finally, Lat phosphorylation.

In addition to serial triggering, antigen sensitivity is further increased by the presence of co-receptors, CD2/CD58 and LFA-1/ICAM-1 adhesion, which all enable the TCR/CD3 complex to operate at its optimum[118,134,137,138]. Additionally,

the unusually high number of ITAMs of the TCR/CD3 complex was also shown to increase the sensitivity of the T-cell machinery[285,286].

It has been a long-standing assumption that antigen discrimination by the TCR/CD3 complex is near-perfect. For instance, some data suggests that affinity differences between non-self and self-peptides as small as 3-fold could abolish T-cell activation[287]. However, this has recently been called into question. The discriminatory power of the TCR, even when a gold-standard APC presents the antigen, is likely several orders of magnitude lower than estimated in the early studies[284] Nevertheless, the TCR remains better at discriminating between ligands than other receptors including the ITAM-containing BCR/CD79 complex and chimeric antigen receptors. Interestingly, while CD2/CD58 and LFA-1/ICAM-1 improve antigen discrimination, co-receptors have the opposite effect[284,288].

Correlating the empirical measurements of antigen discrimination with the molecular models of TCR triggering is non-trivial. The KS model assumes discrimination is based on the dwell time of the pMHC/TCR/CD3 complex in the CD45-depleted CCs[256]. Therefore, the kinetic parameters, particularly the off-rate, should determine the potency of the ligand[257]. Furthermore, it was proposed that if the ratio of net kinase activity inside versus outside the CC and the CC size is appropriate, antigen discrimination could occur without the need for kinetic proofreading[256].

The antigen discrimination in the mechanotransduction model is underpinned by the ability of agonist and non-agonist pMHC to form catch and slip bonds with the TCR under force, respectively. The small differences between self and non-self antigens not captured by kinetic parameters measured in-solution would be accentuated under force. This is supported by experiments showing that a pMHC binding to a cognate TCR with micromolar affinity that does not form catch bonds fails to induce activation[251]. However, not all TCRs were found to conform to this principle. For instance, the 1G4 TCR appears to form slip bonds with some agonist pMHCs[289].

1.5 T cell-redirecting immunotherapies

1.5.1 Immunotherapy targets

T cell-based immunotherapies are reliant on either activating the pre-existing population of tumour-specific T cells or generating anti-tumour responses *de novo* through redirection of polyclonal T cells.[290,291]. Regardless of how the anti-tumour response is achieved, it is conditional on the presence of cancer antigens that can be divided into two broad classes: tumour-associated antigens (TAAs) and tissue-specific antigens (TSAs).

1.5.1.1 Tumour-associated antigens

TAAs encompass a broad spectrum of peptide antigens presented by MHC molecules and non-pMHC surface molecules that are simultaneously expressed by healthy and cancer tissue[292]. TAAs can be targeted by therapeutic agents because either the expression levels of the TAAs on the tumour are significantly higher than on the healthy tissue or destruction of the TAA-expressing healthy cells does not lead to irreversible damage. TAAs are encoded by non-mutated genes and are often shared between patients.

pMHC TAAs can be divided into three classes: tissue differentiation, cancer germline, and overexpressed antigens. The tissue differentiation antigens are exemplified by MART-1 and gp100 proteins which are expressed by melanocytes found in the skin, eye and ear tissues, but are also expressed by melanomas[293,294]. The cancer germline antigens are derived from proteins which are expressed during fetal development, but later in life are restricted to MHC-negative tissues such as testicular germ cells and placenta trophoblasts. Cancer germline antigens include NY-ESO-1 and MAGE-A family proteins and similarly to the so-called differentiation antigens are expressed in melanomas[292]. The third class, the overexpressed antigens, are expressed by multiple healthy tissues but are substantially overexpressed by cancer cells. An example of an antigen belonging to this class is HER2, which is highly expressed by breast and ovarian cancers[292,295].

Additionally, several non-pMHC TAAs are targeted by immunotherapies. For instance, CD19 is expressed by B-cell leukaemias as well as all healthy B-cells and their precursors. CD19 is a target of multiple immunotherapies including adoptive cell transfer and T-cell engagers. HER2 can also be targeted as a non-pMHC TAA.

1.5.1.2 Tumour-specific antigens

TSAs, also known as neoantigens, arise from oncogenes which have either gained driver mutations that aid tumour progression or passenger mutations which accumulate as a result of impeded DNA repair mechanisms[296]. Neoantigens originating from driver mutations are rare but are more likely to be shared between patients[292]. Notable examples include mutation in p53 and Ras family oncogenes. The latter can be found in 22% of tumours[297]. Neoantigens derived from R175H TP53 and G12V KRAS were successfully targeted by T-cell engagers[298,299].

1.5.2 Adoptive cell transfer

Adoptive cell transfer (ACT) involves first harvesting T cells from a patient, then their *ex vivo* modification, such as expansions or genetic engineering, often both, followed by re-infusion of the T cell product into the patient[290]. ACT aims to generate an autologous T cell response against the tumour, which otherwise would have been constrained by scarcity or lack of tumour-reactive T cells.

The ACT therapies can be divided broadly into two classes: tumour infiltrating lymphocyte (TIL)-based ACT and transgenic ACT. The former was developed first and it involves the isolation of T cells from a resected tumour followed by their expansions *ex vivo* with mitogenic factors and re-infusion into the patient[4,290,300,301]. The efficacy of TIL-based ACT is limited by the proportion of T cells expressing cancer-reactive TCRs and is often limited to tumours with the highest mutational load such as melanomas[290,296]. Later advancements in immune engineering, i.e., viral transductions and later CRISPR-Cas9 engineering, allowed for the introduction of TCRs and so-called chimeric antigen receptors

(CAR) into patient-derived T cells[302–304]. Given that no pre-existing cancer-reactive specificity is required, polyclonal T cells isolated from blood can be modified. While the transgenic TCR are predominantly used in the native state, bar CDR modifications to modulate the pMHC binding affinity, CARs are synthetic receptors whose design has undergone multiple iterations since their first conceptualisation[305,306]. The first-generation CARs comprised of a single chain variable fragment (scFv) binding to the tumour antigen and the cytoplasmic tails of the ζ chain[305,306]. Second and third-generation CARs involved the addition of single or two cytoplasmic domains derived from co-simulatory receptors such as CD28 and CD137[306].

More advanced designs or synthetic receptors combining the scFv-based antigen recognition with the signalling domains of the TCR/CD3 complex were developed known as HLA-independent TCR (HIT), T-cell receptor fusion construct (TRuC) and synthetic T cell receptor and antigen receptor (STAR)[307–309].

1.5.3 T-cell engagers

T-cell engagers are a broad class of therapeutic whose main purpose is to redirect a polyclonal T-cell response to eliminate cancerous cells[291]. Most T-cell engagers indiscriminately interact with $CD4^+$ and $CD8^+$ T cells, but the primary focus is on harnessing the cytotoxic activity of $CD8^+$ T cells. Nevertheless, $CD4^+$ T cells can contribute to the elimination of tumours by modulating the tumour microenvironment or themselves killing cancer cells[30,31,310–312].

T-cell engagers typically are either bispecific antibodies or are composed of antibody-derived segments (Figure 1.10)[313]. The latter category includes bispecific formats such as bispecific T-cell engagers (BiTE) and dual-affinity re-targeting molecules (DART), both of which are composed of two scFv segments, but are differently linked (Figure 1.10A and B). The two scFv's in a BiTE are connected via a single linker whereas in the DART format, two linkers are in place, one generated using an engineered disulphide. DARTs were found to be more potent than BiTEs, possibly due to reduced flexibility and size[314]. Additionally, there

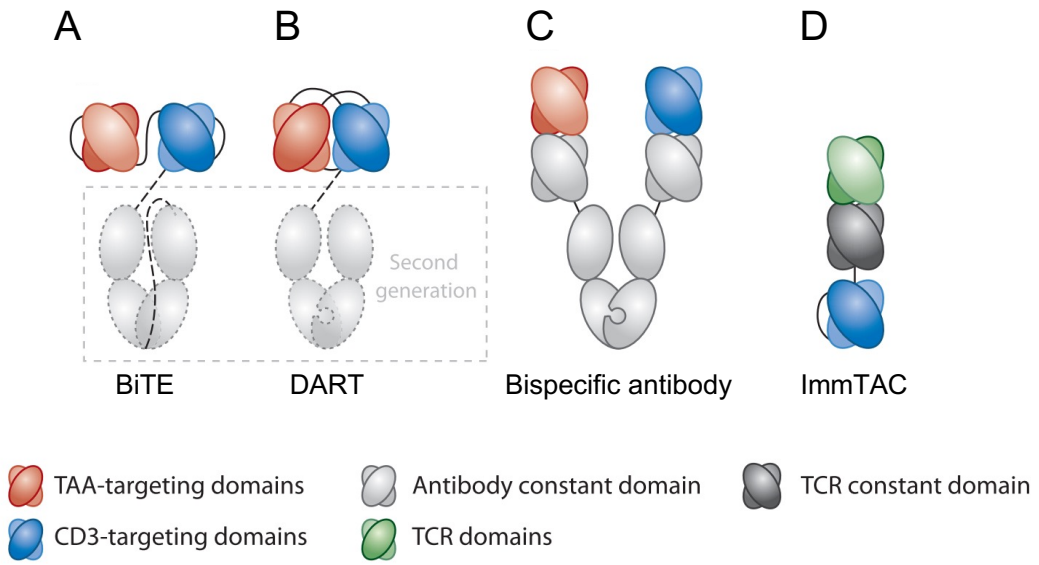


Figure 1.10: Formats of bispecific T-cell engagers. A. Bispecific T-cell engager (BiTE) is composed of two single-chain variable fragments (scFv) targeting a tumour-associated antigen (TAA) or tumour-specific-antigen (TSA) and the CD3ϵ chain of the TCR/CD3 complex. **B**. Dual affinity re-targeting molecule (DART) similar to BiTEs is composed of two scFvs targeting a TAA/TSA and the CD3ϵ chain. The linkage of the two scFv moieties includes a disulphide link which restricts the flexibility of the bispecific molecule. Variants of both BiTEs and DART were engineered to contain the constant region (Fc) of antibodies to improve their pharmacokinetic properties. **C**. Bispecific antibody engineered through knob-into-hole approach with a CD3ϵ-targeting arm and a TAA/TSA-targeting arm **D**. TCR-directed bispecific also known as ImmTAC composed of a CD3ϵ-targeting scFv and an extracellular domain of TCR$\alpha\beta$ or TCR$\gamma\delta$ directed against a TAA/TSA. Figure was adapted from Clynes et al.[291]

are also more unique architectures, such as TCR-directed bispecifics known as ImmTACs, which are composed of an antibody-derived scFv and either TCR$\alpha\beta$ or TCR$\gamma\delta$ segment (Figure 1.10D).

Typically one of the arms of a T-cell engager binds the CD3ϵ chain of the TCR/CD3 complex whereas the other arm binds to a TAA or TSA. Blinatumomab, a bispecific in a BiTE format targeting CD19 was the first T-cell engager to gain approval for use in the clinic for treatment of acute lymphoblastic leukemia[315]. Shortly after followed others including Tebentafusp, a TCR-targeted bispecific which targets HLA-A2 molecule presenting a peptide derived from a gp100 protein overexpressed in uveal melanoma[316]. The advances in protein engineering have also allowed the construction of trispecific engagers. The third arm of such

molecules often binds to co-stimulatory receptors on the T cell, such as CD28, with the aim of reducing exhaustion and tolerogenic responses[313,317].

1.6 Methods for imaging of T-cell activation

1.6.1 Cellular substrates

The early imaging of $CD4^+$ and $CD8^+$ T cells interacting with B cells led to the discovery of the immune synapse and provided the first indication that CD45 might be excluded from cellular interfaces[202,205,207]. Other cell types such as DC, fibroblasts and cancer cells were instrumental in defining non-classical synapses and the assembly of the secretory apparatus by $CD8^+$ T cells before release of cytotoxic granules[210,211,214,215]. While imaging of cell/cell interfaces significantly advanced the understanding of immune cell interactions, it is associated with several challenges. First, the non-planar interaction interface means that large volumes need to be acquired to capture the events of interest, thereby limiting the temporal resolution. Second, the orientation of the cell/cell conjugates often curtails the achievable resolution as often the *en face* position with conjugate arranged along the xy plane is more readily captured. As a result, the axial, rather than the planar resolution, which for common imaging methods is 2-fold lower, determines the level of observable detail. Third, using cellular substrates limits the capacity to modify and control the molecular composition of the target-cell surface and thus the role of specific receptors at the interface is more difficult to dissect[318]. These challenges notwithstanding, cellular substrates have unique features that so far have not been trivial to recapitulate using APC surrogates. Firstly, the deformability of cellular surface is greater than any of APC surrogates – glass is 10^7-10^8 stiffer than immune cells[319]. Second, the interactions of T cells with certain APCs are not unidirectional, for instance, DCs were shown to remodel their surface to enhance interactions with T cells[320]. Third, the cellular surface contains a wide range of molecules whose properties are challenging to replicate on surrogate surfaces e.g. hyaluronan/CD44 network.

1.6.2 APC and target cell surrogates

A few attempts to simplify the T cell/APC interface and capture the early T cell-target cell interaction involved using antibody-coated glass as an APC surrogate. This allowed for visualization of signalling structures that later came to be known as TCR microclusters by Bunnel et al. and later microvillar tips during the early stages of the T cell interactions[197,198,201]. The principal disadvantage of using glass substrates is that the attached ligands are immobile, precluding remodelling of the cellular interface. Therefore, the progression of the T cell across the consecutive stages of the immune interaction cannot be captured. Additionally, glass surfaces can be stimulatory due to non-specific glass-protein interactions.

Supported lipid bilayers (SLB) mimicking the plasma membrane were developed as APC surrogates[321]. Typically, SLBs are produced by the fusion of unilamellar vesicles on solid surfaces to create a continuous planar bilayer[321]. To differentiate from suspended bilayer technologies, the term 'supported' was included. The mobility of the lipids is permitted by the thin layer of water (~1 nm) separating the supporting substrate and the bilayer[321]. Nonetheless, SLBs remain almost as stiff as glass, but their stiffness can be reduced by the introduction of a polydimethylsiloxane layer between the glass and the bilayer[271]. Due to their planar topology SLBs have proved to be an optimal substrate for imaging of T cell interactions. Initially, the T cell/SLB interface was imaged using epifluorescence, confocal and internal reflection microscopy techniques, but these methods were superseded by total internal reflection fluorescence microscopy (TIRFM)[321]. As the TIRFM only illuminates objects located ~200 nm upwards from the surface of the glass, this allowed for efficient removal of the out-of-focus fluorescence while maintaining high temporal resolution.

The SLBs can be functionalised by attachment of ECDs of surface proteins to the lipids in the upper leaflet which allows precise control of the SLB composition. The attachment can be achieved either through direct integration of the protein into the bilayer via glycosylphosphatidylinositol (GPI) anchor or attachment of the protein to Ni^{2+}-chelating lipids via histidine tags. The critical difference between

the two types of attachments is the methodology required for protein insertion into the SLB. While the GPI-tagged proteins are inserted into the unilamellar vesicles before the formation of the SLB, the histidine-tagged proteins can be directly attached to the SLB. Additionally, the proteins can be directly conjugated to organic dyes affording the use of a wide array of photostable fluorophores. The proteins attached to the bilayer are highly mobile, more so than in cellular plasma membranes, which might alter their functional properties[321–323]. For instance, the mobility of CD58 is positively correlated with its adhesive properties[322,323]. On the other hand, immobile ICAM-1 is better at activating LFA-1-based adhesion (M. Dustin, unpublished data).

In the early studies of T cell interactions, the SLBs were functionalised with ICAM-1, agonist pMHC and infrequently CD86. Springer and colleagues had also incorporated CD58 alongside ICAM-1, but in most imaging studies ICAM-1 has been the sole adhesion molecule[135,322,323]. The absence of CD58 on the SLB likely forces the TCR-pMHC interactions to compensate for the absence of the small adhesion molecules, thus forcing pMHC into a dual antigen/adhesion role. Several recent studies re-incorporated CD58 into the SLBs[86,137,208,258]. Davis and colleagues have used T-cell/SLB systems permitting solely CD2/CD58 adhesion to observe the evolution of CCs and demonstrate that CC dimensions are critical for antigen discrimination[86]. The use of CD58/ICAM-1/pMHC SLBs by Demetriou et al. led to the discovery of a new immune structure known as CD2-corolla[208]. There were also several successful attempts to include bulky molecules which segregate from the sites of CC. For instance, Cai et al. incorporated quantum dots (QD) into the standard ICAM-1/pMHC SLBs. Due to their size, QDs were found to be excluded from the points of cellular interaction, allowing microvillar contacts to be mapped[168]. Jenkins et al. developed the system further by expanding the CD58/ICAM-1/pMHC bilayer by the addition of large glycoproteins CD43 and CD45, both of which, akin to QDs, were excluded from the sites of microvillar contacts[324]. It is worth noting that the barrier function of some glycocalyx

components is reinforced by their attachment to the cytoskeleton[32]. Hence, T-cell microvilli will face a greater resistance while parting the glycocalyx layer *in situ*.

1.7 Aims of this thesis

The details of the very first interactions between T cells and target cells were obtained using APC surrogates, but little is known about the nature of these events at genuine cell/cell interfaces. The dimensions of cellular contacts and their molecular composition, particularly levels of the CD45 phosphatase underpin the decision-making by T cells. The pioneering work by Krummel and colleagues established the role of microvilli in the scanning of target cells but failed to observe any substantial CD45 exclusion from their tips, contradicting the evidence from T cell/SLB systems[137,168,194]. To gain a better understanding of the role of microvilli in the recognition of target cells, a cellular system, suitable for live-cell fluorescence imaging, will be created. A novel bispecific molecule, known as ImmTAC, will be used as a universal T-cell agonist to study T cells in the native state. To validate the ImmTACs as model TCR ligands, the mechanisms of ImmTAC-induced T-cell activation will be examined using a combination of fluorescence imaging and functional assays. Finally, the two-cell system will be used to visualize the dynamics of interactions between cancer cells and T cells and address the inconsistencies surrounding the role of CD45 in TCR triggering.

2
Materials and Methods

2.1 Methods

2.1.1 Molecular gene cloning

2.1.1.1 General

All gene constructs were manufactured as DNA strings by Azenta Life Sciences or Twist Bioscience. The constructs were designed to contain MluI and NotI restriction enzyme sites at the 5' and 3' termini, respectively. All constructs were inserted into lentiviral transfer vectors pHR or pHRi via restriction enzyme cloning, transformed into a competent *E. coli* strain and purified from bacterial cultures.

2.1.1.2 Restriction enzyme DNA digestion

The DNA strings were resuspended in a Tris-EDTA (TE) buffer. For a single ligation, 500 ng and 5000 ng of the DNA string and the pHR or pHRi vector backbone, respectively, were digested using MluI-HF (New England Biolabs) and NotI-HF (New England Biolabs) restriction enzymes. The restriction enzyme reactions were prepared according to the manufacturer's instructions. DNA was digested for at least 1 h at 37 °C. The digested DNA strings were purified using QIAquick Gel Extraction Kit (Qiagen) with the DNA sample first diluted in 250 µl of 1:1 mix of QG buffer and isopropanol otherwise, the purification was

performed according to the manufacturer's instructions. The vector backbone was purified as described in section 2.2.1.3.

2.1.1.3 Agarose gel electrophoresis

To prepare the agarose gel 1% (w/v) solution of agarose in Tris-Borate-EDTA (TBE; Sigma Aldrich) buffer was prepared and warmed up to the boiling point to dissolve the agarose. Next, the 1% agarose solution was cooled to ~50-60°C and ethidium bromide (Sigma-Aldrich) was added to a final concentration of 0.5 μg/ml. After the agarose gel had solidified, it was covered with the TBE buffer. The samples containing the digested vector backbone was combined with a loading buffer at a 1:5 ratio and loaded onto the gel. A 1 kb DNA ladder (Bioline) was loaded alongside the samples. The agarose gel was subjected to electrophoresis for 40-50 min at 100 V. The DNA bands were visualised on a UV transilluminator and excised from the gel. The digested DNA was extracted from the gel using a QIAquick Gel Extraction Kit (Qiagen) according to the manufacturer's instructions. The DNA concentration was measured as absorbance at 260 nm using a spectrophotometer (NanoDrop One^{C}, Thermo Fisher Scientific).

2.1.1.4 DNA ligation

100 ng of the digested pHR backbone was combined with the digested insert at 1:3, 1:5, and 1:10 ratios. T4 DNA Ligase (New England Biolabs) was used and the ligation reactions were prepared according to the manufacturer's instructions. The ligation was performed at 16 °C for at least 1 h.

2.1.1.5 Transformation of *E. coli*

20 μl of TOP10 *E. coli* (produced in-house) suspension were thawed on ice and combined with 2 μl of the ligation reaction in PCR tubes pre-chilled at 4 °C. Alternatively if transforming a stock plasmid, 0.1 ng of DNA in 1 μl of TE buffer was used. The competent bacteria were incubated with the ligated DNA for 20 min at 4 °C, 45 s at 42 °C, and 2 min at 4 °C. Next, 180 μl of lysogeny broth (LB) was added to the PCR tube and the bacteria were incubated for 1 h at 37

°C. The bacteria were plated on LB-agar media supplemented with 100 ng/ul ampicillin prepared in 6-well plates. The plates were incubated for 18 h at 37 °C. The next day the plates containing bacterial colonies were used to set up liquid cultures or stored at 4 °C for up to 2 weeks.

2.1.1.6 Purification of DNA from *E. coli* liquid cultures

Individual colonies were picked from the plate containing the transformed bacteria and added to 15 ml of LB broth supplemented with 100 ng/ul ampicillin. The liquid cultures were incubated for 18 h at 37 °C in a shaking incubator. The following day, DNA was isolated using HiPure Plasmid Miniprep Kit (Thermo Fisher Scientific) according to the manufacturer's instructions. The DNA concentration was measured as absorbance at 260 nm using a spectrophotometer (NanoDrop One^{C}, Thermo Fisher Scientific). The sequence of the constructs was validated using Sanger sequencing (Source Bioscience).

2.1.2 Tissue culture

2.1.2.1 Cell culture media and buffers

Reagent	Source	Catalogue Number
RPMI-1640 medium	Thermo Fisher Scientific	21875-034
RPMI-1640 medium, no phenol red	Thermo Fisher Scientific	11835030
McCoy's 5A medium	Sigma-Aldrich	M9309
DMEM medium	Thermo Fisher Scientific	41965-039
Penicillin/Streptomycin/Neomycin	Sigma-Aldrich	P4083
Sodium pyruvate	Sigma-Aldrich	S8636-100ML
HEPES	Thermo Fisher Scientifc	15630080
L-Glutamine	Sigma-Aldrich	G7513-100ML
Non-essential amino acids	Thermo Fisher Scientific	11140-035
β-mercaptoethanol	Thermo Fisher Scientific	31350010
Fetal Bovine Serum (FBS)	Sigma-Aldrich	10500-064
Human Serum	Sigma-Aldrich	H4522-100ML
EDTA	Thermo Fisher Scientific	15575020
Bovine Serum Albumin (BSA)	Sigma-Aldrich	A7906-100G
IL-4	Biolegend	574004
GM-CSF	Biolegend	572903
LPS	Sigma-Aldrich	LPS25
IL-2	Biolegend	589104

Table 2.1: Tissue culture media and supplements

Phosphate-buffered saline (PBS): Milli-Q water, 137 mM NaCl, 2.7 mM KCl, 10 mM Na_2HPO_4, KH_2PO_4 (provided by the MRC Human Immunology Unit, Weatherall Institute of Molecular Medicine)

Jurkat T cell medium (JTM): RPMI 1640 media, 10% (v/v) FBS, 10 mM HEPES, 50 U/ml Penicillin, 50 μg/ml Streptomycin, 100 μg/ml Neomycin, 2 mM L-Glutamine, 1 mM Sodium pyruvate

Primary T cell medium (PTCM): RPMI 1640 media, 10% (v/v) FBS or 10% human serum (for lentiviral transductions of primary $CD8^+$ T cells), 10 mM HEPES, 50 U/ml Penicillin, 50 μg/ml Streptomycin, 100 μg/ml Neomycin, 2mM L-Glutamine, 1 mM Sodium pyruvate, 50 U/ml hIL-2

U-2 OS cell medium (U2M): McCoy 5A media, 10% (v/v) FBS, 50 U/ml Penicillin, 50 μg/ml Streptomycin, 100 μg/ml Neomycin.

Imaging T cell medium (iRPMI): Phenol red-free RPMI media, 10 mM HEPES

HEK 293T medium (HKM): DMEM media, 10% (v/v) FBS, 50 U/ml Penicillin,

50 µg/ml Streptomycin, 100 µg/ml Neomycin, 2 mM L-Glutamine, 1 mM Sodium pyruvate

CHO-K1 medium: DMEM media, 10% (v/v) FBS, 50 U/ml Penicillin, 50 µg/ml Streptomycin, 100 µg/ml Neomycin, 4 mM L-Glutamine, 1 mM Sodium pyruvate, 1X Non-essential amino acids

moDC medium (MDM): RPMI 1640 media, 10% (v/v) FBS, 2 mM L-Glutamine, 1 mM Sodium pyruvate, 5 nM β-mercaptoethanol, 1X Non-essential amino acids, 100 ng/ml GM-CSF, 10 ng/ml IL-4

Activating moDC medium (aMDM): RPMI 1640 media, 10% (v/v) FBS, 2 mM L-Glutamine, 1 mM Sodium pyruvate, 5 nM β-mercaptoethanol, 1X Non-essential amino acids, 100 ng/ml GM-CSF, 10 ng/ml IL-4, 200 ng/ml LPS

Magnetic-activated cell sorting (MACS) buffer: PBS, 2 mM EDTA, 0.5% (w/v) BSA

Freezing medium (FM): FBS, 10 % (v/v) DMSO.

All cell culture media, buffers and reagents were kept sterile.

2.1.2.2 Maintenance of cell lines

All cell lines were cultured in a humidified incubator at 37 °C and 5% CO_2 (PHC). All incubation steps involving live cells were performed at 37 °C and 5% CO_2 unless specified otherwise. Following the wash steps, cells were centrifuged at 400 x *g* for 5 min at room temperature (RT) unless specified otherwise. For counting, the cell suspension was diluted 1:1 with Trypan Blue (Thermo Fisher Scientific) and counted using an automated cell counter (Countess II, Thermo Fisher Scientific).

All the adherent cell lines (U-2 OS, HEK 293T and CHO-K1 cells) were passaged when ~90% confluence was reached. Cells were washed using PBS and incubated with 5 mM EDTA in PBS for 5-10 min at 37 °C, 5% CO_2. Next, relevant culture medium (5X volume of the EDTA solution) was added to the tissue culture flask and the cell suspension was centrifuged for 5 min at 400 x *g* at RT. Following the centrifugation step, cells were resuspended in the relevant medium, diluted to achieve the desired passage ratio and transferred to a new

tissue culture flask. Jurkat T cells were maintained at a density of 0.2-1.5x10^6 cells per ml. Primary T cells were maintained at a density of 0.5-2x10^6 cells per ml. If a low number of primary T cells were used, 2x10^6 T cells were seeded in 1 ml of PTCM in a 48-well plate and passaged at a 1:2 ratio when ~90% confluent.

2.1.2.3 Cryopreservation of cell lines and primary CD8$^+$ T cells

Cells were harvested and centrifuged for 5 min at 400 x *g* at RT. Adherent cell lines were detached using 5 mM EDTA in PBS as described in section 2.2.2.2. The culture medium was removed and the cell pellet was resuspended in FM to obtain a cell suspension at 2x10^6 cell/ml and 10-30x10^6 cell/ml for cell lines and primary T cells, respectively. 1 ml of cell suspension in FM was transferred into cryovials (Starlab) and then frozen in CoolCell freezing chambers (Corning) at -80 °C. At least 24 h later, the cryovials were transferred to LN_2 tanks for long-term storage.

To thaw both primary T cells and cell lines, the cryovials were incubated in a water bath at 37 °C for 3-4 min. Immediately after thawing, the cell suspension was diluted in 30 ml of pre-warmed, appropriate cell culture medium and centrifuged for 5 min at 400 x *g* at RT. The cell pellet was resuspended in the culture medium and transferred to a humidified incubator (37 °C and 5% CO_2).

2.1.2.4 Isolation of primary CD8$^+$ T cells

Leukocyte cones were provided by the NHS Blood&Transplant service. 15 ml of blood was diluted using RPMI 1640 medium up to 50 ml and layered on 15 ml of Lymphoprep (StemCell Technologies). To isolate peripheral blood mononuclear cells (PBMC), the samples were centrifuged at 800 x *g* for 30 min at RT with the centrifuge deceleration set to zero. The layer of PBMC was extracted and the PBMCs were washed with 50 ml of RPMI 1640 medium and centrifuged at 400 x *g* for 10 min at RT. The PBMCs were resuspended in 50 ml of PTCM. Primary CD8$^+$ T cells were isolated from PBMCs using a MACS system: CD8$^+$ T Cell Isolation Kit (Miltenyi Biotec), LS columns (Miltenyi Biotec) and a manual magnetic separator (Miltenyi Biotec) were used as recommended by the manufacturer. 10^6 purified primary CD8$^+$ T cells were resuspended in 1 ml of PTCM and plated in

a 24-well plate with 75 µl of αCD3/αCD28 Dynabeads (Thermo Fisher Scientific) per well (1:3 cell bead ratio). 5 days later, the dynabeads were removed and the primary $CD8^+$ T cells were pooled and transferred to T-25 flasks. Expanding primary $CD8^+$ T cells were kept in culture for another 10 days and kept at a density of 0.5-2x10^6 cells per ml. On the final day, the T cells were frozen as described in section 2.2.2.3.

2.1.2.5 Lentivirus production

HEK 293T cells were used as a packaging cell line for the production of lentivirus. HEK 293T were seeded in a 6-well plate at 0.5x10^6 cells per well in 2 ml of HKM and cultured for 18 h. 0.5 µg lentiviral envelope plasmid (pMDG, Addgene 187440), 0.5 µg packaging plasmid (p8.91, Addgene 187441) and 1 µg transfer plasmid (pHR, Addgene 187358 or pHRi) containing the gene of interest were combined in 100 µl of unsupplemented DMEM medium. Subsequently, 4.5 µl of GeneJuice (Sigma-Aldrich) was added and gently resuspended. Following a 30-minute incubation at RT, the complexed DNA was added drop-wise to a single well containing the HEK 293T cells. Transfected HEK293T cells were cultured for 48 to 72 h before the supernatant containing the lentivirus was harvested and filtered (0.22 µm, PES). The lentivirus-containing supernatant was used within 4 h or kept -80 °C for further use. Protocol was proportionally scaled up if necessary.

2.1.2.6 Transduction of cell lines

The transduction of U-2 OS cells and Jurkat T cells was performed in either 6-well plates or T-25 flasks. CHO-K1 cells were only transduced in T-25 flasks. For the transduction in the 6-well plate, 0.25-0.5x10^6 cells were harvested and seeded in 1 ml of appropriate media per well. 1-2 ml of lentiviral supernatant was then added to the well. To achieve a range of expression levels, a twofold serial dilution of the lentiviral supernatant was used. The next day the lentiviral supernatant was removed and replaced with fresh media. For the transduction in a T-25 flask, cells were harvested and seeded in 2 ml of media. 2 ml of lentiviral supernatant was then added to the flask. The next day, the flask was topped

up to 10 ml with appropriate tissue culture media. For all cell lines, transgene expression was verified by flow cytometry or Western blotting no earlier than 3 days after transduction. If necessary the cell lines were re-transduced to boost the expression levels and ensure uniform transgene expression. Alternatively, the expression levels of the transgene were adjusted by FACS.

2.1.2.7 Preparation of lentivirus-coated retronectin plates for transduction of primary CD8$^+$ T cells

To maximise the transduction efficiency of primary CD8$^+$ T cells, lentivirus-coated plates were prepared. A solution of retronectin (Takara Bio) at 25 ug/ml in PBS was used to coat non-treated 48-well plates (250 µl/well). The plates containing the retronectin solution were incubated at 4 °C for 24-48 h before coating with the lentivirus. Following the incubation, the retronectin solution was removed and incubated for 30 min with 300 µl of a 2% (w/v) BSA solution in PBS at RT. Next, the BSA solution was removed and the wells were washed with 1 ml of PBS. 1.5 ml of the lentiviral supernatant was added to each well and the plate was centrifuged at 2000 x *g* for 90 min at 32 °C. Most of the lentiviral supernatant was removed leaving 50-100 µl in each well. The plates were used immediately as described in section 2.2.2.9.

2.1.2.8 Rapid expansion mix

PBMCs were isolated from the blood of at least three donors as described in section 2.2.2.4 and irradiated for 10 min at 3000 rad. The irradiated PBMCs were then centrifuged at 300 x *g* for 5 min and resuspended in PTCM at 2x10^6 cell/ml. The suspensions of irradiated PBMCs from different donors were mixed in equal numbers and supplemented with 200 U/ml hIL-2, phytohemagglutinin-L (Thermo Fisher Scientific) at 2.5 µg/ml and OKT3 antibody (Biolegend) at 50 ng/ml to produce a rapid expansion mix (REM). The REM was kept in the incubator (37 °C, 5% CO_2) and used within 48 h.

2.1.2.9 Transduction of primary CD8$^+$ T cells with ZAP70-HaloTag construct

PBMCs were isolated as described in section 2.2.2.4 and diluted 1:1 with RPMI 1640 media. The diluted PBMCs were centrifuged at 400 x *g* for 10 min at RT. The obtained pellet was resuspended in PTCM to a density of 2-3x10^6 T cells per ml and αCD3/αCD28 dynabeads were added at a 1:1 bead-to-cell ratio. The mix of primary T cells with dynabeads was then plated in a 24-well plate (2 ml per well) and incubated for 48 h (37 °C, CO_2. The αCD3/αCD28 dynabeads were removed and T cells were used for lentiviral transduction. The lentivirus-coated retronectin plates were prepared as described in section 2.2.2.7. 10^6 T cells were seeded in 1 ml of PTCM per well in the lentivirus-coated plate. The plate was then centrifuged at 500 x *g* for 1 min at RT with acceleration and deceleration rates set to 1. T cells were cultured in 48-well plate and split at a 1:2 ratio when confluence was reached.

4 days later, the transduced T cells were harvested and resuspended in 200 µl of 0.2 µM dilution of Janelia Fluor 646 HaloTag Ligand (Promega) in PTCM, then incubated for 20 min at 37 °C. Next, T cell were washed with 10 ml of MACS buffer, resuspended in a 1% (v/v) FITC anti-CD8 antibody in PTCM and incubated for 15 min at 37 °C. T cells were washed twice with 10 ml of MACS buffer and kept at 4 °C in 500 µl of PTCM until FACS. T cells were then sorted with a gate set on CD8$^+$ ZAP70-HaloTag$^+$ T cells. Immediately after FACS, T cells were washed with 40 ml of PTCM and combined with the REM at a 1:200-1:500 ratio of sorted T cells to irradiated PBMCs. REM was prepared as described in section 2.2.2.8. At least 8 ml of T cell suspension with REM was then seeded in a T-25 flask. 5 days later, 5 ml of PTCM was added to the flask without disturbing the proliferating T cells. T cells were further cultured in a T-25 flask until an opaque layer of T cells at the bottom of the flask became visible. Next, 20 ml of PTCM was added and T cells were transferred into a T-75 flask. 14 days after FACS, T cells were subjected to another expansion cycle or frozen and kept in LN_2 until further use.

2.1.2.10 Electroporation of U-2 OS cells with RNP

Guide RNA (gRNA) was prepared by mixing 6.25 µl of 400 µM tracrRNA (IDT) and 400 µM CD58-targeting crRNA (target sequence: GTACTCATGGGATTGTCCTA; IDT). The combined RNA oligonucleotides were then incubated at 95 °C for 5 min and cooled to RT. To generate ribonucleoproteins (RNP), the gRNA was combined with 2.5 µl of 10 µg/µl S.p HiFi Cas9 Nuclease V3 (IDT) and incubated for a minimum of 30 min at RT.

82 µl of P3 Primary Cell Nucleofector Solution (Lonza) and 18 µl of Supplement 1 (Lonza) to make the electroporation buffer. $5x10^6$ U-2 OS cells were harvested and resuspended in 100 µl of the electroporation buffer. The U-2 OS cell suspension was mixed with 15 µl of the RNP solution and transferred into a 4D-Nucleofector cuvette (Lonza). The electroporation was performed using a 4D-Nucleofactor (Lonza) using an E0115 pulse sequence. Immediately following the electroporation, 500 µl of U2M was added to the cuvette. The electroporated U-2 OS cells were cultured for three weeks and CD58 expression was regularly monitored by flow cytometry.

2.1.3 Protein expression and purification

2.1.3.1 C-tag affinity purification

CHO-K1 cells were transduced twice as described in section 2.2.2.6 with a 5-day recovery period between the successive transductions. The CHO-K1 cell culture was scaled up from a single T-25 to 10 T-175 flasks. At the final stage of CHO-K1 cell culture, when cells were grown in 10 T-175 flasks, the FBS content in the cell culture medium was reduced to 1% (v/v). The ImmTAC was purified from CHO-K1 tissue culture supernatant harvested 22 days following transduction. Up to 2 repeated harvests were conducted at 7-day intervals. Cell debris was removed from the supernatant using a vacuum filtration system (0.22 µm, PES). The filtered supernatant was then passed through an Econo-Column (Bio-Rad) packed with 5 ml of CaptureSelect C-tagXL Affinity Matrix (Thermo Fisher Scientific) by gravity flow (0.2-0.5 l/h). The resin was washed with 20 column volumes (CV)

of the equilibration buffer (Mili-Q water, 20 mM Tris, 150 mM NaCl, pH 7.5). The ImmTAC was then eluted from the affinity resin by using an elution buffer (Milli-Q water, 20 mM Tris, 2M MgCl2, pH 7.5) into 3 ml fractions. Absorbance at 280 nm of each fraction was measured using a spectrophotometer (NanoDrop One^{C}, Thermo Fisher Scientific). The protein-containing fractions were pooled and concentrated to 0.5 ml using a centrifugal filter unit with a 10 kDa weight cutoff (Sigma-Aldrich). The concentrated sample was centrifuged at 17,000 x *g* for 10 min at 4 °C. The concentrated ImmTAC protein was further purified using size exclusion chromatography (see section 2.2.3.2). The resin was regenerated using 10 CVs of a regeneration buffer (Milli-Q water, 0.2 M glycine, pH 2).

2.1.3.2 Size exclusion chromatography

Size exclusion chromatography (SEC) was conducted to isolate monodisperse protein. The Superdex 200 10/300 GL column (Cytiva) was equilibrated with a running HBS buffer (20 mM HEPES, 150 mM NaCl, pH 7.5). The concentrated sample was loaded onto the SEC column using a 0.5 ml loop and eluted with 1.1 CV of the HBS buffer into 0.5 ml fractions. The fractions were analyzed using SDS-PAGE (see section 2.2.3.3) and a spectrophotometer (NanoDrop One^{C}, Thermo Fisher Scientific).

2.1.3.3 Polyacrylamide gel electrophoresis

Polyacrylamide gel electrophoresis (PAGE) was used to assess the purity of the SEC fractions. The fractions were diluted 1:1 in either a non-reducing or reducing (2.5% v/v β-mercaptoethanol) Laemmli buffer. The molecular weight marker, Precision Plus Protein All Blue Standards (Bio-Rad) was run alongside the samples for reference. If the SDS-PAGE gel was further analysed by Western blotting then a Rainbow Marker (Sigma-Aldrich) was used instead. Samples were denatured by a 5-minute incubation at 95 °C. The denatured samples were loaded onto NuPAGE 4-12% Bis-Tris (ThermoFisher Scientific) and run at 150 V for 1 h with NuPAGE MES SDS Running Buffer (ThermoFisher Scientific). The gels were stained using Quick Coomassie Stain (ProteinArk) for 1 h and

then destained in deionized water. The gels were imaged using the iBright CL1500 Imaging System (Invitrogen).

2.1.3.4 Western blotting

Western blotting was used to test the expression of ImmTAC following lentiviral transduction of CHO-K1 cells. 12 days after lentiviral transduction, the CHOK1 tissue culture supernatants were collected and subjected to SDS-PAGE as described in section 2.2.3.3. Next, the proteins were transferred onto a nitrocellulose membrane using a Trans-Blot Turbo Transfer System (Bio-Rad) for 7 minutes at 25 V. The membrane was then blocked for 18 h with a filtered 5% (w/v) non-fat dry milk solution in PBS with 0.05% (v/v) Tween 20 (PBS-T). The membrane was incubated with 3.3% (v/v) anti-C tag antibody (Thermo Fisher Scientific) in the blocking solution for 30 min at RT, followed by four washes with PBS-T. Next, the membrane was incubated with 2.5% (v/v) HRP-conjugated anti-Ilama antibody (Thermo Fisher Scientific) for 30 min at RT. The membrane was then washed four times with PBS-T and developed using ECL Western Blotting Reagents (Thermo Fisher Scientific) according to the manufacturer's protocol and imaged using iBright CL1500 Imaging System (Invitrogen).

2.1.3.5 Surface Plasmon Resonance

The binding of ImmTACs to their ligands: GP100-HLA-A2-His_{12} and biotinylated CD3$\epsilon\gamma$ was assessed using surface plasmon resonance (SPR) as implemented by Biacore 8K (Cytiva). All measurements were performed at 37 °C. The corresponding running buffer, HBS-P^+ or HBS-EP^+ (Cytiva), was used to dilute the ImmTAC for binding measurements to GP100-HLA-A2-His_{12} and biotinylated CD3$\gamma\delta$, respectively. All runs were reference subtracted as well as blank subtracted. Both protein samples were prepared as a twofold serial dilution. Both buffers were filtered and degassed using a vacuum filtration system (0.22 µm, PES)

For affinity and kinetic measurements of ImmTACs to GP100-HLA-A2-His_{12}, Series S Sensor Chip NTA (Cytiva) was used according to the manufacturer's

instructions and multi-cycle analysis was conducted. The GP100-HLA-A2-His_{12} (50 nM) was captured on the chip for 60 s. The ImmTAC dilutions were injected for 60 s and the dissociation was monitored for 900 s. A serial dilution ranging from 200 nM to 1.56 nM was used. HBS-P+ was used as a running buffer. The NTA Chip was regenerated using the regeneration solution (350 mM EDTA in the HBS-P^+ buffer) according to the manufacturer's instructions.

For affinity and kinetic measurements of ImmTACs to the biotinylated CD3$\epsilon\gamma$, Series S Sensor CAPture Chip (Cytiva) was used and a single-cycle analysis was conducted. The CAP reagent (Cytiva) was injected for 300 s. The biotinylated CD3$\epsilon\gamma$ (50 nM) was captured on the chip for 180 s. The ImmTAC dilutions were injected for 120 s and the dissociation was monitored for 60 s before the next injection. A serial dilution ranging from 800 nM to 6.25 nM was used. HBS-EP+ was used as a running buffer. The CAPture Chip was regenerated with the regeneration solution (6M guanidine-HCl, 0.25 M NaOH) according to the manufacturer's instructions.

The analysis of binding kinetics was carried out using Biacore Insight Evaluation Software (Cytiva).

2.1.4 Flow cytometry

Reagent (fluorophore, target)	**Source**	**Catalogue Number**
PE HA tag	Biolegend	901518
PE CD43	Biolegend	343203
PE CD45	Biolegend	368509
PE CD54	Biolegend	353105
PE CD58	Biolegend	330905
PE HLA-A2	Biolegend	343305
PerCP-Cy5.5 CD14	Biolegend	367110
PB CD1a	Biolegend	300124
FITC CD83	Biolegend	305306
PB CD69	Biolegend	310920
PE-Cy7 CD8α	Biolegend	344712
AF647 CD25	Biolegend	302618
FITC CD3	Biolegend	300440
FITC CD8	Biolegend	344704
BV421 ICAM-1	BD Biosciences	564077
CD3	Biolegend	317302
MOPC21	Biolegend	400102
PE MOPC21	Biolegend	400111
BV421 MOPC21	Biolegend	400157
PB MOPC21	Biolegend	400131
AF647 MOPC21	Biolegend	400130
JF646 HaloTag ligand	Promega	GA1120
Zombie Yellow Viability Stain	Biolegend	423104

Table 2.2: Antibodies and staining reagents for flow cytometry

2.1.4.1 General flow cytometry

0.5-0.2x10^6 cells were harvested and washed twice in an ice-cold PBS buffer. All the processing steps were performed in either 96-well U-bottom plates or 5 ml round-bottom polystyrene tubes. The centrifugation step after each washing step was carried out at 757 x g for 3 minutes at 4 °C. The cells were resuspended in ice-cold 100-200 µl of PBS and stained with a selected antibody cocktail. Antibodies were diluted 1:100 for analysis of transgene expression and 1:200 for analysis of activated T-cells. The stained cells were incubated for 45-60 minutes at 4 °C in the dark. After the incubation, the cells were washed twice with ice-cold PBS buffer, and then centrifuged at 757 x g for 3 minutes. The

resultant cell suspension was fixed using 1% (v/v) paraformaldehyde in PBS and stored at 4 °C until analysis. Samples were analysed using the Attune NxT Flow Cytometer (Thermo Fisher Scientific). Flow cytometry data was analysed using FlowJo software (BD Sciences).

If PE-conjugated antibodies were used to quantify the copy numbers of molecules on the cell surface, Quantibrite PE kit (BD Biosciences) was used for calibration. The Quantibrite PE beads were resuspended at 0.5 ml of ice-cold PBS and within the same flow cytometry experiment as the samples of interest. The copy-number analysis was performed according to the manufacturer's protocol. For staining of GP100-MHC on the U-2 OS cell surface, ImmTACs were conjugated to Alexa Fluor 647 dye using Alexa Fluor 647 Antibody Labelling Kit (Thermo Fisher Scientific) as per the manufacturer's protocol.

2.1.4.2 Fluorescence-activated cell sorting

For sorting of cell lines, 5-10x10^6 cells were harvested and washed twice in an ice-cold MACS buffer. All the processing steps were performed in 5 ml round-bottom polystyrene tubes. Cells were resuspended in ice-cold 100-200 µl of MACS and stained with selected antibodies (1:100 dilution) for 30-45 minutes at 4 °C in the dark. After the incubation, the cells were washed twice with ice-cold MACS buffer, passed through a filter (30 µm, CellTrics), resuspended at ~0.5x10^6 cell/ml and kept on ice until FACS. Fluorescence-associated cell sorting (FACS) was performed by the staff of the WIMM sorting facility using Aria III (BD Bioscience) or Symphony S6 (BD Bioscience) instruments.

2.1.4.3 Co-culture assays of T cells with U-2 OS cells

Co-culture assays of primary $CD8^+$ T cells or Jurkat T cells with various U-2 OS cell lines were used to establish the correlates of T-cell activation. 2.5x10^4 U-2 OS cells were plated in a 96-well flat-bottom plate and incubated for 18 h (37 °C, 5% CO_2) in 200 µl of U2M to form continuous monolayers. If U-2 OS cells not expressing the GP100-SCT were used, the media were supplemented with a 10-fold serial dilution of heteroclitic GP100 peptide (YLEPGPVTV, GenScript)

ranging from 10^{-5} to 10^{-12} M. The next day, the culture media was gently removed from each well and the U-2 OS cells were washed twice with 200 µl of PBS. 100 µl of ImmTAC dilution in PTCM media was then added to each well. Peptide-pulsed U-2 OS were labelled with 10 nM ImmTAC. The GP100-SCT U-2 OS were labelled with a 10-fold serial dilution of ImmTAC ranging from 10^{-10} to 10^{-17} M. Following a 30 min incubation (37°C and 5% CO_2), ImmTAC-containing culture media were removed from the peptide-pulsed U-2 OS cells were washed once with 200 µl of PBS. For T-cell activation with anti-CD3ϵ antibodies, 96-well flat-bottom plates were coated either with OKT3 antibody or MOPC21 isotype control. 50 µl of 10 µg/ml of the antibody in PBS was transferred to a single well. Plates were incubated for 4 h at 37 °C and then washed three times with 200 µl of PBS. $5x10^4$ T cells in PTCM were added to a final volume of 200 µl of PTCM and incubated in the antibody-coated wells or co-cultured with the ImmTAC-labelled U-2 OS cells for 18 h (37 °C, 5% CO_2). Following the incubation, T cells were removed from the 96-well flat-bottom plate and transferred into a 96-well U-bottom plate for staining. T cells were washed twice with ice-cold PBS and centrifuged at 757 x *g* for 3 minutes between washing steps. T cells were stained with Zombie Yellow Fixable Viability stain (Biolegend) for 20 min at RT. After staining, T cells were washed again with ice-cold PBS and centrifuged at 757 x *g* for 3 min and stained in 50 µl of antibody cocktail (FITC anti-CD3, PE-Cy7 anti-CD8α, AF647 anti-CD25 and PB anti-CD69) in ice-cold PBS for 45 minutes at 4 °C. Next, T cells were washed twice with ice-cold PBS and centrifuged at 757 x *g* for 3 minutes between the washing steps. Finally, T cells were resuspended in 100 µl of 1% (v/v) formaldehyde in PBS and stored at 4 °C until analysis.

2.1.4.4 Analysis of monocyte-derived dendritic cells

Monocytes were isolated from PBMCs (see section 2.2.2.4 for details) using MACS with CD14 microbeads (Miltenyi Biotec), LS columns (Miltenyi Biotec) and a manual magnetic separator (Miltenyi Biotec). The isolation was performed

according to the manufacturer's instructions. For differentiation into monocyte-derived dendritic cells, $1x10^6$ monocytes were resuspended in 1 ml of MDM and plated in non-treated 24-well plates. Monocytes that were to remain undifferentiated to serve as negative control were plated in moDC media without the cytokines (IL-4, GM-CSF). Following a 72 h incubation, culture media were removed and replaced with fresh MDM with or without the cytokines for monocytes and moDCs, respectively. Following 48 h incubation, immature moDCs and monocytes were harvested and stained as described below. To activate the immature moDCs, the culture media was replaced with aMDM. After 48 h incubation, the mature DCs were harvested and stained.

Harvested monocytes, immature moDCs and mature moDCs were washed twice in an ice-cold PBS buffer. Cells were first stained with Zombie Yellow Fixable Viability stain for 20 min at RT. Next, cells were washed with ice-cold PBS and stained in 50 µl of antibody cocktail (PB CD1a, PerCP-Cy5.5 CD14, FITC CD83) in ice-cold PBS for 60 minutes at 4 °C. Additionally, the mature moDCs were stained with an antibody against one of the selected cell surface molecules: CD43, CD45, CD54, CD58, HLA-A2 and β_2M. Cells were stained for 60 min at 4 °C in the dark and then washed twice with ice-cold PBS and resuspended in 2X IC fixation buffer (Thermo Fisher Scientific) for 30 min at RT. Fixed cells were washed with ice-cold PBS and resuspended in 1X Fixation buffer (Thermo Fisher Scientific) diluted in PBS. Fluorescence minus one stained mature moDCs and single-stained OneComp beads (Invitrogen) were included as compensation controls.

Reagent	Source	Catalogue Number
SiR/AF488 CD45 (Gap8.3)	Davis Laboratory	N/A
Unlabelled/AF488 N-MED ImmTAC	Immunocore Ltd.	N/A
Unlabelled N-NED ImmTAC	Davis Laboratory	N/A
JF549 HaloTag ligand	Promega	GA1110
JF646 HaloTag ligand	Promega	GA1120
Fluo-4 AM, cell-permeant	Thermo Fisher Scientific	F14201
CellMask Deep Red Membrane Stain	Thermo Fisher Scientific	C10046
MitoTracker Deep Red	Thermo Fisher Scientific	M22426

Table 2.3: Antibodies and staining reagents for microscopy

2.1.5 Live-cell imaging

For all imaging experiments, primary $CD8^+$ T cells were thawed the day before the imaging experiment as described in section 2.2.2.3. On the day of the imaging experiment, dead T cells were removed by MACS using the dead cell removal kit (Miltenyi Biotec), LS columns (Miltenyi Biotec) and a manual magnetic separator (Miltenyi Biotec). The wash steps were followed by centrifugation of T cell at 200 x *g* for 2 min unless specified otherwise. All media and buffers were syringe-filtered (0.22 µm, PES) before use. Imaging data was viewed and processed using ImageJ software. The theoretical diffraction limit for a given instrument and fluorophore was calculated using Abbe's formula ($D=\lambda/2NA$).

2.1.5.1 Calcium release assays

For calcium release assays, 1-1.5x10^5 U-2 OS cells in 300 µl of U2M were seeded in a glass-bottom 8-chamber coverslip (Ibidi). The U2M media was supplemented with the heteroclitic GP100 peptide (YLEPGPVTV, GenScript) as required. Next, U-2 OS cells were cultured for 18 h (37 °C, 5% CO_2). Before calcium imaging the hGP100-containing media were removed, U-2 OS cells were washed twice with McCoy medium and incubated with ImmTAC diluted in McCoy medium for 20 min. Before the addition of T cells, the ImmTAC solution was removed, and U-2 OS cells were washed twice with RPMI 1640 media and left in 300 µl of RPMI 1640 media for imaging.

1-2x10^6 T cells were harvested and centrifuged at 200 x *g* for 2 min. The cell pellet was resuspended in 0.5% (v/v) Fluo4-AM in RPMI 1640 media and

incubated for 5 min (37 °C, 5% CO_2). Fluo-4 AM was reconstituted in 100% DMSO according to the manufacturer's instructions. Next, T cells were washed twice with RPMI 1640 media and resuspended in 50 µl of RPMI 1640 media.

Calcium imaging was performed using a Zeiss LSM 880 inverted microscope with an incubator chamber at 37 °C. 10x air objective was used and the sample was illuminated using a 488 nm (Argon laser) and white light. The image was acquired at 0.5 frame/s with line scan averaging set to 2. The coverslip was placed on the stage and the focal plane containing the U-2 OS cell monolayer was identified. 20-50 µl of T cells labelled with Fluo-4 AM were gently added to the chamber containing the U-2 OS cells. Image acquisition was initiated as soon as the first T cell settled on the U-2 OS cell monolayer. 600 frames (20 min) were acquired. The images were analysed using a bespoke MATLAB code written by Dr. Jane Humphrey https://github.com/janehumphrey/calcium.

2.1.5.2 Preparation of primary T cells and U-2 OS cells for multi-colour imaging

For epifluorescence widefield microscopy (eWM) and epi-illumination selective plane illumination microscopy (eSPIM), 1-1.5x10^5 U-2 OS cells in 300 µl of U2M were seeded in a glass-bottom 8-chamber coverslip (Ibidi). The U2M media was supplemented with 10 µM heteroclitic GP100 peptide (YLEPGPVTV, GenScript) as required. The following day, the culture media was removed, U-2 OS cells were washed with 300 µl of iRPMI and incubated with 200 µl of 0.2 µM Janelia Fluor 549 (JF549) HaloTag Ligand solution in iRPMI for 15 min (37 °C, 5% CO_2) to label the intracellular HaloTag. Next, U-2 OS cells were washed twice with 300 µl of iRPMI and incubated in 300 µl iRPMI for 15 min (37 °C, 5% CO_2) to remove the residual JF549 dye from the cytoplasm. Optionally, 10 nM N-MED ImmTAC (Immunocore) or 10 nM AF488-conjugated N-MED ImmTAC (Immunocore) were included in the iRPMI used for the incubation step. After the incubation, the U-2 OS cells were washed three times with 300 µl of iRPMI or PBS supplemented with 10 mM HEPES and 2 mM $MgSO_4$. After the final

wash, U-2 OS cells were left in either 300 µl of iRPMI or PBS supplemented with 10 mM HEPES and 2 mM $MgSO_4$ until imaging.

1-2x10^6 T cells were harvested and centrifuged at 200 x g for 2 min. The cells were washed with 1 ml of iRPMI, resuspended in 50 µl of SiR or AF488-conjugated anti-CD45 antibody at 0.04 mg/ml and incubated for 10 min (37 °C, 5% CO_2). Optionally, the iRPMI was supplemented with 0.5% (v/v) Fluo4-AM, 0.2 µM Janelia Fluor 646 HaloTag Ligand or 1µg/ml CellMask Deep Red Plasma Membrane Stain. Next, T cells were washed twice with iRPMI and resuspended in 20-50 µl of iRPMI or PBS supplemented with 10 mM HEPES and 2 mM $MgSO_4$.

The interactions between T cells and U-2 OS were imaged using a custom-built eWM and eSPIM instruments or a commercial SDCM instrument. eSPIM and eWM instruments were fitted with an incubator chamber which maintained the samples at 37 °C, but the SDCM imaging was performed at RT. The 8-chambered coverslip was placed on the stage and 20-50 µl of T-cell suspension was gently added to the chamber containing the U-2 OS cells. The acquisition was initiated as soon as the first T cell settled on the U-2 OS cell monolayer.

2.1.5.3 Epifluorescence widefield microscopy

The eWM instrument was fitted with a 100x Plan Apo TIRF, NA 1.49 oil immersion objective (Nikon) mounted on an inverted microscopy body (Eclipse Ti2, Nikon) contained within an incubation chamber (DigitalPixel). The sample was illuminated using the following lasers: 488 nm (iBeam-SMART, Toptica), 561 nm (LaserBoxx, DPSS, Oxxius) and 641 nm (Obis Coherent). The laser beams were circularly polarised, collimated, expanded and aligned. The excitation light was directed through the centre of the back focal plane of the objective to generate widefield illumination. The emitted fluorescence passed through the objective lens, dichroic mirror (Di01-R405/488/561/635, Semrock), filter wheel (FF01-520/44-25, BLP01-488R, LP02-568RS-25, FF01-587/35-25, FF01-692/40-25; Semrock) and a tube lens (1.5x). The signal was recorded by an electron-multiplying charge-coupled device (Evolve 512 Delta, Photometrics). The three- or two-colour images

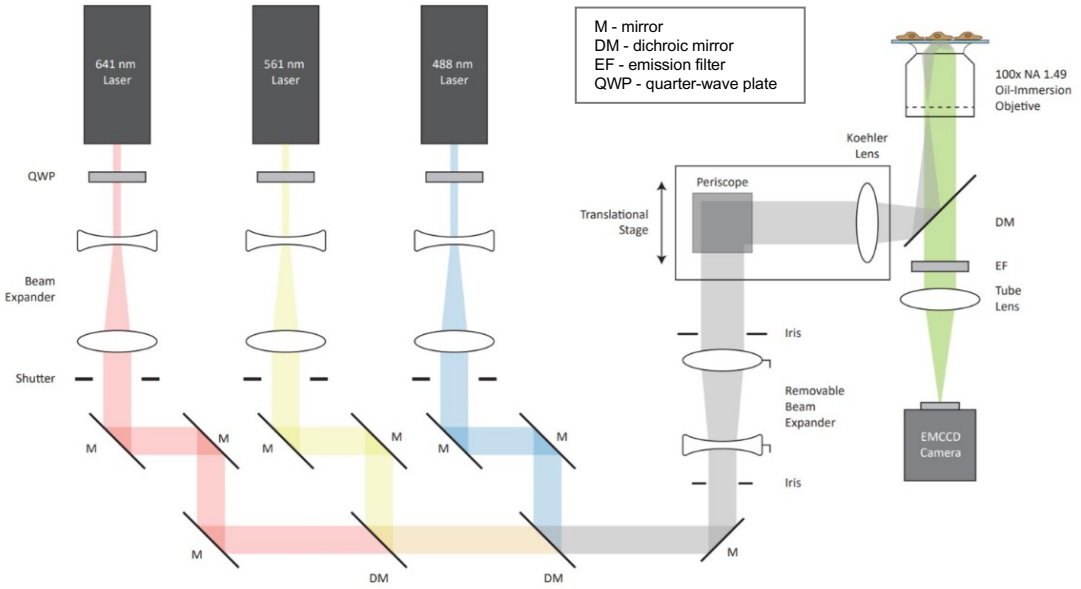


Figure 2.1: Layout of the epifluorescence widefield microscope. Simplified schematic showing the layout of the epifluorescence widefield microscope.

were acquired sequentially with 100 ms exposure time. The images were processed in ImageJ and analysed using a bespoke code written by Dr. Markus Koerbel https://github.com/mkoerbel/contactanalysis_2D.

2.1.5.4 Epi-illumination selective-plane illumination microscopy

The eSPIM instrument was fitted with a 60x CFI Plan Apo IR, NA 1.27, water immersion objective (Nikon) mounted on an inverted microscope body (Eclipse Ti-U, Nikon) contained within an incubation chamber (DigitalPixel). In contrast to other volumetric imaging methods, the eSPIM instrument uses a single objective to generate the light-sheet illumination and collect the emitted fluorescence. The sample was illuminated with the following lasers: 561 nm (Cobolt) and 638 nm (Cobolt). The excitation light was filtered (MF559-34; Semrock, FF01-637/7-25; Thorlabs), attenuated, expanded and collimated. The laser lines were then combined into a single excitation path. The combined laser lines were directed through a cylindrical lens to generate a Gaussian beam and its optical properties were modulated by an adjustable slit. The Gaussian beam was then projected through the edge of the back focal plane of the primary objective to produce a

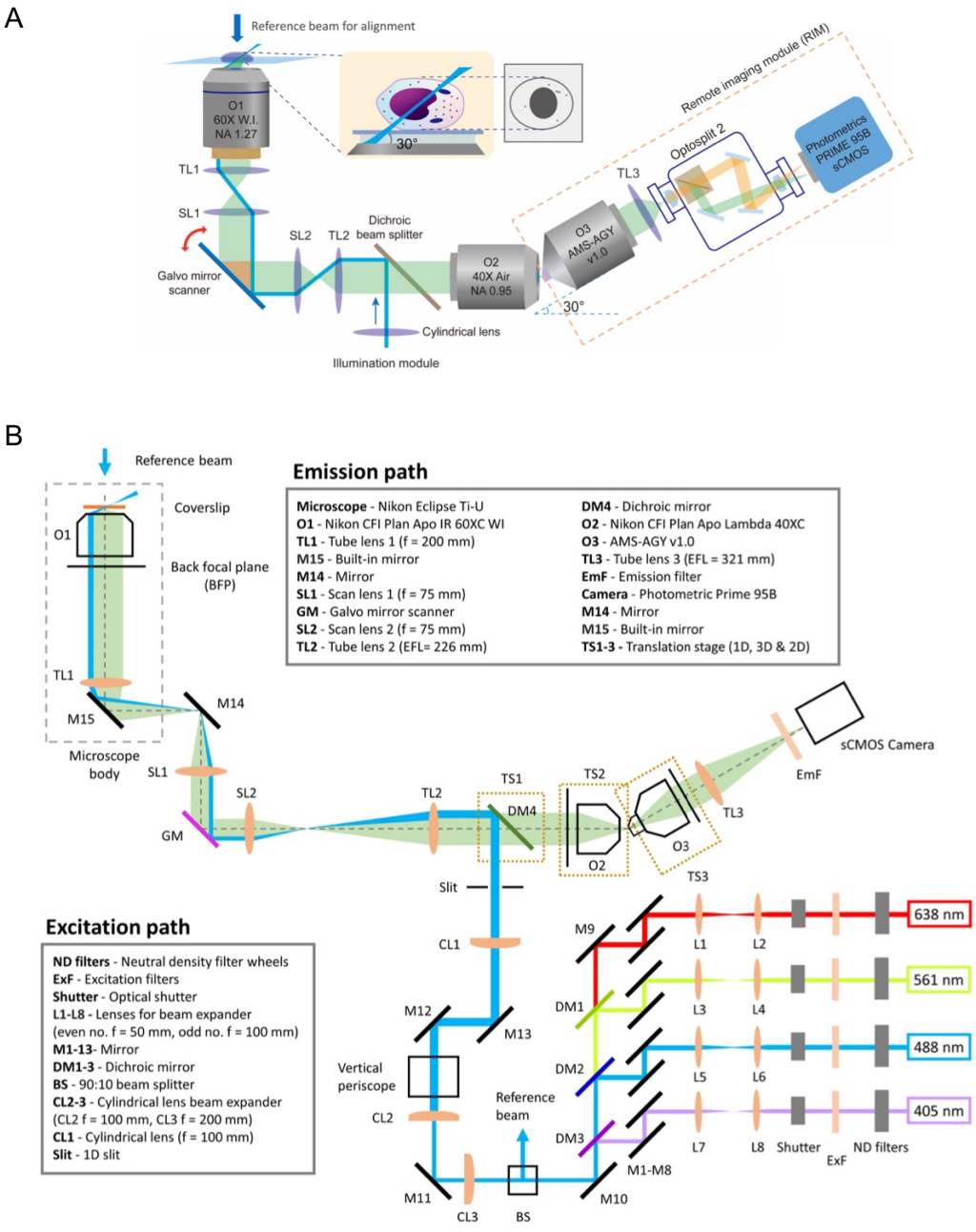


Figure 2.2: Layout of the epi-illumination selective-plane illumination microscope. A. Simplified schematic of the epi-illumination selective-plane illumination microscope (eSPIM) **B**. Complete layout of the epi-illumination selective-plane illumination microscope including the remote imaging module as well as complete excitation and emission paths. In A and B, the blue and green light paths correspond to the excitation light and the emission light, respectively. Figures were provided by Dr. Ziwei Zhang.

tilted (30°) light-sheet illumination onto the sample. The emitted fluorescence was collected through the same primary objective and passed through a dichroic mirror (Di01-R406/488/561/635; Semrock), a secondary 40x CFI Plan Apo Lambda, NA 0.95 air objective (Nikon) and a tertiary glass-tipped objective (Calico). The emission light was directed into an optical splitter (OptoSplit III, Prior) to separate the fluorescence channels which were then projected onto distinct portions of a sCMOS camera chip (Prime 95B, Photometrics). The two-colour images were acquired simultaneously with an exposure time of 30 ms. The images were deskewed and converted into focal stacks or 3D projections using a bespoke code (unpublished). The eSPIM instrument and the reconstruction code were designed and implemented by Dr. Ziwei Zhang. Quantification of the number of T cell interacting with U-2 OS cell monolayers at t = 10 min was performed through visually inspection of the reconstructed images.

2.1.5.5 Spinning disk confocal microscopy

The SDCM instrument (3i intelligent imaging) was fitted with a 100x Plan Apo TIRF, NA 1.46 oil immersion objective (Zeiss) mounted on an inverted microscope body (Zeiss Axio Observer 7). The sample was illuminated by the following lasers: 488 nm (LuxX), 561 nm (OBIS) and 638 nm (LuxX). The excitation light was field flattened (Yokogawa-Uniformizer) and relayed through a spinning disk unit (Yokogawa CSU-W1 T2, SoRa Dual Microlens Disk) and a dichroic mirror (FF01-440/521/607/700, Semrock). The emission light was filtered (FF01-525/45-25-STR, FF01-692/40-25-STR, FF02-617/ 73-25-STR; Semrock). The fluorescence signal was recorded using a sCMOS camera (Prime 89B, Teledyne Photometrics)

2.1.6 Fixed-cell imaging

2.1.6.1 Scanning electron microscopy

For scanning electron microscopy (SEM), 13 mm glass slides were placed in 12-well plates and incubated with 0.1% (w/v) Poly-L-Lysine (PLL, 70-150 kDa

MW; Sigma-Aldrich) for 30 min at RT. The coverslip was then washed twice with 2 ml of Milli-Q water and air-dried in the tissue culture hood for 2 h.

Primary $CD8^+$ T cells were fixed with 0.8% paraformaldehyde and 0.2% glutaraldehyde in PBS for 30 min at 4 °C. Next, 10^6 T cells in 1 ml of the fixative were added to a single well containing the PLL-coated glass slide. The plate was centrifuged for 1 min at 400 x *g* at RT and incubated for a further 30 min at 4 °C. Next, the fixative was removed and replaced with 1 ml of PBS. Fixed T cells were kept at 4 °C until further processing. The PBS was removed and the sample was washed 3 times with a 0.1 M phosphate buffer. Secondary fixation was performed in a 1% (w/v) OsO_4 in 0.1 M phosphate buffer for 1 h at 4 °C. The sample was washed three times with Milli-Q water and dehydrated using step-wise dilutions of ethanol (50%, 70%, 90%, 95% and 100% (v/v)) incubating the sample for 5 min at RT at each step. The 100% ethanol was replaced with 50% (v/v) hexamethyldisilazane (HMDS) in ethanol and then 100% (v/v) HMDS and incubated for 2 min each time. HMDS was removed and the sample was air-dried overnight. The dried sample was then sputter coated with gold (10-15 nm) and imaged using a JEOL-6390 Scanning Electron Microscope. The images were then processed in Fiji and the diameter of the microvilli was measured manually. A line profile through the central section of microvilli oriented along the xy plane was drawn and the full-width at half-maximum was taken as the diameter.

2.1.6.2 Confocal imaging of U-2 OS cells

1-2x10^4 U-2 OS cells in 300 µl of U2M were seeded in a glass-bottom 8-chamber coverslip (Ibidi). The next day, U-2 OS cells were washed with 300 µl of U2M and incubated with 5 µg/ml CellMask Deep Red Plasma Membrane Stain in U2M for 10 min (37 °C, 5% CO_2). Next, U-2 OS cells were washed three times with 300 µl of U2M and fixed 0.8% paraformaldehyde and 0.2% glutaraldehyde in PBS for 15 min at RT. Fixed U-2 OS cells were washed three times with 300µl of PBS and left in 300µl of PBS for imaging.

The U-2 OS cells were imaged using a Zeiss LSM 880 inverted microscope with AiryScan. 63x oil immersion objective was used and the sample was illuminated using a 633 nm laser (He-Ne) with the pinhole size set to 1 AU. The z-stacks were taken from the apical to the basal plasma membrane with an interplane interval of 200 nm and line scan averaging set to 8. The surface area of U-2 OS cells was calculated using ImageJ. The images were first thresholded using the MaxEntropy algorithm to produce a binary mask for each image plane. The circumference of each binary mask, except for the one corresponding to the apical plane, was multiplied by 200 nm (interplane interval). The resultant value was added to the area of the binary masks corresponding to the apical and the basal planes.

2.1.6.3 3D-SIM imaging of cryo-fixed T cell/U-2 OS cell conjugates

For three-dimensional structured-illumination microscopy, 0.25-0.5x10^6 U-2 OS cells in 2 ml of U2M were seeded in a 35-mm glass-bottom tissue culture dish containing six 4-nm sapphire coverslips. The sapphire coverslips were pre-treated with 95% ethanol (5 min), Milli-Q water (30 min), PBS (15 min) and U2M (1 h). The U2M media was supplemented with 10 µM hGP100 peptide (YLEPGPVTV, GenScript). The U-2 OS cells were incubated for 18 h (37 °C, 5% CO_2).

For experiments involving the unmodified primary $CD8^+$ T cells and CD58LO U-2 OS cells, the following staining protocol was used. After the 18 h incubation, the culture medium was removed, U-2 OS cells were washed twice with 1 ml of iRPMI and incubated with 0.2 µM dilution of Janelia Fluor 549 (JF549) HaloTag Ligand in 1 ml of iRPMI for 15 min (37 °C, 5% CO_2). Next, U-2 OS cells were washed twice with 1 ml of iRPMI and incubated with 10 nM N-MED ImmTAC ('In-house') in 1 ml of iRPMI for 15 min (37 °C, 5% CO_2). Next, the U-2 OS cells were washed with 1 ml of iRPMI and incubated with 100 nM MitoTracker Deep Red in 1 ml of iRPMI for 2 min at RT. Finally, U-2 OS cells were washed three times with 1 ml of iRPMI and left in 2 ml of iRPMI until the addition of T cells.. 2x10^6 T cells were harvested and centrifuged at 200 x g for 2 min. T cells were washed with 1 ml of iRPMI, resuspended in 200 µl of AF488-conjugated anti-CD45

antibody at 0.04 mg/ml and incubated for 15 min (37 °C, 5% CO_2). Next, T cells were washed twice with 1 ml of iRPMI and resuspended in 200 µl of iRPMI.

For experiments involving the primary ZAP70-HaloTag $CD8^+$ T cells and WT U-2 OS cells, the following staining protocol was used. After the 18 h incubation, the culture media was removed, U-2 OS cells were washed twice with 1 ml of iRPMI and incubated in 10 nM N-MED ImmTAC ('In-house') in 1 ml of iRPMI for 15 min (37 °C, 5% CO_2). Next, the U-2 OS cells were washed with 1 ml of iRPMI and left in 1 ml of iRPMI and incubated for 2 min at RT with 100 nM MitoTracker Deep Red in 1 ml of iRPMI. Finally, U-2 OS cells were washed three times with 1 ml of iRPMI and left in 2 ml of iRPMI until the addition of T cells. $2x10^6$ ZAP70-HaloTag T cells were harvested and centrifuged at 200 x *g* for 2 min. The cells were washed with 1 ml of iRPMI, resuspended in 1 ml of 0.2 µM dilution of Janelia Fluor 549 (JF549) HaloTag Ligand and incubated for 15 min (37 °C, 5% CO_2). Next, T cells were washed twice with 1 ml of iRPMI and resuspended in 200 µl of AF488-conjugated anti-CD45 antibody at 0.04 mg/ml and incubated for 15 min (37 °C, 5% CO_2). Next, T cells were washed twice with 1 ml of iRPMI and resuspended in 200 µl of iRPMI.

To form T cell/U-2 OS cell conjugates, 100 µl of the T cell sample was added to the 35-mm dish containing the U-2 OS cells making sure that T cells were evenly distributed across the six coverslips. The cells were allowed to settle on the U-2 OS monolayer and co-cultured for ~20 min (37 °C, 5% CO_2). Before freezing, the culture media within was removed and replaced with a 25% (w/v) solution of 40,000 MW dextran (Sigma) and 200 nM Tetraspeck microspheres (Thermo Fisher Scientific) in iRPMI. The coverslips were placed between two planchettes (Technotrade International) and high-pressure frozen (Wohlwend HPF Compact). The empty surface of the coverslip was scraped of residual ice using razor blades (Fine Science Tools) while submerged in LN_2. Next, the coverslips were mounted on the cryostat (Janis Research Company) of the 3D-SIM instruments where they were kept at 77K.

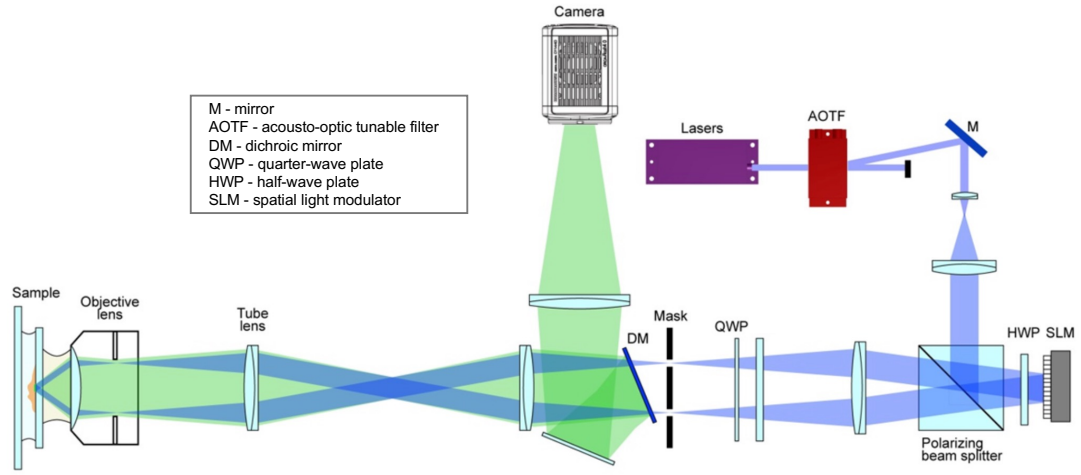


Figure 2.3: Layout of the cryogenic three-dimensional structured illumination microscope. Simplified schematic showing the light path of the cryo 3D SIM microscope. The blue and green light paths correspond to the excitation light and the emission light, respectively. The figure was adapted from Li et al.[325]

The cryogenic 3D-SIM instrument was fitted with a 100x CFI Plan Achro LWD, NA 0.85, air objective (Nikon). The excitation light was provided by 488 nm (Genesis CX STM, Coherent), 561 nm (2RU-VFL- P-5000-560-B1R, MPB Communications) and 642 nm (2RU-VFL-P-2000-642-B1R, MPB Communications) laser lines. The laser light was filtered (AA Quanta Tech, Optoelectronic AOTF AOTFnC-400.650-TN) and expanded. To achieve 3D-SIM illumination patterns excitation light was projected onto a spatial light modulator (Forth Dimension Displays, QXGA-3DM). The phase modulation was achieved by passing the excitation light through a polarising beam splitter (Newport, 10FC16PB.3), half-wave plate (Bolder Vision Optik, AHWP3) and quarter-wave plate (Bolder Vision Optik, AQWP3). The patterned excitation light is passed through a mask to remove unwanted diffraction. As a results the sample was illuminated with a pattern displayed at 3 angles and 5 phases (15 images per focal plane). The emitted fluorescence was filtered (Finger Lakes Instrumentation, HS-625) and detected using a cCMOS camera (Orca Flash, Hamatsu). 3D-SIM images were reconstructed using an optimised Gustaffson algorithm (AIC, Janelia Research Campus) and widefield images were produced by group z-projection of the raw

images. See Hoffman et al.[326]. and Li et al.[325] for details.

2.1.6.4 FIB-SEM imaging of cryo-fixed T cell/U-2 OS cell conjugates

Coverslips containing the selected for FIB-SEM imaging were subjected to freeze substitution (FS). FS was performed in FS media (2% (w/v) OsO_4, 0.1% (w/v) uranyl acetate 3% (v/v) water in acetone) using an automated FS system (AFS2, Leica Microsystems). The samples were gradually brought to RT over 40 h. Next, the samples were washed three times with acetone and embedded in Eponate 12 with BDMA (Ted Pella). Resin embedding was performed by successive incubations in eponate/acetone solutions and Eponate 12. Following acetone/eponate solutions and incubation times were used: 2:1 (denotes the acetone:eponate ratio) 1 h, 1:1 1 h, 1:2 1 h. Finally, the samples were transferred into Eponate 12 over 18 h. Next, the samples were incubated for 48 h at 65 °C to polymerise the Eponate 12 resin. The coverslip was detached from the eponate-embedded specimen by immersion in LN_2 and hot water. Then the face of the sample previously containing the coverslip was embedded in Durcupan resin (Sigma Aldrich). Blocks containing the selected cells were trimmed using an ultramicrotome (EM UC7, Leica Microsystems) and trimming was monitored using X-ray tomography (XRadia, 510 Versa, Zeiss). The blocks were sputter-coated with gold (10 nm) and carbon (100 nm).

FIB-SEM imaging was performed using a modified FIB-SEM system comprised of Zeiss Capella FIB column and Zeiss Merlin SEM. Successive 4 nm layers of the resin block were removed using a focused Ga^+ beam. The exposed face of the block was then imaged by the SEM module with xy pixel size set to 4x4 nm. A new block face was exposed approximately every minute. See Xu et al.[327] for details.

3

A cellular system for study of primary $CD8^+$ T-cell activation

Contents

3.1 Introduction 80
3.2 Results 81
3.2.1 Biophysical characterisation of an ImmTAC panel . . 81
3.2.2 Characterisation of U-2 OS cells and their modification for T-cell activation assays 83
3.2.3 Isolation and characterisation of primary human $CD8^+$ T cells 91
3.2.4 Optimisation and analysis framework for co-culture assays 92
3.2.5 Relationship between ImmTAC potency and affinity . 94
3.2.6 Relationship between ImmTAC potency and topology 95
3.3 Discussion 96
3.3.1 Biophysical characterisation of an ImmTAC panel . . 96
3.3.2 Characterisation of U-2 OS cells and their modification for T-cell activation assays 100
3.3.3 Isolation and characterisation of primary human $CD8^+$ T cells 102
3.3.4 Measurements of ImmTAC potency with respect to affinity and size 102

3.1 Introduction

To date, the molecular understanding of T-cell activation has been informed by studies relying on either human T-cell lines engineered to express a TCR of known specificity or murine T cells isolated from TCR-transgenic animals. These models provided important insights into T-cell biology, but are suboptimal representations of human T lymphocytes. Progress in the field of genetic engineering allowed for efficient transduction of primary human T cells with a TCR of choice, but it results in a heterogeneous T-cell population expressing the transgenic and endogenous TCR. Moreover, the pseudorandom nature of viral integration means that it can alter T-cell behaviour[328,329]. With the advances in gene editing technology, it has become possible to generate primary human T-cell lines expressing a preferred TCR from the endogenous loci, but this approach requires multiple expansion cycles before a sufficient number of cells is generated, thus risking perturbation of T-cell function[302]. To study T-cell activation in primary human CD8$^+$ T cells whilst circumventing the practical hurdles of producing TCR-transgenic T cells, a universal T-cell agonist that subverts TCR specificity can be used instead. Such an approach reduces the number of steps in preparation of primary T cells for experimentation thus keeping them as close to their native state as it is practically attainable. Pathogenic superantigens were once adopted for this purpose, but these molecules are not favourable to the study of CD8$^+$ T cells as they only engage MHC-II molecules[330]. Here, a synthetic TCR ligand in the format of a bispecific molecule targeting the TCR/CD3 complex and MHC-I molecules will be characterised and used to probe the mechanism of TCR triggering.

Due to the challenges associated with the manipulation of the target cell surface and its complex morphology, target cells are commonly substituted with SLBs. Reductionist T cell/SLB systems are a mainstay of T-cell biology as they allow precise control of the protein composition on the surrogate cell surface and simplify the topography of the cellular interface. However, they do not faithfully replicate the features of genuine T cell/target cell interactions and are not conducive to large-scale functional assays. To improve on these

shortcomings, a cellular system compatible with flow cytometry-based assays and imaging of T cell/target cell interactions will be assembled. The first part of this chapter provides a biophysical description of the T-cell agonists, followed by a characterisation of primary $CD8^+$ T cells and a U-2 OS cell line constituting the cell/cell system. In the final section, a co-culture assay will be optimised and used to establish the functional properties of the TCR ligand.

3.2 Results

3.2.1 Biophysical characterisation of an ImmTAC panel

A TCR-targeted bispecific molecule known as an ImmTAC was selected as a model TCR ligand. ImmTACs used in this study consisted of two segments connected via a five amino acid residue linker (Figure 3.1). The first segment was composed of the soluble portion of the TCR$\alpha\beta$ derived from an affinity-matured GPa3b17 TCR$\alpha\beta$ engineered to bind HLA-A2 molecules (MHC-I) presenting a GP100 peptide (aa280-288 of glycoprotein 100, YLEPGPVTA)[57,331,332]. TCR chains were linked via an engineered disulphide generated by T48C and S57C mutations within the constant α and β regions, respectively to promote their assembly and stabilise the heterodimer[333]. The other segment was an scFv derived from an anti-CD3ϵ UCHT1 antibody.

The scFv was linked to the TCR$\alpha\beta$ segment either at the N- or C-terminus of the TCRβ chain resulting in two architectures further denoted with an 'N' or 'C' prefix, respectively. The two linkages place the scFvs ~7.5 nm apart along the TCR$\alpha\beta$ scaffold resulting in topologically distinct ligands. The TCR$\alpha\beta$ component was invariant for all ImmTACs used in this study, while the scFv segment exists as three affinity variants: 'LO', 'MED' and 'HI' denoting their relative affinities for CD3ϵ. Whilst the CDRs of the scFv in the MED variant were identical to those of the UCHT1 antibody, the LO and HI variants were engineered for lower- and higher-affinity binding[334]. Mutating a single anti-CD3ϵ antibody to achieve a range of binding affinities rather than using several distinct anti-CD3ϵ antibodies of different affinities meant that the binding topology of the ImmTACs

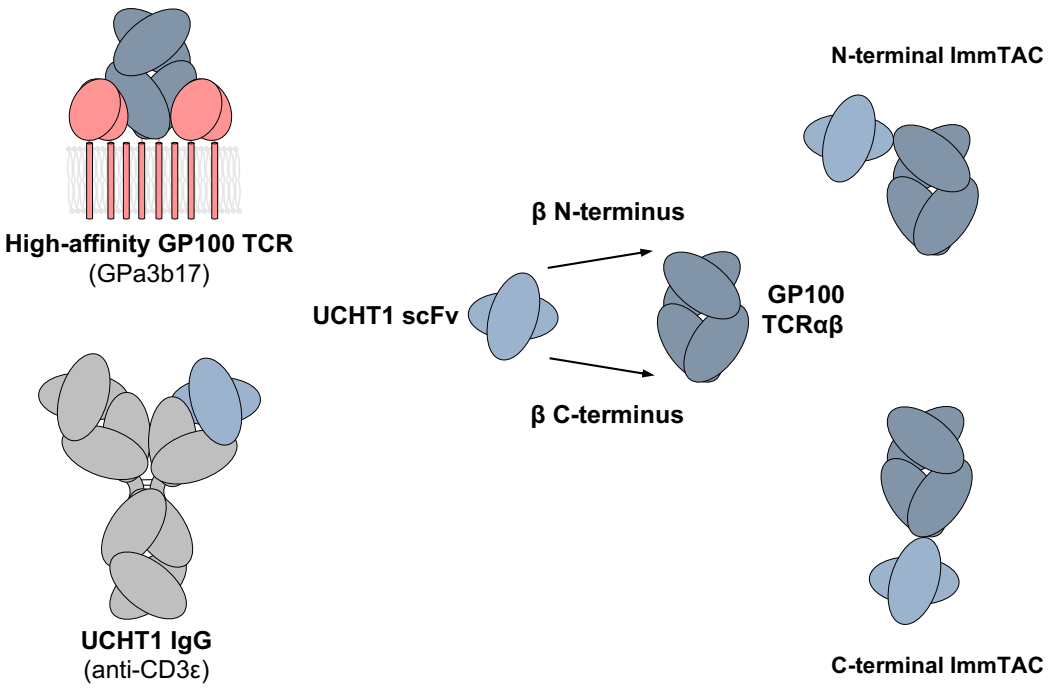


Figure 3.1: Architecture of TCR-targeted bispecifics. Schematic showing the architecture of TCR-targeted bispecifics also known as ImmTACs. ImmTACs were derived from TCRαβ chains of a high-affinity TCR directed to GP100-HLA-A2, a melanoma TAA and an scFv moiety taken from an UCHT1 antibody. The scFv can be linked to either the N-terminus or the C-terminus of the TCRβ chain resulting in two ImmTAC architectures. In the N-terminal ImmTAC the scFv and TCRαβ are closely apposed (top right), but they are ~7.5 nm apart in the C-terminal ImmTAC (bottom right).

of the same architecture (N vs. C) was minimally perturbed. Ultimately, a panel comprising four ImmTACs was produced: i) three N-terminal ImmTACs: N-LO, N-MED and N-HI (Figure 3.2A, left) and ii) a single C-terminal ImmTAC: C-MED (Figure 3.2A, right). Of note is that N-MED ImmTAC is analogous to Tebentafusp which is used in the clinic for treatment of uveal melanoma[316]. Due to its clinical relevance, the MED variants was produced in both the 'N' or 'C' formats. All four ImmTACs were expressed and produced by Dr. Ben de Wet at Immunocore Ltd. as monodisperse proteins (personal communications).

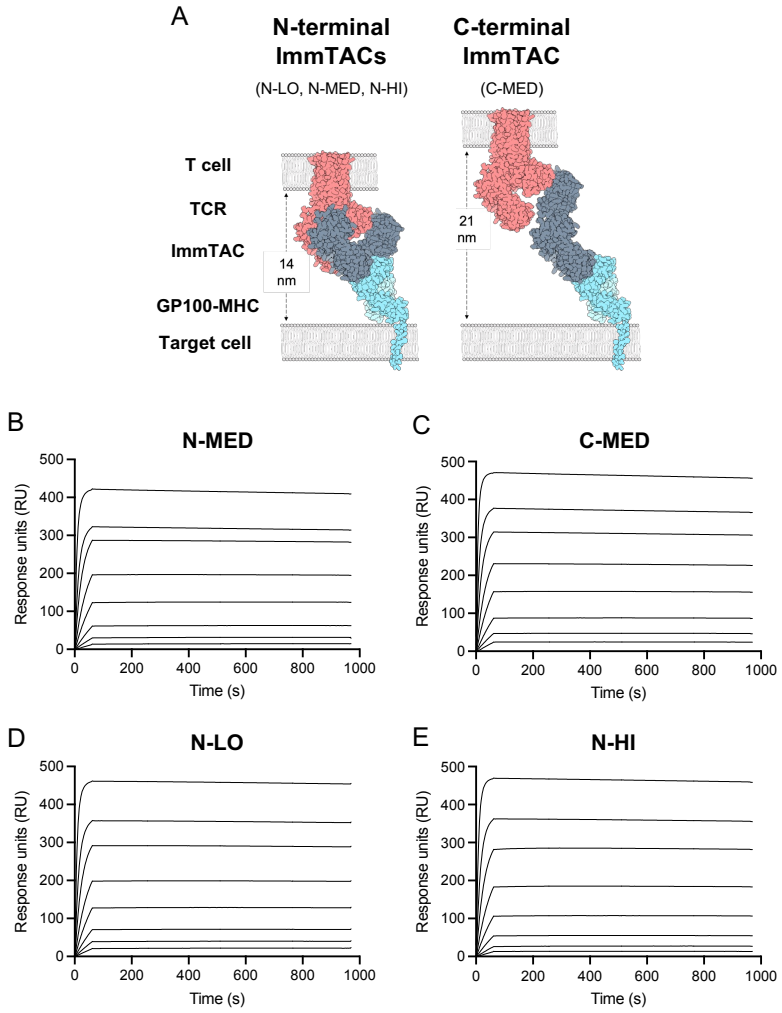
The binding affinities of the four ImmTACs were validated using SPR as implemented by the Biacore 8K. To measure the kinetics of ImmTAC binding to the pMHC ligand, 2xHis_6-tagged GP100-HLA-A2 (produced by Mai Vuong) was

immobilised on an NTA chip and ImmTACs were injected as analytes (Figure 3.2B-E). All four ImmTACs displayed near-identical picomolar K_D values (Figure 3.2F). For the SPR measurements of ImmTAC binding to CD3ϵ, biotinylated Avi-tagged CD3$\epsilon\gamma$ heterodimer (provided by Immunocore Ltd.) was immobilised on a CAP chip and the ImmTACs were injected as analytes (Figure 3.3A-D). Both N-MED and C-MED bound to the ligand with high nanomolar affinities with K_D values of 197 nM and 399 nM, respectively (Figure 3.3F). N-LO and N-HI displayed K_D values 20-fold higher and 100-fold lower than the N-MED variant, respectively (Figure 3.3E).

Overall, the ImmTAC panel can be subdivided into an 'affinity' panel (N-LO, N-MED, N-HI) and a 'size' panel (N-MED and C-MED) which allowed for TCR behaviour to be probed with respect to these two ligand properties.

3.2.2 Characterisation of U-2 OS cells and their modification for T-cell activation assays

The adherent U-2 OS cell line derived from an osteosarcoma tumour of a 15-year-old female patient was chosen as a model target cell. This selection was made based on the characterisation of their morphology and surface expression of immune molecules critical to T cell-target cell interactions. Intending to image the interface of the primary T cells and cancer cells, it was important to use a uniformly thin cell to limit light diffraction as it passes through the cell and enable the use of instruments with limited depth of imaging. Individual U-2 OS cells whose membrane was stained with a membrane dye before fixation were imaged using laser scanning confocal microscopy (LSCM) to map the topology of their cell membrane (Figure 3.4A). U-2 OS cells were on average ~3.5 μm thick in the area surrounding the nucleus and between 1-2 μm towards the edge of the cell (Figure 3.4A, top and middle). While the surface of the U-2 OS cells was largely flat, it was sparsely covered with tubular protrusions which were up to 2 μm in length (Figure 3.4A, bottom). Additionally, the target cell needed to form monolayers so that T cells could interact with a continuous cellular surface mimicking tissue

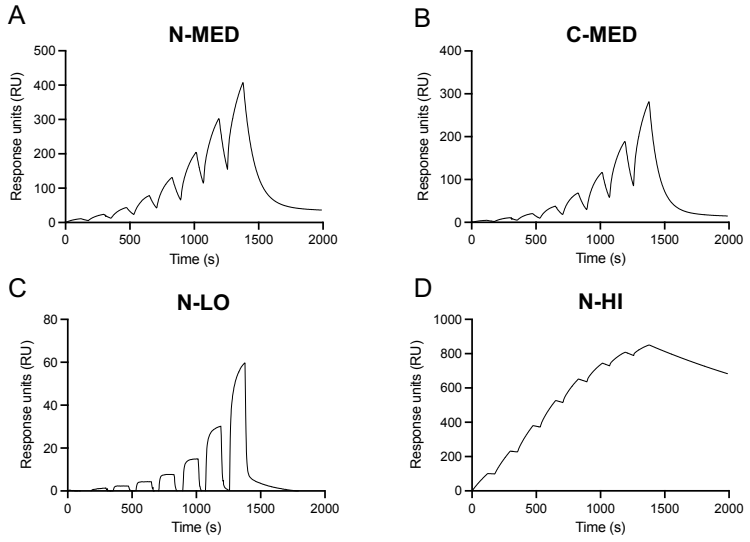


F

ImmTAC	Replicate	k_{on} ($M^{-1}s^{-1}$)	k_{off} (s^{-1})	K_D (pM)
N-MED	1	4.45×10^5	3.73×10^{-5}	83.8
	2	1.31×10^6	3.52×10^{-5}	26.8
	Average	**8.78×10^5**	**3.63×10^{-5}**	**55.3**
C-MED	1	4.96×10^5	4.83×10^{-5}	97.5
	2	1.06×10^6	4.14×10^{-5}	39.1
	Average	**7.78×10^5**	**4.49×10^{-5}**	**68.3**
N-LO	1	3.85×10^5	3.20×10^{-5}	83.0
	2	9.64×10^5	2.93×10^{-5}	30.4
	Average	**6.75×10^5**	**3.07×10^{-5}**	**56.7**
N-HI	1	3.20×10^5	3.77×10^{-5}	118
	2	1.45×10^6	3.56×10^{-5}	24.6
	Average	**8.85×10^5**	**3.67×10^{-5}**	**71.3**

Figure 3.2: (Following page)

Figure 3.2: SPR measurements of ImmTAC/GP100-MHC binding. A. Schematic of N-terminal (left) and C-terminal (right) ImmTACs bound to their targets: GP100-MHC antigen and TCR/CD3 complex. **B-E**. Multi-cycle SPR analysis of the ImmTAC panel binding to GP100-HLA-A2. 2xHis_6-tagged GP100-HLA-A2 was immobilised on an NTA chip and fluid-phase ImmTACs were injected as analytes. Twofold dilution series ranging from 1.56 nM to 200 nM was used. Sensorgrams were blank subtracted. All sensorgrams were fitted into a 1:1 Langmuir model to produce the kinetic parameters shown in the table below. **F**. Kinetic parameters (k_{on}, k_{off}, and K_D) derived from the SPR data in (B)-(E).



E

ImmTAC	Replicate	k_{on} ($M^{-1}s^{-1}$)	k_{off} (s^{-1})	K_D (nM)
N-MED	1	$6.18x10^4$	$1.21x10^{-2}$	196
	2	$5.91x10^4$	$1.17x10^{-2}$	197
	Average	**$6.05x10^4$**	**$1.19x10^{-2}$**	**197**
C-MED	1	$4.13x10^4$	$1.68x10^{-2}$	408
	2	$4.42x10^4$	$1.72x10^{-2}$	389
	Average	**$4.28x10^4$**	**$1.70x10^{-2}$**	**399**
N-LO	1	$9.09x10^3$	$9.45x10^{-2}$	9450
	2	$1.48x10^4$	$9.30x10^{-2}$	6290
	Average	**$1.19x10^4$**	**$9.38x10^{-2}$**	**7870**
N-HI	1	$1.11x10^5$	$2.19x10^{-4}$	1.97
	2	$1.36x10^5$	$2.22x10^{-4}$	1.64
	Average	**$1.24x10^5$**	**$2.21x10^{-4}$**	**1.81**

Figure 3.3: SPR measurements of ImmTAC/CD3$\epsilon\gamma$ binding. A-D. Single-cycle SPR analysis of the ImmTAC panel binding to CD3$\epsilon\gamma$. A biotinylated CD3$\epsilon\gamma$ heterodimer was immobilised on a CAP chip and fluid-phase ImmTACs were injected as analyte. Twofold dilution series ranging from 6.25 nM to 800 nM was used. Sensorgrams were blank subtracted. All were fitted into a 1:1 Langmuir model to produce the kinetic parameters shown in the table below. **E**. Kinetic parameters (k_{on}, k_{off}, and K_D) derived from the SPR data in (A)-(D).

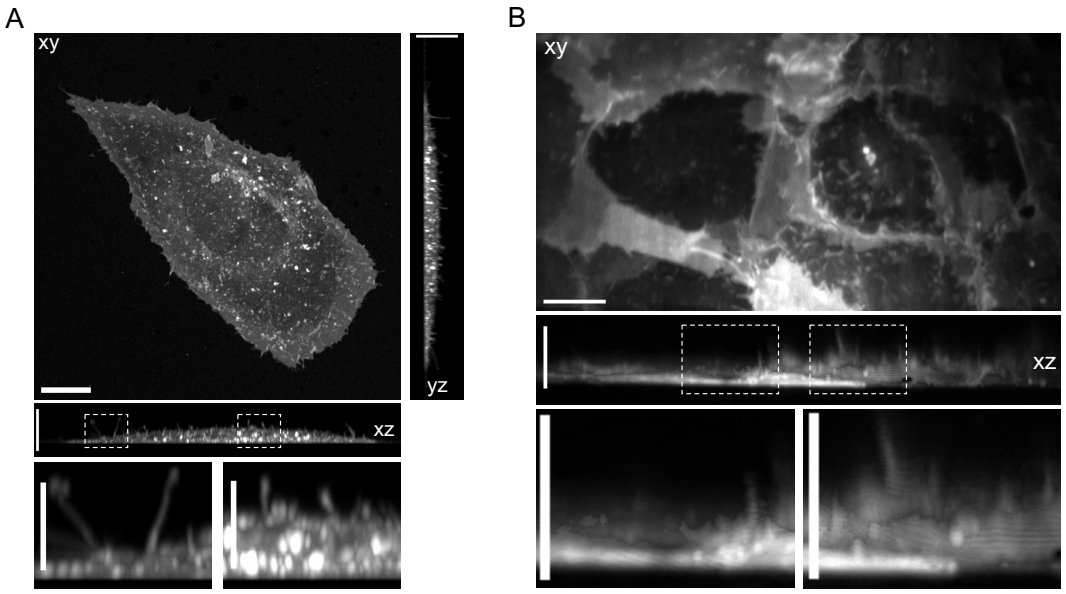


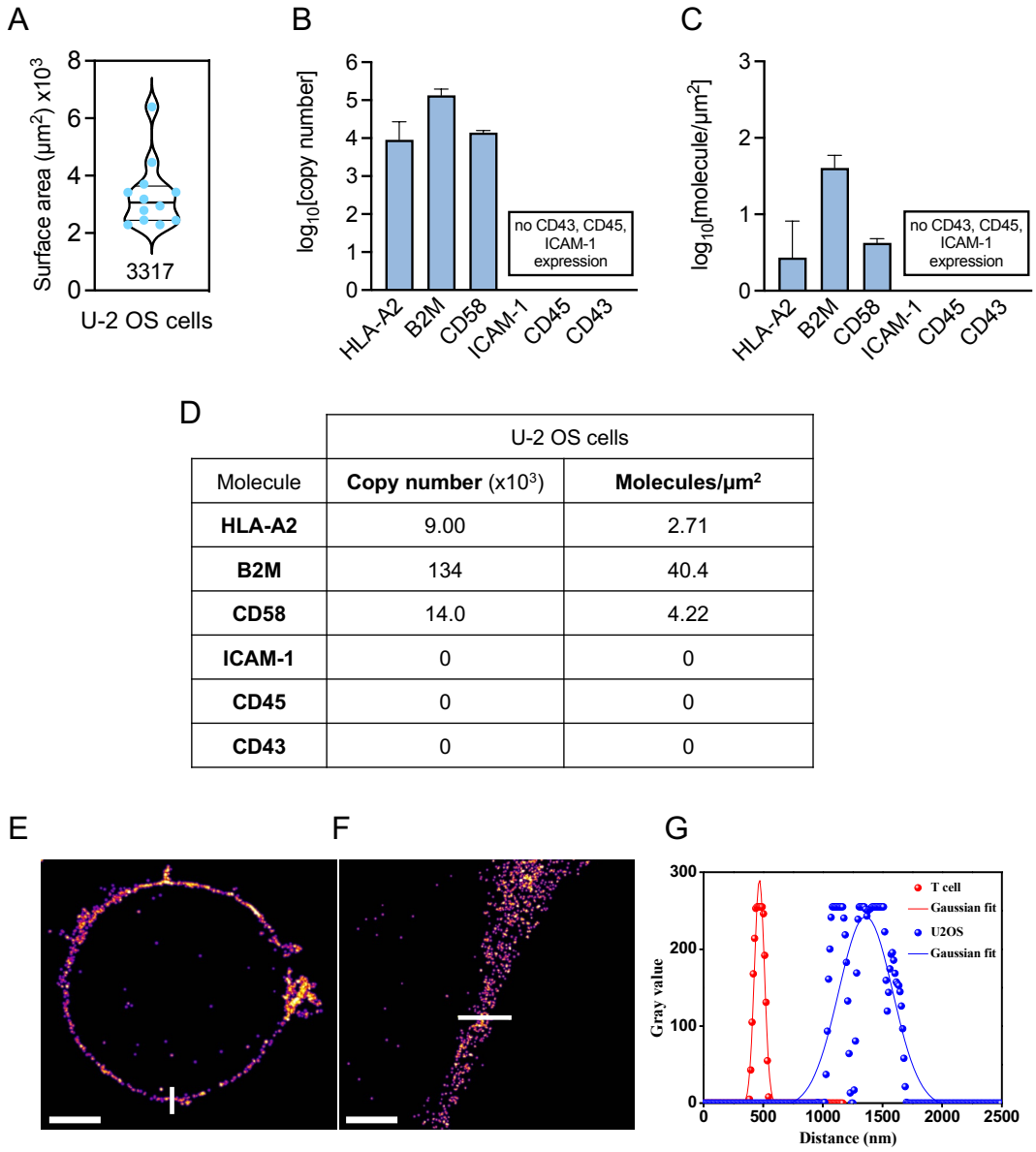
Figure 3.4: Topography of an individual U-2 OS cell and a U-2 OS cell monolayer. A. Representative LSCM image of a fixed U-2 OS cell labelled with membrane dye. MIPs of raw image stacks for the three orthogonal planes are shown. Scale bar = 10 μm (top). Close-up views of the xz MIP showing the details of the U-2 OS cell surface topography. Scale bar = 2 μm (bottom). **B**. Representative eSPIM image of live U-2 OS cell monolayer. U-2 OS cells overexpressing a CD58-HaloTag fusion protein, serving as a membrane marker, were labelled with JF549 HaloTag ligand. MIPs of deskewed image stacks for xy and xz planes are shown. Scale bar = 10 μm (top). Selected views of the xz MIP showing the details of the U-2 OS cell surface topography. Scale bar = 10 μm (bottom)

and without interference from the glass coverslip. U-2 OS cells readily formed monolayers (Figure 3.5B, top) and despite the tight packing of cells the surface remained thin, ranging from ~3-5 μm in the z dimension (Figure 3.4B, bottom)

U-2 OS cells were tested for surface expression of key molecules involved in the T cell/target cell interactions. These molecules included: i) MHC-I complexes, specifically HLA-A2 required for binding of ImmTACs, and β_2M, a constitutive component of all MHC-I molecules, ii) adhesion molecules CD58 and ICAM-1 required for the formation of T cell/target cell conjugates, and iii) components of the immune cell glycocalyx CD43 and CD45 which act in concert with adhesion molecules to regulate intercellular interactions. To enable quantification of expression levels as two-dimensional (2D) densities, LSCM images of individual U-2 OS cells were used to calculate their surface area yielding

an estimate of 2500-3500 μm^2 (Figure 3.5A). The expression levels were converted into copy numbers using calibration beads and then into 2D densities by dividing the copy numbers by the surface area of U-2 OS cells (Figure 3.5A-D). U-2 OS cells expressed HLA-A2 and CD58 at densities of 2.7 and 4.2 molecules/μm^2, but neither ICAM-1, CD43 or CD45 were detected. Whilst expression of CD43 and CD45 is ubiquitous in the immune system, cancer cells are well-documented to have a thick glycocalyx layer composed of, *inter alia*, mucin, syndecan or glypican family proteins[32]. To test whether this is the case for U-2 OS cells, 2D super-resolution microscopy was utilised to image fixed U-2 OS cells labelled with wheat germ agglutinin (WGA) conjugated to HMSiR. WGA binds to the N-acetylglucosamine and sialic acid residues found in mammalian glycans allowing visualisation of the glycocalyx (data collected by Dr. Debasis Banik). The glycocalyx of primary human CD8$^+$ T cells was imaged to serve as a model of the immune cell glycocalyx and provide a reference point (Figure 3.5E). Glycocalyx on the surface of U-2 OS cells extended ~533 nm beyond the cell membrane, and it was ~5-fold thicker than the glycocalyx of T cells. (Figure 3.5F-G). Given the presence of HLA-A2 required for ImmTAC binding, basic adhesion in the form of CD58 necessary for the formation of close contacts, and model glycocalyx, U-2 OS cells were deemed a suitable target cell model.

To contextualise the properties of the U-2 OS cell surface, activated DCs, benchmark professional APCs, were characterised in a similar manner. The scarcity of DCs in human blood necessitated the use of monocyte-derived DCs (moDC). To this end, primary monocytes were isolated from blood, differentiated into dendritic cells using a cytokine cocktail and stimulated with LPS. The presence of mature moDCs following the procedure was confirmed through staining for key markers: CD14$^-$, CD83$^+$ and CD1a$^+$ (Figure 3.6A). In contrast to U-2 OS cells, the surface of moDCs was covered by membrane ruffles rather than tubular protrusions (Figure 3.6B). The surface area of moDCs was 1700-2800 μm^2 (Figure 3.6C). Akin to U-2 OS cells, moDC expressed HLA-A2, β_2M and CD58, albeit at densities ~230-, ~190- and ~25-fold higher, respectively. moDCs also expressed



D

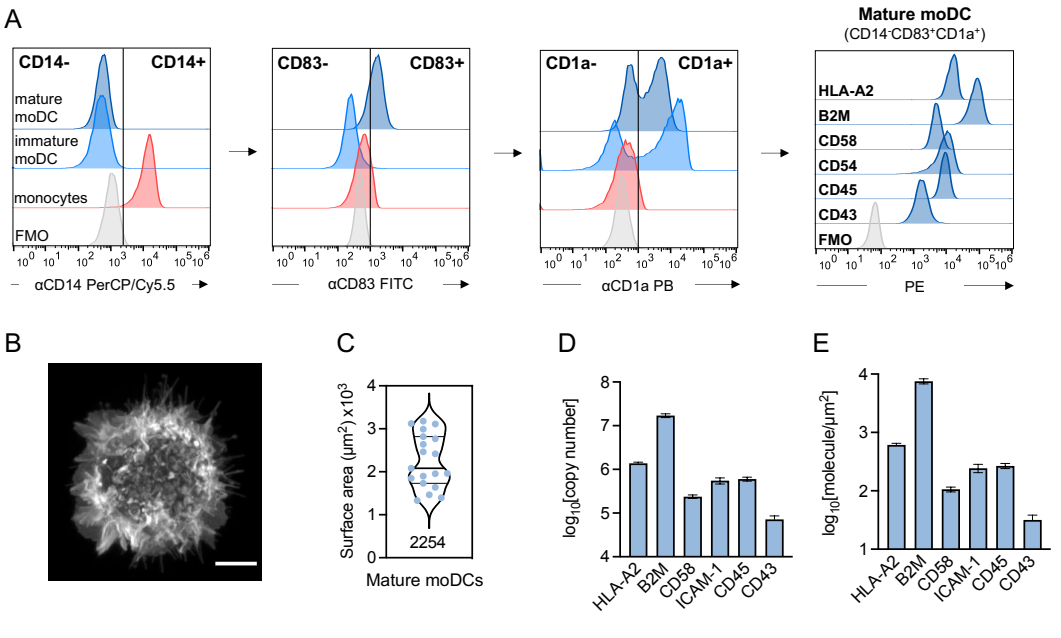
Molecule	U-2 OS cells	
	Copy number (x10³)	**Molecules/µm²**
HLA-A2	9.00	2.71
B2M	134	40.4
CD58	14.0	4.22
ICAM-1	0	0
CD45	0	0
CD43	0	0

Figure 3.5: Characterisation of the U-2 OS cell surface. A. Estimated surface area of U-2 OS cells calculated using the LSCM images of fixed U-2 OS cells (Figure 3.4A). n=12. **B**. Expression of key immune molecules on the surface on U-2 OS cells shown as copy numbers. Expression levels were measured by flow cytometry of U-2 OS cells stained with PE-conjugated antibodies and then converted to copy numbers using PE calibration beads **C**. As in (B), but levels expressed as densities. The density values were calculated using the estimated U-2 OS cell surface area (A) and the respective copy numbers (B). **D**. Table summarising the copy numbers and densities of the selected immune molecule. **E**. Representative 2D resPAINT image of a primary CD8+ T cell stained with WGA-HMSiR **F**. As in (E), but a edge of U-2 OS cell was imaged. **G**. Quantification of the glycocalyx thickness on the shown T cell (E) and U-2 OS cell (F). Line profiles were drawn across the membrane at the the midplane of both cells. The full width at half maximum of the Gaussian fit was used to determine glycocalyx thickness producing values of 98 nm and 533 nm for the T cell and U-2 OS cell, respectively. Scale bar = 2.1 µm. resPAINT imaging was performed by Dr. Debasis Banik.

ICAM-1, CD43 and CD45 at densities of ~240, ~270 and ~320 molecules/μm^2, respectively, all of which were absent from the U-2 OS cell surface (Figure 3.6D-F).

For all experiments requiring TCR engagement, GP100-MHC was first generated on the U-2 OS cell surface and then it was tagged with one of the ImmTACs. The GP100-MHC was used in two functionally identical, but structurally distinct formats. The first one capitalised on the endogenous expression of HLA-A2 and relied on pulsing of U-2 OS cells with the GP100 peptide for 18 h (Figure 3.7A and B). Hereafter, this type of antigen will be referred to as 'GP100-HLA'. The poor loading efficiency of the wild-type (WT) GP100 necessitated the use of its variant (YLEPGPVTV) which bears a A9V substitution at the anchor position. The substitution markedly improves the affinity of the peptide for the HLA-A2 molecule without significantly altering the interaction with the anti-GP100 TCRs[335] Such peptide is often referred to as a heteroclitic GP100 peptide (hGP100).

The second type of GP100-HLA-A2 antigen was in the format of a disulphide-trapped single chain trimer (SCT) in which the GP100-β_2M-HLA-A2 were sequentially linked by a series of G_4S linkers (Figure 3.7D)[336]. To ensure that the peptide is stably bound to the groove of the MHC, the SCT had a disulphide bond engineered between the peptide-β_2M linker and the neighbouring portion of the peptide-binding groove referred to as a 'disulphide trap'. Such GP100-MHC was lentivirally transduced into U-2 OS cells as a monocistronic construct (Figure 3.7E). The expression of GP100-SCT was quantified in relation to the endogenous HLA-A2 levels. The GP100-SCT constituted 99.7% of total HLA-A2 (Figure 3.7C, F, G) thus making the GP100 peptide a dominant HLA-A2-presented antigen. Therefore, the SCT format allowed supraphysiological levels of the GP100-MHC antigen to be generated on the U-2 OS cell surface. The key advantage of this strategy is that the HLA-A2 molecule presenting the GP100 peptide can be selectively manipulated which allows the dependencies between the MHC structure and TCR signalling to be examined. Hereafter, this format of GP100-MHC will be referred to 'GP100-SCT' while the term 'GP100-MHC' will be used to describe both GP100-HLA and GP100-SCT formats.



F

	U-2 OS cells		Mature moDCs	
Molecule	**Copy number** (x10^3)	**Molecules/μm^2**	**Copy number** (x10^3)	**Molecules/μm^2**
HLA-A2	9.00	2.71	1380	612
B2M	134	40.4	17000	7540
CD58	14.0	4.22	238	106
ICAM-1	0	0	551	244
CD45	0	0	601	267
CD43	0	0	715	320

Figure 3.6: Characterisation of the mature monocyte-derived DC surface. **A**. Primary human monocytes were isolated from PBMCs and differentiated into DCs using a cytokine cocktail. Immature moDCs were activated with LPS. Presence of mature DCs was confirmed by staining for CD14, CD83 and CD1a. Expression levels of key immune molecules on the surface of mature DCs ($CD14^-CD83^+CD1a^+$) were quantified by staining with PE-conjugated antibodies **B**. Representative LSCM image of fixed moDC stained with membrane dye. MIP of the raw image stack shown. Scale bar = 5 μm. **C**. Estimated surface area of mature moDCs calculated using the LSCM images of fixed moDCs (B). n=19 **D**. Expression of key immune molecules on the surface on mature moDCs shown as copy numbers **E**. As in (D), but levels are expressed as 2D densities. The density values were calculated using the estimated moDC surface area (C) and the respective copy numbers (D) **F**. Table summarising the copy numbers and densities of the selected immune molecule on U-2 OS cells and mature moDCs. LSCM imaging of moDCs was performed by Dr. Edward Jenkins and the images were included in Jenkins et al.[137]

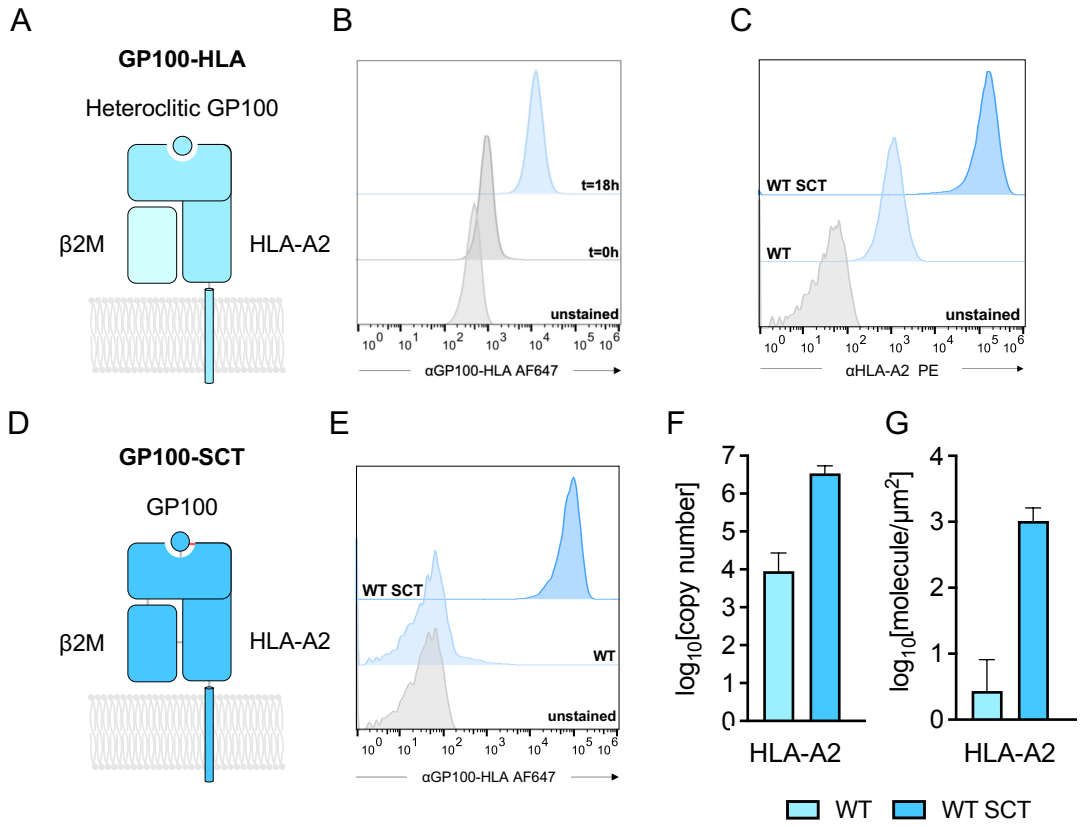


Figure 3.7: Generation and quantification of GP100-MHC antigen on the surface of U-2 OS cells. A. Schematic of an HLA-A2 molecule bound to hGP100 peptide. **B**. Expression levels of GP100-HLA-A2 on the U-2 OS cell surface stained with AF647-conjugated N-MED ImmTAC following 18h incubation with 0.1 mM hGP100 peptide. **C**. Expression levels of HLA-A2 on the surface of WT and GP100-SCT U-2 OS cell surface stained with a PE-conjugated anti-HLA-A2 antibody **D**. Schematic of a GP100-SCT antigen where GP100 peptide is integrated into an peptide-β_2M-HLA-A2 single chain trimer **E**. Expression levels of GP100-SCT on the GP100-SCT U-2 OS cell surface stained with AF647-conjugated N-MED ImmTAC **F**. Expression levels of HLA-A2 on the surface of WT and GP100-SCT U-2 OS cell surface stained with a PE-conjugated anti-HLA-A2 antibody shown as copy numbers **G**. As in (F), but densities are shown.

3.2.3 Isolation and characterisation of primary human CD8+ T cells

To generate primary human CD8+ T cells, PBMCs were isolated from leukocyte cones and then subjected to negative selection using a MACS (Figure 3.8A). This method yielded a polyclonal CD8+ T cell population which was stimulated using magnetic beads coated with anti-CD3ϵ and anti-CD28 antibodies for 5 days and subsequently expanded for another 10 days. Poorly expanding T cell populations

were discarded. Following the expansion stage, rested T cells were cryopreserved and tested for their ability to respond to TCR stimulation. To this end, T cells were placed in wells coated either with the OKT3, a potent T-cell stimulating antibody or MOPC21 acting as an isotype control. After 16 h incubation, the T-cell activation state was assessed based on upregulation of the surface markers CD25 and CD69, a high-affinity chain of the IL-2 receptor (IL-2Rα) and a type II C-lectin receptor without a known ligand, respectively. The degree of CD25 and CD69 upregulation was quantified by flow cytometry and computed as the percentage of T cells expressing the respective marker (Figure 3.8B and 3.4C). The data was quantified as percentages as both activation markers largely display binary expression patterns. The data in the current and the following chapters was also quantified as mean fluorescence intensities yielding identical results.

Upwards of 95% of all T cells from each donor were CD25$^+$ and CD69$^+$ following the overnight incubation in OKT3-coated wells (Figure 3.8D and E). T cells incubated in MOPC21-coated wells displayed background activation levels ranging from 7.8% to 24.8% for CD25 and 13.8% to 43.6% for CD69. The background levels for the two markers did not appear to be correlated. T cells from donors which had undergone successful expansion and had been tested for activation were deemed suitable for further study. Primary CD8$^+$ cells produced as described above will be used throughout this thesis unless specified otherwise.

3.2.4 Optimisation and analysis framework for co-culture assays

T cells and U-2 OS cells were combined into a co-culture assay intended to study the effects of the model ligands. Two protocols were developed, one for GP100-HLA, and the other for GP100-SCT, each differing in their approach to producing a range of antigen densities on the U-2 OS cells surface. In both cases, U-2 OS cells were plated and cultured for 18 h to form contiguous monolayers. However, when GP100-HLA was used, the U-2 OS cell medium was supplemented with a 10-fold serial dilution of the hGP100 peptide. Following the 18 h incubation,

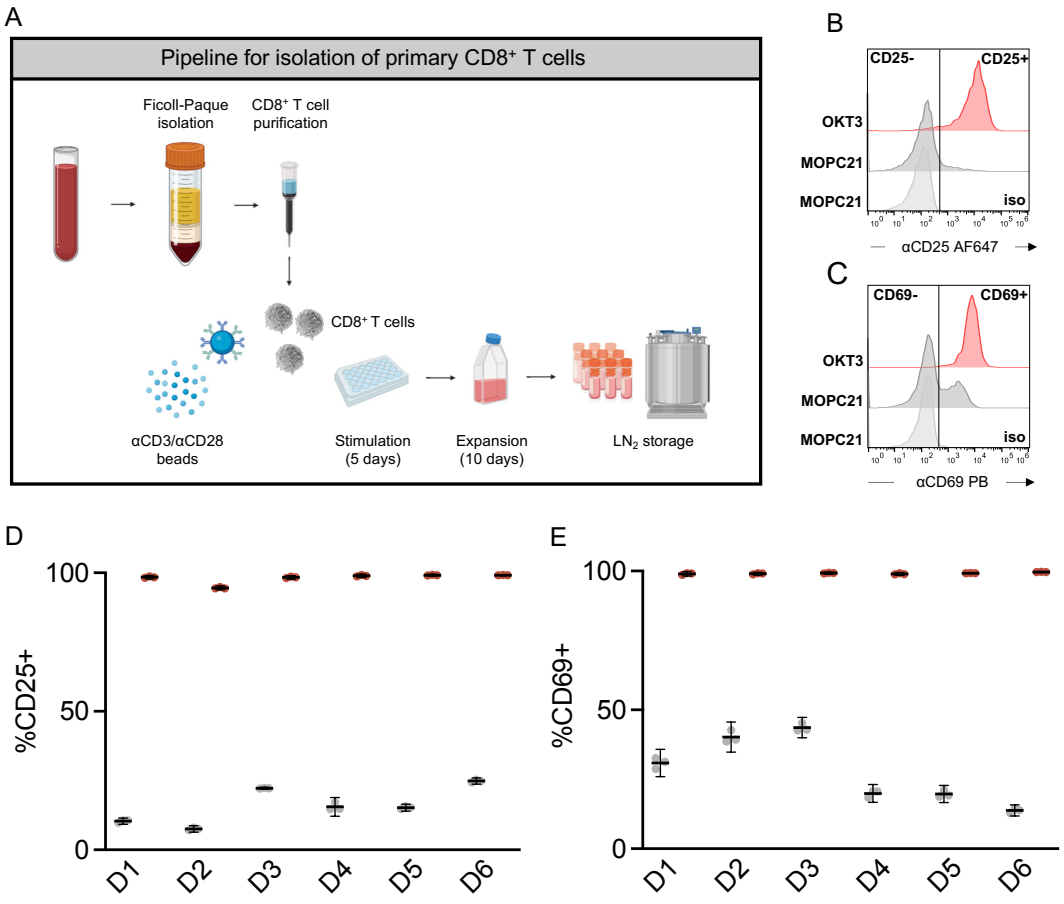


Figure 3.8: Preparation and testing of primary human CD8$^+$ T cells. **A**. Diagram showing the pipeline for isolation and expansion of primary CD8$^+$ T cells. PBMCs were isolated from human blood using Ficoll-Paque method and untouched CD8$^+$ T cells were isolated through MACS. Polyclonal CD8$^+$ T cell pool was stimulated using beads coated with anti-CD3 and anti-CD28 antibodies at a 1:3 ratio. Following a 5-day stimulation, T cells were expanded and rested for 10 days. At this point the proliferative burst was over and T cells were moved to LN_2 for long-term storage. **B**. Flow cytometry plot showing the gating strategy used to calculate the proportion of CD25$^+$ T cells. T cells incubated in OKT3-coated (top) or MOPC21-coated (middle and bottom) wells. T cells were stained with either AF647-conjugated anti-CD25 antibody or MOPC21 (isotype control) The gate was drawn so that between 0.1-1% T cells stained with isotype control antibody were classified as CD25$^+$. **C**. As in (B), but for CD69 **D**. Proportion of CD25$^+$ T cells following 18h incubation in either OKT3- or MOPC21-coated wells. Data collected for six healthy donors. **E**. As in (D), but for CD69$^+$. D = donor.

the peptide-pulsed U-2 OS cells were labelled with 10 nM ImmTAC while the GP100-SCT U-2 OS cells were labelled with a 10-fold serial dilution of the ImmTAC instead. Next, T cells were plated onto the U-2 OS cell monolayers and co-cultured for a further 18 h. Finally, the T cells were harvested and the upregulation of CD25 and CD69 was measured by flow cytometry.

Two parameters were extracted from the flow cytometry data: background activation levels (B) and half-maximal effective concentration (EC_{50}) values (Figure 3.9). To calculate the EC_{50} values the activation data was first subjected to min-max normalisation to remove the effects of background, and then a four-parameter variable slope Hill model was fitted to the data to produce dose-response curves. For clarity, EC_{50} values extracted from CD69 and CD25 data hereafter will be denoted as $EC_{50:CD69}$ and $EC_{50:CD25}$, respectively. The B values correspond to the percentage of CD25$^+$ and CD69$^+$ T cells in the absence of the TCR ligand and were derived before min-max normalisation. From this point, the B values will be abbreviated as B_{CD25} and B_{CD69} to denote the respective activation marker.

3.2.5 Relationship between ImmTAC potency and affinity

First, the ability of the N-terminal ImmTACs, i.e., the 'affinity' panel to activate T cells was tested using the two protocols relying on either GP100-HLA or GP100-SCT (Figures 3.10A and B). In the GP100-HLA system, the EC_{50} values indicated that N-MED is the most potent of the three ligands (Figure 3.10C, D, G, H). N-LO was only marginally less potent than N-MED with 1.4-fold and 1.9-fold higher $EC_{50:CD25}$ and $EC_{50:CD69}$ values, respectively. N-HI was the least potent variant producing a 14.4-fold and 9.7-fold increase in the $EC_{50:CD25}$ and $EC_{50:CD69}$ values relative to N-MED. In the GP100-SCT system, the three ImmTACs displayed the same ranking of potencies, but the fold shifts between EC_{50} values either increased or remained unchanged (Figure 3.10E, F, I, J). Overall, the most potent bispecific in the panel was N-MED, closely followed by N-LO and then N-HI. The relative EC_{50} values were concordant both between the two GP100-MHC systems and the two activation markers.

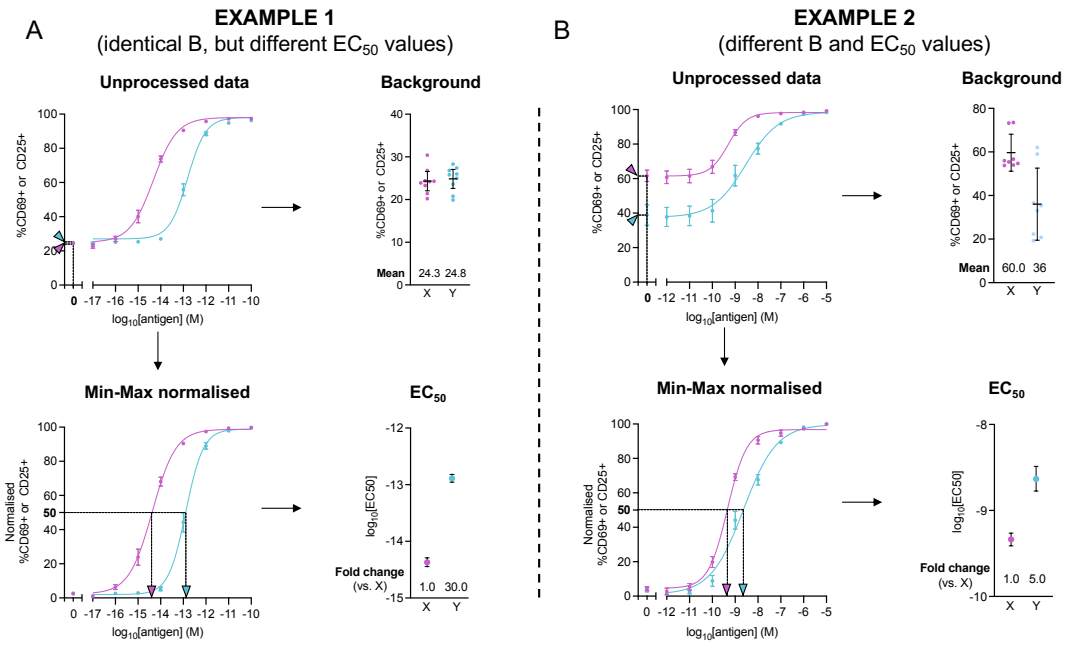


Figure 3.9: Framework for analysis of flow cytometry data from co-culture assays. Flow cytometry was used to analyse the T cells following the co-culture assays. The flow cytometry data was processed to extract the proportion of $CD25^+$ and $CD69^+$ T cells. Gating strategy as in Figure 3.8 was used, but the MOPC21 control was replaced with data collected in the absence of TCR ligand ([ImmTAC] = 0). The background activation data correspond to $CD25^+$ and $CD69^+$ values in the absence of ImmTAC on the U-2 OS cell surface. To calculate the EC_{50} values the activation data was min-max normalised and four-parameter Hill slope model was fitted to the dose-response curves. **A**. Model data where background activation levels are identical for conditions X and Y, but the EC_{50} values are different. **B**. Model data where both background activation levels and EC_{50} values are different for conditions X and Y.

3.2.6 Relationship between ImmTAC potency and topology

Finally, the most potent of the N-terminal ImmTACs, N-MED was compared to its C-terminal counterpart, C-MED to examine the relationship between ligand topology and T-cell responses (Figure 3.11A and B). In the GP100-HLA system, the $EC_{50:CD25}$ and $EC_{50:CD69}$ values for the C-MED ImmTAC were 16.7-fold and 12.8-fold higher than the equivalent values produced using the N-MED ImmTAC (Figure 3.11C, D, G, H). When GP100-SCT U-2 OS cells were used, the difference between the potency of the two bispecifics increased further with the $EC_{50:CD25}$ and $EC_{50:CD69}$ values for the C-MED ImmTAC increased by a factor of 22.0 and 30.1 relative to the corresponding values for the N-MED ImmTAC,

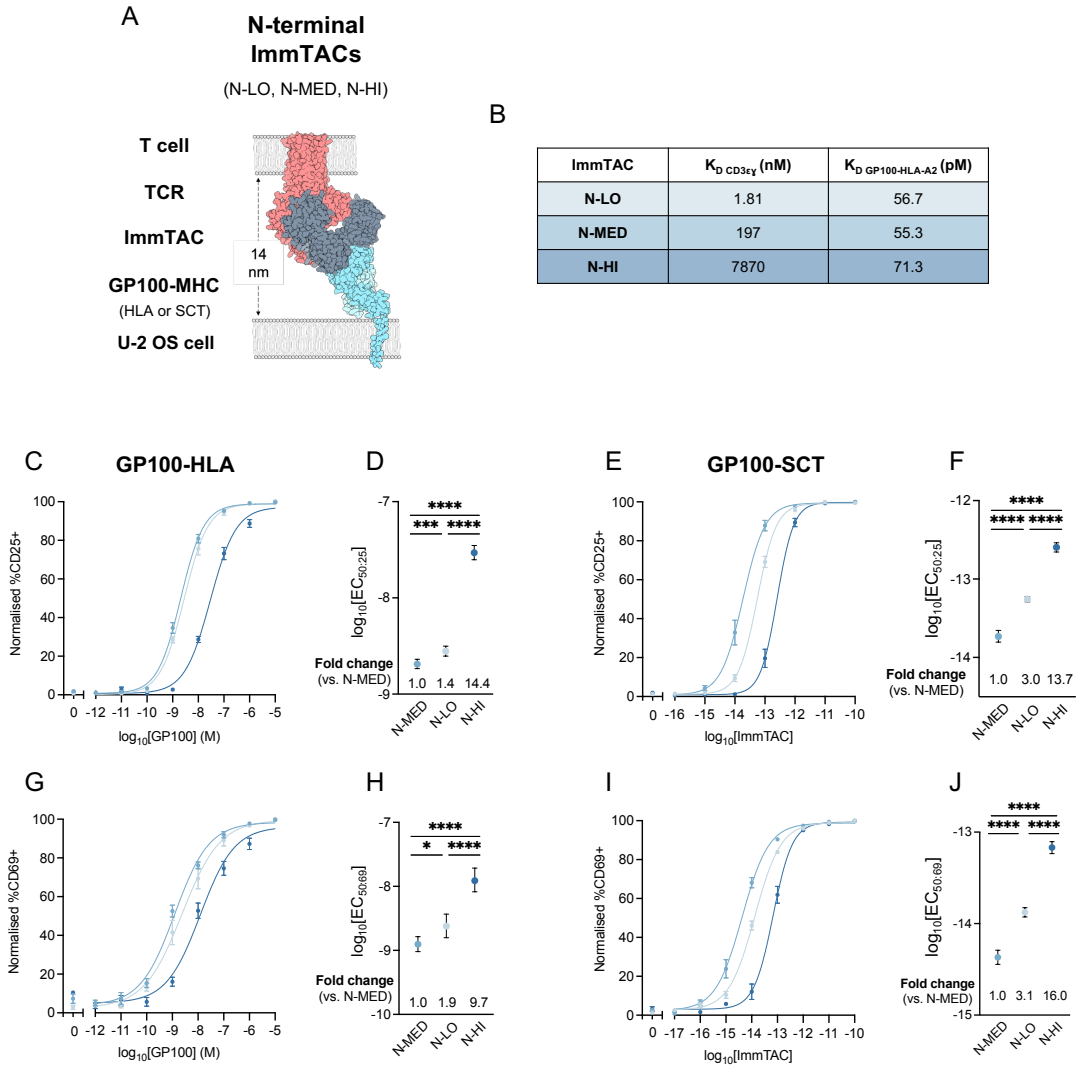
respectively (Figure 3.11E, F, I, J).

3.3 Discussion

In this chapter, a cellular system for the study of T-cell activation and visualisation of T cell/target cell interaction was assembled and characterised. An adherent osteosarcoma U-2 OS cell line was shown to be suitable for both functional and imaging experiments owing to the expression of key surface molecules, flat morphology, and the propensity to form planar monolayers. Polyclonal primary CD8$^+$ T cells were selected as the model T cell population. Novel bispecific molecules, known as ImmTACs, were adopted as synthetic TCR ligands to engage the polyclonal CD8$^+$ T cells. Four ImmTACs with different affinities for the TCR/CD3 complex and architectures were characterised through SPR measurements and grouped into the 'affinity' and 'size' panels. The first panel was composed solely of N-terminal ImmTACs with varying affinities for CD3ϵ (N-HI, N-MED, N-LO). The second panel was composed of two ImmTACs with identical affinities for CD3ϵ, but different architectures – a compact N-terminal ImmTAC (N-MED) and an extended C-terminal variant (C-MED). Through T cell/U-2 OS cell co-culture assays, the relationship between the ImmTACs potency, affinity and topology was established. The N-MED ImmTAC was found to be the most potent across both panels.

3.3.1 Biophysical characterisation of an ImmTAC panel

SPR measurements of TCR/pMHC three-dimensional (3D) binding parameters are a mainstay of T-cell research. Whilst the 3D K_D and k_{off} values commonly serve as proxies of TCR ligand potency, the exact relationship between binding kinetics and potency remains under debate[251,281]. The four ImmTACs bound to GP100-MHC with K_D values ranging from ~55.3-71.3 pM with an average K_D value of 62.9 pM and a half-life of 5.2 h. The differences between these affinities are unlikely to be significant. The K_D values for binding of the three N-terminal affinity variants N-LO, N-MED, N-HI to CD3ϵ were 7870 nM, 197



ImmTAC	$K_{D\ CD3\epsilon\gamma}$ (nM)	$K_{D\ GP100\text{-}HLA\text{-}A2}$ (pM)
N-LO	1.81	56.7
N-MED	197	55.3
N-HI	7870	71.3

Figure 3.10: Relationship between the potency of N-terminal ImmTACs and the ImmTAC/CD3ϵ affinity. A. Schematic of an N-terminal ImmTAC bound to the GP100-MHC antigen and the TCR/CD3 complex. The axial dimension of the ternary complex is estimated to be ~14 nm based on the structures of the constituent molecules assuming rigid-body behaviour **B**. Table summarising the K_D values for ImmTAC binding to CD3$\epsilon\gamma$ and GP100-MHC measured in section 3.2.1 **C**. Dose-response curves showing T-cell activation by upregulation of CD25 following 18h of co-culture with hGP100-pulsed U-2 OS cells **D**. $EC_{50:25}$ values extracted from unconstrained four-parameter variable slope Hill model fitted into the dose-response curves from (C). **E**. As in (C), but T cells were co-cultured with GP100-SCT U-2 OS cells **F**. $EC_{50:25}$ values extracted from four-parameter variable slope Hill model fitted into the dose-response curves from (E) **G**. Dose-response curves showing T-cell activation by upregulation of CD69 following 18h of co-culture with hGP100-pulsed U-2 OS cells. **H**. $EC_{50:69}$ values extracted from unconstrained four-parameter variable slope Hill model fitted into the dose-response curves from (G) **I**. As in (C), but T cells were co-cultured with GP100-SCT U-2 OS cells. **J**. $EC_{50:69}$ values extracted from four-parameter variable slope Hill model fitted into the dose-response curves from (I). All co-culture assays were performed as three biological repeats in triplicates. Data was collected using T cells isolated from at least two donors. EC_{50} values were compared using an F-test of normalised data *P-value $\leq$ 0.05, **P-value $\leq$ 0.01, ***P-value $\leq$ 0.001, ****P-value $\leq$ 0.0001

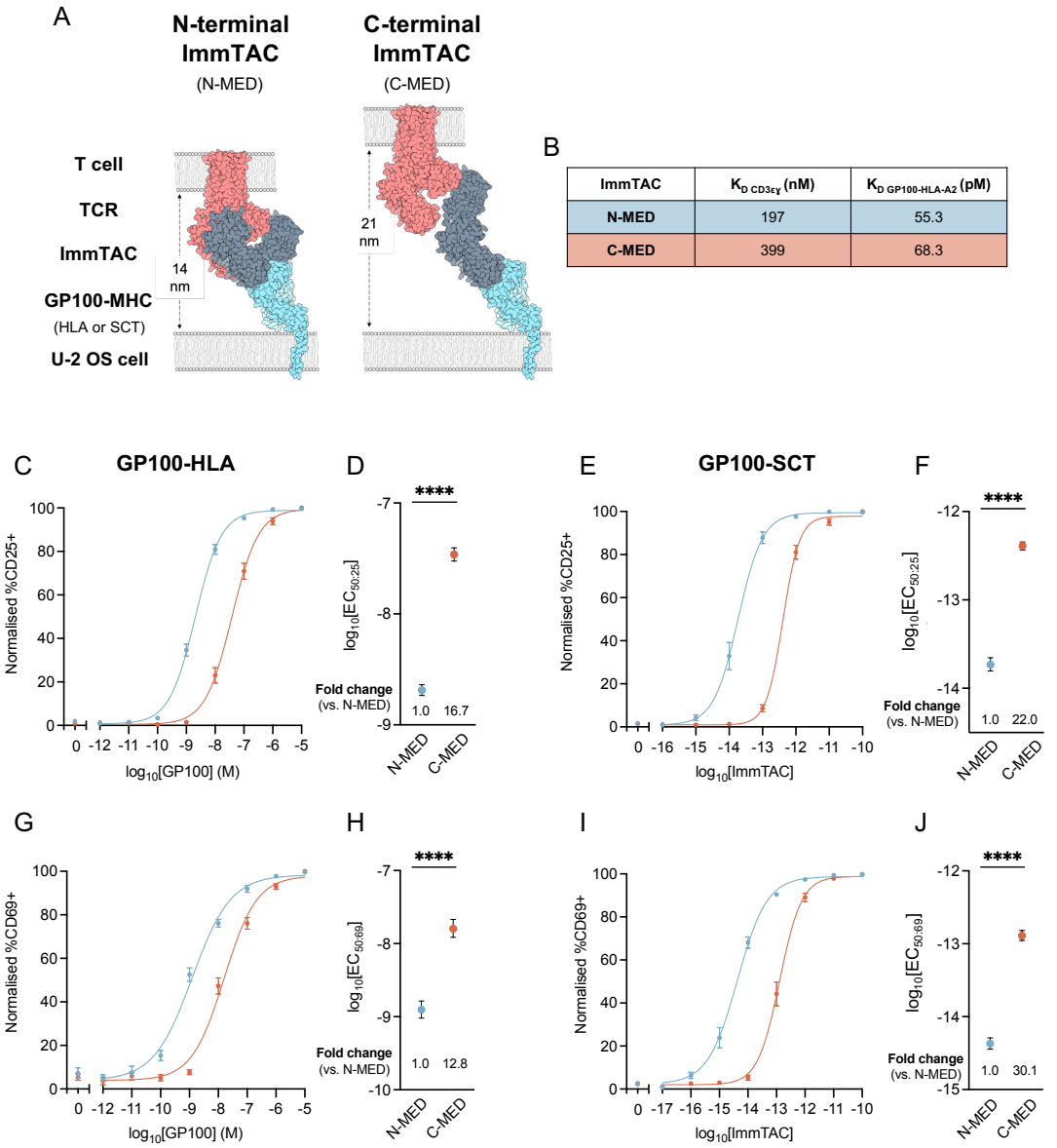


Figure 3.11: (Following page)

nM and 1.81 nM according to the SPR measurements, respectively. The C-MED ImmTAC containing the same scFv as N-MED bound to CD3ϵ with a K_D value of 399 nM. The difference in the affinities of N-MED and C-MED for binding to CD3ϵ are unlikely to be significant and the two-fold shift can be attributed to inter-batch variation involved in protein purification or the distinct architectures of these two bispecifics. Recently, Robertson et al. measured the binding kinetics of N-terminal ImmTACs composed of identical scFv variants, but a different TCRαβ segment, specific for a NY-BR-1-HLA-A2 antigen[334]. The

Figure 3.11: Relationship between the potency of ImmTACs and their topology. A. Schematic of an N-terminal (left) and a C-terminal (right) ImmTACs bound to the GP100-MHC antigen and the TCR/CD3 complex. The axial dimensions of the ternary complexes containing the N-MED and C-MED ImmTACs are estimated to be ~14 nm and ~21 nm, respectively. Dimensions were inferred from the structures of the constituent molecules assuming rigid-body behaviour. **B**. Table summarising the K_D values for ImmTAC binding to CD3$\epsilon\gamma$ and GP100-MHC measured in section 3.2.1 **C**. Dose-response curves showing T-cell activation by upregulation of CD25 following 18h of co-culture with GP100-pulsed U-2 OS cells **D**. $EC_{50:25}$ values extracted from unconstrained four-parameter variable slope Hill model fitted into the dose-response curves from (C). **E**. As in (C), but T cells were co-cultured with GP100-SCT U-2 OS cells **F**. $EC_{50:25}$ values extracted from four-parameter variable slope Hill model fitted into the dose-response curves from (E) **G**. Dose-response curves showing T-cell activation by upregulation of CD69 following 18h of co-culture with GP100-pulsed U-2 OS cells **H**. $EC_{50:69}$ values extracted from unconstrained four-parameter variable slope Hill model fitted into the dose-response curves from (G) **I**. As in (G), but T cells were co-cultured with GP100-SCT U-2 OS cells **J**. $EC_{50:69}$ values extracted from four-parameter variable slope Hill model fitted into the dose-response curves from (I) All co-culture assays were performed as three biological repeats in triplicates. Data was collected using T cells isolated from at least two donors. EC_{50} values were compared using an F-test of normalised data *P-value $\leq$ 0.05, **P-value $\leq$ 0.01, ***P-value $\leq$ 0.001, ****P-value $\leq$ 0.0001

reported K_D values for the equivalent N-LO, N-MED and N-HI ImmTACs were 615 nM, 34 nM and 0.25 nM, respectively[334]. Thus, the K_D values measured by Robertson et al. are ~9-fold lower than the corresponding K_D values produced in the present study. This discrepancy could be due to the different formats of CD3 heterodimers used as ligands for the SPR experiments. Robertson et al. used a CD3$\epsilon\underline{\delta}$ heterodimer stabilised by an Fc domain rather than a disulphide-linked CD3$\epsilon\underline{\gamma}$ heterodimer[334]. While the two data sets agree on the relative CD3ϵ affinities of the three ImmTAC variants, the absolute K_D values from the two datasets should be approached with caution.

The ImmTAC panel provides a range of affinities spanning three orders of magnitude, whereas physiological TCR/pMHC affinities required for a productive interaction tend to range from 1 μM to 100 μM for commonly studied TCRs such as 1G4 or OT-1[337]. The N-LO ImmTAC with a K_D value of 7.8 μM falls into this affinity window providing a native-like reference point. The key consequence of the large gap between the affinities of the TCR$\alpha\beta$ and the scFv arms is that the

TCR/CD3 complex is more likely to engage an ImmTAC/GP100-MHC complex, rather than exist in an ImmTAC-bound form and then interact with GP100-MHC on the target cell surface. The probability of the former binding sequence will increase with the $K_{D,\ CD3\epsilon}/K_{D,\ GP100\text{-}MHC}$ ratio.

One shortfall of the ImmTAC/CD3ϵ affinity measurements using SPR is that the organisation of the CD3ϵ on the chip does not reflect the oligomeric state of CD3ϵ in the TCR/CD3 complex which contains both CD3ϵγ and CD3ϵδ heterodimers. At low densities of ImmTAC/GP100-MHC complex on the target cell, each TCR/CD3 complex is likely to be engaged by a single ImmTAC, but increasing the ligand densities would favour 2:1 binding stoichiometry and thus introduce avidity effects which cannot be replicated by the SPR experiments reported in this chapter. Primary cancer cells display up to ~50 antigenic peptides such as NY-ESO-1 or GP100[298,338,339] and thus the avidity effect is likely to have little physiological relevance; however, it could play a role in *ex vivo* co-culture assays where supraphysiological ligand densities are generated. It also needs to be noted that 3D binding parameters measured in-solution are not a faithful representation of the interaction between receptors and ligands which are confined to 2D surfaces *in situ*. Nonetheless, both 2D and 3D binding parameters were successfully used to predict ligand potency[256,257,340].

3.3.2 Characterisation of U-2 OS cells and their modification for T-cell activation assays

The densities of immune molecules on the surface of U-2 OS cells and monocyte-derived DCs were estimated using the copy numbers and cell surface area calculated using flow cytometry and LSCM, respectively. Strikingly, the expression of both HLA-A2 and CD58 on U-2 OS cells was ~230-fold and ~25-fold lower relative to moDCs, respectively, and U-2 OS cells did not express ICAM-1. This approach serves well for comparative purposes, but the densities are likely to be an overestimate in absolute terms. The surface of both cell types is covered in fine membrane structures such as ruffles or tubular protrusions which are challenging

to analyse using standard segmentation algorithms employed in this thesis, likely yielding an underestimate of the surface area and resulting in overestimated density values. Higher-resolution imaging techniques and better analysis tools would be needed to obtain more accurate estimates.

Some of the key cancer glycocalyx components include glycoproteins belonging to the mucin family. MUC1 and MUC4 were estimated to extend ~200 and ~300 nm beyond the plasma membrane, whereas MUC16 was proposed to extend even further[32,341]. Additionally, hyaluronans anchored to the cell surface by CD44 can measure up to 500 nm[32,342]. Using an 2D-SMLM technique known as resPAINT, the glycocalyx layer of U-2 OS cells was found to extend ~500 nm beyond the cell membrane, in line with the reported dimensions of the common glycocalyx components. However, previous measurements of glycocalyx thickness on cancer cells relying on bioorthogonal labelling of sialic acid residues combined with 2D-SMLM yielded values of ~70 nm and ~50 nm for cell lines and primary cancer cells, respectively[343]. The disparity between the measurements presented in this chapter and those taken by Mockl et al. is likely due to use of different cancer cell lines as well as the methodology used to quantify the glycocalyx thickness. Mockl et al. solely examined the glycocalyx layer of the tubules projecting from the cancer cell surface, here the bulk glycocalyx layer extending from the cell body was measured. The thickness of the glycocalyx can serve as a proxy for the accessibility of the cancer cell surface, but it only accounts for its height. To obtain a better measure of the glycocalyx barrier function, the thickness measurements should be combined with the quantification of the glycocalyx density as demonstrated by Paszek and colleagues[344]. In the future, 3D-SMLM methods could be used to map glycocalyces with greater precision and to simultaneously quantify their thickness and density[345].

3.3.3 Isolation and characterisation of primary human CD8+ T cells

Polyclonal primary CD8+ T cells were chosen as a model T-cell population for this study. To produce them at numbers permitting large-scale experiments, bulk primary CD8+ T cells were isolated from human blood, stimulated and expanded. While the resultant T-cell population was not profiled in this thesis, RNA sequencing of CD8+ T cells isolated from healthy donors indicates that the unstimulated population of T cells was likely to be composed of an amalgam of subsets including naïve, memory and effector T cells; listed here in the order of putative differentiation trajectory[346,347]. Following stimulation, the expanded T-cell population was likely depleted of the naïve compartment and would have progressed toward the memory and effector subsets[346,347]. Polyclonal populations of T cells were successfully used in the past to investigate functional T-cell responses and underlying molecular mechanisms[137,281,284,348,349]. The key advantage to the use of a heterogeneous T-cell population is the broader applicability of findings as a population derived from a single T-cell subset or clone would be more likely to display idiosyncratic behaviour associated with a particular cell state or genetic background. The primary CD8+ T cells efficiently activated in response to anti-CD3ϵ antibody stimulation confirming the suitability of CD25 and CD69 for measurement of T-cell activation. CD69 is a well-established marker of CD8+ activation and the incubation time of the flow cytometry-based assays was matched to the time of optimal CD69 expression[28,350]. Expression of CD25 was reported to peak at 48h; nonetheless, saturating responses were achieved for both activation markers with concordant results[350].

3.3.4 Measurements of ImmTAC potency with respect to affinity and size

The co-culture assays of T cells with U-2 OS cells were used to delineate the relationships between ImmTAC potency, affinity and geometry. Two types of

GP100-MHC antigens were used for these measurements: GP100-HLA and GP100-SCT generated by peptide-pulsing and constitutive expression from a lentiviral vector, respectively. The former is conventionally used for co-culture assays involving T cells, but there is a precedent for the use of SCTs when targeted modification of the MHC structure is required[264,267].

Despite the thick glycocalyx and limited adhesion system on the U-2 OS cell surface, T cells exhibited saturating responses to all of the ImmTACs. N-MED was the most potent N-terminal variant followed by N-LO and then N-HI. This is in line with other studies of T-cell responses to ligands with supraphysiological affinities showing optimum activation by those with K_D and k_{off} values below the native levels[334,351]. Furthermore, the top potency of the N-MED ImmTAC is consistent with mathematical models of T-cell activation incorporating the features of serial triggering and kinetic proofreading[279–281].

The most potent of the N-terminal ImmTACs was also produced in a C-terminal format increasing the distance between its GP100-MHC and CD3ϵ binding sites by ~7.5 nm. The stipulated size difference was inferred from the structure of the TCRαβ ECD and does not account for the flexibility of the connecting linkers between the two segments. More advanced, experimental measurements are required to obtain a better estimate of the molecular reach afforded by these two ImmTAC architectures. Such analyses were performed for antibodies and B-cell antigens using biophysical methods based on SPR or X-ray scattering[352–354]. The C-MED ImmTAC was ~20-fold less potent than the N-MED ImmTAC. The negative relationship between the size of ligands and T-cell activation was shown for multiple types of antigen receptors. Extension of pMHC curtailed activation of both αβ and γδ T cells even when the size of the ligand was increased by a single IgSF domain and in some studies activation was completely abolished for extensions of over ~10 nm[264,265,267]. Similar size-dependency was also established for synthetic TCR ligands, similar to ImmTACs in binding to CD3ϵ, albeit the impact of size was typically less pronounced likely due to the

high affinity of the ligand/CD3ϵ interactions[263,264,355]. Moreover, the increased size of synthetic antigen receptors was also shown to abrogate T-cell activation[356]

4

Mechanistic correlates of TCR triggering by ImmTAC ligands

Contents

4.1 Introduction 106
4.2 Results 107
4.2.1 Role of small adhesion molecules in ImmTAC-induced T-cell activation 107
4.2.2 Effect of engineered extension of pMHC on ImmTAC potency 113
4.2.3 Interactions of the CD8αβ co-receptor with the ternary TCR/ImmTAC/pMHC complex 115
4.2.4 Truncation of CD45 phosphatase attenuates ImmTAC-induced T-cell activation 121
4.3 Discussion 124
4.3.1 Role of small adhesion molecules in ImmTAC-induced TCR triggering 125
4.3.2 Effect of engineered extension of pMHC in ImmTAC potency 126
4.3.3 Interactions of CDαβ co-receptor with ternary TCR-ImmTAC-pMHC complex 127
4.3.4 Truncation of CD45 phosphatase attenuates ImmTAC-induced T-cell activation 128

4.1 Introduction

In the previous chapter, the co-culture assays demonstrated that the potency of ImmTACs is a function of their affinity and size. These relationships are consistent with the principles of T-cell signalling in response to the native TCR ligands. Nonetheless, the mechanisms underlying T-cell activation by ImmTACs are unclear, ergo, ImmTACs cannot be considered to be authentic TCR ligands. To examine the mechanisms that control ImmTAC-induced TCR triggering, molecules involved in the earliest stages of antigen recognition were systematically modified. The expression, structure and biophysical properties of the following molecules were manipulated: CD58, CD8, CD45 and MHC-I. The contributions of these molecules to TCR triggering by pMHCs are well-characterised and therefore they can effectively serve as 'yardsticks' to determine the suitability of ImmTACs as model TCR ligands.

All of these surface molecules exhibit differential interactions with TCR ligands of varying affinities and topologies. For instance, CD58 primarily augments TCR signalling in response to low-affinity pMHC molecules and antagonises ligands that extend beyond the critical ~14 nm[138,269,349]. Artificial extension of pMHC molecules attenuates T-cell responses but the effect is reduced for high-affinity TCR ligands or when TCR ligands are presented at supraphysiological densities[263–265,267,268]. Recruitment of the CD8 co-receptor only benefits pMHC-TCR/CD3 complexes that meet strict geometric constraints and enhances signalling in an affinity-dependent manner[57,112,357]. The segregation of CD45 away from the TCR/CD3 complex is a critical step in T-cell activation, but its impact is diminished for high-affinity ligand/TCR interactions[86,137,255,261,263,264,270].

In this chapter, U-2 OS cells and T cells bearing suitable modifications will be generated and then integrated into the co-culture assay established in the previous chapter. The effects of these modifications will be measured and assessed as relative shifts in the EC_{50} values reflecting the potencies of each ImmTAC in an altered T cell/U-2 OS cell context. Furthermore, through measurements

of T-cell activation in these modified contexts in the absence of TCR ligand, additional correlates of TCR triggering will be determined.

Other surface molecules such as LFA-1 and its ligand ICAM-1 also modulate T-cell responses, but due to its dimensions the CD2/CD58 pair has a unique role in formation of close contacts[86,134,137]. Thus, modifying the CD2/CD58 adhesion is more likely to reveal the mechanistic details of TCR triggering by ImmTACs. The effects of LFA-1/ICAM-1 pair on T-cell activation by these synthetic ligands will be considered in Chapter 5.

4.2 Results

4.2.1 Role of small adhesion molecules in ImmTAC-induced T-cell activation

The axial dimensions of CCs created by the apposition of the microvillar tip and the surface of the target cells are set by the CD2/CD58 adhesion pair[137,169]. The network of CD2/CD58 complexes not only provides an environment for the TCR to effectively 'scan' pMHC complexes without having to act as an adhesion molecule, but it also sets an energetic barrier for entry of membrane molecules and complexes whose axial dimensions exceed ~14 nm (Figure 4.1A)[269,349,358]. Hence, TCR/ImmTAC/GP100-MHC complexes containing the N-terminal rather than C-terminal ImmTACs should form more readily within the CCs. Moreover, TCR/pMHC is a poor adhesion molecule due to the suboptimal orientation of the binding interface, but high-affinity interactions may compensate for this deficiency[57,359]. Therefore, it should follow that ligands such as the N-HI ImmTAC should be less dependent on CD2/CD58 adhesion than the N-LO variant[359]. Furthermore, the amount of CD2/CD58 adhesion determines the area of CCs which is critical to effective antigen discrimination – increased density of the CD2/CD58 pair was shown to induce ligand-independent T-cell activation[86,137,256,259].

To test the role of CD2/CD58 adhesion in TCR triggering by ImmTACs, a series of U-2 OS cell lines with varying expression of CD58 was generated (Figure

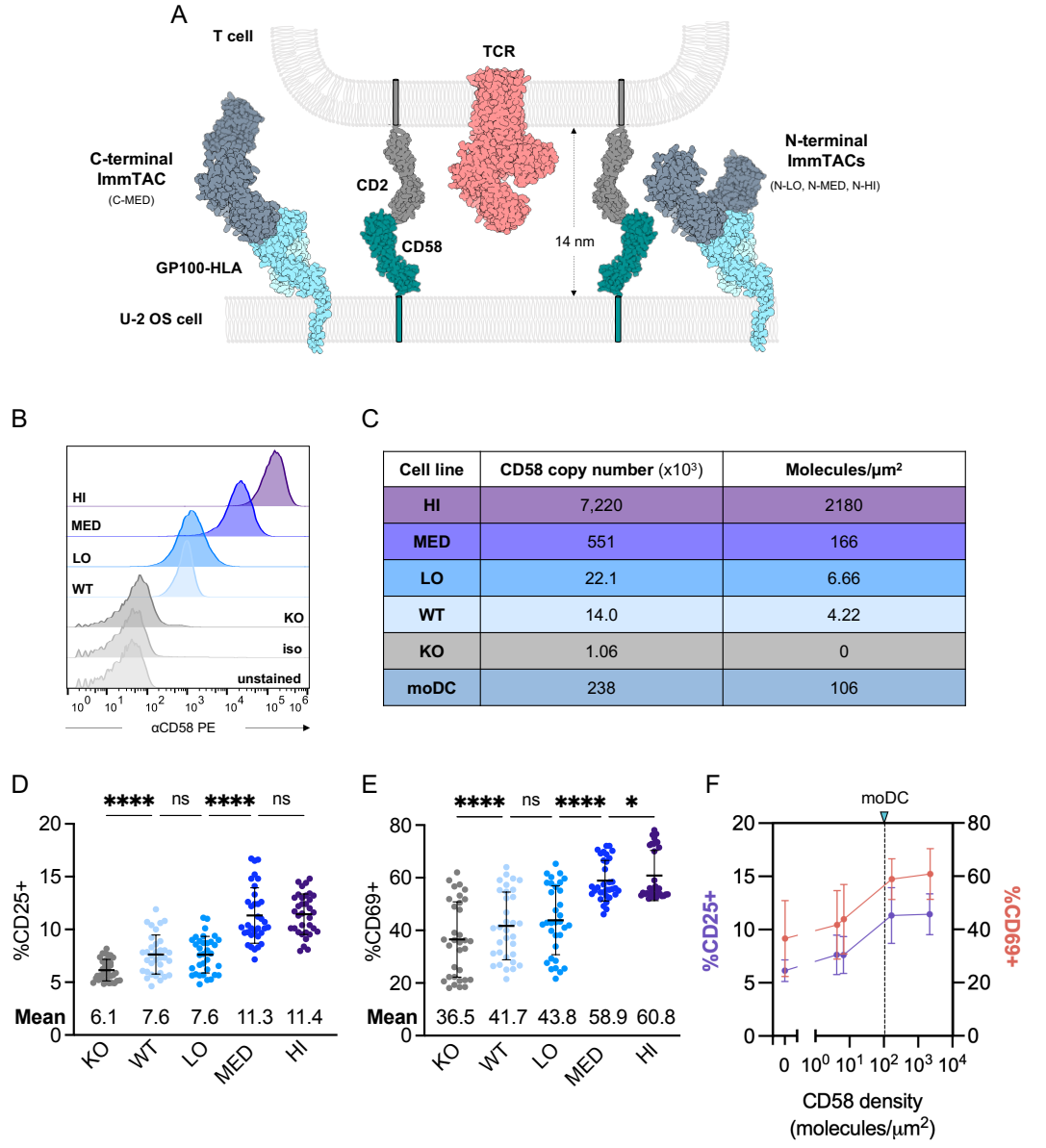


Figure 4.1: (Following page)

4.1B). The expression of endogenous CD58 was ablated from U-2 OS cells by electroporation of a CD58-targeting gRNA-Cas9 RNP complex. The resultant CD58 knock-out (KO) U-2 OS cells were then transduced with a CD58 construct modified in the following way: i) the TM region of CD58 was replaced with that of CD2 which leads to higher transduction efficiency and expression levels (personal communication, data not shown), ii) the cytoplasmic tail of CD58 was truncated to create a passive U-2 OS cell surface, and iii) a HaloTag was attached to the C-

Figure 4.1: Panel of U-2 OS cell lines expressing a ~7000-fold range of CD58 and their effect on T-cell activation in the absence of ligand. A. Schematic of a close contact formed between the U-2 OS cell membrane and T-cell microvillar projection. The axial dimensions of the close contact are determined by the CD2/CD58 adhesion pair measuring ~14 nm across the two membranes. The ImmTAC/GP100-MHC complexes containing the C-terminal (left) and N-terminal (right) ImmTACs are shown. **B**. Expression levels of CD58 on the surface of U-2 OS cell lines stained with PE-conjugated anti-CD58 antibody. The cell lines are as follows, listed from the highest to the lowest CD58 expresser: CD58HI > CD58MED > CD58LO = WT > CD58KO. **C**. Table summarising the CD58 expression levels of the five U-2 OS cell variants. Mature moDCs were included for reference. The expression levels are provided as copy numbers and densities calculated using the estimates of U-2 OS cell and mature moDC surface areas. **D**. CD25 upregulation by T cells following co-culture with the five U-2 OS cell lines in absence of TCR ligand. **E**. As in (D), but for CD69 instead of CD25. **F**. Plot showing the relationship between CD58 density on the U-2 OS cell surface and CD69 and CD25 expression by T cells in the absence of TCR ligand. The dashed line indicates CD58 density on mature moDCs. All co-culture assays were performed as three biological repeats in triplicates. Data was collected using T cells isolated from at least two donors. The $\%CD25^+$ and $\%CD69^+$ values were compared using RM one-way ANOVA with with Geisser-Greenhouse correction. Mean values with error bars corresponding to standard deviation are shown. Only statistical comparison of interest are shown. *P-value ≤ 0.05, **P-value ≤ 0.01, ***P-value ≤ 0.001, ****P-value ≤ 0.0001

terminus of CD58 to ensure compatibility of these U-2 OS cell lines with imaging experiments (Chapters 5 and 6). In total, three CD58KO CD58-HaloTag U-2 OS cell lines were created expressing distinct levels of CD58-HaloTag: CD58LO (6.6 CD58/μm^2), CD58MED (170 CD58/μm^2) and CD58HI (2200 CD58/μm^2) (Figure 4.1B). The CD58-HaloTag expression levels of the CD58LO cell line were matched to those of endogenous CD58 in WT U-2 OS cells thus controlling for any differences in signalling that might arise from the modifications of CD58-HaloTag. Including CD58KO and WT U2OS cells, a 'CD58' panel of five U-2 OS cell lines expressing four different CD58 levels was generated. For each cell line, CD58 copy numbers were quantified using flow cytometry and converted into densities using the U-2 OS cells surface area calculated in section 3.2.2 (Figure 4.1C). T-cell responses to the four ImmTACs were measured in co-culture assays of T cells with each U-2 OS cell line in the 'CD58' panel. As these cell lines did not express GP100-SCT, the binding sites for ImmTACs were produced by peptide-pulsing.

The key comparisons in the dataset are as follows: i) WT vs. CD58KO U-2 OS cells – informs on the effect of removing CD2/CD58 adhesion ii) WT vs. CD58LO U-2 OS cells – controls for modifications of CD58-HaloTag, and iii) CD58LO vs. CD58MED and CD58HI – tests the effect of ~25-fold and ~500-fold CD58 overexpression, respectively.

The B_{CD25} and B_{CD69} values, describing the T-cell activation in the absence of TCR ligand, were positively correlated with CD58 expression levels (Figure 4.1D-F). The lowest B_{CD25} and B_{CD69} values were recorded for T cells co-cultured with CD58KO U-2 OS cells and they were 18.7% and 12.4% lower than the respective values for WT U-2 OS cells. T cells co-cultured with CD58LO and WT U-2 OS cells displayed statistically indistinguishable background activation levels suggesting that the CD58-HaloTag modifications were inconsequential for the T cell/U-2 OS cell interactions in the absence of a ligand. The B_{CD25} and B_{CD69} values for the co-cultures of T cells with CD58MED U-2 OS cell increased by 48.7% and 34.4% relative to the corresponding CD58LO data. T cells incubated with CD58HI U-2 OS cells displayed a further 3.3% increase of B_{CD69} value relative to CD58MED, but the B_{CD25} values increased marginally and the shift was below the level of significance. This suggested that the background activation, i.e., ligand-independent signalling, was near saturation (Figure 4.1F).

The potency of the four ImmTACs in the context of the five U-2 OS cell lines was expressed as $EC_{50:CD25}$ and $EC_{50:CD69}$ values calculated from the dose-response curves (Figure 4.2A and B). For ease of comparison, the EC_{50} value for each ImmTAC/U-2 OS cells pair was normalised against the EC_{50} value for the same ImmTAC paired with WT U-2 OS cells and the relative changes were expressed as fold shifts (Figure 4.2C and E).

For the N-MED ImmTAC, the ablation of CD58 resulted in 2-fold and 1.5-fold increases in $EC_{50:CD25}$ and $EC_{50:CD69}$ values, respectively. In contrast, for C-MED the $EC_{50:CD25}$ value did not change and the $EC_{50:CD69}$ value was minimally reduced, but the downward shift was below the significance level. For both N-LO

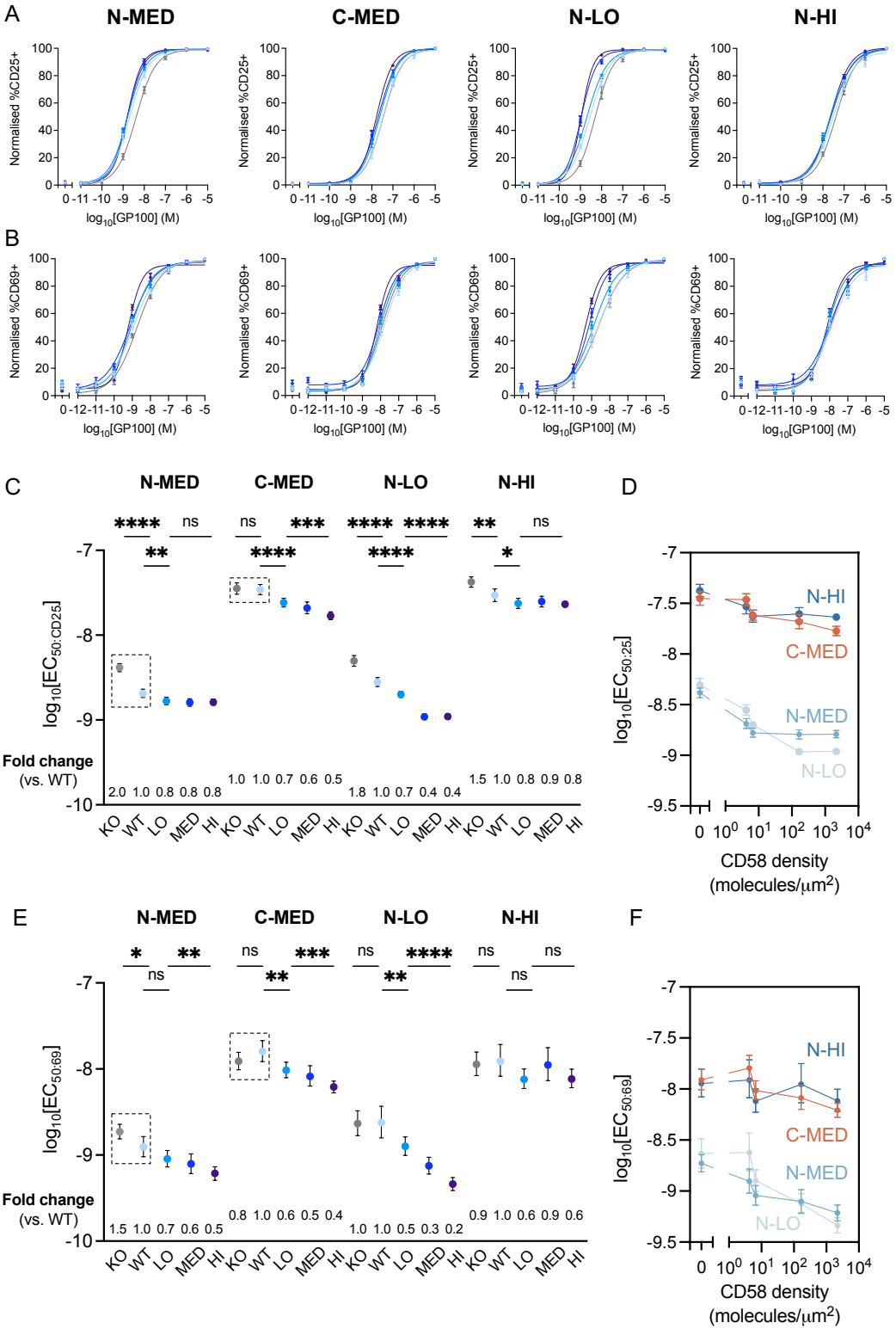


Figure 4.2: (Following page)

Figure 4.2: Relationship between CD58 expression levels and T-cell activation by ImmTACs. A. Dose-response curves showing T-cell activation as upregulation of CD25 in response to the four ImmTACs following 18h of co-culture with hGP100-pulsed U-2 OS cells expressing various CD58 densities. **B**. As in (A), but upregulation of CD69 is shown instead of CD25. **C**. $EC_{50:25}$ values extracted from unconstrained four-parameter variable slope Hill model fitted into the dose-response curves from (A). The $EC_{50:25}$ values for N-MED and C-MED ImmTAC on WT and CD58KO U-2 OS cell background are highlighted. **D**. Plot showing the relationship between CD58 density and potency of each ImmTAC expressed as $EC_{50:25}$ values. **E**. $EC_{50:69}$ values extracted from unconstrained four-parameter variable slope Hill model fitted into the dose-response curves from (B). The $EC_{50:69}$ values for N-MED and C-MED ImmTAC on WT and CD58 KO U-2 OS cell background are highlighted. **F**. Plot showing the relationship between CD58 density and potency of each ImmTAC expressed as $EC_{50:69}$ values. All co-culture assays were performed as three biological repeats in triplicates. Data was collected using T cells isolated from at least two donors. Error bars corresponding to SEM for (A-B) and to 95% CI for (C-F). EC_{50} values were compared using an F-test of normalised data. Only statistic comparison of interest are shown. *P-value $\leq$ 0.05, **P-value $\leq$ 0.01, ***P-value $\leq$ 0.001, ****P-value $\leq$ 0.0001

and N-HI ImmTACs, removing CD58 led to a ~1.6-fold increase in $EC_{50:CD25}$, but had no appreciable effect on the $EC_{50:CD69}$ values.

Substitution of the endogenous CD58 in WT U-2 OS cells with the CD58-HaloTag construct in the CD58LO U-2 OS led to a reduction in both $EC_{50:CD25}$ and $EC_{50:CD69}$ values across all of the ImmTACs. The fold shifts ranged from 0.5 to 0.8 and were all statistically significant with the two exceptions of $EC_{50:CD69}$ values for the N-MED and N-HI ImmTACs. Thus, while T-cells co-cultured with CD58LO and WT U-2 OS behaved identically in the absence of the TCR ligand, the former U-2 OS cell line enhanced ligand-dependent T-cell activation.

In the presence of high CD58 density on the surface of CD58HI U-2 OS cells, the potency of the N-MED ImmTAC did not increase in terms of CD25 levels, but the $EC_{50:CD69}$ value fell by 28.6% relative to CD58LO. CD58 overexpression in CD58HI U-2 OS cells potentiated the C-MED ImmTAC with the corresponding $EC_{50:CD25}$ and $EC_{50:CD69}$ values decreasing by 28.6% and 33.3%. The most profound shift upon transition from CD58LO to CD58HI U-2 OS cells occurred when T cells were stimulated with the N-LO ImmTAC – corresponding $EC_{50:CD25}$ and $EC_{50:CD69}$ values decreased by ~2-fold on average. In contrast, T cells responding to the N-HI ImmTAC were unperturbed by changes in CD58 expression levels.

4.2.2 Effect of engineered extension of pMHC on ImmTAC potency

The size-potency relationship is well-established for native TCR ligands, whereby native pMHCs are more potent than artificially extended pMHC chimeras[264,265,267,268]. In Chapter 3, it was shown that the C-MED ImmTAC is ~20-fold less potent than N-MED due to the presumed elongated geometry of the C-MED ImmTAC. However, this result could be intrinsic to the properties of the C-terminal ImmTAC rather than ImmTACs as a ligand class. To test whether the size-potency relationship applies to all ImmTACs, both N-terminal and C-terminal, the effective size of the 'ligand unit' i.e. ImmTAC/GP100-MHC was increased by engineered extension of the GP100-SCT.

To this end, the ECD of murine CD4 (mCD4) co-receptor was inserted between the TM region and the ECD of the GP100-SCT to create a GP100-SCT-mCD4 chimera (Figure 4.3A). This modification extended the GP100-SCT by ~14 nm, approximately twice the size difference between the C-MED and N-MED ImmTACs. Together, the combinations of the N-MED and C-MED formats with GP100-SCT and GP100-SCT-mCD4 yield four MED-affinity ligands increasing in size in ~7.5 nm increments (Figure 4.3A). The LO and HI affinity variants were only available in two sizes corresponding to N-terminal ImmTAC/GP100-SCT and N-terminal ImmTAC/GP100-SCT-mCD4 'ligand units'. The GP100-SCT-mCD4 construct was lentivirally transduced into WT U-2 OS cells and its expression was matched to that of GP100-SCT in the GP100-SCT U-2 OS cell line (Figure 4.3B).

In the absence of the TCR ligand, the B_{CD25} and B_{CD69} were discordant, with the former decreasing by 15.6% and the latter increasing by 6.6% upon extending the pMHC (Figure 4.4C-D). The $EC_{50:CD25}$ and $EC_{50:CD69}$ values for the N-MED ImmTAC increased by 6.5-fold and 9.5-fold, respectively, when it was bound to the GP100-SCT-mCD4 variant (Figure 4.4C, D). Despite its elongated structure, the potency of the C-MED ImmTAC was further reduced by the pMHC extension with the $EC_{50:CD25}$ and $EC_{50:CD69}$ values increasing by 2.2- and 3-fold, respectively. For both the N-LO and N-HI ImmTACs, the effect of

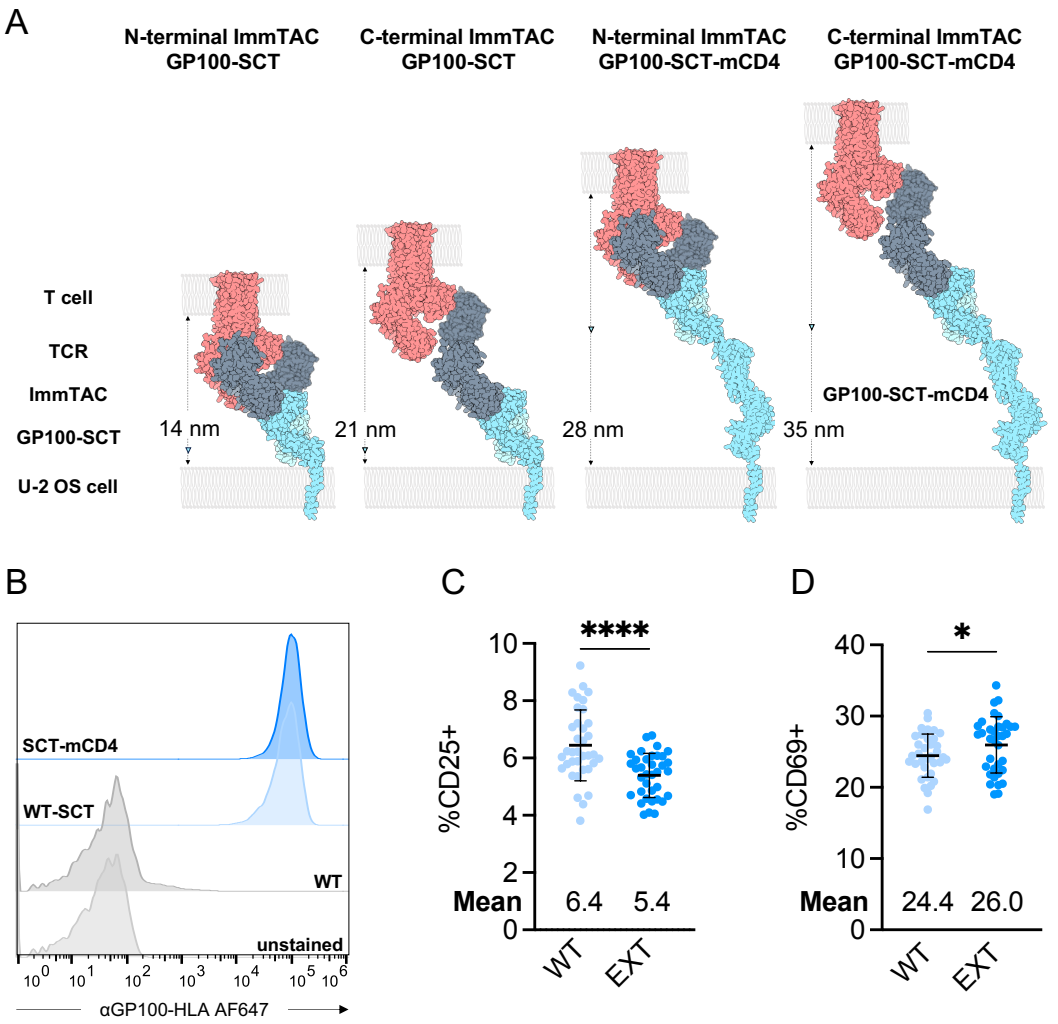


Figure 4.3: Extension of the GP100-MHC antigen and its effect on T-cell activation in the absence of TCR ligand. A. Schematic of N-terminal (first and third from the left) and C-terminal (second and fourth from the left) ImmTACs bound to TCR/CD3 complex and either GP100-SCT (WT) or GP100-SCT-mCD4 (EXT) antigen. The estimated axial dimension of the ligand/TCR/CD3 complexes shown to scale. Blue arrowheads mark the distance between the T-cell surface and MHC-I $\alpha 3$ domain where CD8α binding site is located. **B**. Expression levels of GP100-SCT and GP100-SCT-mCD4 on the U-2 OS cell surface stained with AF647-conjugated N-MED ImmTAC. **C**. CD25 upregulation by T cells following co-culture with the GP100-SCT (WT) or GP100-SCT-mCD4 (EXT) U-2 OS cell lines in the absence of TCR ligand. **D**. As in (C), but for CD69 instead of CD25. All co-culture assays were performed as three biological repeats in triplicates. Data was collected using T cells isolated from at least two donors. The %CD25$^+$ and %CD69$^+$ values were compared using a Wilcoxon test. Mean values with error bars corresponding to standard deviation are shown. *P-value $\leq$ 0.05, **P-value $\leq$ 0.01, ***P-value $\leq$ 0.001, ****P-value $\leq$ 0.0001

increased size was smaller than for N-MED with their $EC_{50:CD25}$ and $EC_{50:CD69}$ values increasing by ~3-fold on average.

Overall, T cells responded less readily to all four ImmTACs when bound to the longer GP100-SCT-mCD4 chimera. Interestingly, the N-MED/GP100-SCT-mCD4 ligand was more potent than the C-MED/GP100-SCT ligand, despite the former 'ligand unit' being ~7.5 nm longer suggesting that there might be a secondary mechanism associated with the consequences of the two different approaches to the extension of the TCR ligands (Figure 4.4C-D, relevant comparison in a dashed box). Notably, inserting the mCD4 scaffold into the GP100-SCT extends the intermembrane distance by moving the pMHC further away from the U-2 OS cell surface, whereas the switch from N-terminal to C-terminal ImmTAC architecture does so by increasing the distance between the pMHC and the T-cell surface (Figure 4.3A). This distance might be crucial for the availability of the CD8 binding site on the GP100-MHC molecule, suggesting a role for the CD8 co-receptor in ImmTAC-induced TCR triggering.

4.2.3 Interactions of the CD8αβ co-receptor with the ternary TCR/ImmTAC/pMHC complex

The CD8 co-receptor binds to the membrane-proximal α3 domain of MHC-I with a K_D of 137 μM (Figure 4.5A-B)[360]. To test whether the co-receptor is recruited to the ImmTAC/GP100-MHC complexes, two GP100-SCT variants containing modified CD8α binding sites were designed. The first variant bore D227K and T228A mutations which completely abrogate CD8αβ binding[273] (Figure 4.5B). The second variant known as A2-K^B was composed of the α1-2 domains of HLA-A2 and α3 domain of a murine H2-K^B molecule[360,361]. This chimeric MHC-I molecule displays an enhanced affinity for CD8αβ with its K_D ~13-fold lower than that of the WT interaction (Figure 4.5B)[360]. Hereafter, these two variants will be referred to as a KA and A2-k^B GP100-SCTs. WT U-2 OS cells were transduced with these variants and their expression was matched to

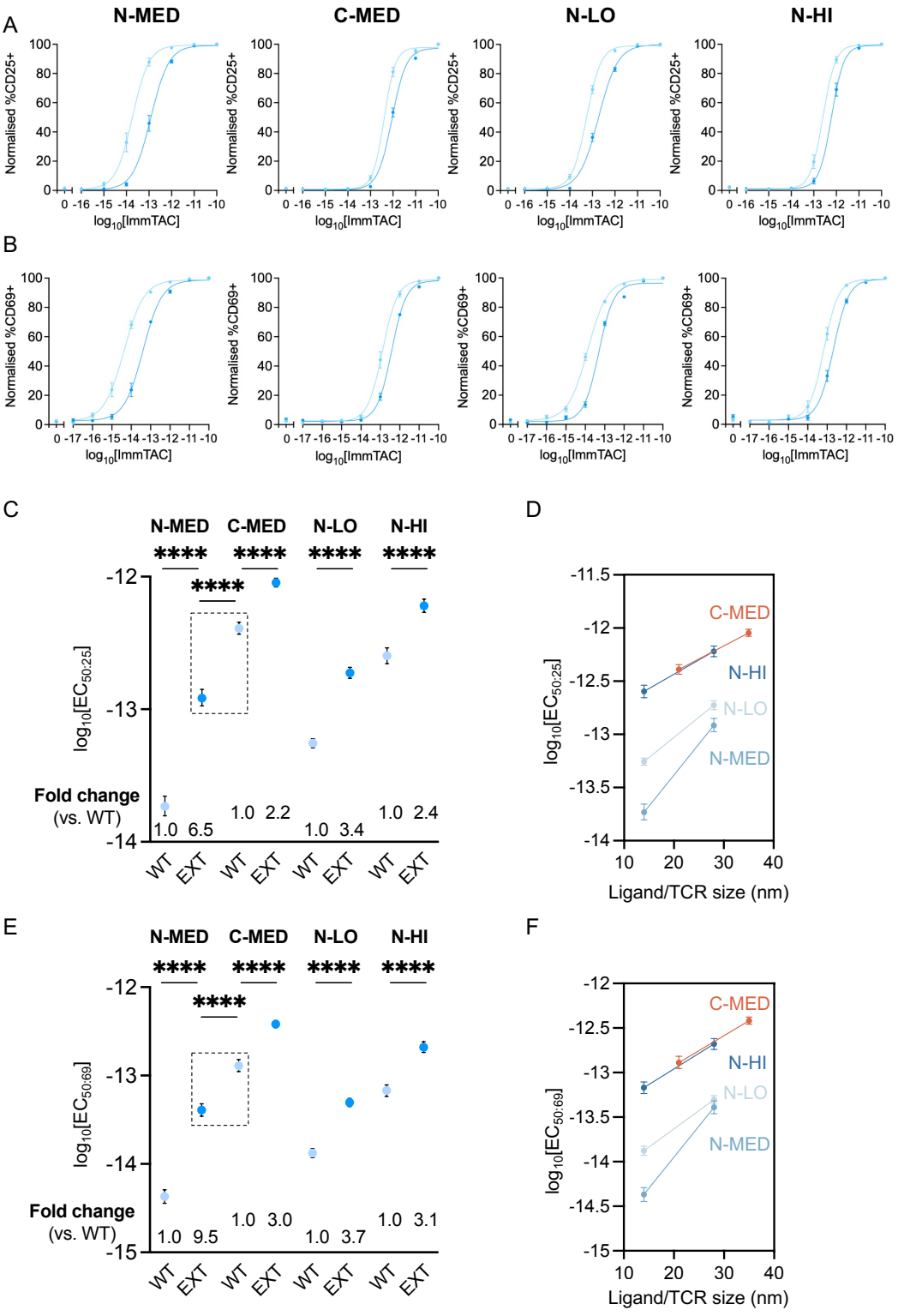


Figure 4.4: (Following page)

Figure 4.4: Relationship between the size of the ImmTAC/GP100-MHC ligand and T-cell activation. A. Dose-response curves showing T-cell activation as upregulation of CD25 in response to the four ImmTACs following 18h of co-culture with U-2 OS cells expressing either GP100-SCT (WT) or GP100-SCT-mCD4 (EXT) antigen **B**. As in (A), but upregulation of CD69 is shown instead of CD25. **C**. $EC_{50:25}$ values extracted from unconstrained four-parameter variable slope Hill model fitted into the dose-response curves from (A). The $EC_{50:25}$ values for N-MED/GP100-SCT-mCD4 and C-MED/GP100-SCT ligands are highlighted. **D**. Plot showing the relationship between the estimated size of the ligand/TCR/CD3 complex size and potency of each ImmTAC expressed as $EC_{50:25}$ values. **E**. $EC_{50:69}$ values extracted from unconstrained four-parameter variable slope Hill model fitted into the dose-response curves from (B). The $EC_{50:69}$ values for N-MED-GP100-SCT-mCD4 and C-MED-GP100-SCT ligands are highlighted. **F**. Plot showing the relationship between the estimated size of the ligand/TCR/CD3 complex and potency of each ImmTAC expressed as $EC_{50:69}$ values. All co-culture assays were performed as three biological repeats in triplicates. Data was collected using T cells isolated from at least two donors. Error bars corresponding to SEM for (A-B) and to 95% CI for (C-F). EC_{50} values were compared using an F-test of normalised data. Only statistical comparison of interest are shown. *P-value $\leq$ 0.05, **P-value $\leq$ 0.01, ***P-value $\leq$ 0.001, ****P-value $\leq$ 0.0001

that of WT GP100-SCT to ensure that any measured differences are due to the affinity of the CD8$\alpha\beta$/MHC-I interaction (Figure 4.5C).

In the absence of the TCR ligand, T cells showed a 22.6% reduction in B_{CD25} when WT GP100-SCT was replaced with the KA variant (Figure 4.5D). The B_{CD69} value followed the same downward trend, but the shift was statistically insignificant (Figure 4.5E). The enhanced CD8α/MHC-I affinity led to an increase in background activation with B_{CD25} and B_{CD69} values going up by 19.4% and 36.3% relative to WT GP100-SCT, respectively. Overall, the background activation level was positively correlated with the affinity of MHCI-$\alpha\beta$ binding (Figure 4.5F). These changes in T-cell activation levels in response to the shifts in the CD8α/MHC-I affinity can be attributed to the adhesion-like properties of the CD8α/MHC-I interaction which are accentuated by the high expression levels of the GP100-SCTs in the three U-2 OS cell lines. Due to the association of CD8 with the Lck, the kinase activity within close contacts is likely to increase with the CD8α/MHC-I affinity in effect promoting spontaneous triggering of the TCR.

Next, the effect of the CD8α/MHC-I affinity on ligand-dependent T-cell responses was examined. T cells activated less readily when N-MED ImmTAC was

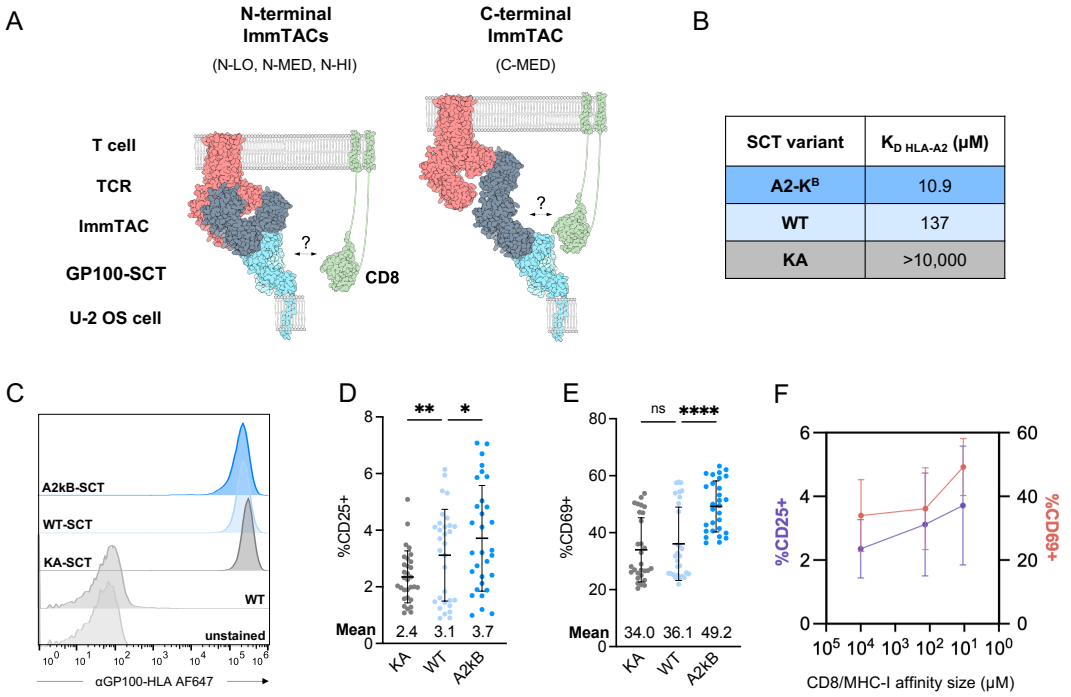


Figure 4.5: U-2 OS cell lines expressing A2-K^B, WT and KA variants of GP100-MHC and their effect on T-cell activation in the absence of TCR ligand. **A**. Schematic of N-terminal (left) and C-terminal (right) ImmTACs bound to the GP100-MHC antigens and TCR/CD3 complexes along with the CD8 co-receptor. **B**. Table summarising the the CD8$\alpha\alpha$-MHC-I binding affinites for A2-K^B, WT and KA variants of the MHC-I[360] **C**. Expression levels of A2-K^B, WT and KA MHC-I variants in the GP100-SCT format on the U-2 OS cell surface stained with AF647-conjugated N-MED ImmTAC. **D**. CD25 upregulation by T cells following co-culture with the A2-K^B, WT and KA GP100-SCT U-2 OS cell lines in the absence of ImmTACs. **E**. CD69 upregulation by T cells following co-culture with the A2-K^B, WT and KA GP100-SCT U-2 OS cell lines in the absence of ImmTACs. **F**. Plot showing the relationship between the CD8$\alpha\beta$/MHC-I affinity and CD69 and CD25 expression by T cells in the absence of TCR ligand. K_D values for CD8$\alpha\beta$-KA-MHC-I binding was assumed to be 10 mM for comparative purposes. All co-culture assays were performed as three biological repeats in triplicates. Data was collected using T cells isolated from at least two donors. The %CD25$^+$ and %CD69$^+$ values were compared using RM one-way ANOVA with with Geisser-Greenhouse correction. Mean values with error bars corresponding to standard deviation are shown. Only statistical comparisons of interest are shown. *P-value $\leq$ 0.05, **P-value $\leq$ 0.01, ***P-value $\leq$ 0.001, ****P-value $\leq$ 0.0001

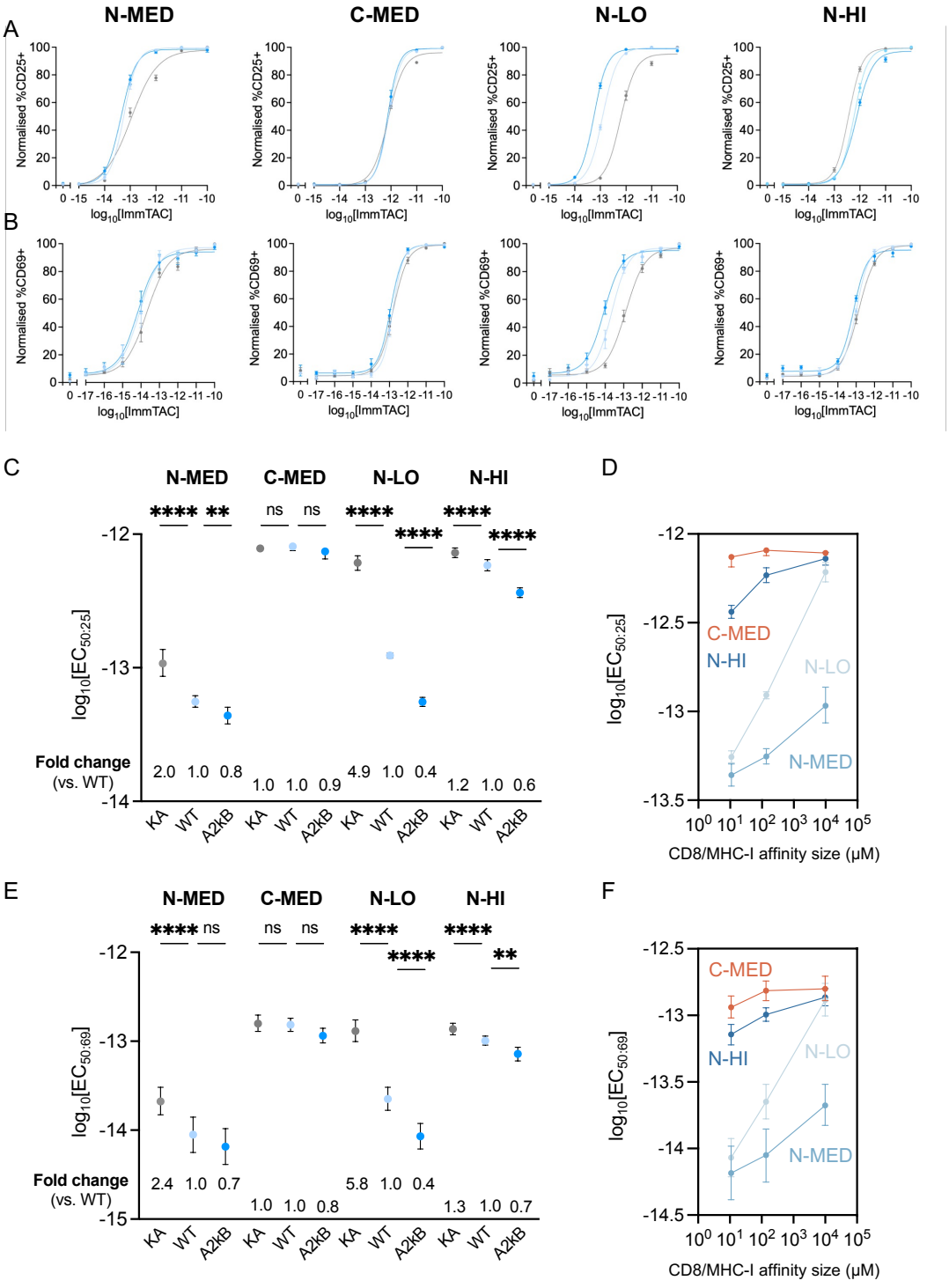


Figure 4.6: (Following page)

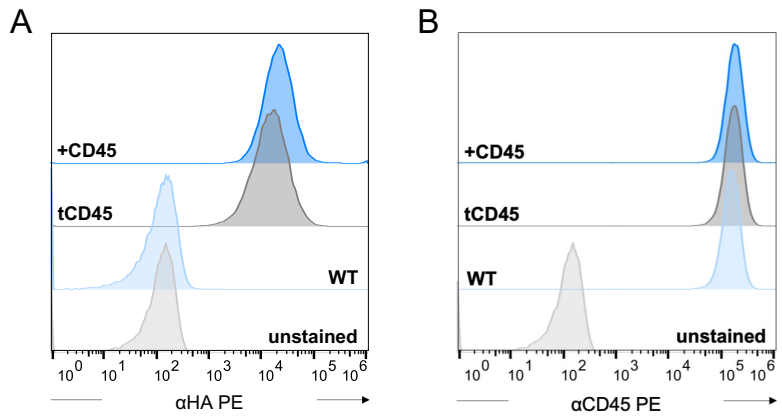
Figure 4.6: Relationship between the CD8αβ/MHC-I affinity and T-cell activation by ImmTACs. A. Dose-response curves showing T-cell activation by upregulation of CD25 in response to the four ImmTACs following 18h of co-culture with U-2 OS cells expressing the A2-K^B, WT and KA GP100-SCT variants **B**. As in (A), but upregulation of CD69 is shown instead of CD25. **C**. $EC_{50:25}$ values extracted from unconstrained four-parameter variable slope Hill model fitted into the dose-response curves from (A). **D**. Plot showing the relationship between the CD8αβ/MHC-I affinity and the potency of each ImmTAC expressed as $EC_{50:25}$ values. K_D value for CD8αβ/KA-MHC-I binding was assumed to be 10 mM for comparative purposes **E**. $EC_{50:69}$ values extracted from unconstrained four-parameter variable slope Hill model fitted into the dose-response curves from (B). **F**. Plot showing the relationship between the CD8αβ/MHC-I affinity and the potency of each ImmTAC expressed as $EC_{50:69}$ values. K_D value for CD8αβ/KA-MHC-I binding was assumed to be 10 mM for comparative purposes. All co-culture assays were performed as three biological repeats in triplicates. Data was collected using T cells isolated from at least two donors. Error bars corresponding to SEM for (A-B) and to 95% CI for (C-F). EC_{50} values were compared using an F-test of normalised data. *P-value $\leq$ 0.05, **P-value $\leq$ 0.01, ***P-value $\leq$ 0.001, ****P-value $\leq$ 0.0001

bound to the KA variant rather than the WT GP100-SCT and the corresponding $EC_{50:CD25}$ and $EC_{50:CD69}$ values increased by 2-fold and 2.4-fold, respectively. Conversely, the potency of the N-MED ImmTAC increased when the bispecific was bound to the A2-k^B variant, but it did so marginally and only the shift in the $EC_{50:CD25}$ value was statistically significant. Similar to the N-MED ImmTAC, the potency of the N-LO ImmTAC was negatively and positively influenced by the KA and A2-k^B variants relative to the WT GP100-SCT, respectively; however, the shifts in the EC_{50} values increased. Abrogation of CD8 recruitment reduced T-cell responses to the N-LO ImmTAC by ~5.5-fold, whereas enhanced CD8α/MHC-I binding led to a ~2.5-fold increase in activation across both markers. Like the other two N-terminal ImmTACs, the potency of the N-HI ImmTAC was impacted by the changes in the CD8α/MHC-I affinity, albeit with smaller shifts in the EC_{50} values. In contrast, T-cell responses to the C-MED ImmTAC were unaffected by the modifications of the GP100-SCT. These results suggest that CD8 co-receptor is recruited to the ImmTAC/GP100-MHC complexes containing the N-terminal, but not the C-terminal bispecifics.

4.2.4 Truncation of CD45 phosphatase attenuates ImmTAC-induced T-cell activation

T-cell responses to native ligands are dependent on spatial segregation of TCR and CD45 which is driven by the mismatch in the size of the CD45 ECD and intermembrane distance within CCs. Truncation of the CD45 ECD has been shown to attenuate T-cell responses and CD45 deletion prevents T-cell activation[86,90,261,262,266,362]. To test whether this principle holds for ImmTAC ligands, T cells expressing a truncated version of CD45 (tCD45) were created. The introduction of the tCD45 into T cells would increase the total amount of phosphatase, meaning that the parental T cells couldn't be reliably used as a control since CD45 expression determines antigen sensitivity[90]. Hence, an additional T cell line was to be created whose total phosphatase levels were matched to those of tCD45-expressing T cells using a full-length CD45 (+CD45) construct.

The tCD45 construct consisted of the ECD of rat CD90 linked to the TM region and cytoplasmic domain of human CD45. The ECD of rCD90 is composed of a single IgSF domain whose axial dimensions are ~3.5 nm meaning that tCD45 should have unobstructed access to CCs. Additionally, tCD45 was appended with an HA tag and a HaloTag on its N- and C-termini, respectively. The +CD45 construct was composed of the ABC isoform of CD45 and had an HA tag and a SNAP-tag on its N- and C-termini, respectively. The HA tags were included to track expression of the CD45 variants using the same monoclonal antibody whereas the self-labelling tags permited the use of these cell lines in future imaging work. For these experiments, an engineered Jurkat T cell line known as 'J8' (created by Edward Jenkins) was used instead of the primary $CD8^+$ T cells due to the ease with which the former can be genetically manipulated[137]. In short, to produce the J8 cell line, the endogenous TCRα and TCRβ chains were deleted and the α and β chains of the 1G4 TCR were introduced. Since the 1G4 TCR is MHC-I-restricted, the CD4 co-receptor was replaced with CD8$\alpha\beta$. Additionally, the expression levels of LFA-1 of J8s were matched to those of



C

Cell line	Transgenic CD45 ($x10^3$)	Endogenous CD45 ($x10^3$)	Total phosphatase ($x10^3$)
+CD45	12	107	119
tCD45	7	111	118
WT	0	101	101

Figure 4.7: Jurkat T cell lines expressing truncated CD45 and its effect on T-cell activation in the absence of TCR ligand. A. Expression levels of transgenic +CD45 and tCD45 phosphatase variants in Jurkat $CD8^+$ T cell lines stained with PE-conjugated anti-HA tag antibody. **A**. Expression levels of CD45 phosphatase in +CD45, tCD45 and WT Jurkat $CD8^+$ T cell lines stained with PE-conjugated anti-CD45 tag antibody. For tCD45 and WT T cell lines this measurement corresponds to endogenous CD45 only, but for +CD45 T cells it includes both the endogenous and transgenic CD45. **C**. Table summarising the expression levels of the transgenic, endogenous and total CD45 phosphatase in +CD45, tCD45 and WT Jurkat $CD8^+$ T cell lines as copy numbers.

primary $CD8^+$ T cells. J8s were lentivirally transduced with both tCD45 and +CD45 constructs. The expression of +CD45 and tCD45 in the two cell lines was matched (Figure 4.7A) and copy numbers of both the transgenic and the endogenous phosphatase were quantified to confirm that both tCD45 and +CD45 T cells have comparable phosphatase levels (Figure 4.7A-C).

Only N-terminal ImmTACs were used in these experiments as the C-MED ImmTAC was not available at the time. Unlike primary $CD8^+$ T cells, Jurkat-derived cell lines did not appreciably upregulate CD25 following a 18-h co-culture with U-2 OS cells (data not shown) and thus, only CD69 was used to measure the T-cell activation state. The background activation levels of tCD45 and +CD45 J8 cells did not shift relative to the parental cell line (Figure 4.8D). The effect

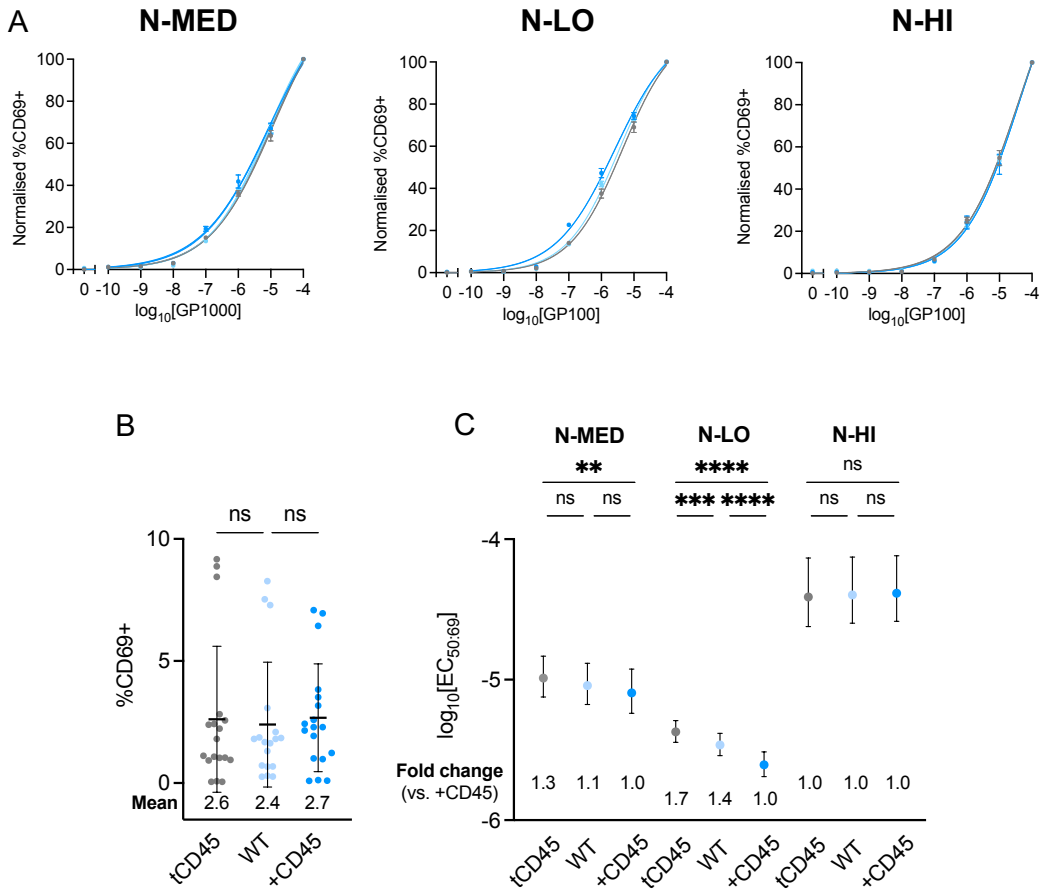


Figure 4.8: Impact of CD45 truncation on T-cell activation by ImmTACs. **A**. Dose-response curves showing activation of +CD45, tCD45 and WT Jurkat CD8$^+$ T cell lines by upregulation of CD69 in response to the three N-terminal ImmTAC ImmTACs following 18h of co-culture with hGP100-pulsed U-2 OS cells. **B**. CD69 upregulation by +CD45, tCD45 and WT Jurkat CD8$^+$ T cell lines following co-culture with the hGP100-pulsed U-2 OS cells in the absence of TCR ligand. **C**. $EC_{50:69}$ values extracted from the constrained four-parameter variable slope Hill model (bottom = 0) fitted into the dose-response curves from (A). All co-culture assays were performed as two biological repeats in triplicates. Error bars correspond to SEM for (A), and 95% CI for (B-C). $EC_{50:69}$ values were compared using an F-test of normalised data. Only statistical comparisons of interest are shown. *P-value $\leq$ 0.05, **P-value $\leq$ 0.01, ***P-value $\leq$ 0.001, ****P-value $\leq$ 0.0001

of tCD45 expression on T-cell activation was only observable for the N-LO and N-MED variants. For the tCD45 J8s stimulated with the N-MED ImmTAC, the $EC_{50:CD69}$ value increased by 1.3-fold relative to the +CD45 T cells. The shift was greater for the low-affinity ligand, N-LO, for which a 1.7-fold increase in the $EC_{50:CD69}$ value was recorded. The relative shifts between activation of tCD45 and +CD45 T cells resulted from simultaneous increase and decrease in the responses of the +CD45 and tCD45 T cells relative to the parental cell line, respectively. In contrast, J8 activation by the N-HI ImmTAC was not affected by the expression of tCD45 versus +CD45 phosphatase.

4.3 Discussion

In this chapter, the correlates of T-cell activation by ImmTACs were systematically examined through a series of modifications of the T cell/U-2 OS cell system. First, the effect of CD58 overexpression on T-cell activation by ImmTACs was examined. T cells responding to the low-affinity ImmTAC (N-LO) benefited the most from the CD58 overexpression, whereas T-cell activation by the high-affinity variant (N-HI) was unaffected by changes in the CD58 density on the U-2 OS cell surface. Through the extension of GP100-MHC, it was demonstrated that the negative relationship between the ligand size and potency applies to all ImmTACs and that the low potency of the C-terminal ImmTAC cannot be explained by its extended geometry alone. Next, it was found that CD8 recruitment to the TCR/CD3 complex is a feature of T-cell activation by N-terminal, but not C-terminal ImmTACs. The degree of dependence of T cells on CD8 recruitment for activation was determined by the ImmTAC/CD3ϵ affinity. Truncation of the CD45 phosphatase attenuated T-cell responses, but it had little effect on T-cell activation by the higher-affinity ImmTACs, N-HI and N-MED. Overall, the interactions of ImmTACs with the modified surface molecules were a function of their topology and the ImmTAC/CD3ϵ affinity. Finally, the determinants of ligand-independent T-cell responses were established. Both CD58 overexpression

and an increase in the affinity of the CD8/MHC-I interactions led to substantial T-cell activation in the absence of ImmTACs.

4.3.1 Role of small adhesion molecules in ImmTAC-induced TCR triggering

To inspect how CD2/CD58 adhesion and signalling influence T-cell activation, a panel of U-2 OS cell lines expressing a 7200-fold range of CD58 densities was generated. To achieve CD58 overexpression, the CD58-HaloTag construct was introduced at three different levels into the CD58KO U-2 OS cell line.

In the absence of the TCR ligand, increasing the expression of CD58 resulted in robust T-cell activation, with the proportion of $CD25^+$ and $CD69^+$ T cells almost doubling when CD58 density increased from 0 to ~2000 molecules/μm^2. No appreciable change in activation levels was observed following the co-culture of T cells with the CD58LO U-2 OS cell line whose CD58-HaloTag expression level was matched to that of the endogenous CD58 in WT U-2 OS cells. Ablation of CD58 from U-2 OS cells reduced the background activation levels suggesting that *in vivo*, T cells experience tonic signalling during surveillance of the secondary lymphoid organs and the periphery.

CD58 expression levels also influenced ligand-dependent T-cell activation. Deletion of CD58 from U-2 OS cells had a disparate impact on the potency of N-MED and C-MED ImmTACs. In the absence of CD58, T-cell responses to the N-MED ImmTAC decreased by ~1.8-fold, whereas the responses to the C-MED ImmTAC remained unchanged relative to those at endogenous CD58 levels. The mechanistic basis for the difference likely stems from the two countervailing roles of the CD2/CD58 pair: i) the more conventional role in stabilisation of the T cell/U-2 OS cells contacts resulting in potentiation of T-cell responses, and ii) its antagonism towards molecules and complexes exceeding ~14 nm. The latter likely does not apply to the N-MED ImmTAC and thus removal of CD58 has a clear-cut negative effect. On the other hand, ablation of CD58 takes the 'brake' off GP100-MHC/C-MED/TCR/CD3 complex formation, but

this positive effect is likely masked by the reduced efficiency of CC formation. If these mechanisms were in place, then it could also be expected that CD58 overexpression would suppress T-cell activation by the C-MED ImmTAC, but not the N-MED ImmTAC. Surprisingly, high levels of CD58 expression favoured T-cell responses to the C-MED ImmTAC rather than the N-MED ImmTAC. Thus, further experiments need to be conducted to precisely establish the relationship between CD2/CD58 adhesion and TCR ligand dimensions. Previously, deleterious effects of a size mismatch between the dimensions of adhesion molecules and antigen receptors on T cell signalling have been shown for pMHC/CAR and native pMHC/TCR interactions[269,349].

Overexpression of CD58-HaloTag in U-2 OS cells potentiated T-cell responses to all of the ImmTACs except for the N-HI variant. In contrast, the reduced ImmTAC/CD3ϵ affinity sensitised T cells to the effects of CD58 overexpression with T-cell responses to the N-LO variant increasing by ~2-fold upon ~330-fold increase in CD58 density. Consistent with these results, Reinherz and colleagues also found that low-affinity ligand/TCR interactions are correlated with an increased dependence on CD2/CD48 adhesion (CD48 is a mouse homolog of CD58)[359] The enhancement of T-cell sensitivity by the CD2/CD48 pair was first described for murine $CD8^+$ T cells and it was found to be independent of CD2 signalling[138,269,363]. This suggests that the mechano-adhesive properties of the CD2/CD58 axis are sufficient to amplify T-cell activation.

4.3.2 Effect of engineered extension of pMHC in ImmTAC potency

In Chapter 3, the size-potency relationship for ImmTAC ligands was inferred on the basis of the reduced ability of the C-MED versus N-MED ImmTAC to activate T cells. To understand whether this effect applies to the entire ligand class, the GP100-SCT was extended by ~14 nm by insertion of IgSF domains derived from murine CD4 co-receptor. The N-MED/GP100-SCT-mCD4 ligand was three times more potent than the C-MED/GP100-SCT ligand despite the former being ~7.5

nm 'taller'. This suggested the involvement of a secondary mechanism which could not be attributed to the size of the TCR ligand *per se* (see next section). Similar to N-MED, the potency of C-MED was reduced upon GP100-SCT extension but to a smaller extent. This is consistent with the elongated structure of the C-MED ImmTAC as additive extensions of membrane molecules have been shown to have progressively smaller impacts on their exclusion from intermembrane contacts once the axial dimensions of the contact are exceeded[358]. The magnitude of the size-potency effect did not correlate with the ImmTAC/CD3ϵ affinity as the EC_{50} values for the N-LO, N-MED and N-HI ImmTAC on average showed 2.8-, 8-, 3.5-fold upward shifts, respectively, upon GP100-SCT extensions. This result stands in contrast to other studies showing a linear relationship between ligand affinity and the magnitude of the size-potency effect[263,264].

IgSF-based scaffolds were successfully used in multiple studies to increase the axial dimensions of native and synthetic TCR ligands and demonstrate the size-potency relationship[264,265,267]. Scaffolds composed of CD43 ECD or fibronecting type III domains were also employed to alter ligand dimensions. This suggests that ECDs comprised concatenated IgSF domains and those bearing dense glycosylation are well-suited for size manipulation experiments[263–265,267,269,353] Recently, TCR ligands were also extended using flexible single-stranded DNA scaffolds leading to attenuation of T-cell responses, but the relationship between scaffold flexibility and ligand potency has not been systematically tested to date[355].

4.3.3 Interactions of CDαβ co-receptor with ternary TCR-ImmTAC-pMHC complex

The participation of CD8αβ in the ImmTAC-induced TCR triggering mechanism was tested using U-2 OS cells expressing KA, WT and A2-K^B GP100-SCT variants. In the absence of the TCR ligand, increasing the CD8α/MHC-I affinity led to ligand-independent T-cell activation with the proportion of $CD69^+$ and $CD25^+$ T cells increasing by ~50% for the KA versus the A2-K^B GP100-SCT variants. In terms of T-cell responses to ImmTACs, the potency of the N-MED

ImmTAC in the context of KA and A2-K^B variants was reduced and enhanced, respectively. The contributions of the CD8 co-receptor to ImmTAC-induced T cell activation were affinity-dependent, for instance, the potencies of the N-LO and N-HI ImmTAC in the context of the KA variant were attenuated ~5.5- and ~1.3-fold, respectively, relative to the WT GP100-SCT. Similarly, the N-LO ligand benefited most from the enhanced CD8 recruitment afforded by the A2-kB variant. Such a relationship between CD8-dependence and ligand affinity was reported for TCR/pMHC interaction using mutated MHC molecules as well as CD8-deficient T cells, but it is the first indication that this principle extends to synthetic ligands[112,349,364]. Finally, the potency of the C-MED ImmTAC was unaffected by either of the GP100-SCT variants suggesting that its elongated structure is prohibitive of CD8 recruitment. The apparent limit on the molecular reach of the co-receptor is consistent with the heavy O-glycosylation of the CD8αβ stalk which likely forces it into its maximally extended conformation evolved for binding to native TCR/pMHC complexes[94–96].

4.3.4 Truncation of CD45 phosphatase attenuates ImmTAC-induced T-cell activation

The role of the CD45 phosphatase in the mechanism of TCR triggering by ImmTACs was tested using $CD8^+$ Jurkat T cells expressing a truncated version of CD45. In contrast to primary $CD8^+$ T cells, $CD8^+$ Jurkat T cells co-cultured with U-2 OS cells did not exhibit saturating responses and only CD69 upregulation could be quantified. Introduction of tCD45 attenuated T cell responses to the N-LO and N-MED ImmTACs by 1.7- and 1.3-fold, respectively, in comparison to the control +CD45 cell line. T-cell activation by the N-HI ImmTAC was unperturbed by expression of either tCD45 or +CD45 in line with observations that the reliance of T cells on CD45 segregation for activation is reduced for high-affinity ligands[263,365]. The negative impact of CD45 truncation on antigen sensitivity was previously demonstrated in both murine and human systems[86,256,261,262]. In previous studies expression of a rCD90-CD45 chimera in Jurkat T cells and T

cell hybridomas almost completely abolished activation in response to anti-CD3ϵ antibodies which could be likened in binding affinity to the N-HI ImmTAC[261,262]. However, direct comparison with these studies should be approached cautiously as the extent of inhibition by tCD45 is likely correlated with the proportion of tCD45 to total CD45 phosphatase.

As referred to throughout the discussion, various features of T-cell signalling in response to physiological ligands could be replicated using the N-terminal, but not the C-terminal ImmTACs. Furthermore, the high affinity of the N-HI ImmTAC for CD3ϵ meant that some of the system modifications had a negligible functional impact on its capacity to activate T cells. The lower affinity ImmTACs, N-LO and N-MED conformed to all tested principles of TCR triggering by pMHC molecules showing that both can be considered to be authentic TCR ligands. Given the clinical relevance of the N-MED ImmTAC, it was selected as a model ligand for imaging experiments in the following chapters.

5

Topography of the T-cell surface and the receptor organisation therein during interactions with cancer cells

Contents

5.1 Introduction 131
5.2 Results 133
5.2.1 Generation of ZAP70-HaloTag primary CD8$^+$ T cells 133
5.2.2 Morphology of the primary CD8$^+$ T-cell surface . . . 133
5.2.3 Proximal signalling of CD8$^+$ T cells in response to the N-MED ImmTAC 134
5.2.4 Generation and characterisation of U-2 OS cell lines for imaging of T cell/target cell interactions 136
5.2.5 ICAM-1 alters the dynamics of the T cell/U-2 OS cell interaction 141
5.2.6 Primary CD8$^+$ T cells form discrete contacts at the interface with target cells 143
5.2.7 A single close contact is sufficient for T-cell activation 153
5.2.8 Scanning behaviour of T cells in the absence of the TCR ligand 154
5.2.9 Hallmarks of KS-based signalling within close contacts 158
5.2.10 Overexpression of CD58 increases the dimensions of close contacts 165
5.3 Discussion 167
5.3.1 Model T cell/target cell system for imaging of cellular interactions 169
5.3.2 CD58 as a close-contact marker 170
5.3.3 Visualisation of the T cell/cancer cell interactions . . 171

5.1 Introduction

The principles of antigen recognition relying on the formation of CCs were proposed over two decades ago[366], but the experimental evidence directly showing the role of T-cell surface topology in TCR triggering has arrived in the last ten years[86,137,168,256,258,367].

The following model of antigen recognition was formulated, informed by studies of the resting T-cell surface morphology and T-cell interactions with either APC surrogates or genuine target cells. T cells probe the target cell surface using microvilli measuring up to 0.5 µm in length and ~100-500 nm in diameter[163,167,168,368]. In addition to having evolved a specialised morphology, the distribution of key receptors along the microvilli primes them for antigen recognition with the TCR/CD3 complex, co-receptors and small adhesion molecules being located at the microvillar tips[162,169,174]. Localisation of CD45 on the surface of resting T cells is more controversial, but most evidence points to its uniform distribution across the plasma membrane[162,168,169,174,256]. The tips of microvilli initiate the interaction between the two apposed cells leading to the formation of CCs which measure ~400-500 nm in diameter[137,162,163,165,168]. Concomitantly with CC formation, small molecule complexes (~14 nm) such as TCR/pMHC and CD2/CD58 accumulate within these sites. Recruitment of ZAP70 to CCs was consistently seen across SLB systems indicating CCs to be the site of TCR phosphorylation, but to date, this observation has not been reproduced at cellular interfaces[137,168]. While large-scale CD45 exclusion at synapses of late-stage T cell/target cell conjugates can be readily observed, it is unclear whether CD45 is excluded from the CCs before TCR triggering[204,207,270]. Studies using model surfaces point towards robust CD45 exclusion from CCs[86,137,194,256,369,370] but they are contradicted by imaging of *bona fide* T cell/APC conjugates[168].

There are several shortcomings in the two state-of-the-art studies that led to the current understanding of the role of microvilli and CCs in antigen recognition. Cai et al. imaged pre-formed T cell/APC conjugates, which precluded the analysis of the dynamics of the initial interactions[168]. Furthermore, rather than detecting the CCs directly, putative contact sites were identified by tracking T-cell microvilli at the cellular interface, based on the assumption that each microvillus engages the target cell. Jenkins et al. provided a more detailed examination of CC properties in an SLB system including their molecular composition and the role of CC dimensions in antigen discrimination. However, the physiological relevance of these findings remains to be determined in a cell/cell system[137]. Additionally, neither of these two studies used primary human T cells as the model T lymphocyte, instead relying on either murine T cells[168] or human T cell lines[137].

In the previous chapters, a primary $CD8^+$ T cell/U-2 OS cell system was established and successfully used to dissect the mechanism of ImmTAC-induced T-cell activation. In Chapter 4, through a series of molecular modifications, the N-MED ImmTAC was validated as an authentic TCR agonist. Here, these components will be used to visualise the events leading to TCR triggering. Jenkins et al. demonstrated that CD58 can act as an effective CC marker and thus the U-2 OS cell lines expressing the Halo-tagged CD58 will be adopted as model target cells. These cell lines will be further modified to provide additional adhesion in the form of ICAM-1. Moreover, the inclusion of ICAM-1 will allow a direct comparison of the imaging data generated in this chapter to the published data sets wherein the ICAM-1-presenting surrogate surfaces and APCs were used. Since the activation markers used in the previous chapters are not suitable for imaging experiments, calcium flux and ZAP70 recruitment will be employed as early signalling markers.

In contrast to the now standard use of TIRFM for imaging of T cells in SLB systems, there is no microscopy technique dedicated to the visualisation of live cell/cell interactions. Three complementary microscopy techniques will be employed, each suitable for a distinct aspect of the specimen: i) epi-illumination selective plane illumination microscopy (eSPIM), ii) epifluorescence widefield

microscopy (eWM), and iii) spinning disk confocal microscopy (SDCM). First, the dynamics of the T cell/U-2 OS cell interaction will be characterised from the formation of the first CC to the early-stage synapse. Next, the molecular composition of CCs will be examined to establish whether cellular CCs are the site of TCR triggering and to assess the involvement of CD45 segregation in that process.

5.2 Results

5.2.1 Generation of ZAP70-HaloTag primary CD8$^+$ T cells

The pipeline for production of unmodified primary CD8$^+$ T cells was described in section 3.2.3 and these T cells will continue to be used for most of the imaging experiments in this chapter. Additionally, primary CD8$^+$ T cells expressing a ZAP70-HaloTag fusion protein were generated to enable the identification of CCs containing phosphorylated TCR/CD3 complexes, hereafter referred to as 'signalling' CCs (Figure 5.1). To this end, freshly isolated PBMCs were first stimulated with magnetic beads coated with anti-CD3ϵ and anti-CD28 antibodies and then lentivirally transduced with the ZAP70-HaloTag construct (Figure 5.1A). Following, the initial burst of expansion, CD8$^+$ T cells expressing ZAP70-HaloTag were isolated by FACS and then expanded using irradiated feeder cells. Two consecutive 14-day expansion cycles were necessary to yield a sufficient number of CD8$^+$ T cells for the imaging experiments. T cells expressing ZAP70-HaloTag constituted ~94% of the final T-cell population as assessed by flow cytometry (Figure 5.1B).

5.2.2 Morphology of the primary CD8$^+$ T-cell surface

Given the direct morphological relationship between CCs and microvilli, primary CD8$^+$ T cells were imaged using SEM to permit a direct comparison of the two structures. The T cell surface was densely covered with microvilli (Figure 5.2A) and the transverse sections of the microvilli positioned along the xy plane were used for measurements (Figure 5.2B). The diameter of microvilli was on average

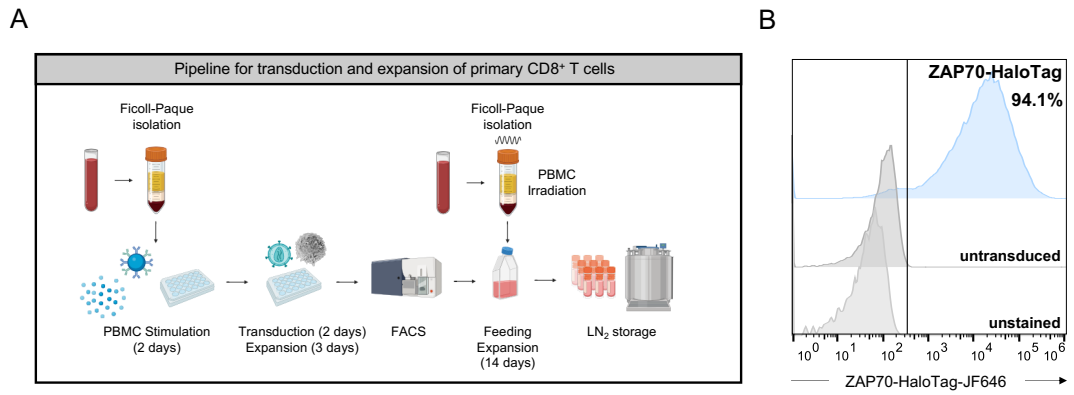


Figure 5.1: Preparation of ZAP70-HaloTag primary CD8$^+$ T cells. A. Schematic of the pipeline for production of ZAP70-HaloTag primary CD8$^+$ T cells. PBMCs were isolated from human blood using the Ficoll-Paque method and stimulated using beads coated with anti-CD3 and anti-CD28 antibodies at a 1:3 ratio. Following a 2-day stimulation, the proliferating cells were plated on retronectin-coated wells pre-incubated with ZAP70-HaloTag-containing lentivirus and further expanded. To purify the primary CD8$^+$ T cells expressing ZAP70-HaloTag, cells were stained with PB-conjugated anti-CD8α antibody and HaloTag ligand JF646, and isolated using FACS. Next, the ZAP70 primary CD8$^+$ T cells were cultured with irradiated feeder cells supplemented with anti-CD3ϵ OKT3 antibody and PHA. The purity of the final T-cell population was assessed by flow cytometry. T cells were transferred to LN_2 for long-term storage. **B**. Flow cytometry plot of ZAP70-HaloTag and untransduced primary CD8$^+$ T cells stained HaloTag ligand JF646 and unstained ZAP70-HaloTag primary CD8$^+$ T cells. The gate used to quantify the purity of ZAP70-HaloTag CD8$^+$ T cells is shown.

81 nm and ranged from 54 nm to 113 nm (Figure 5.2C). The measurements correspond to the full-width at half maximum of the intensity profile at the transverse section of the microvillus. Assuming that microvilli have a circular cross-section, the diameter of the individual microvilli was then converted into a cross-sectional area yielding an average of ~5300 nm^2 (Figure 5.2D).

5.2.3 Proximal signalling of CD8$^+$ T cells in response to the N-MED ImmTAC

In the previous chapters, the state of T-cell activation was assessed via the upregulation of cell surface markers, CD25 and CD69. However, these markers are not suitable for imaging experiments due to the mismatch between the time scales of their expression and antigen recognition. One of the earliest T-cell activation markers compatible with imaging experiments is the release of calcium

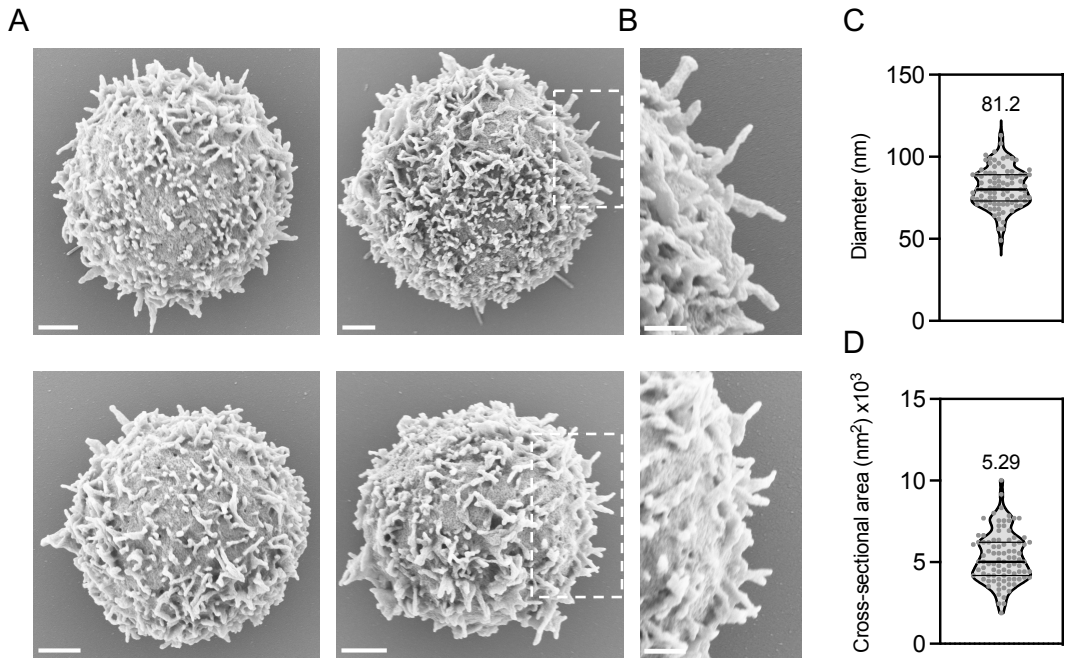


Figure 5.2: Scanning electron microscopy of primary CD8$^+$ T cells. A. Representative SEM images of CD8$^+$ T cell blasts. Scale bar = 1 µm **B**. Close-up view of the boxed regions in (B) showing the details of the microvilli positioned along the xy plane. Scale bar = 0.5 µm **C**. Measurements of T cell microvilli were obtained by measuring the transverse section of the projection. Measurements for 92 microvilli across 10 T cells. **D**. Cross-sectional area of microvilli calculated using the measurements in (C) assuming sphericity.

ions from the ER into the cytoplasm. The cytoplasmic calcium levels can be measured using an intracellular calcium sensor Fluo-4 AM[371] which increases fluorescence upon chelation of calcium ions. Fluo-4 AM can be used to monitor the activation state of large T-cell populations providing a global readout of the T-cell response and individual T cells during single-cell imaging experiments.

To assess whether calcium flux is a suitable marker to measure the responses of primary CD8$^+$ T cells to ImmTACs, an assay based on confocal microscopy was devised to monitor calcium release. In short, monolayers composed of WT U-2 OS cells pulsed with a 10-fold serial dilution of hGP100 peptide were labelled with 10 nM N-MED ImmTAC. T cells stained with Fluo4-AM were allowed to settle on the top of the U-2 OS cell monolayer and imaged for 20 min. An automated pipeline was used to track the movement of each T cell along the monolayer and track their calcium signal. The following metrics were recorded: i)

the proportion of T cells fluxing calcium (Figure 5.3A), ii) the time from landing on the U-2 OS cell monolayer to the first calcium pulse (Figure 5.3B), and iii) the size of the calcium pulse (Figure 5.3C). In the absence of the TCR ligand, background calcium flux was observed for ~16% of T cells (Figure 5.3A). These ligand-independent calcium pulses had a lower magnitude (4.4 vs. 5.8 AU) and occurred later (325 vs. 455 s) than those in the presence of high ImmTAC densities on the U-2 OS cell surface (Figure 5.3B and C). Ligand-specific responses could be measured from peptide concentration of ~0.1 nM and the response reached a plateau at 0.1-1 μM with ~45% of T cells fluxing calcium. The EC_{50} value for this response was ~0.78 nM of hGP100. Based on these results, the ImmTAC density achieved by pulsing of U-2 OS cells with 10 μM hGP100 followed by labelling with 10 nM N-MED ImmTAC was selected for further imaging experiments (Figure 5.3D). The rationale was twofold: i) saturating responses (~45% T cells fluxing calcium) increase the probability of observing genuine triggering in response to the TCR ligand rather than a nonspecific triggering event, ii) increased kinetics of the response (~6 min to calcium flux) ensure that more activation events can be observed within the time scale of the imaging experiment (15-20 min).

5.2.4 Generation and characterisation of U-2 OS cell lines for imaging of T cell/target cell interactions

For imaging of the interactions between T cells and U-2 OS cells, an array of U-2 OS cell lines was prepared. Since the accumulation of CD58 was to be used as a marker of CCs, the CD58LO U-2 OS cell line was repurposed (section 4.2.1) to serve as the base imaging cell line (Figure 5.4A). The CD58LO U-2 OS cells expressed CD58-HaloTag at levels matched to those of endogenous CD58 in WT U-2 OS cells and T-cell responses to ImmTACs in the context of these two cell lines were near-identical (section 4.2.1). Another U-2 OS cell line expressing CD58-HaloTag to be used in this chapter was the CD58HI cell line (section 4.2.1). As previously demonstrated, T cells co-cultured with the CD58HI U-2 OS cells were more sensitive to ImmTACs and activated in the absence of the ligand.

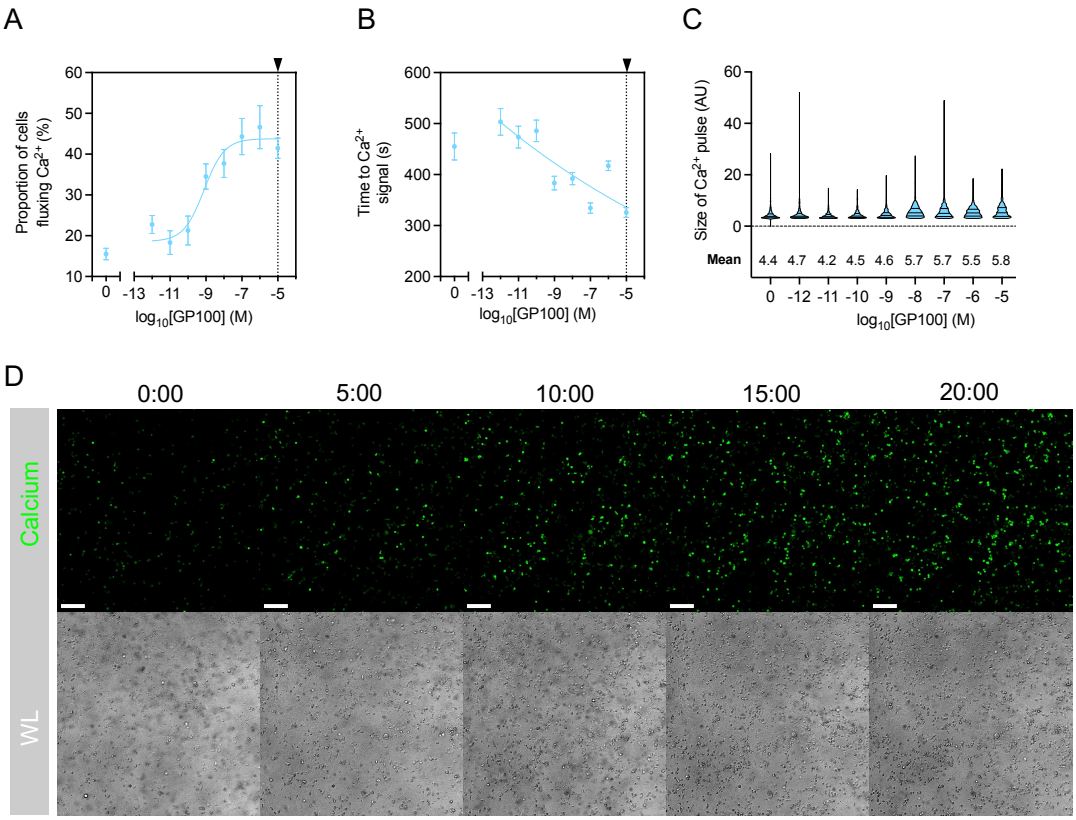


Figure 5.3: Calcium release assays of primary CD8$^+$ T cell responses to the N-MED ImmTAC. Calcium response of primary CD8$^+$ T cell to N-MED ImmTAC represented as **A**. proportion of T cells fluxing calcium **B**. time from landing on the U-2 OS monolayer to first calcium signal. The black arrowheads in (A) and (B) indicate the selected imaging conditions **C**. size of the calcium spike **D**. Confocal fluorescence image series (top) and widefield white light image series (bottom) showing primary CD8$^+$ T cells fluxing calcium on a monolayer of U-2 OS cells pulsed with 10 µM GP100 labelled with 10 nM N-MED ImmTAC i.e. the selected imaging conditions. Scale bar = 100 µm.

Thus, the interactions of T cells with CD58HI U-2 OS cells were to be imaged to provide a molecular basis for these observations.

CD58LO U-2 OS cells were modified to generate an additional surface for the imaging experiments. ICAM-1 is frequently upregulated by melanoma cells and is abundantly expressed on the surface of mature DCs[372–375]. Additionally, the binding of ICAM-1 to LFA-1 on the T-cell surface increases antigen sensitivity and is required for the formation of a mature immune synapse[134,137,202,203,376]. While ICAM-1 had been the primary adhesion molecule in T cell/SLB systems, more recent studies began incorporating CD58 or its homologues[86,137,258]. Furthermore,

given the thick layer of glycocalyx on the surface of U-2 OS cells (section 3.2.2) and the antagonistic relationship between glycocalyx and adhesion, it was hypothesised that ICAM-1 might be necessary to observe productive engagement of U-2 OS by T-cells[137]. CD58LO U-2 OS cells were lentivirally transduced with an ICAM-1 construct lacking the cytoplasmic domain. The truncated ICAM-1 construct was used to eliminate the mechanical feedback from the target cell which could compromise the planar topology of the U-2 OS cell monolayers and in effect hinder imaging of the cellular interactions (Figure 5.4B)[377]. Hereafter, this U-2 OS cell line will be referred to as CD58LO+ICAM-1. In total three different U-2 OS cell lines were to be used for imaging of T cells: CD58LO, CD58LO+ICAM-1 and CD58HI.

The expression levels of both CD58 and ICAM-1 in all three cell lines were measured using flow cytometry and converted to copy numbers and densities (Figure 5.4E and F). CD58LO U-2 OS cells had a minimal adhesion system with CD58-HaloTag expressed at a density of 6.7 molecules/μm^2. The CD58-HaloTag expression in CD58HI U-2 OS cells was ~330-fold greater with 2200 molecules/μm^2. Finally, CD58LO+ICAM-1 U-2 OS cells expressed CD58-HaloTag at the same density as the parental U-2 OS cell line, CD58LO, and ICAM-1 at ~3000 molecules/μm^2. Thus, the combined densities of the two adhesion molecules in CD58LO+ICAM-1 U-2 OS cells and the density of CD58 in the CD58HI cell line are very similar, but the adhesion system of the CD58LO+ICAM-1 U-2 OS cell line is dominated by ICAM-1 while that of CD58HI U-2 OS cells is dominated by CD58.

As reported in Chapter 3, WT U-2 OS cells express low levels of endogenous HLA-A2 (2.7 HLA-A2/μm^2) setting the upper limit on the attainable density of the N-MED ImmTAC/GP100-MHC 'ligand unit'. In contrast, the GP100-SCT is highly expressed in U-2 OS cells reaching ~1000 GP100-SCT/μm^2. Data from T cell/SLB systems suggest that a high density of TCR ligand (>10 cognate pMHC/μm^2) may be necessary to observe some events accompanying antigen recognition, for example, TCR/CD3 complex accumulation and ZAP70

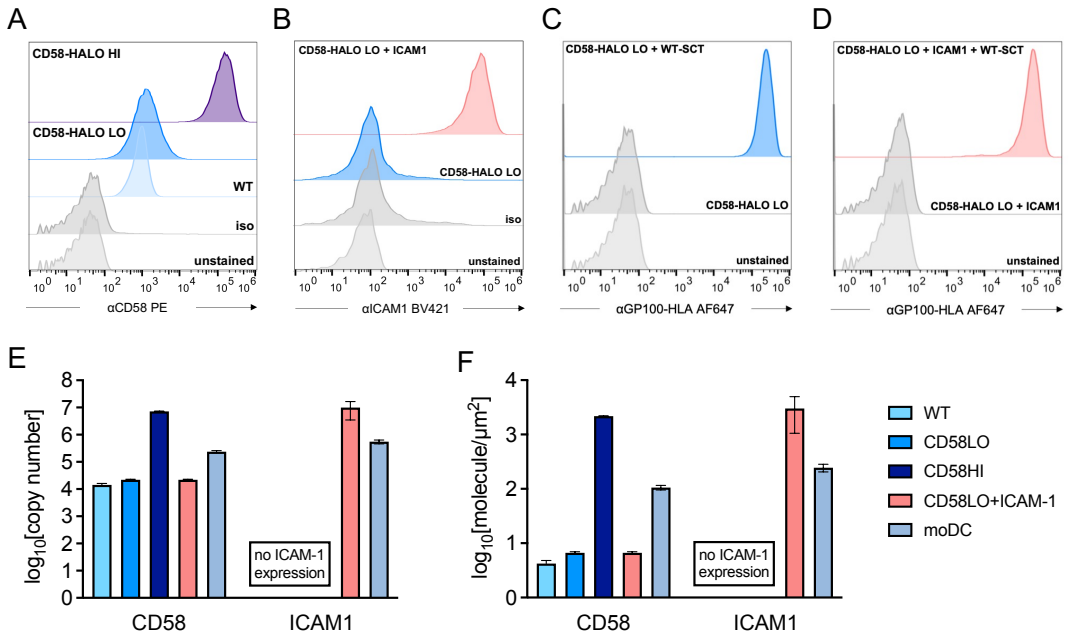


Figure 5.4: Generation of U-2 OS cell lines for imaging of their interactions with primary CD8$^+$ T cells. **A**. Expression levels of CD58 on the surface of WT, CD58LO, and CD58HI U-2 OS cell surface stained with a PE-conjugated anti-CD58 antibody **B**. Expression levels of ICAM-1 on the surface of CD58LO and CD58LO+ICAM-1 U-2 OS cell surface stained with a BV421-conjugated anti-ICAM-1 antibody **C**. Expression levels of WT GP100-SCT on the surface of CD58LO and CD58LO+GP100-SCT U-2 OS cell surface stained with AF647-conjugated N-MED ImmTAC **D**. Expression levels of WT GP100-SCT on the surface of CD58LO+ICAM-1 and CD58LO+ICAM-1+GP100-SCT U-2 OS cell surface stained with AF647-conjugated N-MED ImmTAC **E**. Expression of CD58 and ICAM-1 adhesion molecules on the surface of U-2 OS cell lines and moDCs as copy numbers **F**. As in (E), but the expression levels are shown as 2D densities. The density values were calculated using the estimated U-2 OS cell and moDC surface area values and the respective copy numbers

recruitment to the CCs[137,168,194–196]. To enable imaging at high antigen densities, the GP100-SCT construct was lentivirally transduced into both CD58LO and CD58LO+ICAM-1 U-2 OS cell lines yielding CD58LO+GP100-SCT and CD58LO+ICAM-1+GP100-SCT cell lines (Figure 5.4C and D).

The functional effects of replacing the endogenous CD58 with CD58-HaloTag in CD58LO and CD58HI U-2 OS cell lines were characterised in the previous chapter (sections 4.2.1 and 4.2.2). The effect of ICAM-1 expression in U-2 OS cells on T-cell activation had not been examined. To this end, co-culture assays of T cells with both CD58LO and CD58LO+ICAM-1 U-2OS cells were

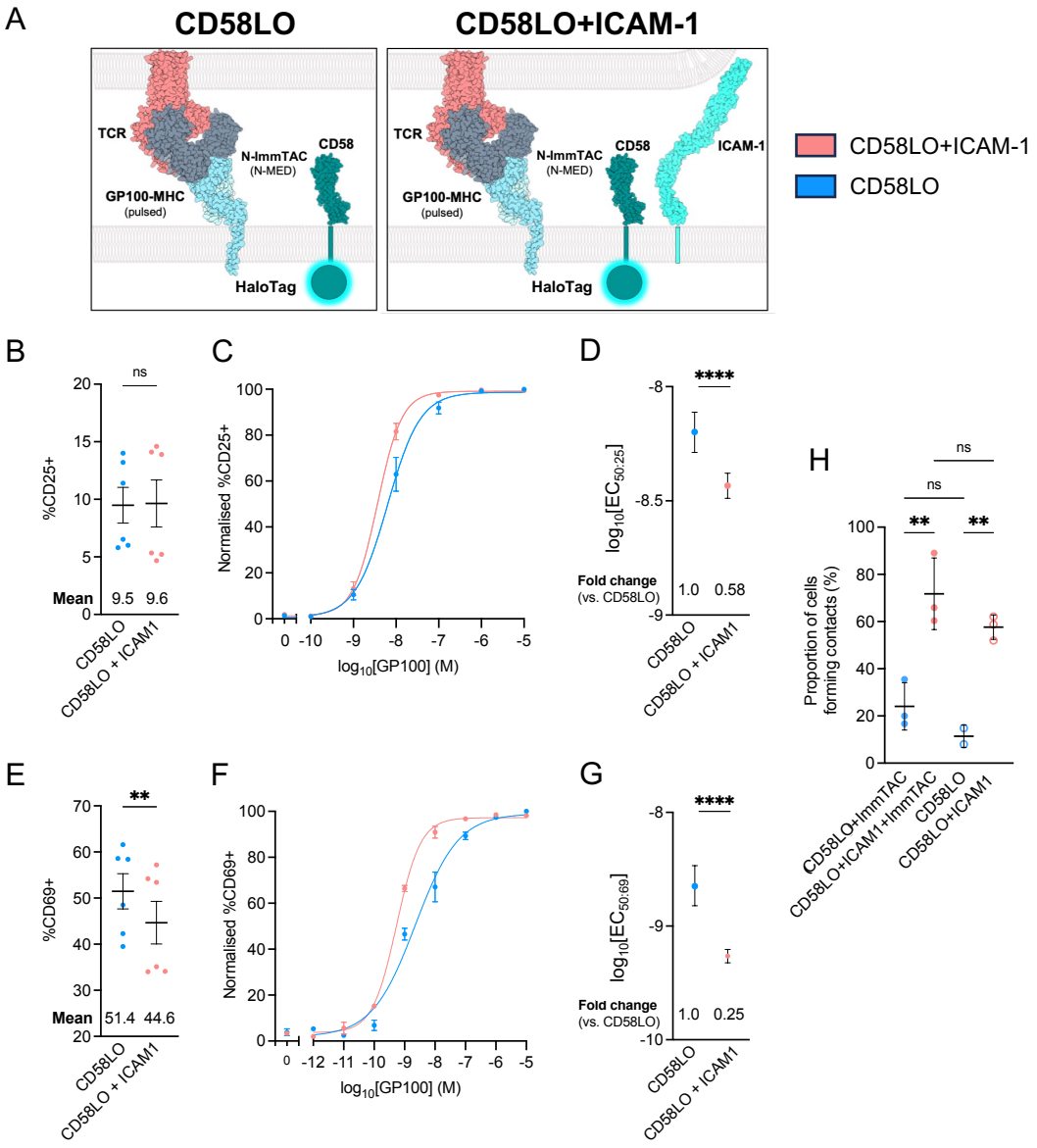


Figure 5.5: (Following page)

performed. The B_{CD25} values were identical for co-culture assays of T cells with the two U-2 OS cell lines (Figure 5.5B and E), but the B_{CD69} was 13.2% lower in the presence of ICAM-1. The $EC_{50:CD25}$ and $EC_{50:CD69}$ values were reduced by twofold and fourfold for T cells co-cultured with the ICAM-1-expressing cell line, respectively (Figure 5.5D and G).

Figure 5.5: Co-culture assays of primary CD8$^+$ T cell with CD58LO and CD58LO+ICAM-1 U-2 OS cell lines. **A**. Schematic of CD58LO and CD58LO+ICAM-1 U-2 OS cell surface showing TCR/CD3 complex and GP100-MHC molecule engaged by the N-MED ImmTAC. Both CD58LO and CD58LO+ICAM-1 U-2 OS cells express Halo-tagged CD58. Additionally, the latter cell line expressed ICAM-1 lacking the cytoplasmic domain. Images are not to scale. **B**. CD25 upregulation by T cells following co-culture with the CD58LO and CD58LO+ICAM-1 U-2 OS cell lines in the absence of ImmTAC. **C**. Dose-response curves showing T-cell activation by upregulation of CD25 in response to the N-MED ImmTAC following 18h of co-culture with CD58LO and CD58LO+ICAM-1 U-2 OS cell lines **D**. $EC_{50:25}$ values extracted from unconstrained four-parameter variable slope Hill model fitted into the dose-response curves from (C). **E**. CD69 upregulation by T cells following co-culture with the CD58LO and CD58LO+ICAM-1 U-2 OS cell lines in the absence of ImmTAC. **F**. Dose-response curves showing T-cell activation by upregulation of CD69 in response to the N-MED ImmTAC following 18h of co-culture with CD58LO and CD58LO+ICAM-1 U-2 OS cell lines **G**. $EC_{50:69}$ values extracted from unconstrained four-parameter variable slope Hill model fitted into the dose-response curves from (C). **H**. Proportion of T cells interacting with U-2 OS cells following a 10 min incubation with CD58LO or CD58LO+ICAM-1 U-2 OS cell lines. The interactions were measured as the appearance of CD58 accumulation at the T cell/U-2 OS cell interface in the eSPIM images (Figure 5.6-5.9). All assays were performed as two biological repeats in triplicates. The data was collected using T cells isolated from at least two donors. Mean values with error bars corresponding to SEM (all, but D and G) or 95% CI (D and G) are shown. The background %CD25$^+$ and %CD69$^+$ values were compared using a paired t-test. EC_{50} values were compared using an F-test of normalised data. The proportions of T cells interacting with U-2 OS cells were compared using a one-way ANOVA. Only statistical comparisons of interest are shown. *P-value $\leq$ 0.05, **P-value $\leq$ 0.01, ***P-value $\leq$ 0.001, ****P-value $\leq$ 0.0001

5.2.5 ICAM-1 alters the dynamics of the T cell/U-2 OS cell interaction

The following strategy was devised to visualise the interaction of T cells with the CD58LO and CD58LO+ICAM-1 U-2 OS cells. U-2 OS cells were plated, pulsed with hGP100 peptide and allowed to form monolayers for 18h. Next, the U-2 OS cell monolayers were incubated with a cell-permeant JF549 HaloTag ligand to generate a covalent CD58-HaloTag-JF549 adduct and then labelled with the N-MED ImmTAC. T cells were labelled using a SiR-conjugated Gap8.3 antibody binding to a common epitope of CD45. Because CD45 is highly expressed and is uniformly distributed on the surface of resting T cells, the antibody-labelled CD45 can effectively serve as a proxy for the plasma membrane[162,168,169]. The

first set of imaging experiments aimed to characterise the topography and the dynamic behaviour of CCs at the T cell/U-2 OS cell interface, rather than assess CD45 exclusion therein, and hence CD45 was initially only considered as a membrane stain.

To characterise the interactions of T cells with CD58LO and CD58LO+ICAM-1 U-2 OS cell, a custom-built epi-illumination selective plane illumination microscopy (eSPIM) instrument permitting volumetric imaging of large fields of view (135x83x24 μm) was used. eSPIM illuminates successive sections of the sample using a Gaussian light-sheet, which improves optical sectioning by limiting the excitation light to the focal plane. Additionally, eSPIM simultaneously captures a multi-channel image permitting fast data acquisition. First, the interactions of T cells with CD58LO and CD58LO+ICAM-1 U-2 OS cells in the presence of the TCR ligand were examined. Before the addition of T cells, CD58-HaloTag was uniformly distributed on the surface of the two U-2 OS cell lines and no spontaneous accumulation of CD58-HaloTag was observed. However, there was some heterogeneity in the CD58-HaloTag surface expression level across the individual U-2 OS cells. T cells labelled with the SiR-conjugated anti-CD45 antibody were delivered to an area where the U-2 OS cells formed a contiguous monolayer, using a micropipette. As soon as the T cells appeared above the monolayer, image acquisition was initiated. T cells appeared to 'glide' along the monolayer of CD58LO U-2 OS cells whereas in the presence of ICAM-1, T cells became immobilised shortly after landing on the U-2 OS cells. Puncta of CD58 accumulation appeared at the interface of T cells with both CD58LO or CD58LO+ICAM-1 U-2 OS cells, albeit in the presence of ICAM-1, the CD58 puncta, likely corresponding to single CCs, evolved more rapidly and emerged at a greater proportion of T cell/U-2 OS cell interfaces (Figures 5.6 and 5.7). After 10 min of interaction, 24.1% and 71.7% of T cells had visible accumulations of CD58 at the interface with CD58LO and CD58LO+ICAM-1 U-2 OS cells, respectively (Figure 5.5H). In the absence of ICAM-1, the putative CCs were spatially restricted and less mobile. Additionally, some of the T cells interacted

transiently with CD58LO U-2 OS cells forming a single CD58 punctum for ~2 min (Figure 5.6, pink arrowheads). Contrastingly, the CD58 accumulation area at the interface between T cells and the CD58LO+ICAM-1 U-2 OS cells rapidly expanded and at later time points (~5 min) the individual CD58 puncta appeared to coalesce into a single patch of CD58 accumulation (Figure 5.7, pink area). The latter observation might have been due to the technical limitations of the instrument rather than a result of the underlying biology – if imaged using a microscope affording better spatial resolution, these patch-like areas might be resolved as closely-spaced puncta.

It was previously established that CCs form in the absence of TCR ligands, and so if the puncta of CD58 accumulation were *bona fide* CCs, they should be observed in the absence of ImmTAC on the U-2 OS cell surface[86,137,258,365]. To test this, the imaging experiments were repeated with no ImmTAC present on the U-2 OS cell surface. CD58 accumulated at the interface of T cells with both U-2 OS cell lines in a ligand-independent manner validating CD58 as a CC marker (Figures 5.8 and 5.9). The differences in the number of T cells interacting with the CD58LO versus CD58LO+ICAM-1 U-2 OS cells persisted, with CD58 accumulation detectable at 11.4% and 57.6% of the cellular interfaces after the 10 min incubation, respectively (Figure 5.5H).

5.2.6 Primary $CD8^+$ T cells form discrete contacts at the interface with target cells

While the puncta of CD58 accumulation, *bona fide* CCs, observed using the eSPIM instrument resembled those described by Jenkins et al.[137], a closer visual inspection indicated that an instrument fitted with optics affording higher sensitivity and resolution might be better suited to capture the earliest CCs and to permit their detailed characterisation. Thus, the imaging experiments were repeated using a custom-built epifluorescence widefield microscope (eWM) with a higher NA objective (eWM NA = 1.49 versus eSPIM NA = 1.27) and a simpler light path affording single-molecule sensitivity. To acquire the volume containing T

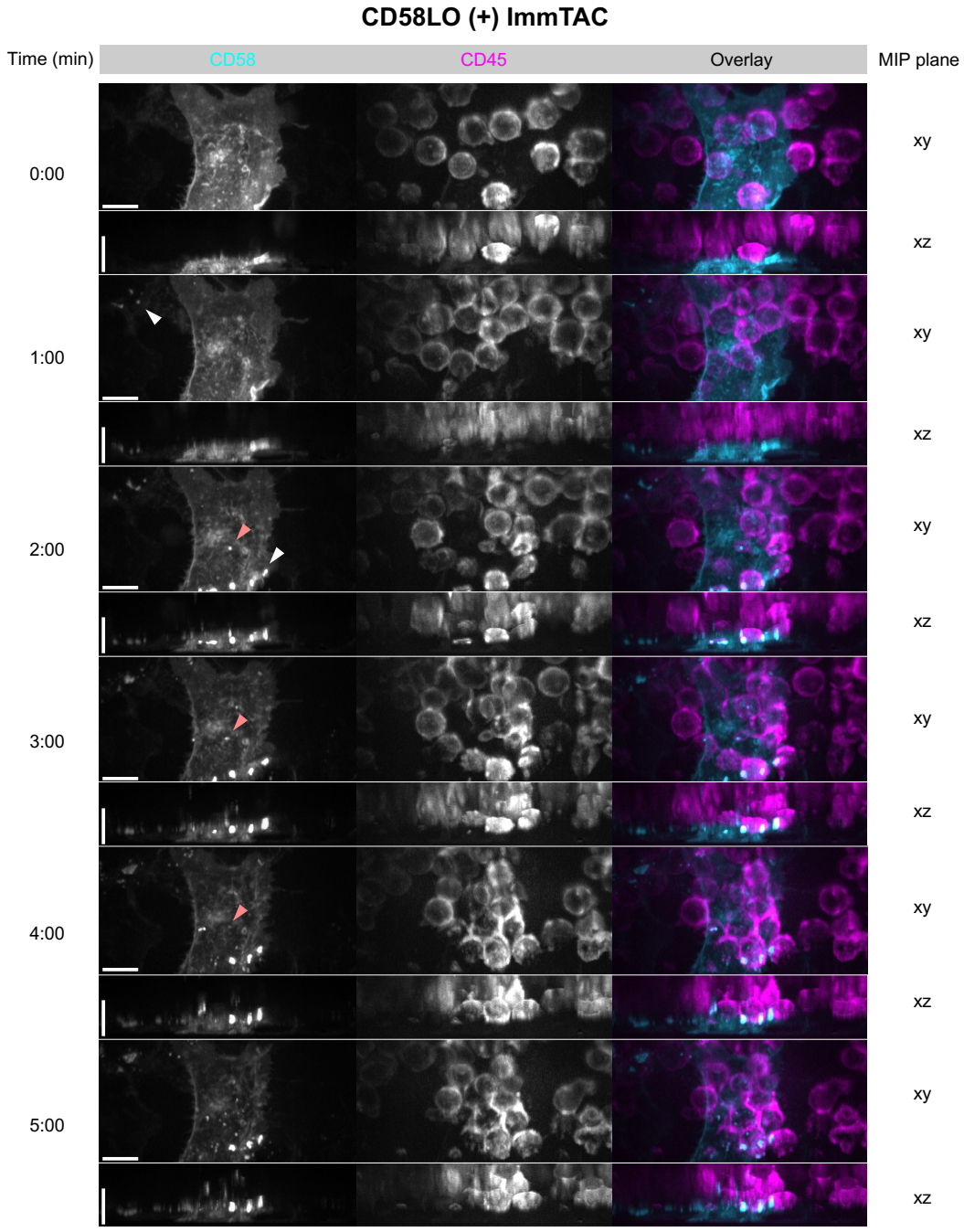


Figure 5.6: eSPIM imaging of interaction between primary CD8$^+$ T cells and CD58LO ImmTAC-labelled U-2 OS cells. eSPIM imaging of interactions of primary CD8$^+$ T cells with a monolayer of CD58LO U-2 OS cells. T cells were stained with a SiR-conjugated anti-CD45 antibody. hGP100-pulsed U-2 OS cells were labelled with the N-MED ImmTAC and JF549 HaloTag ligand to yield CD58-HaloTag-JF549. MIPs of the xy and yz planes are shown. The white arrowheads indicate the first detectable CD58-demarcated CCs. The pink arrowheads indicate a transient CD58-demarcated CC. Scale bar = 10 µm.

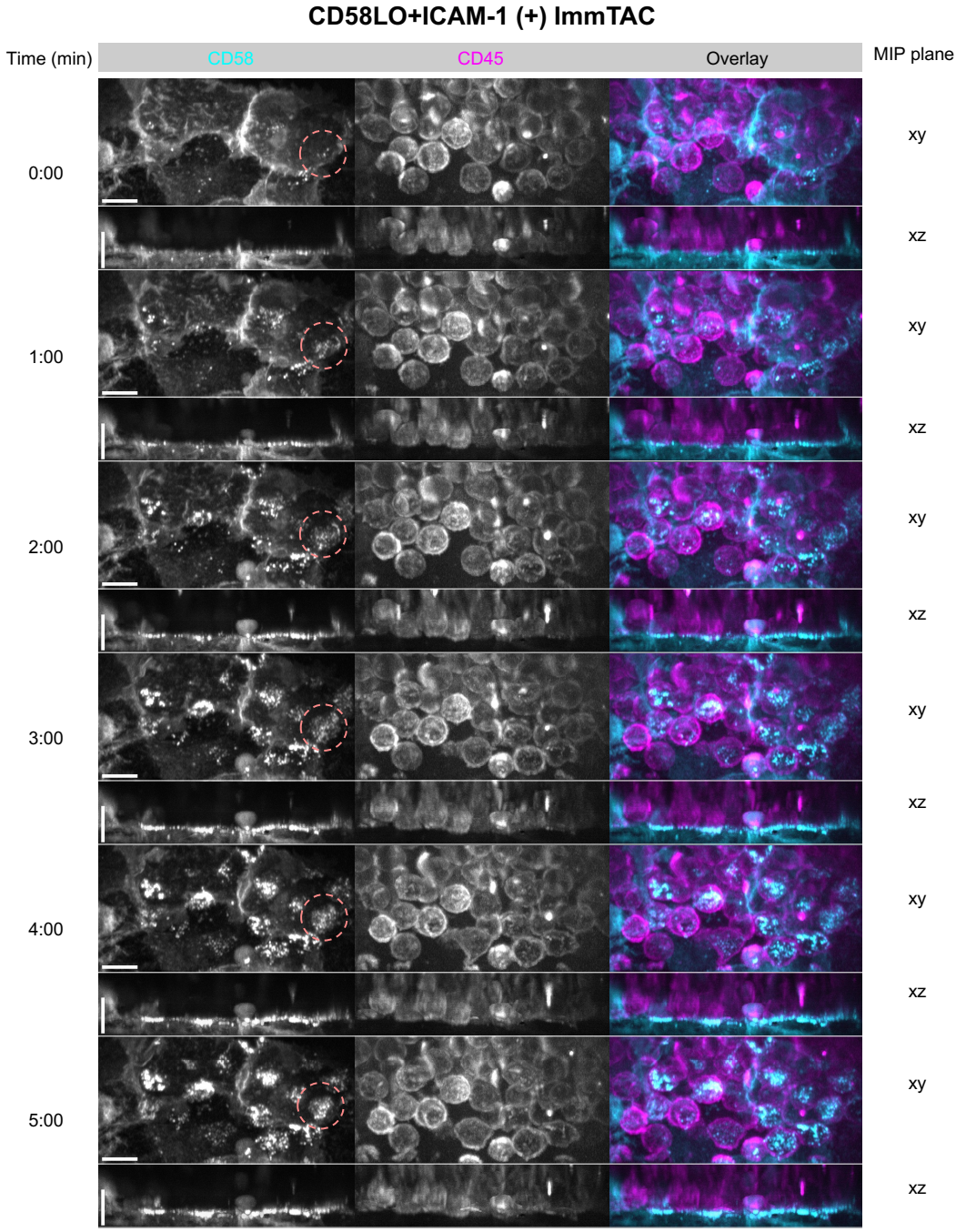


Figure 5.7: eSPIM imaging of interaction between primary CD8$^+$ T cells and CD58LO+ICAM-1 ImmTAC-labelled U-2 OS cells. eSPIM imaging of interactions of primary CD8$^+$ T cells with a monolayer of CD58LO+ICAM-1 U-2 OS cells. T cells were stained with a SiR-conjugated anti-CD45 antibody. hGP100-pulsed U-2 OS cells were labelled with the N-MED ImmTAC and JF549 HaloTag ligand to yield CD58-HaloTag-JF549. MIPs of the xy and yz planes are shown. The pink circle indicates a T cell with progressively increasing and then decreasing interaction footprint. Scale bar = 10 µm.

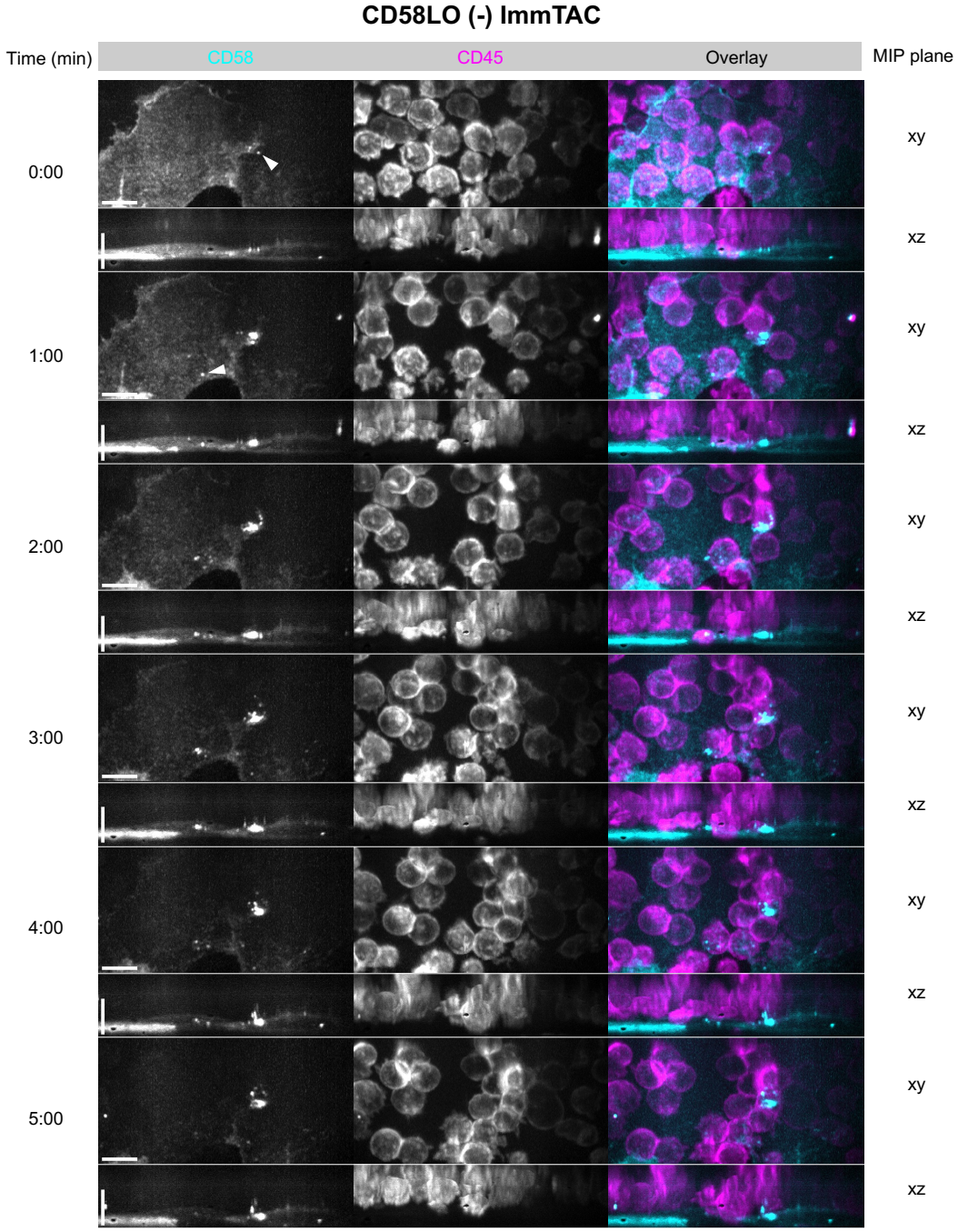


Figure 5.8: eSPIM imaging of interaction between primary CD8$^+$ T cells and CD58LO U-2 OS cells in the absence of TCR ligand. eSPIM imaging of interactions of primary CD8$^+$ T cells with a monolayer of CD58LO U-2 OS cells. T cells were stained with a SiR-conjugated anti-CD45 antibody. U-2 OS cells were labelled with JF549 HaloTag ligand to yield CD58-HaloTag-JF549. MIPs of the xy and yz planes are shown. The white arrowheads indicate the first detectable CD58-demarcated CCs. Scale bar = 10 µm.

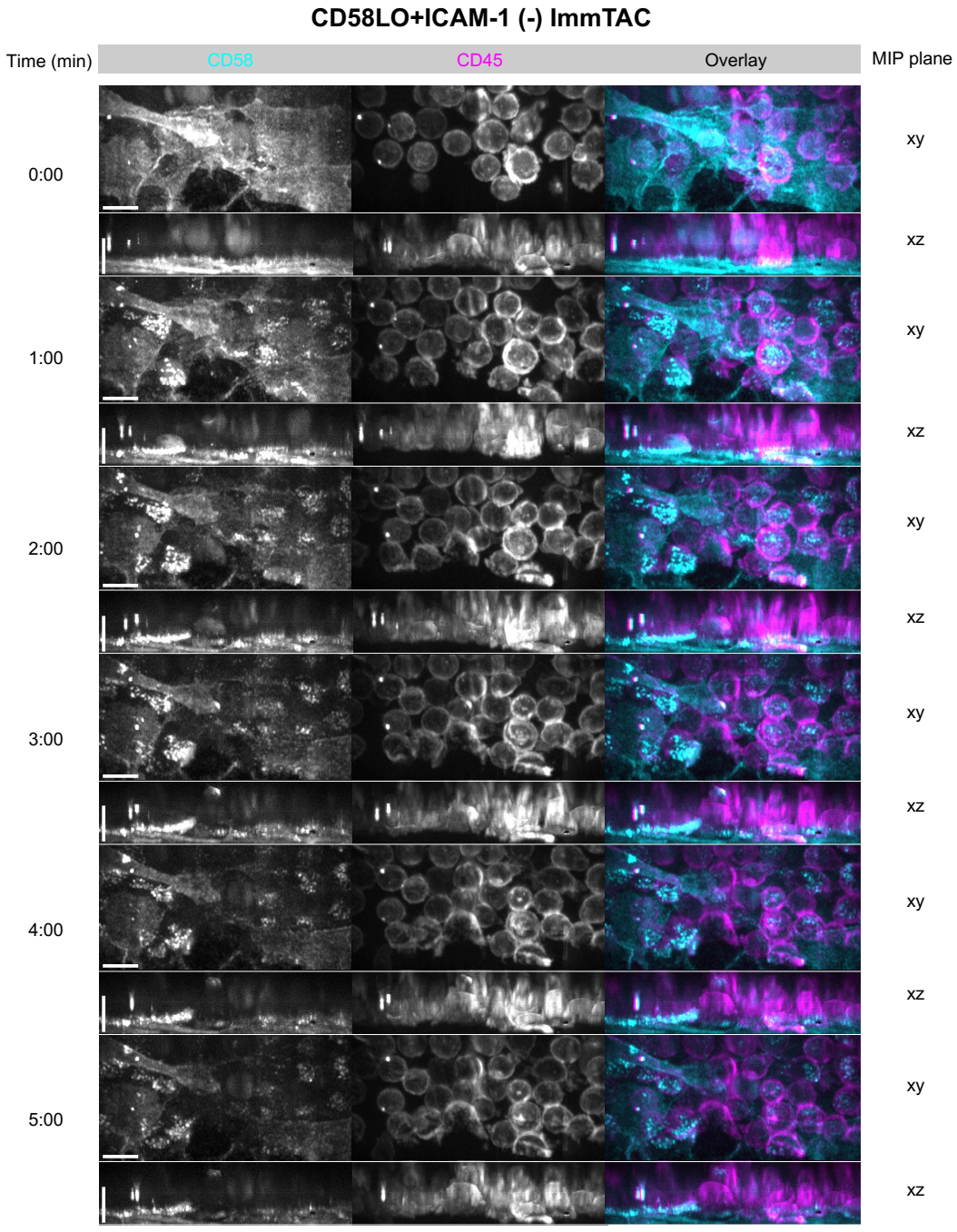


Figure 5.9: eSPIM imaging of interaction between primary CD8$^+$ T cells and CD58LO+ICAM-1 U-2 OS cells in the absence of TCR ligand. eSPIM imaging of interactions of primary CD8$^+$ T cells with a monolayer of CD58LO+ICAM-1 U-2 OS cells. T cells were stained with a SiR-conjugated anti-CD45 antibody. U-2 OS cells were labelled with JF549 HaloTag ligand to yield CD58-HaloTag-JF549. MIPs of the xy and yz planes are shown. Scale bar = 10 µm.

cell/U-2 OS cell interface, eSPIM instrument scans the specimen using an oblique light-sheet and does so simultaneously for two channels. In contrast the eWM needs to acquire the volume as a focal stack, individually for each of the channels, which compromises the temporal resolution. This necessitated a reduction of the acquired volume to achieve a sufficiently high temporal resolution to monitor the dynamics of CCs formation. Ultimately, a volume of 54x54x4 μm extending upwards from the apical membrane of U-2 OS cells was acquired. The eWM images were then analysed using an automated analysis pipeline to quantify the topography of the interaction and dynamics of the CCs (the analysis was conducted by Daniel Heraghty using analysis code written by Markus Koerbel)

First, T cells were imaged on U-2 OS cells presenting the TCR ligand on their surface. Consistent with the eSPIM data, the proportion of interacting T cells, the number of CCs which they formed as well as the kinetics of interactions were enhanced by the presence of ICAM-1 (Figure 5.10 and Figure 5.11). First, the size of the early CCs (<1 min of detectable interaction) was measured as the full width at half maximum of the intensity profile of the CD58-HaloTag fluorescence signal. At the interface of T cells with either CD58LO and CD58LO+ICAM-1 U-2 OS cells, the CCs were ~500 nm in diameter placing them close to the theoretical lateral resolution limit (191 nm for JF549; Figure 5.11B and C). Similar CC dimensions were calculated using an automated analysis indicating the average CC areas to be 0.180 μm^2 and 0.260 μm^2 which, assuming sphericity of the CCs, are equivalent to diameters of 470 nm and 560 nm for the CD58LO+ICAM-1 and CD58LO U-2 OS cell, respectively (Figure 5.12A and B). The average area of a single CC in the presence of ICAM-1 was largely invariant throughout the interaction but it fluctuated for the T cells interacting with the CD58LO U-2 OS cells (Figure 5.12C). In the absence of ICAM-1, the formation of CCs appeared to be spatially restricted to a single area of the T cell/U-2 OS cell interface and appeared to coalesce in some instances (Figure 5.10A, pink arrowheads). With ICAM-1 on the U-2 OS cell surface, the CCs were generally well-separated

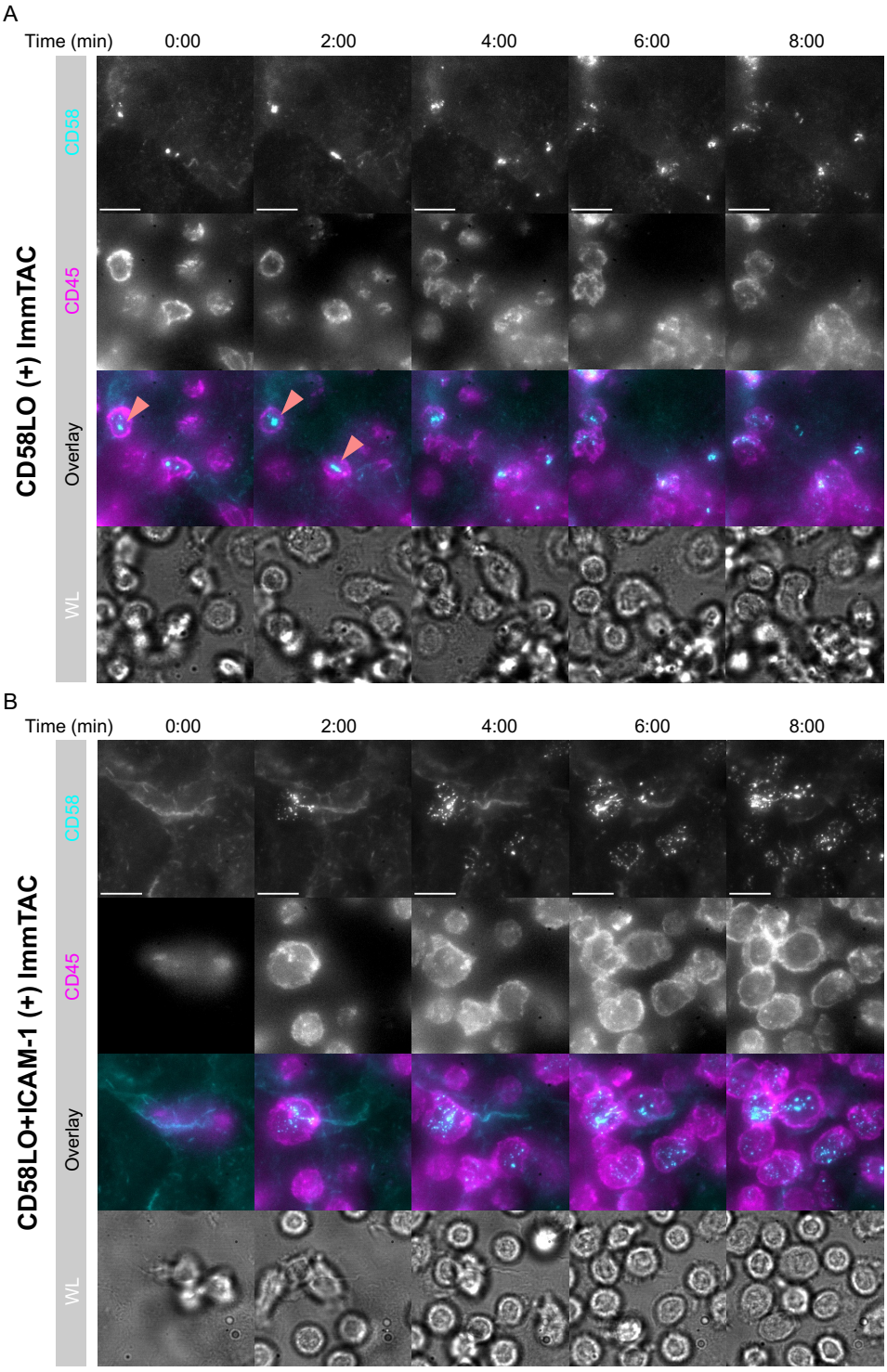


Figure 5.10: eWM imaging of interaction between primary CD8$^+$ T cells and ImmTAC-labelled CD58LO or CD58LO+ICAM-1 U-2 OS cells. A. and **B**. eWM imaging of interactions of primary CD8$^+$ T cells with a monolayer of CD58LO (A) or CD58LO+ICAM-1 (B) U-2 OS cells. T cell were stained with a SiR-conjugated anti-CD45 antibody. hGP100-pulsed U-2 OS cells were labelled with the N-MED ImmTAC and JF549 HaloTag ligand to yield CD58-HaloTag-JF549. The pink arrowheads indicate spatially-confined CCs. For all of the fluorescence images MIPs of the focal stack are shown. Scale bar = 10 µm.

and formed across a larger area, albeit sporadically enlarged puncta of CD58 accumulation were also observed (Figures 5.10B and 5.11D).

Following the onset of the interaction between T cells and the CD58LO+ICAM-1 U-2 OS cells, the number of CCs rapidly increased up to ~28 CCs/cell and once the maximum was reached the number of CCs steadily declined (Figure 5.12D). In contrast, without ICAM-1, the number of CCs gradually increased up to ~10 CCs/cell at a reduced tempo and remained at that level for the remainder of the interaction (Figure 5.12D). The changes in the number of CCs correlated with the total area of CCs, which was consistent with the largely invariant dimensions of the individual CCs (Figure 5.12F).

To quantify the surface area of the T-cell membrane apposed against the target cell, the so-called T-cell footprint, convex hull area (CHA) of the CCs, was selected to act as its proxy. To calculate the CHA, the CCs were approximated as finite points and a polygon enclosing all of them was drawn with its vertices corresponding to outer CCs (Figure 5.12G). Critically, the internal angles of the polygon are all <180°. The changes in the CHA were concomitant with the spreading of T cells across the U-2 OS cell surface. The T-cell footprint increased within the first ~2.5 min up to ~55 μm^2 on average in the presence of ICAM-1, but in its absence, T cells did not display the spreading behaviour with the average CHA values remaining below ~20 μm^2 (Figure 5.12H). This was in line with the observation that the CCs at the interface between the T cell and CD58LO U-2 OS cells were restricted to a smaller area and had a reduced mobility. The maximum CHA values for the interaction with CD58LO and CD58LO+ICAM-1 U-2 OS cells were 28.4 and 72.2 μm^2 on average, respectively (Figure 5.12I). Next, the proportion of the T-cell footprint constituted by the CCs was quantified. While during the early stage of the interaction (<10 s for CD58LO and <90 s for ICAM-1+CD58LO) the CCs constituted over ~50% of the CHA, after the initial increase in the number of the CCs, this value settled at 15-20% (Figure 5.12J).

To quantify the sampling capacity of the microvillar CCs, the cumulative area of the U-2 OS cell surface covered by the CCs was calculated. On both of the U-2

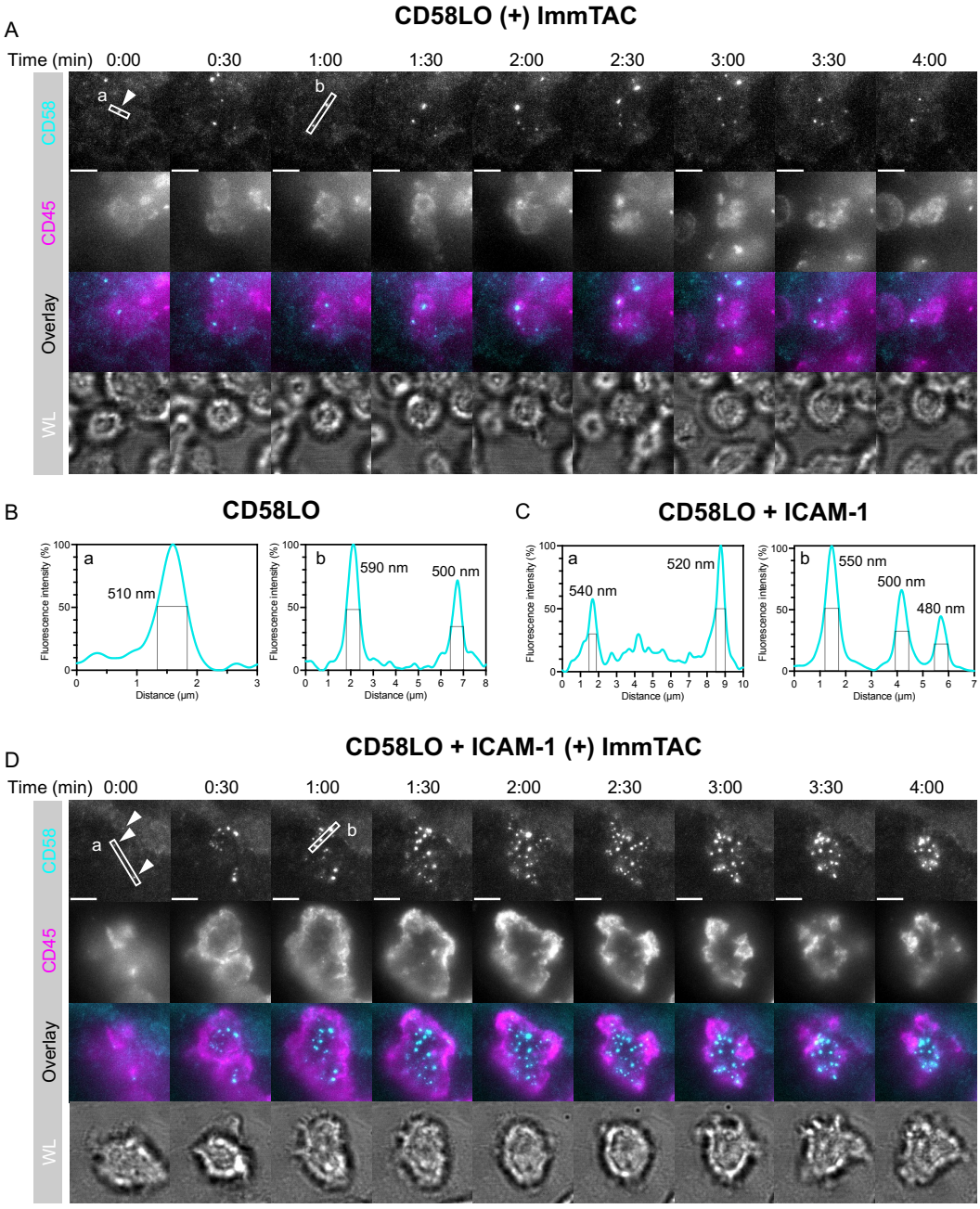


Figure 5.11: eWM imaging of interaction between a single primary CD8$^+$ T cells and ImmTAC-labelled CD58LO or CD58LO+ICAM-1 U-2 OS cells. **A** and **D**. eWM imaging of interactions of primary CD8$^+$ T cells with a monolayer of CD58LO (A) and CD58LO+ICAM-1 (D) U-2 OS cells. T cell were stained with a SiR-conjugated anti-CD45 antibody. hGP100-pulsed U-2 OS cells were labelled with the N-MED ImmTAC and JF549 HaloTag ligand to yield CD58-HaloTag-JF549. The white arrowheads indicate the first detectable CD58-demarcated CCs. **B** and **C**. The min/max normalised intensity line profiles taken across the CCs enclosed by the white rectangles in the image panels (A) and (D), respectively. Measurements correspond to full width at half maximum. For all of the fluorescence images MIPs of the focal stack are shown. Scale bar = 5 µm.

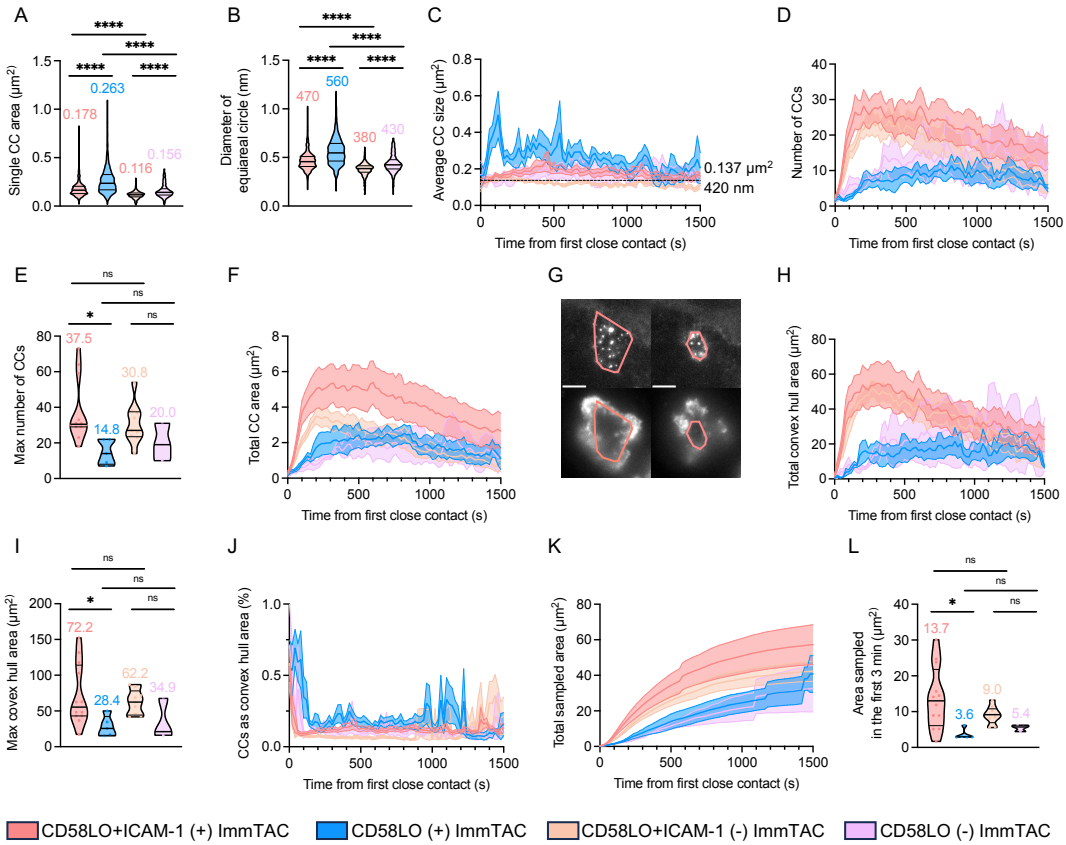


Figure 5.12: Analysis of the topography and the dynamics of close contacts at the interface of T cells and U-2 OS cells. A. Area of a single CC formed between primary $CD8^+$ T cells and U-2 OS cells. Mean values are shown. **B**. Diameter of CCs formed between primary $CD8^+$ T cells and U-2 OS cells. The diameter of the equiareal circle was calculated using the CC area values in (A). Mean values are shown. **C**. Average area of single CCs formed between primary $CD8^+$ T cells and U-2 OS cells across time. The horizontal line corresponds to the average size of a single CC at t = 0 for the four experimental conditions **D**. Number of CCs formed at the interface of primary $CD8^+$ T cells and U-2 OS cells across time. **E**. Maximum number of CCs formed at the interface of primary $CD8^+$ T cells and U-2 OS cells. **F**. Total area of CCs formed at the interface of primary $CD8^+$ T cells and U-2 OS cells across time. **G**. Schematic showing the relationship between the CC distribution and the convex hull area. Scale bar = 5 µm. **H**. Convex hull area for primary $CD8^+$ T cells interacting with U-2 OS cells across time. **I**. Maximum convex hull area for primary $CD8^+$ T cells interacting with U-2 OS cells. **J**. Total CC area as a proportion of the convex hull area for primary $CD8^+$ T cells interacting with U-2 OS cells across time. **K**. Cumulative total area sampled by CCs of primary $CD8^+$ T cells interacting with U-2 OS cells across time. **L**. Total area sampled by CCs of primary $CD8^+$ T cells interacting with U-2 OS cells in 3 minutes. For all line graphs, the error envelopes correspond to the SEM. The average values presented on violin plots were compared using a Kruskal–Wallis test with Dunn's correction. n = 12 (CD58LO+ICAM-1 (+) ImmTAC), 5 (CD58LO (+) ImmTAC), 9 (CD58LO+ICAM-1 (-) ImmTAC), 3 (CD58LO (-) ImmTAC). *P-value $\leq$ 0.05, **P-value $\leq$ 0.01, ***P-value $\leq$ 0.001, ****P-value $\leq$ 0.0001. The analysis was performed by Daniel Heraghty and the analysis code was written by Markus Koerbel.

OS cell surfaces the total sampled area steadily increased, but did so at a higher rate in the presence of ICAM-1 (Figure 5.12K). Previously, it was estimated that the time required for microvilli to scan ~98% of the T-cell footprint in the presence of a cognate antigen is ~3 min[168]. Here, the total area sampled by the CCs within 3 min was 13.7 μm^2 and 3.6 μm^2 for CD58LO+ICAM-1 and CD58LO U2OS cells, respectively (Figure 5.12K); these values corresponded to 27.7% and 26.7% of the respective T-cell footprints at the 3 min time point. To further contextualise these values, only ~0.4% and ~0.1% of the total U-2 OS cell surface was scanned by the CCs in the presence and absence of ICAM-1 in that time, respectively.

Interestingly, T cells interacting with CD58LO+ICAM-1 U-2 OS cells appeared to display two different types of behaviour as indicated by the bimodal distribution of the following three parameters: maximum number of CCs, maximum CHA and the area sampled in 3 minutes (Figure 5.12E, I, L). This implies that two T-cell subsets are present in the polyclonal T-cell population differently benefiting from the additional adhesion provided by the LFA-1/ICAM-1 pair. Notably, the distribution of the CC dimensions for this group of T cells remained unimodal suggesting that the architecture of microvilli, presumed structural basis for CCs, is conserved (Figure 5.12A and B).

5.2.7 A single close contact is sufficient for T-cell activation

To relate the dynamics of T cell/target cell interactions with the time of TCR triggering, the labelling regimen was modified to include a calcium indicator, Fluo-4 AM. Upon TCR triggering, the primary calcium pulse occurs due to the influx of calcium ions from the ER through IP_3-gated channels and it is followed by a secondary influx of extracellular calcium ions through STIM-operated ORAI channels located in the plasma membrane[378]. Thus far, RPMI medium containing calcium ions have been used in the imaging experiments resulting in a prolonged calcium spike making it more challenging to establish the time of triggering (Figure 4.13A). To ensure that a single, distinctive spike of calcium flux occurs following

TCR phosphorylation, RPMI medium was replaced with PBS supplemented with 10 mM HEPES and 2 mM $MgSO_4$, the former supplement acting as a buffer and the latter permitting LFA-1 to adopt the extended conformation[379,380]. The interaction of T cells with U-2 OS cells appeared to be unperturbed by the transition to the PBS-based medium and, critically, the removal of extracellular calcium led to a sharper and shorter calcium pulse (Figure 5.14B). Both in the presence and absence of ICAM-1, the formation of single CCs before the calcium pulse could be observed, underscoring the role of CCs as sites of antigen recognition (Figure 5.13B and Figure 5.14A). For a proportion of T cells, multiple contacts were visible at the time of calcium signalling (data not shown). However, due to the poor temporal resolution of the eWM instrument (20 s frame interval), the timing of the calcium flux could not be precisely related to the dynamics of the CC formation, and so it is likely that for these T cells, only a few of the CCs had formed before the calcium flux. Overall, this suggested that the densities of the TCR ligands used in the imaging experiments thus far resulted in a near-immediate engagement of the TCR/CD3 complex by ImmTAC following CC formation. Therefore, under such conditions, the so-called 'scanning' stage whereby the T-cell microvilli probe the target cell surface for the TCR ligand was short-lived[137]. On that basis, the T cell/U-2 OS cell interactions described in the previous section likely correspond to a post-triggering but pre-synapse stage during which the TCR signalling is integrated with that of other non-catalytic tyrosine-phosphorylated receptors such as CD28 or PD-1 in the CCs[152,381].

5.2.8 Scanning behaviour of T cells in the absence of the TCR ligand

To capture the CCs during the genuine 'scanning' of the target cell surface by T-cell microvilli, the interface between T cells and U-2 OS cells was imaged without the TCR ligand (Figure 5.15 and Figure 5.16). The interactions of T cells with CD58LO U-2 OS cells appeared to be mostly unaffected by the absence of ImmTAC (Figure 5.15) – T cells formed a low number of CCs (<20), the T-cell

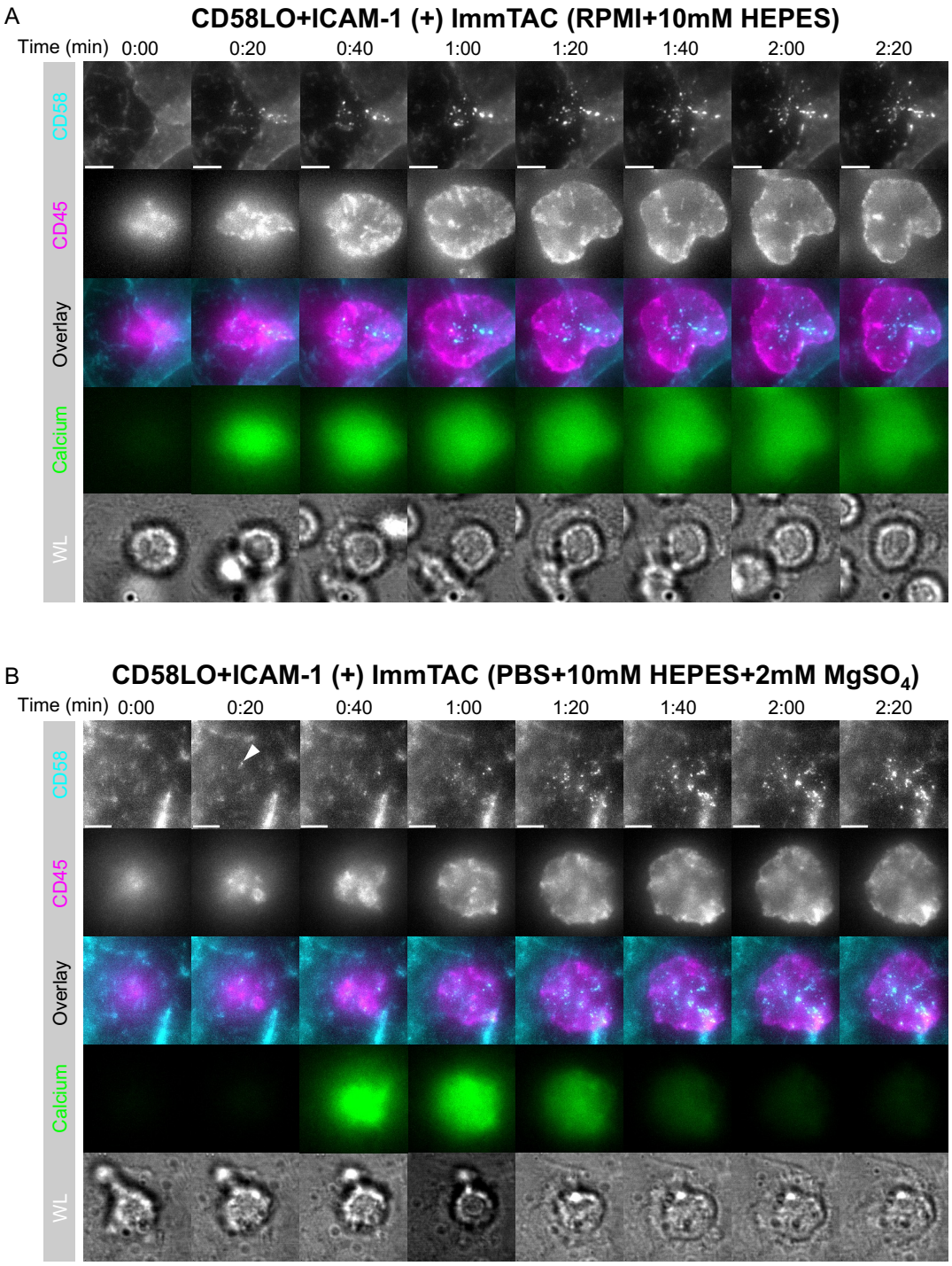


Figure 5.13: eWM imaging of calcium flux during interactions of single primary CD8$^+$ T cells and CD58LO+ICAM-1 U-2 OS cells. A and **B**. eWM imaging of a single primary CD8$^+$ T cell interacting with a monolayer CD58LO+ICAM-1 U-2 OS cells. T cell were stained with a SiR-conjugated anti-CD45 antibody and Fluo-4 AM. hGP100-pulsed U-2 OS cells were labelled with the N-MED ImmTAC and JF549 HaloTag ligand to yield CD58-HaloTag-JF549. Imaging media containing either RPMI 1640 media supplemented with 10 mM HEPES (A) or PBS supplemented with 10 mM HEPES and 2 mM $MgSO_4$ (B) were used. The white arrowhead indicates the first detectable CD58-demarcated CC. For the CD45 and CD58 fluorescence images MIPs of the focal stack are shown. Fluo-4 AM fluorescence was only imaged in the central plane of the focal stack. Scale bar = 5 µm.

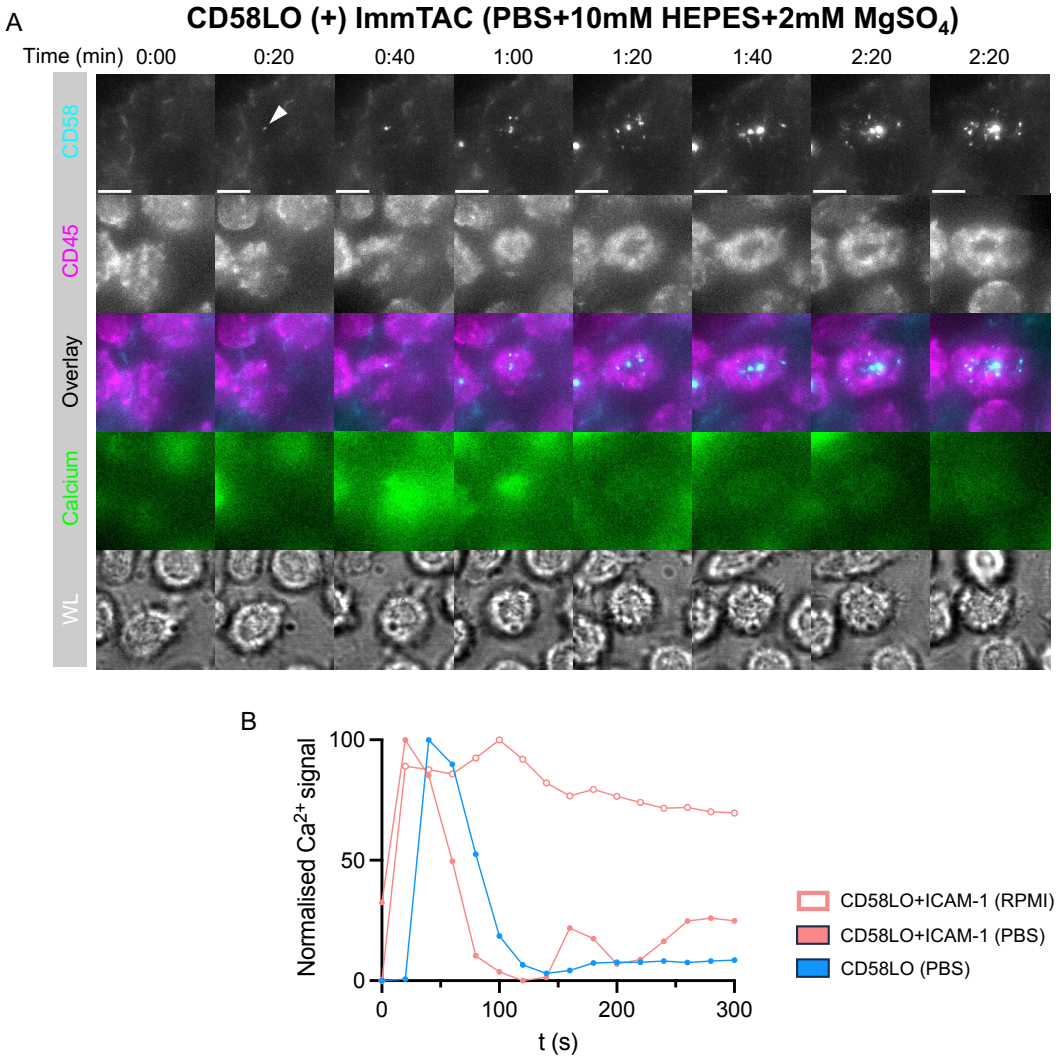


Figure 5.14: eWM imaging of calcium flux during interactions of single primary CD8$^+$ T cells and CD58LO U-2 OS cells. eWM imaging of a single primary CD8$^+$ T cell interacting with a monolayer of CD58LO U-2 OS cells. T cells were stained with a SiR-conjugated anti-CD45 antibody and Fluo-4 AM. hGP100-pulsed U-2 OS cells were labelled with the N-MED ImmTAC and JF549 HaloTag ligand to yield CD58-HaloTag-JF549. Imaging media containing PBS supplemented with 10 mM HEPES and 2 mM $MgSO_4$ were used. The white arrowhead indicates the first detectable CD58-demarcated CC. For the CD45 and CD58 fluorescence images MIPs of the focal stack are shown. Fluo-4 AM fluorescence was only imaged in the central plane of the focal stack. Scale bar = 5 µm. **B**. Calcium signal trace for primary CD8$^+$ T cells shown in (A) and Figure 5.15A and B.

footprint was limited and the sampling of the target cells surface remained slower than on ICAM-1-presenting U-2 OS cells (Figure 5.12D, H, K, L). However, upon removal of ImmTAC from the CD58LO U-2 OS cell surface, the area of the CCs was reduced from 0.263 μm^2 to 0.156 μm^2 and the CC diameter from 560 nm to 430 nm (Figure 5.12A and B). This is consistent with the appearance of the CCs which were more diffuse and transient in the absence of the TCR ligand (Figure 5.15). The difference between the CC sizes on CD58LO U-2 OS cell surface with or without ImmTAC was sustained throughout the interaction (Figure 5.12C).

Once again, the interactions of T cells with CD58+ICAM-1 U-2 OS cells without ImmTAC were more readily imaged. Upon landing on the monolayer of CD58LO+ICAM-1 U-2 OS cells, T cells rapidly formed numerous CCs (up to ~31 CCs; Figure 5.12D and E) and increased their footprint on the U-2 OS cells (up to ~62 μm^2; Figure 5.12H and I) closely mirroring their interactions with the same target cell but in the presence of ImmTAC, according to these two metrics. Without the TCR ligand, a single CC had an average area of 0.116 μm^2, which was equivalent to an equiareal circle with a diameter of 380 nm (Figure 5.12A-C). The smaller size of the CCs without the TCR ligand had a knock-on effect on the scanning capacity of T cells. Both the total CC area and the cumulative area sampled by the CCs were lower for T cells interacting with CD58LO+ICAM-1 U-2 OS cells without ImmTAC than with ImmTAC (Figure 5.12F and L).

The differences between the dynamics of T-cell behaviour on CD58LO versus CD58LO+ICAM-1 U-2 OS cells persisted in the absence of the TCR ligand. Expression of ICAM-1 on the U-2 OS cell surface increased the number of CCs, total CC area, T-cell footprint and the rate of target cell sampling (Figure 5.12D, F, H, K). As previously seen in the presence of ImmTAC, T cells formed slightly larger CCs at the interface with the CD58LO U-2 OS cells than with the CD58LO+ICAM-1 U-2 OS cells (Figure 5.12 A-C).

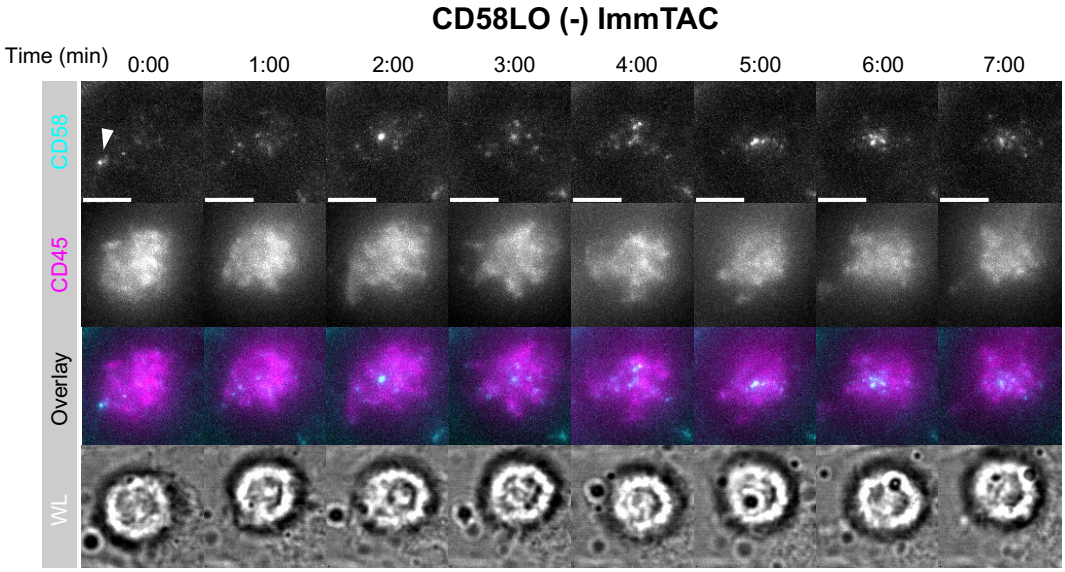


Figure 5.15: eWM imaging of interaction between primary CD8$^+$ T cells and CD58LO U-2 OS cells in the absence of TCR ligand. eWM imaging of interactions of primary CD8$^+$ T cells with a monolayer of CD58LO U-2 OS cells. T cells were stained with a SiR-conjugated anti-CD45 antibody. U-2 OS cells were labelled with JF549 HaloTag ligand to yield CD58-HaloTag-JF549. The white arrowhead indicates the first detectable CD58-demarcated CC. For all of the fluorescence images MIPs of the focal stack are shown. Scale bar = 5 µm.

5.2.9 Hallmarks of KS-based signalling within close contacts

Having characterised the topography and dynamics of the T cell/U-2 OS cell interaction, the molecular composition of CCs was subsequently examined. If the CCs were to be deemed the sites of TCR triggering as per the kinetic-segregation model, the following conditions should be met: i) TCR/CD3-pMHC complex should accumulate within the CCs ii) ZAP70 should be recruited to the phosphorylated TCR/CD3 complex within the CCs, and finally iii) CD45 should be excluded from the CCs.

To test the first condition, T cells were labelled with the SiR-conjugated anti-CD45 antibody and peptide-pulsed U-2 OS cells were labelled with JF549 HaloTag ligand and AF488-conjugated ImmTAC, the latter serving a dual role of the TCR and GP100-MHC label (Figure 5.17A and B). A preliminary experiment was performed using CD58LO+ICAM-1 U-2 OS cells to test whether

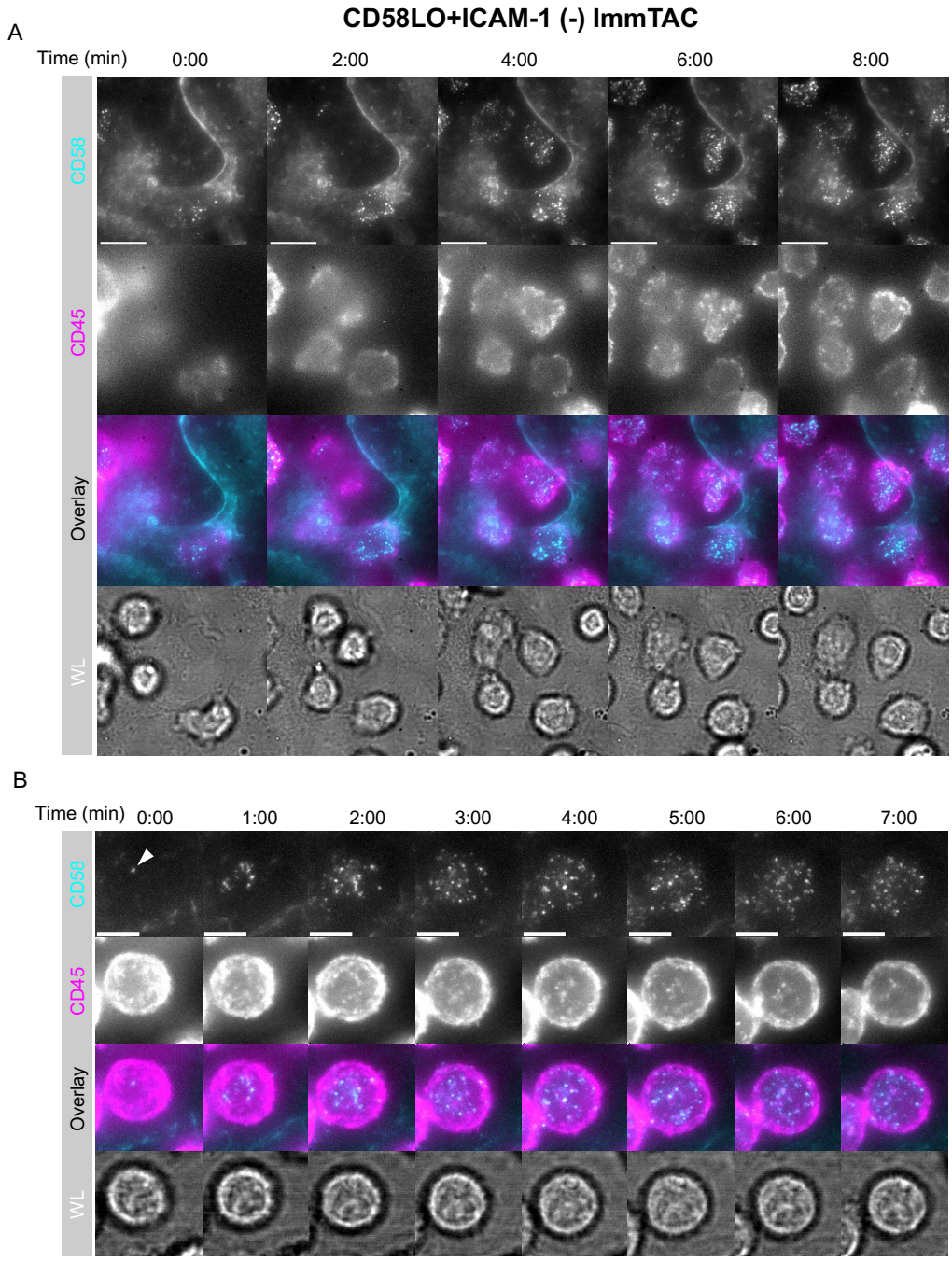


Figure 5.16: eWM imaging of interaction between primary CD8$^+$ T cells and CD58LO+ICAM-1 U-2 OS cells in the absence of TCR ligand. A and **B**. Multicellular overview (A) or single cell (B) imaging of interactions of primary CD8$^+$ T cells with a monolayer of CD58LO+ICAM-1 U-2 OS cells. T cells were stained with a SiR-conjugated anti-CD45 antibody. U-2 OS cells were labelled with JF549 HaloTag ligand to yield CD58-HaloTag-JF549. The white arrowhead indicates the first detectable CD58-demarcated CC. For all of the fluorescence images MIPs of the focal stack are shown. (A) Scale bar = 10 µm. (B) Scale bar = 5 µm.

the antigen density afforded by peptide-pulsing is sufficient to observe TCR accumulation. While a weak ImmTAC signal was visible on the U-2 OS cell surface, no accumulation of the ImmTAC-bound TCR could be observed within 8 min from the formation of the first CC (Figure 5.17C). Thus, it was hypothesised that higher antigen density might be necessary for this purpose. To this end, the CD58LO+GP100-SCT and CD58LO+ICAM-1+GP100-SCT U-2 OS cell lines were used. The higher density allowed weak accumulation of the ImmTAC to be observed within the CCs formed on the surface of the two U-2 OS cell lines (Figure 5.18). ImmTAC accumulation within the CCs was significantly slower than that of CD58 on both U-2 OS cell surfaces. Moreover, ImmTAC accumulation was not uniformly observed across the CCs and it was less persistent than CD58 accumulation.

Next, it was tested whether the downstream TCR signalling originates within the CCs using ZAP70-HaloTag as a marker of TCR/CD3 complex phosphorylation. Given the need for high antigen density to observe the accumulation of the TCR/CD3 complex within the CCs, it was likely that it would also be the case for ZAP70 recruitment. Thus CD58LO+ICAM-1+GP100-SCT U-2 OS cell line and the ZAP70-HaloTag primary $CD8^+$ T cells were used for this experiment. The following labelling regimen was devised. T cells were labelled with an AF488-conjugated anti-CD45 antibody and a JF646 HaloTag ligand reacting with the ZAP70 fusion protein and, as previously, CD58-HaloTag expressed by U-2 OS cells was labelled with JF549 HaloTag ligand. While ZAP70 appeared to be restricted to the cytoplasm at the time of the first CC formation, its recruitment to the first CC was visible 20 seconds later (single frame interval) (Figure 5.19). This is consistent with the earlier observation that a single CC is sufficient to induce a robust calcium response within 20 seconds (section 5.2.7). At later time points, the distribution of ZAP70 within CCs mimicked that of the TCR/CD3 complex – the intensity of the ZAP70-HaloTag signal was unevenly distributed across the CCs and it was undetectable at some of the CCs (Figure 5.19).

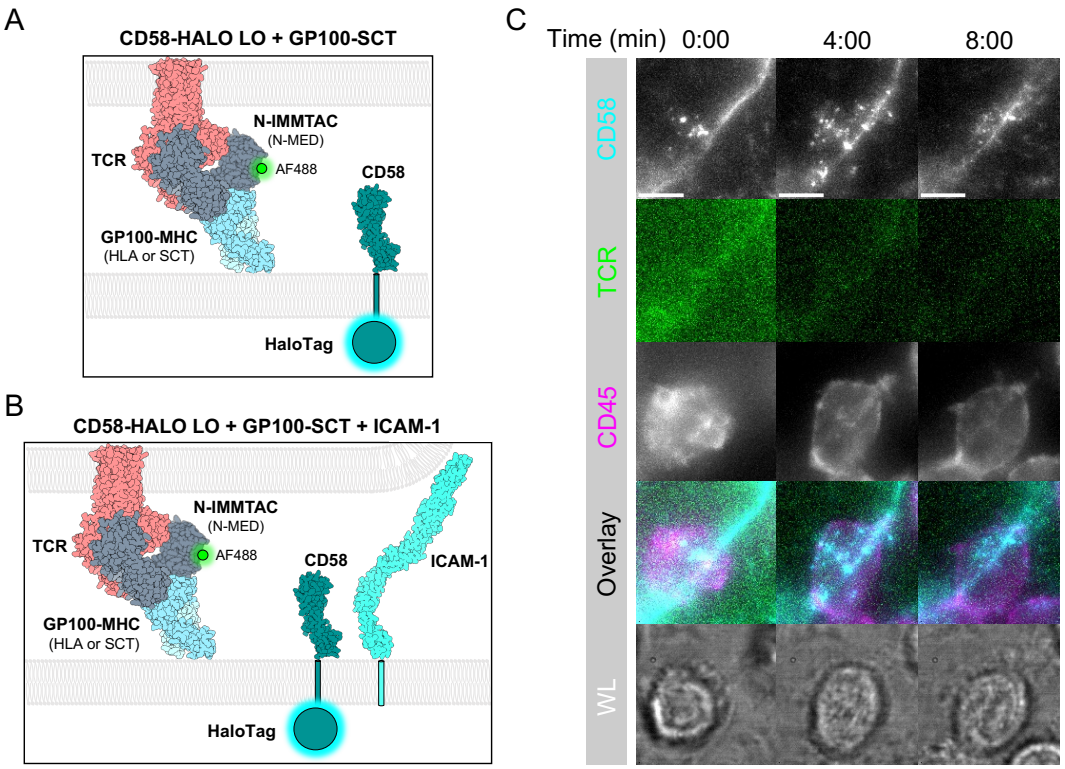


Figure 5.17: eWM imaging of the TCR ligand at the interface between a single primary CD8$^+$ T cell and hGP100-pulsed U-2 OS cells. A. Schematic showing the CD58LO+GP100-SCT U-2 OS cell line presenting the GP100-MHC antigen labelled with AF488-conjugated ImmTAC. **B**. Schematic showing the CD58LO+ICAM-1+GP100-SCT U-2 OS cell line presenting the GP100-MHC antigen labelled with AF488-conjugated ImmTAC. **C**. eWM imaging of a single primary CD8$^+$ T cell interacting with a monolayer of hGP100-pulsed CD58LO+ICAM-1 U-2 OS cells. T cells were stained with a SiR-conjugated anti-CD45 antibody. hGP100-pulsed U-2 OS cells were labelled with the AF488-conjugated N-MED ImmTAC and JF549 HaloTag ligand to yield CD58-HaloTag-JF549. For all of the fluorescence images MIPs of the focal stack are shown. Scale bar = 5 μm.

Next, the distribution of CD45 at CCs was investigated. The following labelling regimen was used for this experiment. CD58-HaloTag was labelled with JF549 HaloTag ligand whereas T cells were labelled with an AF488-conjugated anti-CD45 antibody and a plasma membrane dye, CellMask DeepRed. Staining of the plasma membrane was included to control for the topology of the T cell membrane at the CCs which might result in artifactual depletion of the CD45 signal. For instance, if the focal plane was located above the cellular interface traversing the microvilli, the cytoplasm within the microvilli surrounded by the CD45 signal could appear as *faux* CD45 exclusion. Thus, genuine CD45 exclusion

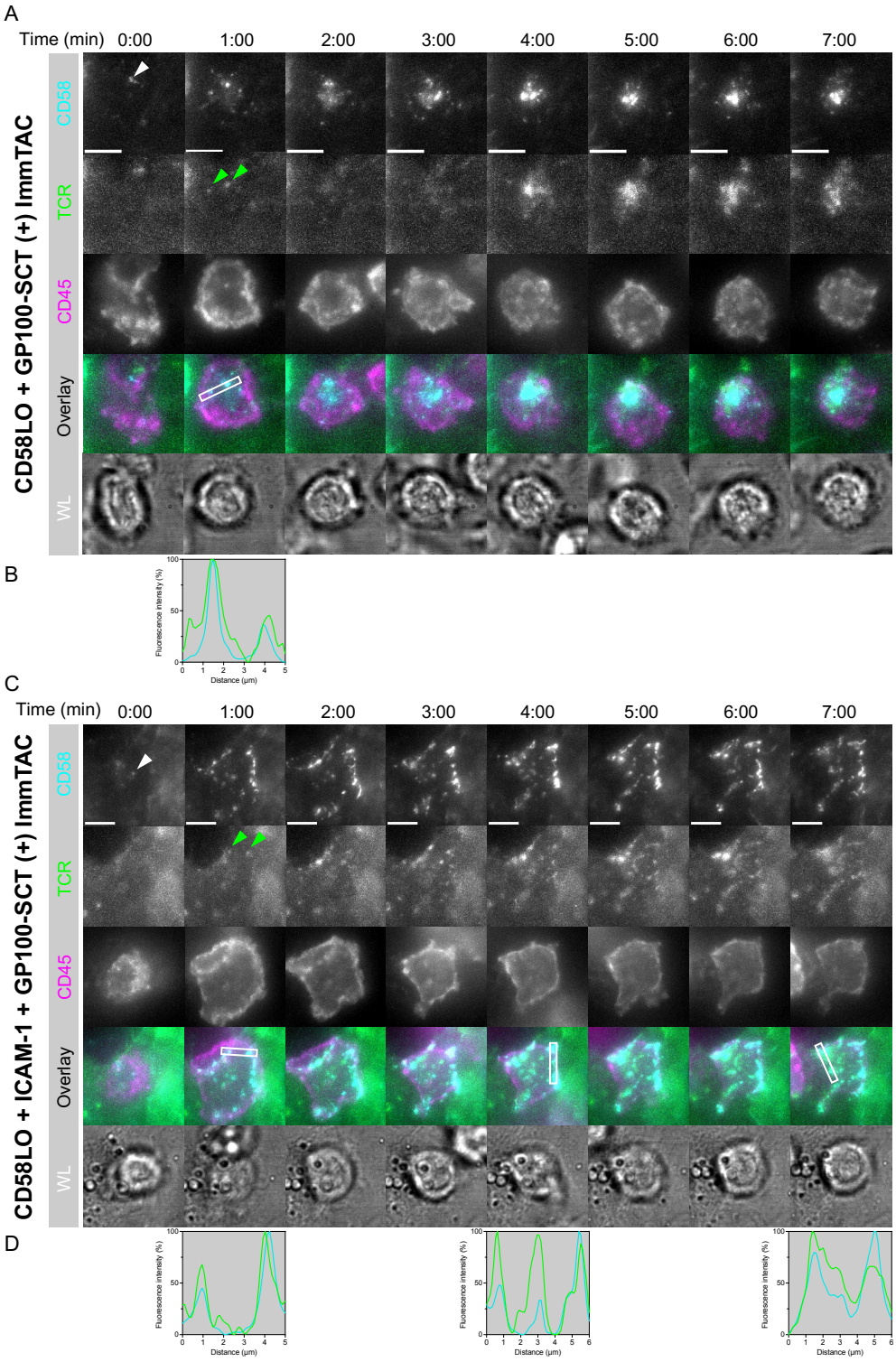


Figure 5.18: (Following page)

Figure 5.18: eWM imaging of the TCR ligand at the interface between a single primary CD8$^+$ T cell and GP100-SCT U-2 OS cells. A. eWM images of a single primary CD8$^+$ T cell interacting with a monolayer of CD58LO+GP100-SCT U-2 OS cells. T cells were stained with a SiR-conjugated anti-CD45 antibody. U-2 OS cells were labelled with the AF488-conjugated N-MED ImmTAC and JF549 HaloTag ligand to yield CD58-HaloTag-JF549. The white arrowhead indicates the first detectable CD58-demarcated CCs. The green arrowheads indicate the first detectable accumulation areas of TCR/CD3 complex in the CCs. **B**. The min/max normalised intensity line profile taken across the CCs enclosed by the white rectangle in the image panel (A). **C**. eWM images of a single primary CD8$^+$ T cell interacting with a monolayer of CD58LO+ICAM-1+GP100-SCT U-2 OS cells. T cell were stained with a SiR-conjugated anti-CD45 antibody. U-2 OS cells were labelled with the AF488-conjugated N-MED ImmTAC and JF549 HaloTag ligand to yield CD58-HaloTag-JF549. The white arrowhead indicates the first detectable CD58-demarcated CCs. The green arrowheads indicate the first detectable accumulation areas of TCR/CD3 complex in the CCs. **D**. The min/max normalised intensity line profiles taken across the CCs are enclosed by the white rectangles in the image panel (C). For all of the fluorescence images MIPs of the focal stack are shown. Scale bar = 5 μm.

at CCs should be accompanied by a flat membrane fluorescence signal.

Imaging of T cells interacting with CD58LO+ICAM-1 U-2 OS cells using the eWM instrument did not reveal appreciable CD45 exclusion at most CCs except larger contacts, perhaps corresponding to coalesced CCs (Figure 5.20; white arrowhead). This observation suggested that the inability to observe CD45 exclusion at the CCs could be due to the poor optical sectioning of the eWM instrument – the out-of-focus CD45 fluorescence signal from adjacent regions of the membrane could be obscuring genuine CD45 exclusion at the CCs. To verify this reasoning, the interactions of primary CD8$^+$ T cells with U-2 OS were imaged using an SDCM instrument fitted with two microlens arrays allowing improved optical sectioning and enhanced resolution.

The appearance and dimensions of CCs formed at the interface of T cells with CD58LO+ICAM-1 U-2 OS cells were identical to those seen in the eWM images (Figure 5.21A). The plasma membrane appeared to be uniformly distributed across the putative cellular interface as seen in both the maximal intensity projection (MIP) of the image stack and the plane containing the interface (Figure 5.21B and E, top panels). In contrast, the CD45 signal at the interface was irregular with the areas of reduced CD45 intensity correlating with the CD58-demarcated CCs. To

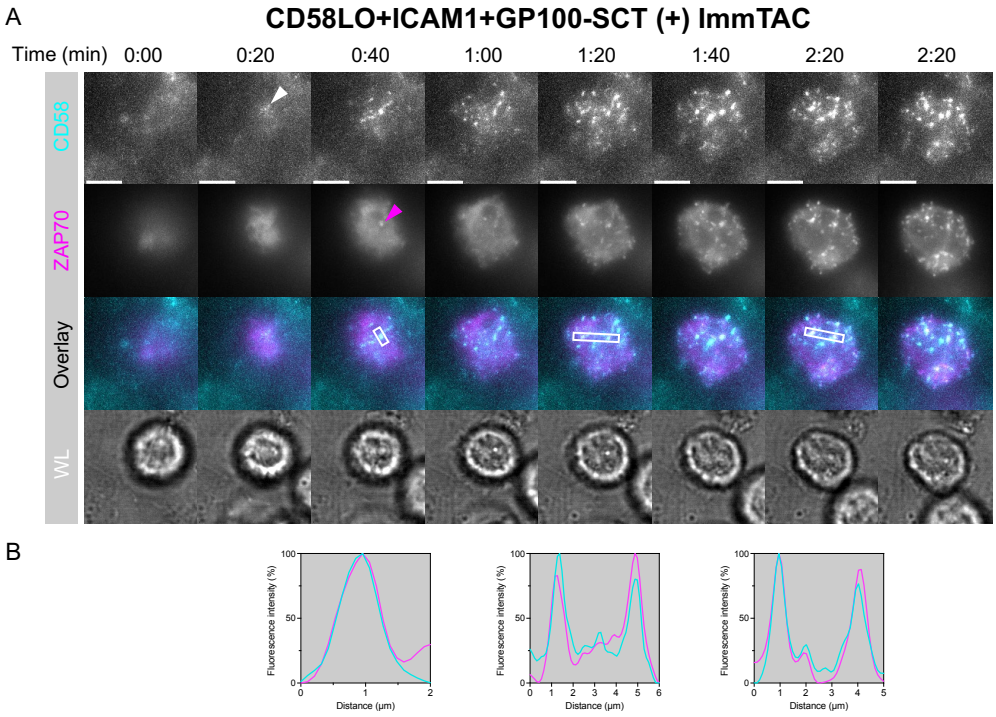


Figure 5.19: eWM imaging of ZAP70 recruitment to the close contacts at the interface between a single ZAP70-HaloTag primary CD8$^+$ T cell and CD58LO+ICAM-1+GP100-SCT U-2 OS cells. A. eWM images of a single ZAP70-HaloTag primary CD8$^+$ T cell interacting with a monolayer of CD58LO+ICAM-1+GP100-SCT U-2 OS cells. T cell were stained with an AF488-conjugated anti-CD45 antibody and a JF646 HaloTag ligand to yield ZAP70-HaloTag-JF646. U-2 OS cells were labelled with JF549 HaloTag ligand to yield CD58-HaloTag-JF549. The white arrowhead indicates the first detectable CD58-demarcated CCs. The magenta arrowhead indicates the first detectable recruitment of ZAP70 to the CCs. **B**. The min/max normalised intensity line profile taken across the CCs enclosed by the white rectangles in the image panels (A). For all of the fluorescence images MIPs of the focal stack are shown. Scale bar = 5 µm. Images were taken by Daniel Heraghty.

control for any variations in the intensity of the cell membrane, the CD45 signal was normalised against the cell membrane signal (CD45/CM) and inverted to aid the visualisation of CD45 exclusion (Figure 5.21B and E, bottom panels). CD45 was excluded at some of the brightest CCs (Figure 5.21C and F), but there was a fraction of CCs which appeared to be misaligned with the CD45-depleted areas. Additionally, areas of weaker CD45 exclusion could be observed around the CCs. According to preliminary CC analysis, the average CD45 exclusion within the CCs was ~12%, but it extended to 25% for some of the CCs this was in contrast to the CM signal which was the same inside and outside the CCs (Figure 5.20D and G).

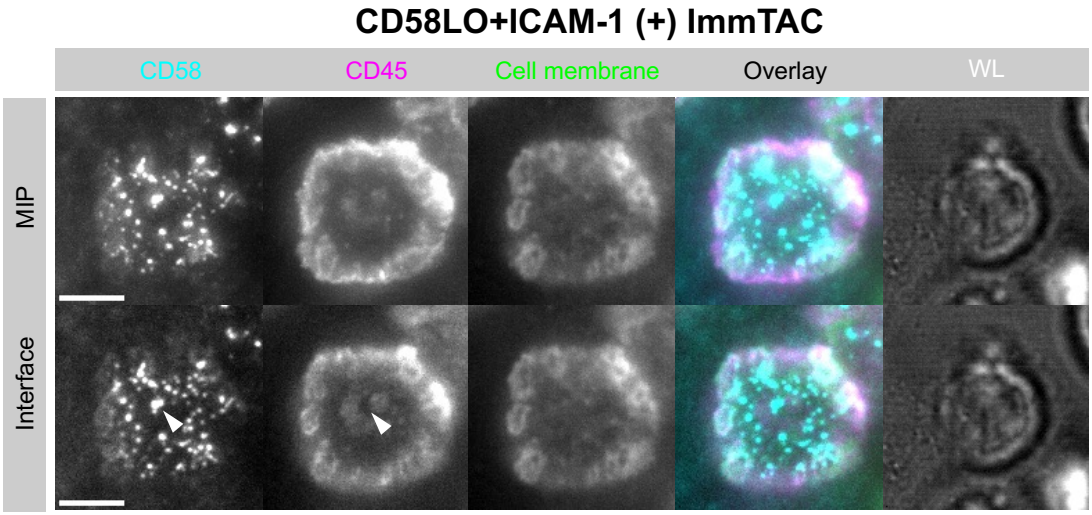


Figure 5.20: eWM imaging of CD45 segregation from the close contacts at the interface between a single primary CD8$^+$ T cell and CD58LO+ICAM-1 U-2 OS cells. A. eWM images of a single primary CD8$^+$ T cell interacting with a monolayer of CD58LO+ICAM-1 U-2 OS cells. T cells were stained with an AF488-conjugated anti-CD45 antibody and CellMask DeepRed. U-2 OS cells were labelled with JF549 HaloTag ligand to yield CD58-HaloTag-JF549. The white arrowhead indicates a site of a putative CD45-depleted CC. For all of the fluorescence images MIPs of the focal stack are shown. Scale bar = 5 μm.

5.2.10 Overexpression of CD58 increases the dimensions of close contacts

In Chapter 4, it was demonstrated that overexpression of CD58-HaloTag led to the activation of T cells in the absence of ImmTAC (section 4.2.1). There is prior evidence to suggest that the mechanism that underlies this effect involves the enlargement of CC beyond their native size[86,137,256]. It was speculated that CD45 exclusion over larger contact areas increases the phosphorylation probability of unligated TCR/CD3 complexes diffusing through such CCs. To test whether this mechanism operates at cellular interfaces, interactions of T cells and CD58HI U-2 OS cells labelled with the SiR-conjugated anti-CD45 antibody and JF549 HaloTag ligand, respectively, were imaged using the eWM instrument. Although the contrast between the CD58 signal within the CC vs. non-CC areas of the U-2 OS cell surface was lower than for the U-2 OS cells expressing CD58-HaloTag at endogenous levels, the CCs could be detected (Figure 5.22A). The CCs had a perturbed morphology and appeared as patches rather than puncta. Furthermore,

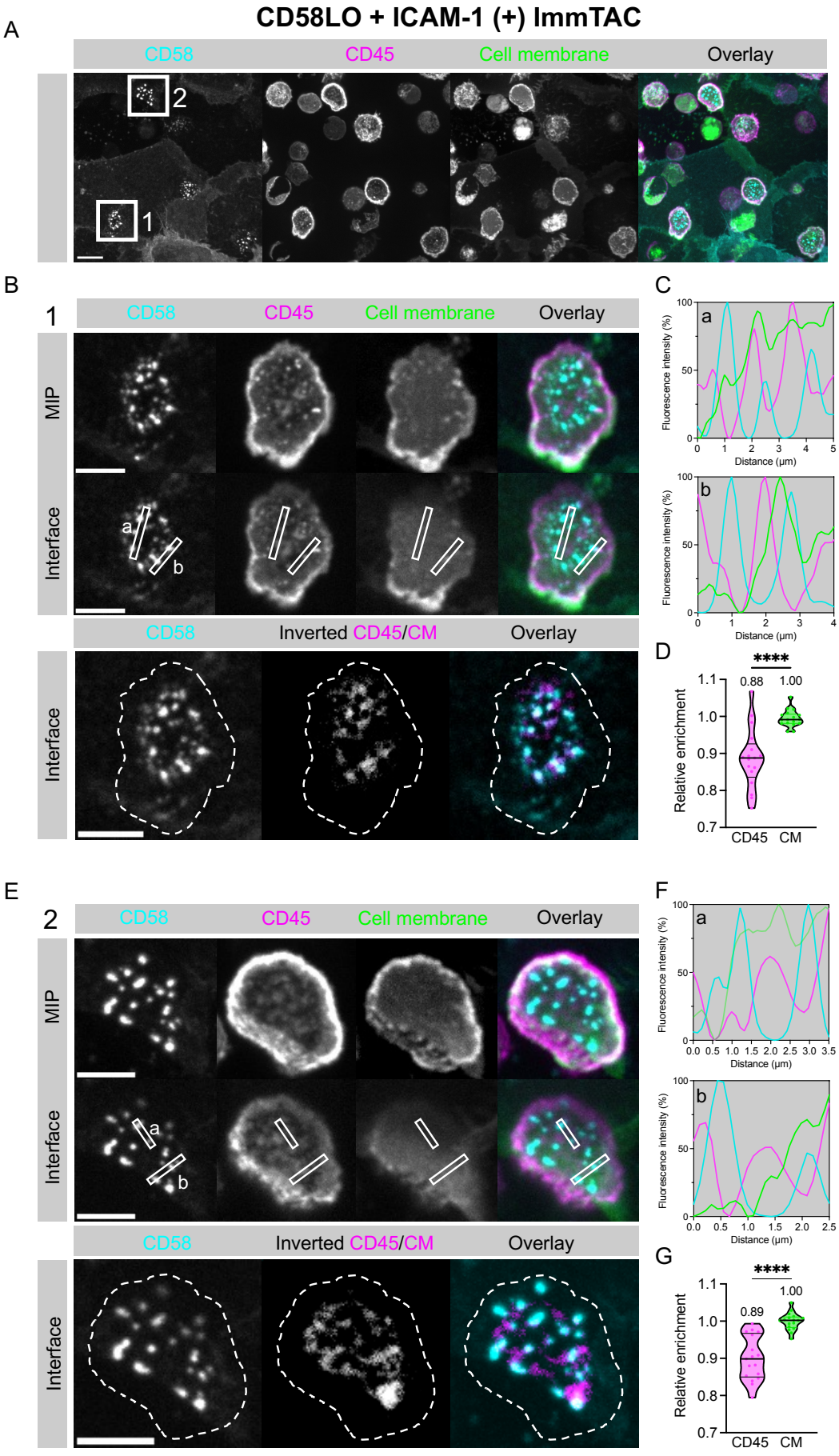


Figure 5.21: (Following page)

Figure 5.21: SDCM imaging of CD45 segregation from the close contacts at the interface between primary CD8$^+$ T cells and CD58LO+ICAM-1 U-2 OS cells. **A**. Multicellular overview of the interactions between primary CD8$^+$ T cell and CD58LO+ICAM-1 U-2 OS cells imaged by SDCM. T cells were stained with an AF488-conjugated anti-CD45 antibody and CellMask (CM) Deep Red. U-2 OS cells were labelled with JF549 HaloTag ligand to yield CD58-HaloTag-JF549. MIPs of the focal stack are shown. Scale bar = 10 μm. **B**. and **E**. Close-up images of single primary CD8$^+$ T cells interacting with a monolayer of CD58LO+ICAM-1 U-2 OS cells from the SDCM image in (A). MIPs of the focal stack and the individual planes containing the T cell/U-2 OS cell interface are shown. For the interface plane, the CD45 fluorescence signal was normalised against the CM fluorescence signal and inverted to provide a more intuitive representation of CD45 distribution at the T-cell surface (bottom panel). **C**. and **F**. The min/max normalised intensity line profiles taken across the CCs enclosed by the white rectangles in the image panels (B) and (E), respectively. **D**. and **G**. Automated analysis of CD45 and CM distribution at the CC vs. non-CC areas for T cell shown in (B) and (E), respectively. Mean values are shown. Scale bar = 5 μm. Relative enrichment values were compared using a Mann-Whitney test. *P-value $\leq$ 0.05, **P-value $\leq$ 0.01, ***P-value $\leq$ 0.001, ****P-value $\leq$ 0.0001. Images were taken by Daniel Heraghty.

some of the contacts had an elongated rather than circular shape. These abnormal CCs had an average area of 0.920 μm^2 and were as large as 2.5 μm^2 (Figure 5.22C). Interestingly, despite the use of the eWM instrument, which previously did not permit detection of CD45 exclusion at native-sized CCs, the large CCs at the T cell/CD58HI U-2 OS cell interface were visibly depleted of CD45. This was likely because the increase in the CC dimensions diminished the relative impact of the out-of-focus CD45 fluorescence (Figure 5.22B).

5.3 Discussion

In this chapter, a cellular system was established to enable imaging of CC at the interface of T cells with their targets. The dimensions of CC were on average ~460 nm in diameter and while their size varied across the U-2 OS cell surfaces, the differences were marginal. The exception was the overexpression of CD58 on the U-2 OS cell surface which led to disruption of the native CC morphology. The presence of ICAM-1 on the U-2 OS cell surface altered the dynamics of the interaction, increasing the number of CCs, T-cell footprint and the sampling capacity of CCs. The CCs were validated as the site of TCR triggering and a single

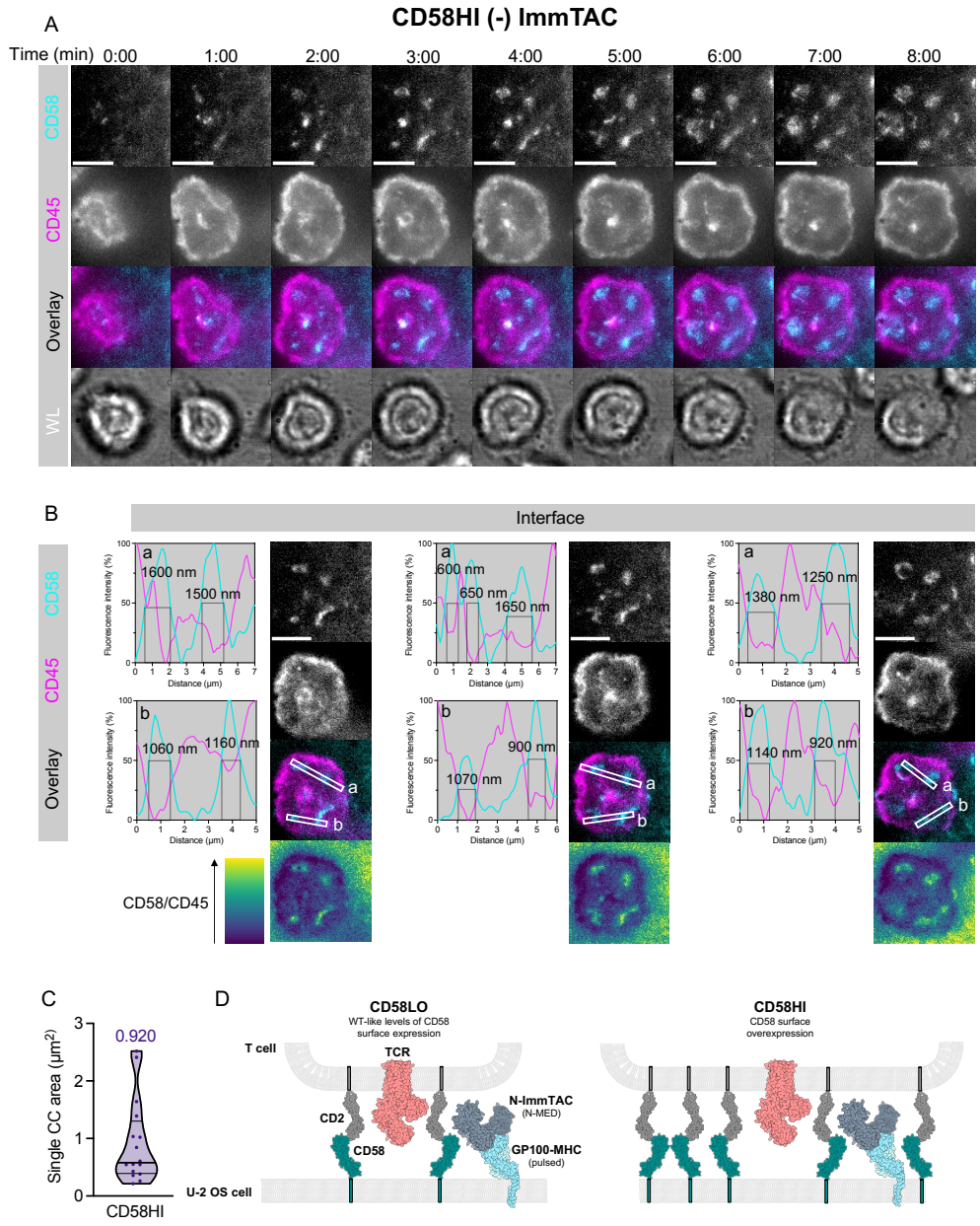


Figure 5.22: eWM imaging of interaction between a single primary CD8$^+$ T cells and CD58HI U-2 OS cells. A. eWM imaging of interactions of primary CD8$^+$ T cells with a monolayer of CD58HI U-2 OS cells. T cells were stained with a SiR-conjugated anti-CD45 antibody. hGP100-pulsed U-2 OS cells were labelled JF549 HaloTag ligand to yield CD58-HaloTag-JF549. For the fluorescence images MIPs of the focal stack are shown. **B**. Images showing the plane of the T cell/U-2 OS interface. Images corresponding to CD58/CD45 ratio showing the relative protein distribution in the CCs are included to aid the visualisation of CD45 exclusion. The min/max normalised intensity line profiles taken across the CCs enclosed by the white rectangles. Scale bar = 5 µm. **C**. Area of a single CCs formed between primary CD8$^+$ T cells and CD58HI U-2 OS cells. The mean value is shown. n=1. **D**. Schematic showing the hypothetical architecture of a CC formed at the interface of primary CD8$^+$ T cells and CD58LO (left) and CD58HI (right) U-2 OS cells.

CC was sufficient to induce calcium flux in a T cell. Preliminary data suggests that CD45 is excluded from the CCs at the cell/cell interface, albeit to a lesser extent than could be expected based on studies of T cells using APC surrogates.

5.3.1 Model T cell/target cell system for imaging of cellular interactions

Microvilli of resting primary $CD8^+$ T cells used in this study were examined using SEM. These membrane protrusions were found to have a diameter of ~81 nm and an estimated cross-sectional area of 0.005 μm^2. Previous studies using SEM and TEM reported similar dimensions with microvillar diameters of ~70-120 nm[162,163]. In contrast, measurements obtained using fluorescence microscopy typically yield 2 to 5 times greater values[137,168,174]. For instance, LSCM imaging of fixed and expanded primary human $CD4^+$ T cell estimated the microvillar diameter to be ~250 nm, while microvilli of fixed Jurkat T cells also measured using LSCM were ~430 nm in diameter[137,174]. LLSM imaging of live primary murine $CD4^+$ T cells provided an estimate of 535 nm[168]. The discrepancies between EM-based measurements and LM-based measurements suggest that the microvillar dimensions reported in the present study might be an underestimate. This could be attributed to the invasive sample preparation required for SEM imaging, including fixation, dehydration, and gold-coating. Conversely, LM methods are diffraction-limited and likely overestimate the dimensions of T-cell microvilli.

Two types of model U-2 OS cell surfaces were used for imaging their interactions with T cells. First, the CD58LO U-2 OS cell line expressing a CD58-HaloTag construct in place of the endogenous CD58. Second, the CD58LO+ICAM-1 U-2 OS cell line expressing ICAM-1 lacking its cytoplasmic domain alongside the CD58-HaloTag construct. The expression of ICAM-1 in the CD58LO+ICAM-1 U-2 OS cells increased the sensitivity of T cells to the N-MED ImmTAC without inducing ligand-independent T-cell activation. Interestingly, the expression levels of CD58-HaloTag in CD58HI U-2 OS cells was comparable to those of ICAM-1 in CD58LO+ICAM-1 U-2 OS cells, but T cells co-cultured with the former cell

line readily activated in the absence of ImmTAC underscoring the distinct roles of ICAM-1- and CD58-mediated adhesion. The ICAM-1-driven increase in T-cell sensitivity was previously observed in multiple studies[137,138,318,349].

The expression of ICAM-1 in the CD58LO+ICAM-1 U-2 OS cells was 8-fold higher than in moDCs. However, in addition to ICAM-1, DCs express a plethora of large adhesion molecules including other LFA-1 ligands as well as more unique adhesion molecules. For instance, DC-SIGN is highly expressed on the surface of DCs and binds ICAM-3 on the T-cell surface with high affinity[324,382,383]. Additionally, DCs themselves express ICAM-3 which competes with ICAM-1 for LFA-1 binding[384]. The adhesive interactions between T cells and DCs are dynamic and the contributions of each adhesion pair may be context-dependent. While there is no universal adhesion system across the diverse cancer lineages, ICAM-1 expression is upregulated by the most aggressive cancer types[373–375]. Nonetheless, in contrast to the idiosyncratic CD2-CD58 interaction, the adhesion orchestrated by large molecules such as integrins and ICAM family proteins is more complex and thus more challenging to faithfully replicate in a model system. This might be aided by the development of target cells whose surfaceome is amenable to rapid alterations such as the 'CombiCell' system established by Patel et al.[318].

5.3.2 CD58 as a close-contact marker

It needs to be emphasised that CCs are spatially restricted intercellular zones and they are not defined by their molecular composition *per se*. Therefore, their direct detection necessitates the use of CC markers which can be broadly divided into two formats: passive and active. The passive markers operate through their segregation from the CCs and do not require intermolecular interactions, whereas the latter type relies on accumulation within CCs, a process that inherently requires binding to partner molecules on the apposed surface. Here, an active marker, HaloTag-tagged CD58 was used to detect CCs at an interface between T cells and a model cancer cell. Previous studies of CC in SLB systems primarily

made use of passive markers to map them e.g. fluorescently-labelled glycocalyx molecules or quantum dots tethered to SLBs[137,168].

The following observations validated CD58 as a suitable CC marker in the T cell/U-2 OS cell system. First, the dimensions of the CD58-demarcated CCs (average diameter of ~460 nm and area of 0.160 μm^2) were similar to those measured in SLB systems using passive markers; diameters of 540 nm and 390 nm were reported by Cai et al. and Jenkins et al., respectively[137,168]. Accumulation of CD58 could be reliably observed before or at the time of calcium flux underscoring the responsiveness of the CD2/CD58 adhesion pair to dynamic remodelling of the cellular interface, consistent with the biophysical properties of this interaction i.e. low affinity with a fast off-rate[130,135,385]. Lastly, in the presence of the TCR ligand, both ZAP70 and TCR co-localised with CD58 suggesting that CD58 accumulation puncta represent genuine CCs.

However, CD58 cannot be considered a universal CC marker as its applicability is limited to tracking of interactions between immune cells and CD58-expressing target cells. Neither can the passive markers be used universally as their introduction to the target cell is likely to perturb the native interaction. For instance, the addition of glycocalyx-based markers to U-2 OS cells would likely perturb CC formation[137]. The development of novel proximity probes is necessary to map the interactions of immune cells with unconventional target cells. The solution could come in the form of cell-anchored fluorescent DNA probes akin to those developed by Tan and colleagues[386].

5.3.3 Visualisation of the T cell/cancer cell interactions

Interactions of T cells with CD58LO and CD58LO+ICAM-1 U-2 OS cells were visualised using three complementary microscopy techniques: eSPIM, eWM and SDCM. T cells formed sparse CCs with CD58LO U-2 OS cells, restricted to a small area. The CCs were transient and their movement across the CD58LO U-2 OS cell surface appeared to be random. The presence of ICAM-1 on the U-2 OS surface dramatically increased the number of CCs and the T-cell footprint on

the U-2 OS cell surface. Following the initial interaction, multiple CC formed as the T cells spread and subsequently, the T-cell footprint contracted with the CCs moving centripetally. In the absence of ImmTAC, the reduction of the T-cell footprint was not accompanied by the centripetal motion of the CCs, but rather a continued directionless movement across a smaller area of the target cell.

In the presence of the TCR ligand, T cells formed CCs measuring 470 and 560 nm in diameter, equivalent to areas of 0.180 μm^2 and 0.260 μm^2, on the CD58LO and CD58LO+ICAM-1 U-2 OS cell surfaces, respectively. When the TCR ligand was removed the CCs were 380 and 430 nm in diameter with the equivalent areas of 0.116 and 0.156 μm^2 with and without ICAM-1, respectively. These measurements need to be carefully interpreted due to the imaging being diffraction-limited. Consequently, as previously noted, it is possible that the apparent size of individual well-separated CCs is an overestimate. Furthermore, some CCs appeared to coalesce into larger contacts, but it could not be determined whether these CCs genuinely merged or remained in close proximity (<200 nm). This behaviour was more frequently observed in the absence of ICAM-1 as the CCs were often confined to a small region on the CD58LO U-2 OS surface, and it likely led to an overestimation of the CC size in the context of this U-2 OS cell line. This effect was of lesser significance in the presence of ICAM-1 as the majority of CC appeared as individual puncta distributed across a larger area. It remains to be determined whether the apparent merging of CCs is a reflection of a biological mechanism or an artefact of the light-diffraction limit.

The CCs appeared to be the site of TCR triggering as illustrated by co-localisation of ZAP70 and TCR with CD58. However, not every CC appeared to be equally permissive to TCR accumulation and subsequent TCR phosphorylation. A similar pattern was observed by Cai et al. where CCs containing the TCR/pMHC complexes were also more persistent. To investigate the distribution of CD45, interactions of T cells with CD58LO+ICAM-1 U-2 OS cells were imaged using SDCM to reduce the out-of-focus CD45 signal. CD45 exclusion was readily observable at the brightest CCs, likely corresponding to the more persistent

interactions. CD45 exclusion was less discernible at fainter CCs and those located at the periphery of the cellular interface. These observations might be explained by the technical limitations of the instrument. First, given the high mobility of CC, the temporal resolution of the SDCM instrument may not been sufficient for effective co-registration of the CD45 and CD58 signals resulting in the 'shifted' appearance of CD45 exclusion versus CD58 accumulation. Second, the non-planar topology of the cellular interface may contribute to the poor detection of CD45 exclusion – the fluorescence signal of CD45 emitted from the lateral portion of microvilli may partially obscure the reduction in CD45 signal within the CC despite the improved optical sectioning of the SDCM versus eWM. These challenges could be addressed by imaging of fixed T cell/U-2 OS cell conjugates which would permit the CD45 signal to be averaged across multiple SDCM images and improve the channel co-registration. Moreover, to build a 3D map of the CCs and obtain a more precise estimate of CD45 exclusion and size, the fixed conjugates could be imaged using volumetric SMLM microscopy techniques such as light field or double helix SMLM[345,387–389].

6

Ultrastructure of CD8$^+$ T cell/U-2 OS cell conjugates imaged using correlative light and electron microscopy

Contents

6.1 Introduction 174
6.2 Results 176
6.2.1 Purification and validation of the N-MED ImmTAC . 176
6.2.2 Cryogenic 3D-SIM imaging of primary CD8$^+$ T cell/U-2 OS cell conjugates 178
6.2.3 FIB-SEM imaging of the primary CD8$^+$ T cell/U-2 OS cell conjugates 187
6.3 Discussion 191
6.3.1 Production and validation of the N-MED ImmTAC . . 191
6.3.2 CLEM imaging of the T cell/U-2 OS cell interactions 192

6.1 Introduction

T cell/target cell interactions are initiated by the formation of contacts between the microvilli and the target cell membrane according to imaging data generated using both electron (EM) and light (LM) microscopy[137,165,167,168,368]. However, it is not clear how the morphology of the T-cell membrane and its relationship

with the CCs evolve following TCR triggering. Imaging of T cells in SLB systems suggests that in response to TCR phosphorylation, the T-cell membrane adopts a 'corrugated-sheet' topology with the CCs located at the 'ridges' with a flat central region corresponding to the cSMAC[137,168]. In contrast, EM imaging of T cell/target cell conjugates suggests the microvilli collapse and the T-cell membrane flattens against the target cell forming an interface that can be likened to two flat sheets[166,167,368]. The live-cell imaging data presented in the previous chapter provide limited three-dimensional information about the T-cell surface and the individual CCs. To simultaneously identify the sites of cellular contact and correlate them with the topography of the T-cell surface, fluorescence imaging can be combined with EM. Recently, Ritter et al. showed the utility of a correlative light and electron microscopy (CLEM) pipeline comprised of cryogenic 3D-SIM with FIB-SEM to map T cell/target cell conjugates during T-cell killing[390].

In this chapter, CLEM will be used to establish the spatial relationship between the CCs and the membrane ultrastructure. First, cryo-preserved samples will be imaged using a 3D-SIM instrument (lateral and axial resolutions of ~150 nm and ~800 nm, respectively) and FIB-SEM (isotropic 4 nm resolution). Due to the low throughput of the FIB-SEM pipeline (2 weeks per single conjugate) and limited access to the instrument, two combinations of T cell/U-2 OS cell lines were trialled at the LM stage. First, unmodified primary CD8$^+$ T cells interacting with CD58LO U-2 OS cells were tested. This experiment aimed to map the CD58-demarcated CCs onto the membranes of U-2 OS cells and T cells. Second, primary ZAP70-HaloTag CD8$^+$ T cells interacting with WT U-2 OS cells were imaged whereby 'signalling' CC were to be related to the conjugate topography. Additionally, in both experimental conditions, T cells will be labelled using the anti-CD45 antibody to infer the relationship between the intermembrane distance and CD45 distribution. Hereafter, this first experimental condition will be referred to as 'CD58-HaloTag' and the second as 'ZAP70-HaloTag'.

It needs to be noted that the experiments were carried out before the creation of the CD58LO+ICAM-1 U-2 OS cell line.

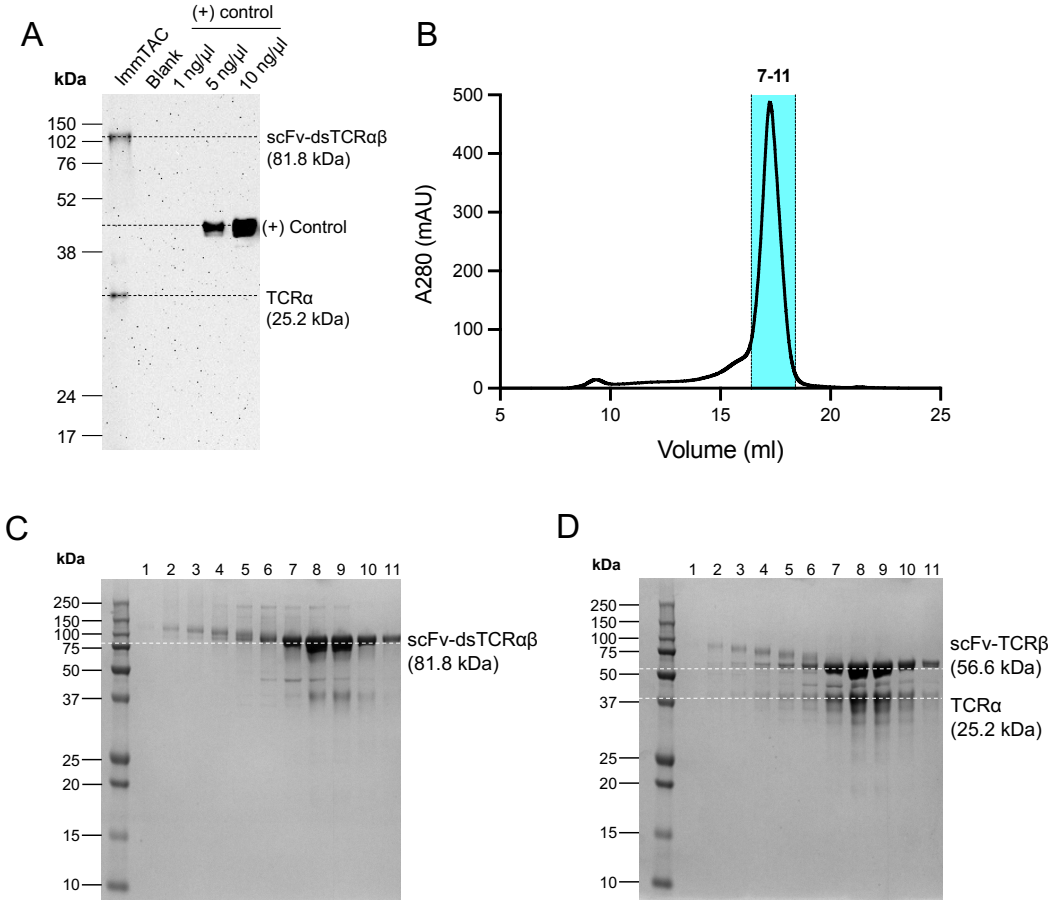


Figure 6.1: Expression and purification of the N-MED ImmTAC. A. Western blot of cell culture supernatant of CHO-K1 cells expressing from the N-MED ImmTAC. Anti-C-tag camelid antibody and HRP-conjugated anti-llama antibody were used for primary and secondary staining, respectively. Samples were tested under non-reducing conditions. Protein bands corresponding to the disulphide-linked N-MED ImmTAC (scFv-dsTCRαβ) and unpaired TCRα chain were detected. Recombinant TCRγδ C-tagged protein was used as a positive control and used at 1 ng/µl, 5 ng/µl and 10 ng/µl. **B**. SEC profiles (A280) of the N-MED ImmTAC. S200 10/300 GL column was used. Collected fractions corresponding to monodisperse protein are highlighted. **C**. Non-reducing SDS-PAGE gel of the SEC fractions stained with Coomassie blue. **D**. Reducing SDS-PAGE gel of the SEC fractions stained with Coomassie blue. For both SDS-PAGE gels the corresponding SEC fractions are noted at the top. The calculated molecular weights of the respective polypeptide chains are shown in brackets.

6.2 Results

6.2.1 Purification and validation of the N-MED ImmTAC

As in the previous chapter, the N-MED ImmTAC was to serve as a model TCR ligand for CLEM imaging of T cell/U-2 OS cell conjugates. Due to the logistical

issues associated with the transfer of research materials to the site of the CLEM instruments, the N-MED ImmTAC was purified in-house. A bicistronic N-MED ImmTAC construct was designed with the encoded polypeptide split into two chains by a T2A self-cleaving peptide. The first cistrons encoded the UCHT1 scFv linked to the N-terminus of the β chain of the GPa3b17 TCR and the second, the α chain of the GPa3b17 TCR with an affinity tag (C-tag, EPEA) on its C-terminus for purification purposes. C-tag was used as it is small and weakly charged at physiological pH, thus unlikely to interfere with the structure of the ImmTAC. The N-MED ImmTAC construct was lentivirally transduced into CHO-K1 cells and its expression was confirmed by a Western blot of the cell culture supernatant 12 days after transduction (Figure 6.1A). Following a 10-day expansion of the CHO-K1 cell culture, the CHOK-1 cell supernatant was passed through an anti-C-tag antibody affinity purification column and the eluted fractions were pooled and concentrated. The concentrated sample was then subjected to size exclusion chromatography (SEC) (Figure 6.1B) and SDS-PAGE analysis was used to evaluate the purity and the oligomeric state of the protein (Figure 6.1D and E). The SEC fractions containing the monodisperse protein were then pooled, concentrated to ~1 mg/ml and stored at -80 °C for further use. Hereafter, the N-MED ImmTAC purified in this section will be referred to as the 'in-house' ImmTAC, whereas the N-MED ImmTAC produced by Immunocore Ltd. as the 'Immunocore' ImmTAC.

The binding affinities of the in-house and the Immunocore ImmTACs were measured by SPR as implemented by the Biacore 8K (Figure 6.2). For the SPR measurements of ImmTAC binding to CD3ϵ, biotinylated Avi-tagged CD3ϵγ heterodimer (provided by Immunocore Ltd.) was immobilised on a CAP chip and the ImmTACs were injected as analytes. The in-house and the Immunocore N-MED ImmTACs bound to the ligand with K_D values of 197 nM and 273 nM, respectively (Figure 6.2A-C). To measure the binding kinetics of the ImmTAC-GP100-MHC interaction, 2xHis_6-tagged GP100-HLA-A2 (purified by Mai Vuong) was immobilised on an NTA chip and ImmTACs were injected as analytes.

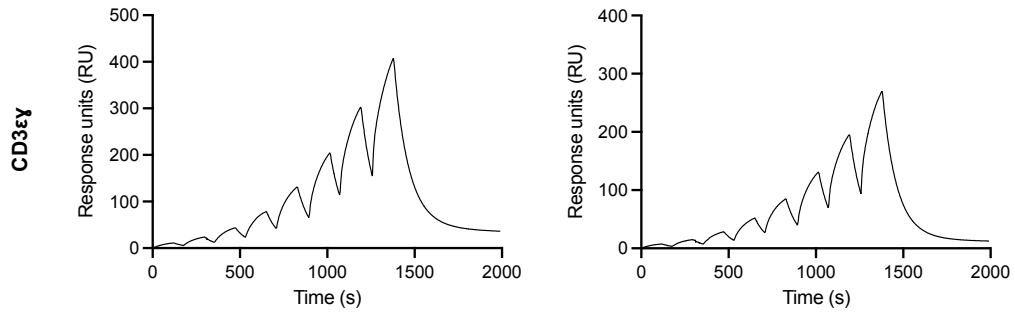
Both of the ImmTACs had picomolar K_D values, but the Immunocore ImmTAC bound to GP100-MHC with a ~6-fold greater affinity (Figure 6.2D-F). The R_{max} values at the equivalent ImmTAC concentrations were consistently ~20% lower for the in-house ImmTAC suggesting that a smaller proportion of the protein was biologically active.

The functional properties of the in-house ImmTAC were examined using co-culture assays of primary CD8$^+$ T cells and hGP100-pulsed WT U-2 OS as described in section 3.2.4 (Figure 6.3A and C). The $EC_{50:CD25}$ and $EC_{50:CD69}$ values were 1.4 and 1.8-fold lower for the Immunocore ImmTAC versus the in-house ImmTAC (Figure 6.3B and D). The lower potency of the in-house ImmTAC was consistent with its reduced biological activity and the higher K_D value for binding to the GP100-MHC antigen, both of which would result in decreased density of the TCR ligand on the U-2 OS cell surface. Nonetheless, the in-house N-MED ImmTAC retained the ability to activate T cells even at the sub-nanomolar hGP100 concentrations and was deemed suitable for the CLEM experiments. Hereafter, the use of only the in-house ImmTAC will be referred to.

6.2.2 Cryogenic 3D-SIM imaging of primary CD8$^+$ T cell/U-2 OS cell conjugates

The T cells and U-2 OS cells were prepared for the 3D-SIM experiments as follows. CD58LO or WT U-2 OS cells were plated on 4-nm sapphire coverslips, pulsed with hGP100 peptide, and grown in culture for 18h. Since mitochondria are easily segmented in EM images lending themselves well as a fiducial marker required for EM and LM image co-registration, both U-2 OS cell lines were labelled with a mitochondrial dye (Mito Tracker Deep Red) and the ImmTAC. Additionally, the CD58LO U-2 OS cells were labelled with the JF549 HaloTag ligand as described in the previous chapter. Both T cell lines were labelled with an AF488-conjugated anti-CD45 antibody and the ZAP70-HaloTag T cells were also labelled with the JF549 HaloTag ligand. T cells were gently layered onto the U-2 OS cell monolayers and allowed to settle for 20 min to accommodate for the

A

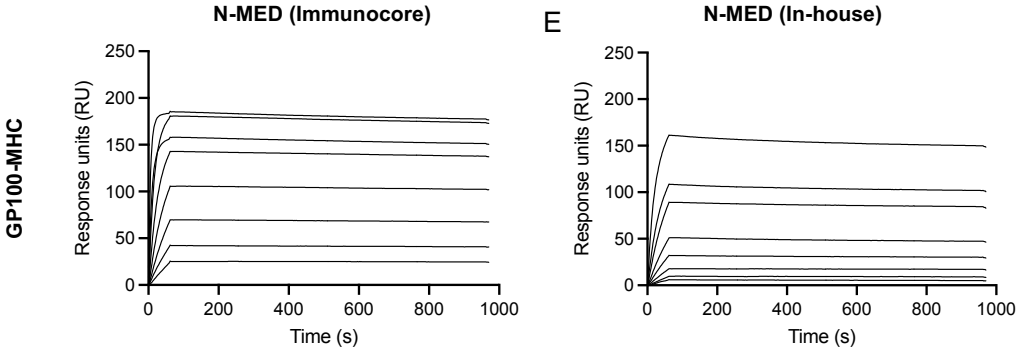


B

C

ImmTAC	Replicate	k_{on} ($M^{-1}s^{-1}$)	k_{off} (s^{-1})	K_D (nM)
N-MED (Immunocore)	1	$6.18x10^4$	$1.21x10^{-2}$	196
	2	$5.91x10^4$	$1.17x10^{-2}$	197
	Average	**$2.96x10^4$**	**$1.19x10^{-2}$**	**197**
N-MED (In-house)	1	$3.63x10^4$	$9.11x10^{-3}$	251
	2	$3.31x10^4$	$9.73x10^{-3}$	294
	Average	**$3.46x10^4$**	**$9.42x10^{-3}$**	**273**

D



E

F

ImmTAC	Replicate	k_{on} ($M^{-1}s^{-1}$)	k_{off} (s^{-1})	K_D (pM)
N-MED (Immunocore)	1	$4.45\ x10^5$	$3.73x10^{-5}$	83.8
	2	$1.31x10^6$	$3.52x10^{-5}$	26.8
	Average	**$8.78x10^5$**	**$3.63x10^{-5}$**	**55.3**
N-MED (In-house)	1	$1.99x10^5$	$7.07x10^{-6}$	354
	2	$1.5x10^5$	$5.05x10^{-5}$	336
	Average	**$1.75x10^5$**	**$2.89x10^{-5}$**	**345**

Figure 6.2: (Following page)

Figure 6.2: Biophysical validation of the N-MED ImmTAC. A and **B**. Single-cycle SPR analysis of the in-house (A) and Immunocore (B) N-MED ImmTAC binding to CD3$\epsilon\gamma$. Biotinylated CD3$\epsilon\gamma$ heterodimer was immobilised on a CAP chip and fluid-phase ImmTACs were injected as analytes. Twofold dilution series ranging from 6.25 nM to 800 nM was used. Sensorgrams were blank subtracted. All sensorgrams were fitted into a 1:1 Langmuir model to produce the kinetic parameters shown in the table below. **C**. Kinetic parameters (k_{on}, k_{off}, and K_D) derived from the SPR data in (A) and (B). **D**. and **B**. Multi-cycle SPR analysis of the ImmTAC panel binding to GP100-HLA-A2. 2xHis_6-tagged GP100-HLA-A2 was immobilised on an NTA chip and fluid-phase ImmTACs were injected as analytes. Twofold dilution series ranging from 1.56 nM to 200 nM was used. Sensorgrams were blank subtracted. All were fitted into a 1:1 Langmuir model to produce the kinetic parameters shown in the table below. **F**. Kinetic parameters (k_{on}, k_{off}, and K_D) derived from the SPR data in (D) and (E).

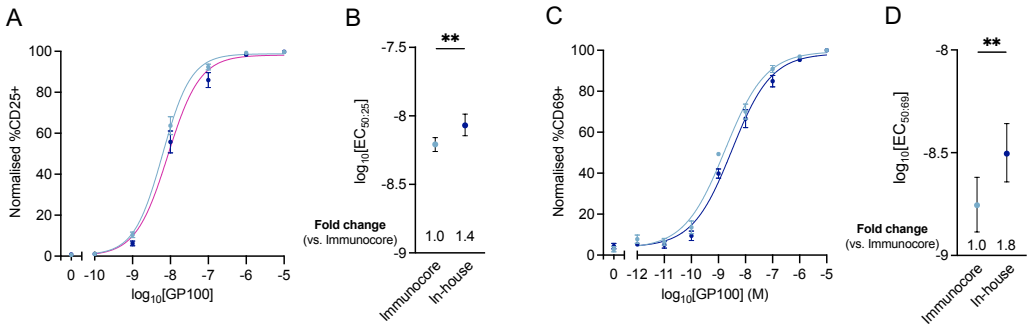


Figure 6.3: Functional validation of the N-MED ImmTAC. A. Dose-response curves showing T-cell activation by upregulation of CD25 in response to the in-house and Immunocore N-MED ImmTACs following 18h of co-culture with WT U-2 OS cells. **B**. $EC_{50:25}$ values extracted from unconstrained four-parameter variable slope Hill model fitted into the dose-response curves from (B). **C**. Dose-response curves showing T-cell activation by upregulation of CD69 in response to the in-house and Immunocore N-MED ImmTACs following 18h of co-culture with WT U-2 OS cells. **D**. $EC_{50:69}$ values extracted from unconstrained four-parameter variable slope Hill model fitted into the dose-response curves from (C). Data was collected using T cells isolated from at least two donors. Mean values with error bars corresponding to 95% CI are shown. EC_{50} values were compared using an F-test of normalised data. *P-value $\leq$ 0.05, **P-value $\leq$ 0.01, ***P-value $\leq$ 0.001, ****P-value $\leq$ 0.0001

extended interaction time needed for CC formation in the absence of ICAM-1 (only ~20% T cells form CCs in the first 10 min, section 5.2.4). Before freezing, the culture medium was substituted with freezing medium containing TetraSpeck microspheres which would be later used to correct any chromatic aberration in the cryo 3D-SIM images. Next, the samples were high-pressure frozen and stored in LN_2 until loading onto the cryo 3D-SIM instrument.

A total of 3 coverslips for each of the two experimental conditions were transferred from LN_2 storage to the cryostat of the cryo 3D-SIM instrument. To locate T cells that have engaged the U-2 OS cells, cryo-fluorescence widefield montages of the whole coverslips were generated (Figures 6.4 and 6.5). Due to the low NA of the objective (NA = 0.85) and short exposure times used to create the montages, the accumulation of CD58-HaloTag or ZAP70-HaloTag at the cellular interface was indiscernible at this point. In consequence, the conjugates for the 3D-SIM imaging were initially selected based on the proximity of the T cells and U-2 OS cells which was assessed through the CD45 and mitochondrial fluorescence signals. 10-40 regions of interests (ROIs) per coverslip were selected, most containing a single T cell/U-2 OS cell conjugate and infrequently a pair of conjugates if they were sufficiently close (see ROI2.1/2.2). The conjugates were individually re-examined in widefield mode to verify CD58-HaloTag and ZAP70-HaloTag accumulation and then imaged in 3D-SIM mode. For conjugate selection for the FIB-SEM imaging, the imaging data was reviewed in the widefield format. For each conjugate, MIP of the focal stack was generated and the plane containing most of the T cell/U-2 OS cell interface was identified (Figures 6.6 and 6.7).

Under both conditions T cells adopted two types of morphology: i) 'rounded' – characterised by limited spreading, more frequently observed for T cells that appeared to have interacted with the apical membrane of U-2 OS cells, ii) 'spread' – characterised by the extension of the T cell membrane along the cellular interface, more frequently observed for T cells that engaged the edge of the U-2 OS cells. T cells interacting with the CD58LO U-2 OS cells formed sparse CD58-demarcated CCs akin to those seen in the live-cell imaging data (Figure

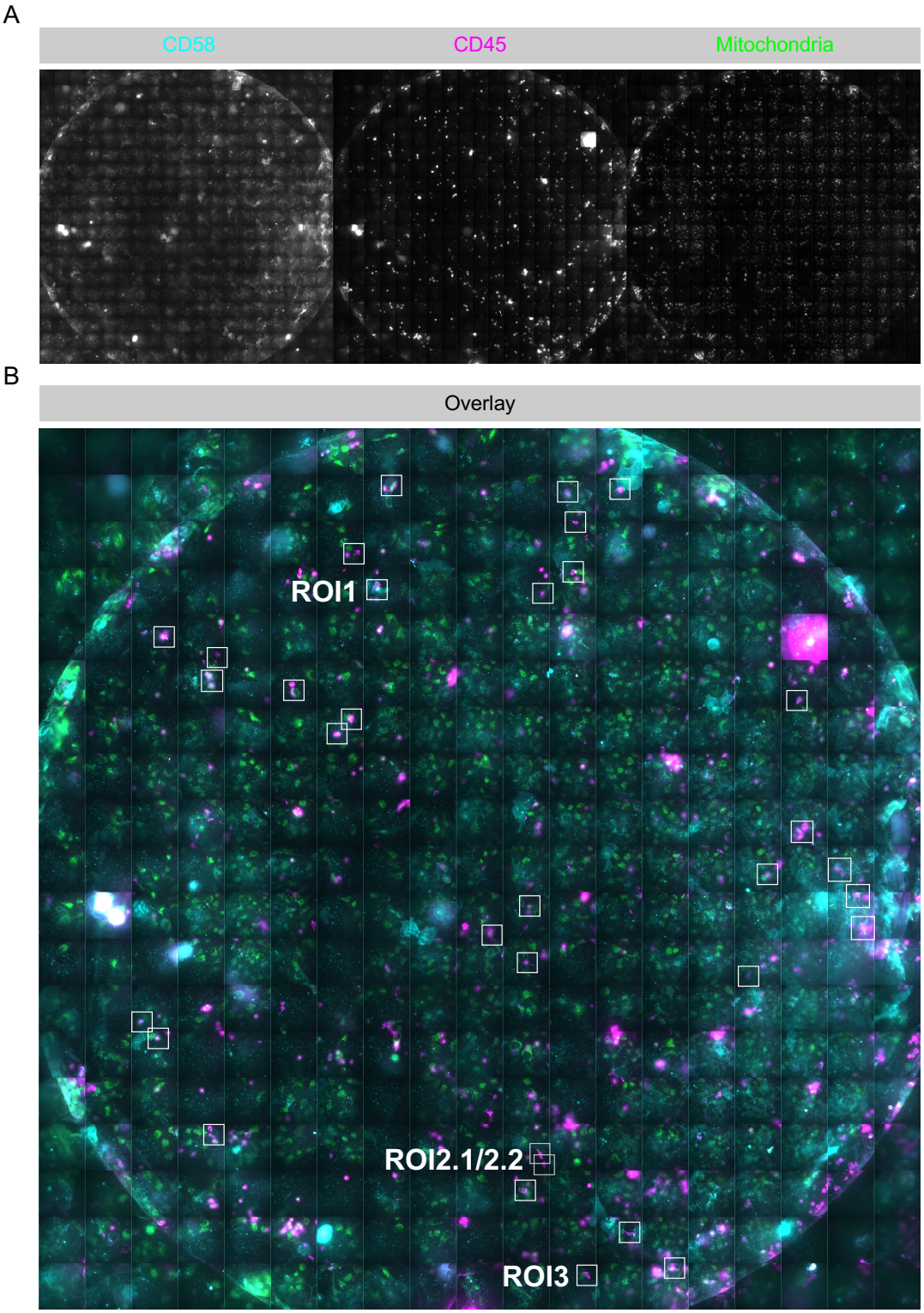


Figure 6.4: Cryo-fluorescence widefield montage of a coverslip containing primary CD8$^+$ T cell/CD58LO U-2 OS cell conjugates. A. and **B**. Representative montage assembled from a widefield tile scan of the coverslip containing CD8$^+$ T cell/CD58LO U-2 OS cell conjugates. One of three coverslips is shown. Single colour images corresponding to CD58-HaloTag-JF549 in CD58LO U-2 OS cells, CD45 labelled with AF488-conjugated antibody on the primary CD8$^+$ T-cell surface and MitoTracker-stained mitochondria in both cell types are shown in (A). The overlay of the single colour images is shown in (B).

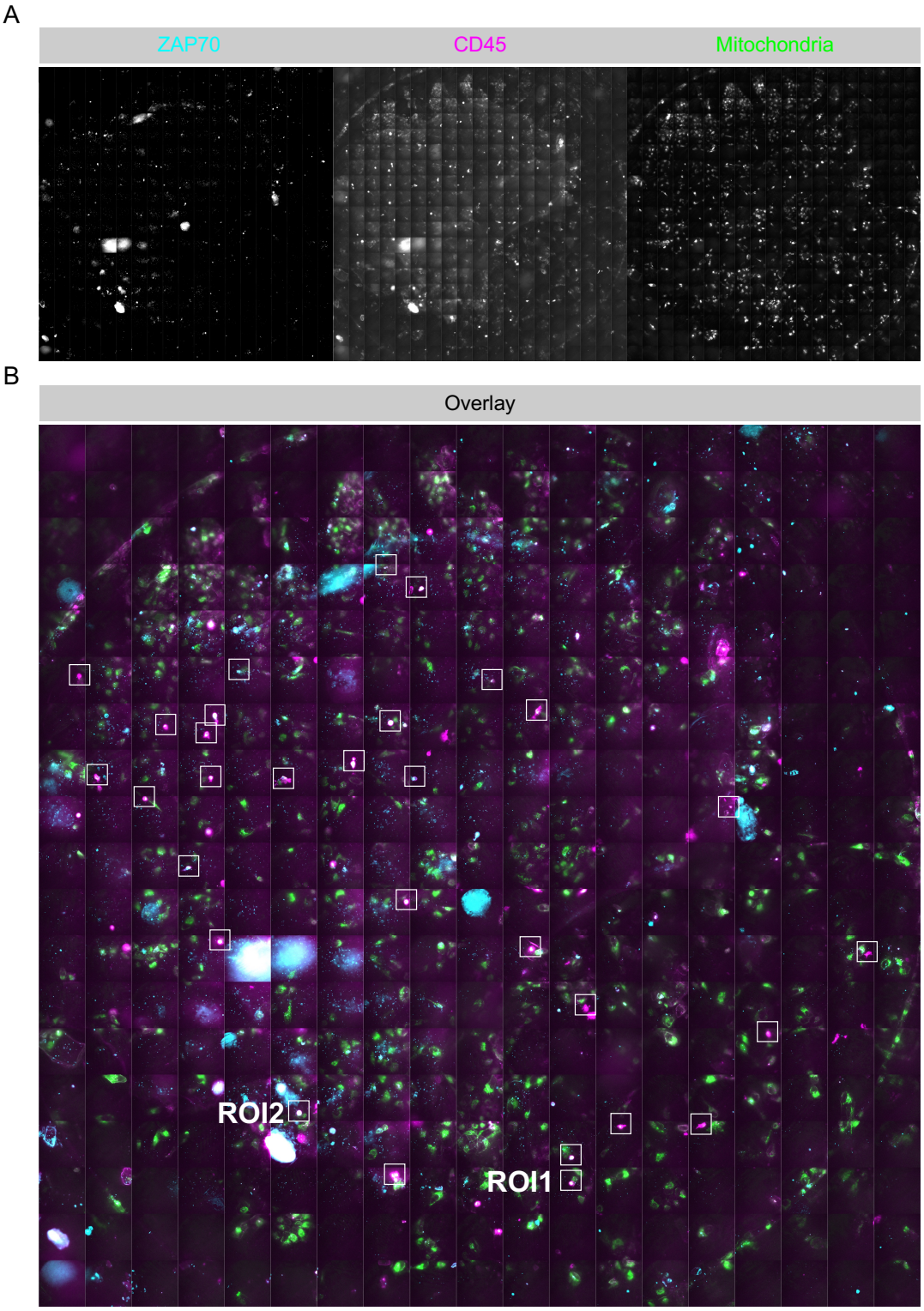


Figure 6.5: Cryo-fluorescence widefield montage of a coverslip containing ZAP70-HaloTag primary CD8$^+$ T cell/WT U-2 OS cell conjugates. A and **B**. Representative montage assembled from a widefield tile scan of the coverslip containing ZAP70-HaloTag primary CD8$^+$ T cell/WT U-2 OS cell conjugates. One of three coverslips is shown. Single colour images corresponding to ZAP70-HaloTag-JF549 in the T cells, CD45 labelled with an AF488-conjugated antibody on the T-cell surface and MitoTracker-stained mitochondria in both cell types are shown in (A). The overlay of the single colour images is shown in (B).

6.6). The number of visible CD58 puncta at the cellular interfaces was within the range established in the previous chapter. Puncta of ZAP70-HaloTag were readily observed at the interface with the WT U-2 OS despite the background fluorescence of the cytoplasmic ZAP70-HaloTag (Figure 6.7). No CD45 exclusion was visible at the T cell/U-2 OS interface for either of the conjugate types. In both unmodified and ZAP70-HaloTag T cells, spots of autofluorescence were observed in the channel corresponding to the JF549 (561 nm laser) that were not previously seen in the live-cell imaging data. Additionally, despite a high dilution (1:10,000) of the mitochondrial dye used for labelling of U-2 OS cells and two wash steps during sample preparation, the residual dye penetrated T cells resulting in fluorescent T-cell mitochondria.

Due to the restricted capacity of the CLEM pipeline, only two conjugates could be advanced to the FIB-SEM stage at the time. In the previous chapter, U-2 OS cells exclusively expressing CD58-HaloTag were used as a cancer cell model and interactions between T cells and WT U-2 OS cells were not imaged. Therefore, two ROIs containing a total of three 'CD58-HaloTag' conjugates were prioritised for this study and selected for FIB-SEM imaging to ensure continuity with the live-cell imaging experiments. ROI1 contained a single T cell/U-2 OS cell conjugate wherein the T cell retained the 'rounded' topology and engaged the apical membrane of the target cell (Figure 4.8A). ROI2 contained two T cell/U-2 OS cell conjugates wherein the T cell adopted the 'spread' morphology (Figure 4.8B). The cryo 3D-SIM images reconstructed using an optimised Gustaffson algorithm alongside the widefield images are shown in Figure 6.8. The improvement in resolution and the quality of the reconstruction were assessed using the Fourier transform (FT) of the images showing the 'interface' plane of the CD45 channel. In reciprocal space, the low resolution information corresponds to areas closer to the centre of the FT and the higher resolution is located further away. Consistent with the principles of SIM, the resolution of the 3D-SIM images was increased by ~2-fold as indicated by the 'rings' offset from the origin of the FT, corresponding to the high-resolution information within the observable region of the 3D-SIM

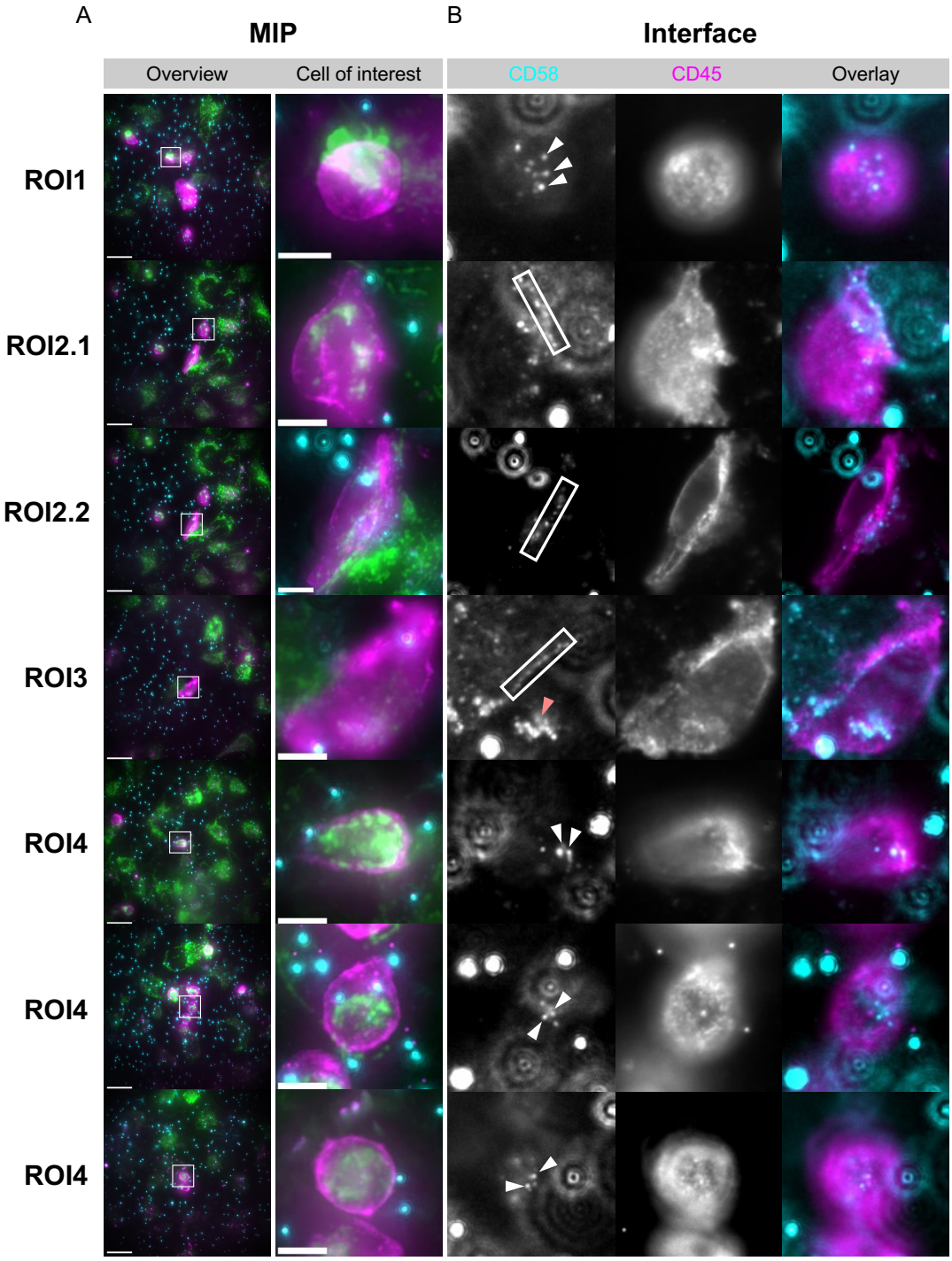


Figure 6.6: (Following page)

Figure 6.6: Cryo-fluorescence widefield microscopy images of primary CD8$^+$ T cell/CD58LO U-2 OS cell conjugates. A. Cryo-fluorescence widefield images of representative primary CD8$^+$ T cell/CD58LO U-2 OS cell conjugates. Images are shown as MIPs of the focal stack. T cells were stained with an AF488-conjugated anti-CD45 antibody (magenta) and JF549 HaloTag ligand to yield CD58-HaloTag-JF549 (cyan). The mitochondria of T cells and U-2 OS cells (green) were stained with MitoTracker. Bright spots uniformly distributed across the images correspond to the TetraSpeck microspheres. Overview of the entire ROI (left) and a close-up view of the cell of interest (right) are shown. Scale bar = 20 µm for the overview image. Scale bar = 5 µm for the close-up view. **B**. Cryo-fluorescence widefield images of planes corresponding to the T cell/U-2 OS cell interface. The white arrowheads and boxes indicate CD58 accumulation puncta corresponding to putative CCs. The pink arrowhead shows autofluorescence within the T-cell cytoplasm from an unidentified source.

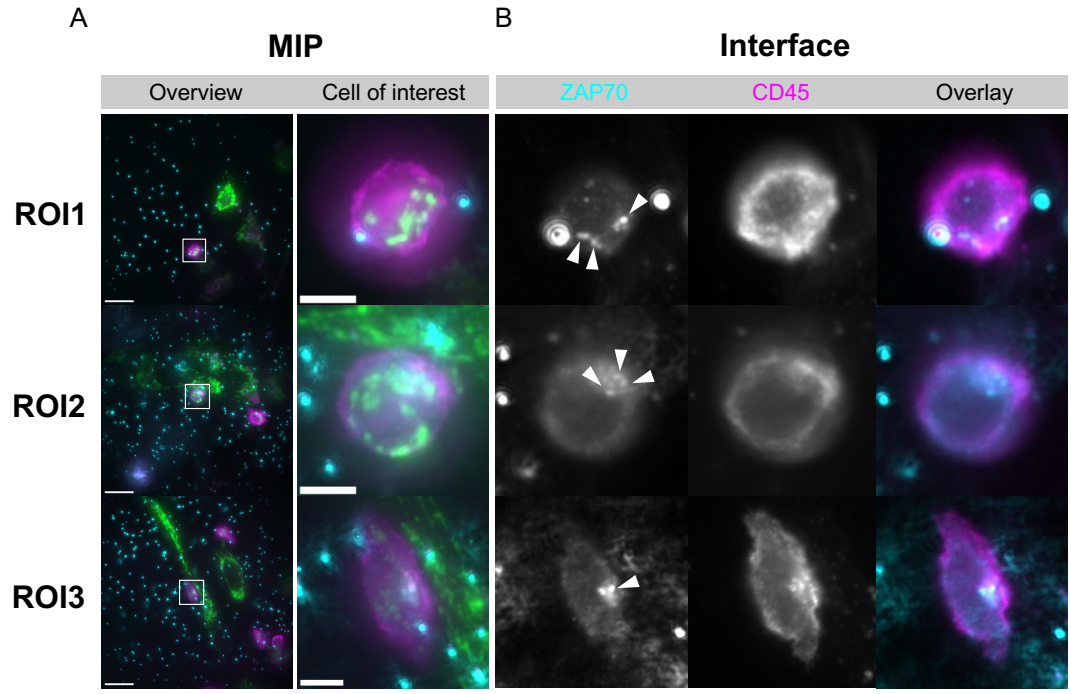


Figure 6.7: Cryo-fluorescence widefield microscopy images of ZAP70-HaloTag primary CD8$^+$ T cell/WT U-2 OS cell conjugates. A. Cryo-fluorescence widefield images of representative ZAP70-HaloTag primary CD8$^+$ T cell/WT U-2 OS cell conjugates. Images are shown as MIPs of the focal stack. T cells were stained with an AF488-conjugated anti-CD45 antibody (magenta) and JF549 HaloTag ligand to yield ZAP70-HaloTag-JF549 (cyan). The mitochondria of T cells and U-2 OS cells (green) were stained with MitoTracker. Bright spots uniformly distributed across the images correspond to the TetraSpeck microspheres. An overview of the entire ROI (left) and a close-up view of the cell of interest (right) are shown. Scale bar = 20 µm for the overview image. Scale bar = 5 µm for the close-up view. **B**. Cryo-fluorescence widefield images of planes corresponding to the T cell/U-2 OS cell interface. The white arrowheads indicate the ZAP70 accumulation puncta corresponding to putative 'signalling' CCs.

instrument. The FTs had a symmetrical appearance implying a good quality of the reconstructed 3D-SIM data.

6.2.3 FIB-SEM imaging of the primary CD8$^+$ T cell/U-2 OS cell conjugates

Preparation of the samples for FIB-SEM involved two procedures: freeze substitution (FS) followed by resin embedding. For the purposes of the cryo 3D-SIM, the samples were kept at ~77 K, but the FIB-SEM is performed at room temperature (~295 K). Thus, freeze substitution was performed to incrementally bring the samples up to the operating temperature of the FIB-SEM instrument over ~40 h. Immediately after, the samples were embedded in an eponate resin and individual resin blocks containing each of the ROIs were isolated using an ultramicrotome. The location of the conjugates within the resin was visualised using X-ray tomography before (Figure 6.9A) and after the ultramicrotome processing (Figure 6.9B and C). Following gold coating, the samples were mounted on the FIB-SEM instrument. Consecutive planes were removed from the face of the block at 4 nm intervals using a beam of gallium ions. Each newly exposed face was then imaged by the SEM module with the xy pixel size set to 4x4 nm resulting in 4x4x4 nm voxels. FIB-SEM imaging of ROI1 revealed that the T cell was not in contact with the U-2 OS cells (data not shown) and hence only FIB-SEM data for the two T cell/CD58LO U-2 OS cell conjugates in ROI2 were collected.

Both T cells in ROI2 engaged the respective U-2 OS cells from the 'side' with their basal membranes in contact with the coverslip (Figure 6.10). The cellular interface was primarily constituted by the lateral face of the T cells and partially by the apical membrane which led to the detachment of the interacting portion of the U-2 OS cell membrane from the surface of the coverslip. The interfacial T-cell membrane had a corrugated morphology and the microvilli-like protrusions on the T-cell surface appeared to be involved in direct interaction with U-2 OS. While most of the protrusions radiated directly from the cell body, portions of the T-cell membrane formed membrane 'microdomains' from which multiple

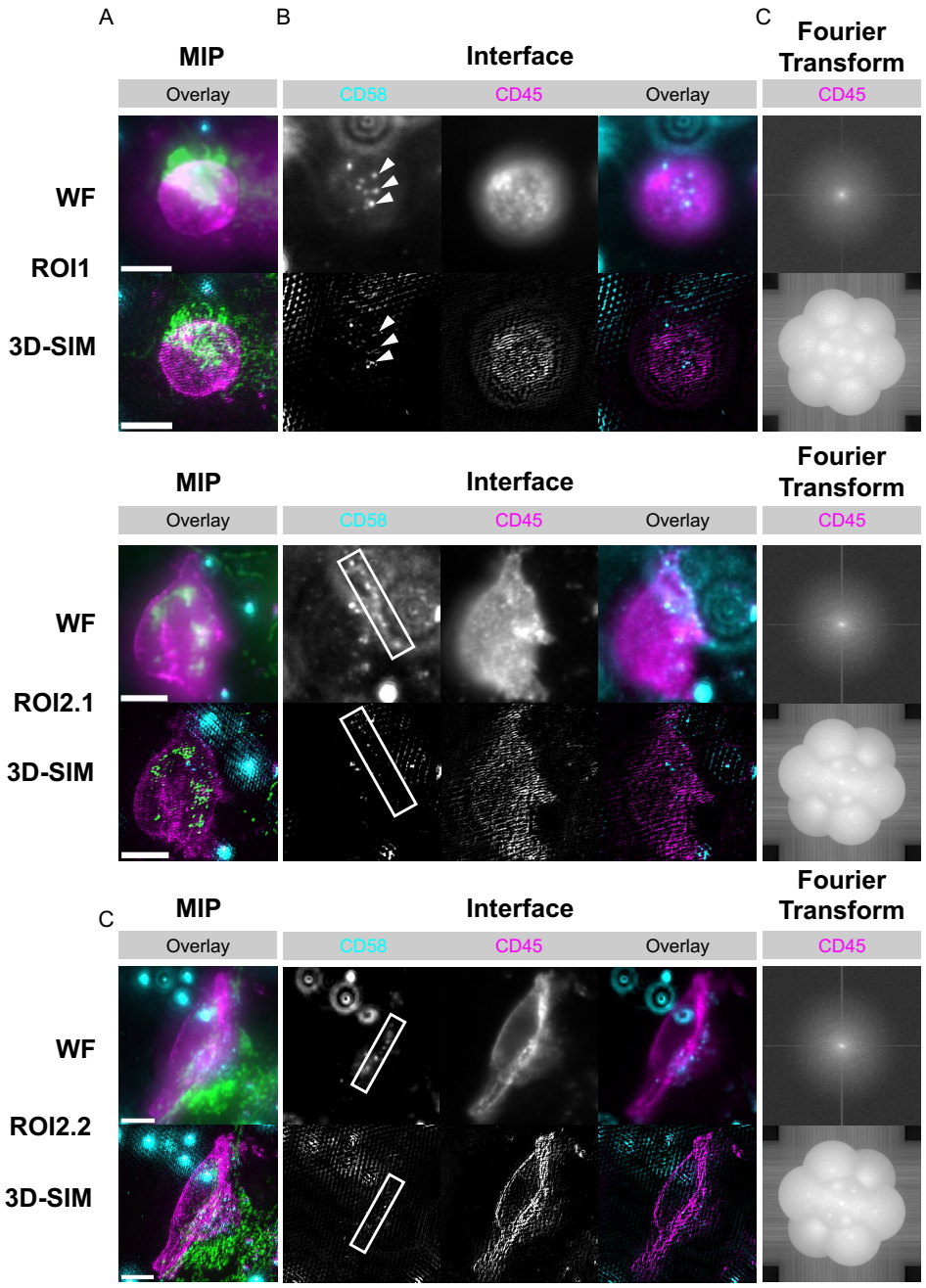


Figure 6.8: Cryo 3D-SIM images of primary CD8$^+$ T cell/CD58LO U-2 OS cell conjugates. A. Cryo-fluorescence widefield (top of each panel) and 3D-SIM images (bottom of each panel) of primary CD8$^+$ T cell/CD58LO U-2 OS cell conjugates selected for FIB-SEM imaging. Images are shown as MIPs of the focal stack. T cells were stained with an AF488-conjugated anti-CD45 antibody (magenta) and JF549 HaloTag ligand to yield CD58-HaloTag-JF549 (cyan). The mitochondria of T cells and U-2 OS cells (green) were stained with MitoTracker. **B**. Cryo-fluorescence widefield (top of each panel) and 3D-SIM (bottom of each panel) images of planes corresponding to the T cell/U-2 OS cell interface. The white arrowheads and boxes indicate CD58 accumulation puncta corresponding to putative CCs. **C**. Fourier transforms of the widefield and 3D-SIM images representing the resolution limit for the respective image type. The Fourier transforms were generated using the interface plane of the CD45 channel. Scale bar = 5 µm.

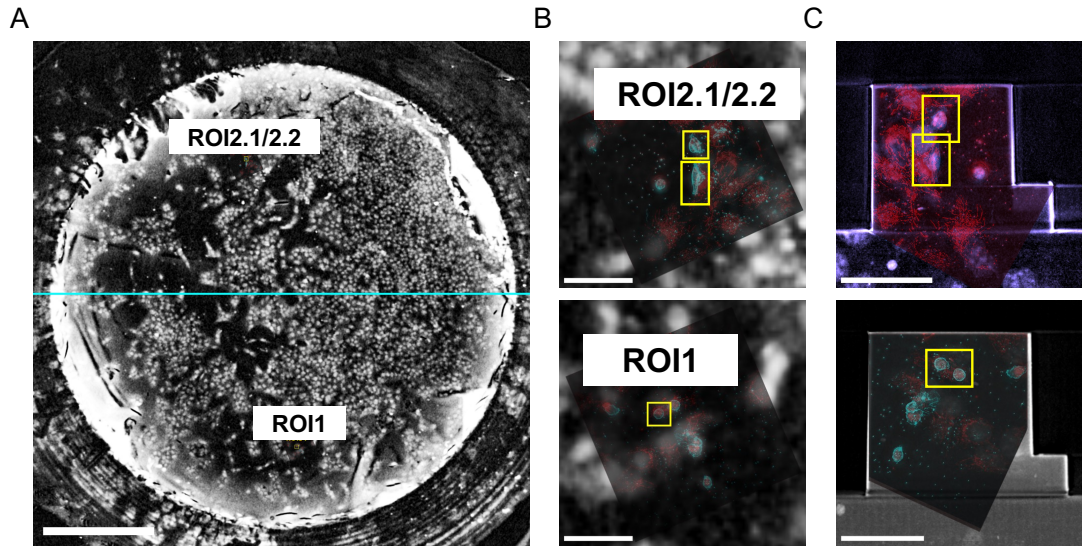


Figure 6.9: X-ray tomography images of resin-embedded primary CD8$^+$ T cell/CD58LO U-2 OS cell conjugates. A. X-ray tomography images of a coverslip containing primary CD8$^+$ T cell/CD58LO U-2 OS cell conjugates. The images were taken prior to ultramicrotome processing. The ROIs containing the conjugates selected for FIB-SEM imaging are highlighted. Scale bar = 500 µm **B**. Close-up views of the ROIs selected for FIB-SEM overlaid with the respective cryo-fluorescence widefield images. Scale bar = 5 µm **C**. X-ray tomography images of a coverslip containing primary CD8$^+$ T cell/CD58LO U-2 OS cell conjugates after ultramicrotome processing. The X-ray tomography images were overlaid with the respective cryo-fluorescence widefield images. Scale bar = 10 µm. X-ray tomography and sample preparation for FIB-SEM imaging were performed by Jesse Aaron.

protrusions extended towards the U-2 OS cell surface (Figure 6.10C, white box). The protrusions were less than 0.5 µm in diameter and significantly varied in morphology – some adopting a more extended, microvilli-like appearance, others had a globular shape. While the raw FIB-SEM data shown here are not sufficient to identify the protrusions that formed the CCs visible in the 3D-SIM images, several protrusions whose membrane density was located 8-16 nm (2-4 pixels) away from the U-2 OS cell surface are shown (Figure 6.10B and C). The intermembrane space that was not occupied by the T-cell protrusions was populated with extracellular vesicles, possibly ectosomes or exosomes[368,391]. Strikingly, the posterior T-cell membrane was predominantly smooth and contained very few microvilli.

At the time of writing the processing and combined analysis of the 3D-SIM and the FIB-SEM data was ongoing to produce 3D overlays of the two data sets. In the

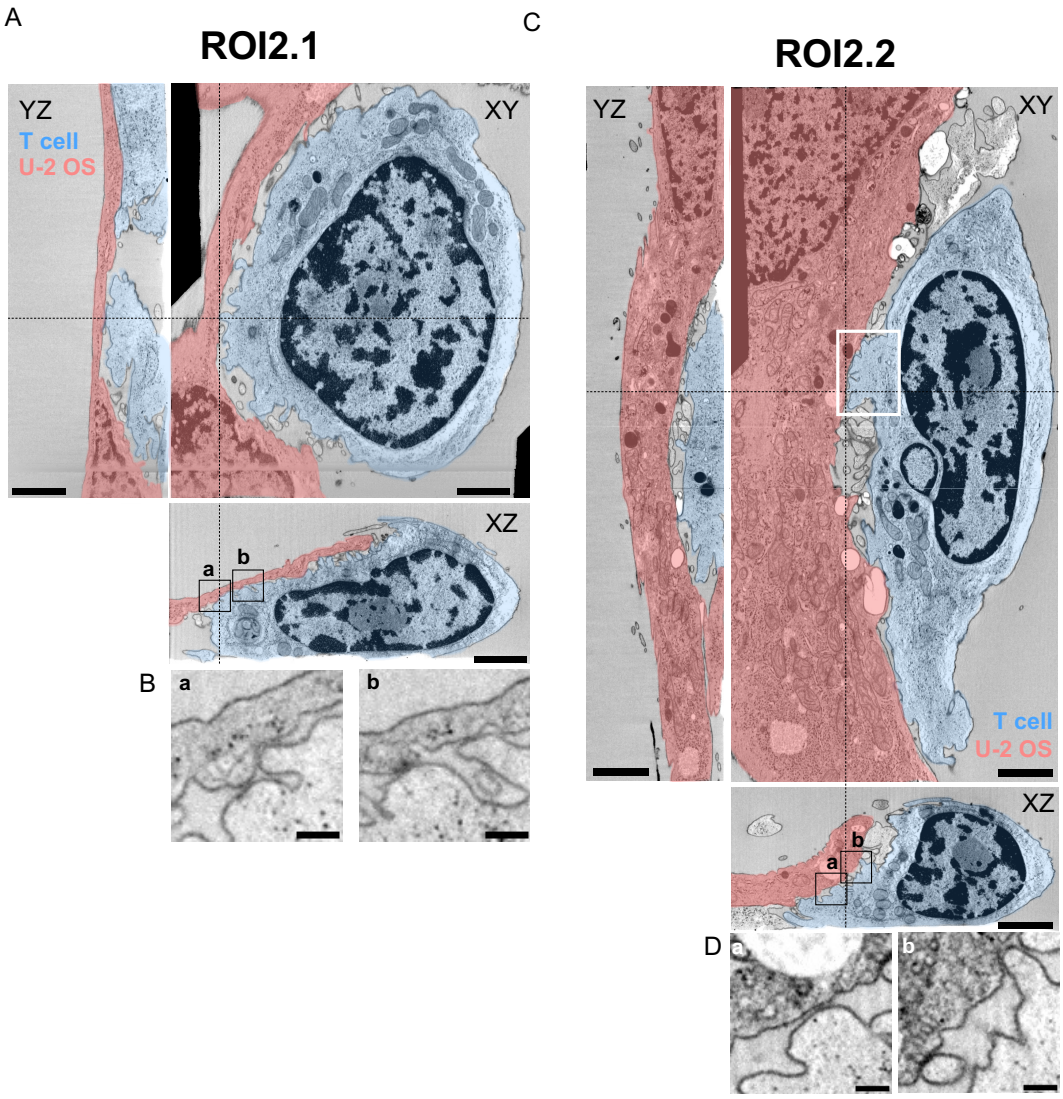


Figure 6.10: FIB-SEM images of primary CD8$^+$ T cell/CD58LO U-2 OS cell conjugates. A. FIB-SEM images of a primary CD8$^+$ T cell/CD58LO U-2 OS cell conjugate. Selected orthogonal planes corresponding to the interface between CD58LO U-2 OS cells (red) and primary CD8$^+$ T cells (blue). Cross-hairs indicate the relative positions of the orthogonal planes. Scale bar = 2 µm **B**. Close-up views of the microvilli-like protrusions on the T-cell surface forming putative contacts with the U-2 OS cell surface. Scale bar = 0.2 µm **C**. FIB-SEM images of a primary CD8$^+$ T cell/CD58LO U-2 OS cell conjugate. Selected orthogonal planes corresponding to the interface between CD58LO U-2 OS cells (red) and primary CD8$^+$ T cells (blue). Cross-hairs indicate the relative positions of the orthogonal planes. White boxes show T-cell membrane 'microdomains'. Scale bar = 2 µm **D**. Close-up views of the microvilli-like protrusions on the T-cell surface forming putative contacts with the U-2 OS cell surface. Scale bar = 0.2 µm. FIB-SEM imaging was performed by Jesse Aaron.

final format, the fluorescence of CD58-HaloTag and CD45 will be mapped onto the FIB-SEM data to verify which protrusions effectively engaged the target cell and analyse the relationship between the CD45 signal and the intermembrane distance.

6.3 Discussion

6.3.1 Production and validation of the N-MED ImmTAC

For the CLEM experiments, the N-MED ImmTAC was produced in-house. The in-house ImmTAC was expressed in a mammalian system in a soluble form, unlike the Immunocore ImmTAC which was expressed as inclusion bodies in *E. coli* and then refolded. Thus, the in-house ImmTAC contains a native set of N-linked glycans in contrast to the Immunocore-produced variant. It is important to note that in a native state, the variable regions of antibodies (V_L and V_H) which constitute the scFv typically bear little glycosylation, whereas TCR$\alpha\beta$ ECD contains ~5 N-linked glycans distributed across the variable and constant domains of both chains[392,393]. The SEC A_{280} trace and SDS-PAGE analysis indicated that the in-house ImmTAC was monodisperse.

The biophysical and functional properties of the in-house ImmTAC were validated using SPR as implemented by the Biacore 8K and co-culture assays, respectively. The binding affinities of the two ImmTACs to CD3ϵ were near-identical, but the in-house ImmTAC had a ~6-fold lower affinity for the GP100-MHC antigen than the Immunocore ImmTAC. The shift in the K_D value was primarily caused by the reduction in the on-rate which can perhaps be explained by the presence of N-glycosylation of the TCR$\alpha\beta$ chains. Previously negative effects of TCR glycosylation on binding to pMHC tetramers were reported, albeit no equivalent measurements were conducted for monomeric interactions[392]. Alternatively, the reduced k_{on} for binding of GP100-MHC, but not CD3ϵ by the in-house ImmTAC could be explained by a proportion of the bispecific containing a functional scFv segment and a misfolded, less biologically active TCR$\alpha\beta$ segment.

The in-house N-MED ImmTAC also had a lower biological activity than the Immunocore-produced counterpart. The merits of SPR as a tool for measurements

of scFv-CD3ϵ binding are discussed in section 3.3. The weaker binding of the in-house N-MED ImmTAC to GP100-MHC and the apparent lower biological activity led to ~1.6-fold decrease in its potency relative to the Immunocore ImmTAC. This was likely caused by reduced densities of the in-house TCR ligand at the apparently identical concentrations of both ImmTACs.

6.3.2 CLEM imaging of the T cell/U-2 OS cell interactions

The CLEM pipeline was used in an effort to establish the spatial relationship between the CCs and the membrane topography of the T-cell/U-2 OS cell interface. To this end, primary CD8$^+$ T cells and U-2 OS cell lines described in the preceding chapters were first imaged using cryo 3D-SIM followed by FIB-SEM. Two types of conjugates were imaged: primary CD8$^+$ T cells interacting with CD58LO U-2 OS cells or primary ZAP70-HaloTag CD8$^+$ T cell lines interacting with WT U-2 OS cells. Thus, CD58-HaloTag and ZAP70-HaloTag were employed as markers of CCs and 'signalling' CCs, respectively. Due to the limited capacity of the CLEM pipeline, three conjugates of the former type were chosen for FIB-SEM and only two were successfully imaged. The low throughput nature of CLEM is a significant downside of this method as it precludes statistically robust analysis.

The 3D-SIM images of the selected conjugates showed that multiple puncta of CD58 accumulation formed at the T cell/U-2 OS cell interfaces, similar in appearance to the CCs imaged in the previous chapter. Given the live-cell imaging data showing that CC formation was soon followed (~20-40 s) by calcium flux at the TCR ligand densities used here (section 5.2.7), likely, the selected T cells had triggered before high-pressure freezing. FIB-SEM images of the two conjugates showed that the T-cell membrane at the cellular interfaces was populated with numerous protrusions conferring a corrugated morphology. This was in contrast with the non-interacting T-cell membrane that lacked any substantial deformations. While some of the protrusions appeared to have an elongated morphology characteristic of microvilli, some of them had a 'stumpy' appearance. It could be speculated that these protrusions correspond to a

temporary state of the microvilli accompanying the transition to the flattened T cell/target cell interface previously described by Griffiths and colleagues[167,394]. It remains to be determined whether these structures have the properties of microvilli proper such as high mobility or a specialised protein distribution. It needs to be noted that the basal membranes of the two T cells extensively interacted with the sapphire coverslip which might have influenced their morphology. For instance, the T cell/coverslip interactions might have allowed the T-cell membrane to spread underneath the U-2 OS cells. A similar effect was seen by Ritter et al. where the mouse CD8$^+$ T cells also had substantial interface with the coverslip.

In contrast to non-cryogenic 3D-SIM which typically relies on high-NA immersion objectives, the cryo 3D-SIM imaging requires a non-immersion objective compromised by a low NA. The consequences of this feature are twofold i) reduced sensitivity, potentially precluding detection of dimmer objects such as transient CCs, ii) diminished resolution which decreases the precision with which the LM and EM images can be effectively correlated. This might be particularly detrimental for objects located along the axial direction. To overcome these challenges, CLEM pipelines were developed allowing 3D SMLM imaging techniques such as interferometric photoactivated localisation microscopy integrated with EM, but the low imaging depth limits the applicability of these methods[395]. The incompatibility of EM and SMLM sample preparation protocols and the lack of fluorescent labels compatible with both techniques pose another challenge to their combined use[396]. Alternatively, the fluorescent protein labels could be replaced with enzymes whose products can be readily visualised by EM. Examples of such EM-compatible tags include HRP, miniSOG or APEX2 with the latter being the superior option[397–400]. This strategy is also not without limitations as it would require imaging of conjugates expressing only one fusion protein at a time. Nonetheless, Stinchcombe et al. successfully used APEX fusion proteins to map the localisation of the TCR/CD3 complex and actin cytoskeleton onto the ultrastructure of CD8$^+$ T cells engaged in the killing of a cancer cell[368].

7
General discussion

The current understanding of the T cell/cancer cell interactions is incomplete. Intratumoural imaging provided useful insights into the dynamics of T-cell behaviour at a multicellular scale whilst imaging of T cell/cancer cell conjugates revealed the organisation of the cellular interface following antigen recognition. To date, the details of the very first interactions between T cells and target cells remained elusive. Furthermore, the mechanisms that initiate TCR phosphorylation and thus underlie T-cell activation beyond the context of cancer immunity are not agreed. Mounting evidence suggests that TCR triggering is driven by the segregation of the CD45 phosphatase and that antigen recognition occurs within CCs formed by the tips of T-cell microvilli interacting with the target cell. Yet conflicting evidence exists regarding the exclusion of the CD45 phosphatase from these sites and its role in TCR triggering. In Chapter 3, capitalising on studies of T cells in surrogate systems, a novel cellular system for the investigation of antigen recognition was created and characterised. To study unmodified primary $CD8^+$ T cells, a bispecific molecule known as an ImmTAC was used as an artificial TCR ligand. In Chapter 4, the molecular correlates of ImmTAC potency were identified through a series of modifications showing that N-terminal ImmTACs effectively emulate properties of native TCR ligands. Additionally, these experiments pointed to a central role of CC architecture and the local kinase/phosphatase balance in

TCR triggering. In Chapter 5, the CCs and the molecular organisation therein were visualised at authentic T cell/cancer cell interfaces using live-cell fluorescence imaging. In the final results chapter, the topography of this interface was mapped to begin exploring the structural relationship between CCs and the T-cell surface.

7.1 ImmTACs as synthetic TCR ligands and immunotherapeutics

The search for a universal T-cell agonist capable of eliciting physiological signalling in a polyclonal T-cell population has yielded a series of ligands mimicking pMHC molecules[355,401–403]. In this study, a novel bispecific therapeutic, known as an ImmTAC, was adopted as a model TCR ligand. The functional features of ImmTACs established in this work will be discussed in terms of the fundamental properties of native TCR ligands: single-molecule potency, compact architecture, and compatibility with accessory molecules. ImmTACs are also the first-in-class TCR-based bispecifics approved for use in the clinic. Therefore, they will also be compared to other types of T cell-redirecting therapeutics.

7.1.1 ImmTAC potency rivals that of native TCR ligands

The potency of TCR ligands is determined by a balance between two countervailing effects: serial triggering and kinetic proofreading[257,278,280,281,404]. As a result, the relationship between the TCR/pMHC affinity and potency is not linear but rather follows a bell-shaped curve. T-cell activation by ImmTACs conformed to this trend. The N-MED ImmTAC ($K_{D,\ CD3\epsilon}$ = 197 nM) was the most potent of the three N-terminal ImmTAC and was closely followed by the twofold less potent N-LO variant ($K_{D,\ CD3\epsilon}$ = 7.87 μM). The potency of the N-HI ImmTAC ($K_{D,\ CD3\epsilon}$ = 1.81 nM) was 14-fold lower than that of the N-MED ImmTAC. However, all N-terminal ImmTACs induced identical T-cell responses at saturating doses. The subpar potency of the N-HI ImmTAC is in line with experimental evidence suggesting that serial triggering is only functionally relevant for ligands with a supraphysiological affinity for the TCR/CD3 complex at low densities[279,282,351].

Remarkably, a single pMHC molecule can activate a T cell[59,61,62,234,274]. Studies of synthetic ligands, similar to ImmTACs in their engagement of the TCR/CD3 complex through antibody-derived fragments, demonstrate that a single Fab-based ligand is sufficient for productive T-cell activation[355]. Consistently, in Appendix 1, through TIRFM imaging of primary $CD8^+$ T cells on SLBs, it was demonstrated that a single N-MED ImmTAC is sufficient to induce calcium flux.

7.1.2 Topological requirements of synthetic TCR ligands

It is well-established that a ligand's dimensions are a key determinant of its capacity to activate T cells. The extension of native and artificial ligands of both αβ and γδ TCRs was shown to reduce their potency[263–265,267,365]. To assess the impact of size on the signalling capacity of ImmTACs, two complementary approaches were taken to change their dimensions. The first involved altering the linkage of the scFv and TCRαβ ImmTAC segments to generate a C-terminal variant (C-MED) of the most potent N-terminal ImmTAC (N-MED) extending it by ~7 nm. The second approach relied on the insertion of an inert scaffold composed of 4 IgSF domains (~14 nm) into the GP100-MHC structure. For all of the tested configurations of the CD3ϵ/ImmTAC affinity with the two types of extension, T-cell signalling was substantially reduced (30- to 3-fold). These topology-driven principles have been applied to other T-cell redirecting therapies beyond ImmTACs. Staufer et al. found that reducing the distance between the CD3ϵ- and TAA-binding Fab arms of antibody-based bispecifics improved their potency[352]. Moreover, targeting membrane-proximal epitopes of TAAs generally yields more efficacious T cell-redirecting bispecific antibodies[405,406]. The differences in the potency of compact versus extended ligands can be explained in part by the CD2/CD58 pair acting as a 'contact gatekeeper'. As illustrated by the imaging of T cell/U-2 OS cell interactions in Chapters 5 and 6, the CCs are stabilised by the CD2/CD58 pair. As a result, access of the larger TCR ligands to the signalling-permissive CC is restricted and their binding to TCR/CD3 complex within the CC would be hindered. In Chapter 4, the

interactions between the CD2/CD58 pair and two TCR ligands of different sizes, but identical affinities (N-MED and C-MED ImmTAC) were examined showing that the small adhesion molecules likely antagonise the larger ligand. Burton et al. demonstrated that a similar mechanism is likely responsible for poorer antigen sensitivity of CARs relative to the TCR/CD3 complex as the artificial antigen receptor likely cannot efficiently co-localise with the CD2/CD58 pair due to its extended architecture[349]. An alternative mechanism explaining the reduced potency of the larger TCR ligands has been proposed[267,352,406]. Large ligand/TCR/CD3 complexes could contribute to overall adhesion within CCs along with the CD2/CD58 pair increasing the intermembrane distance and reducing the CD45 exclusion therein[265,267,352,406]. The balance of these two mechanisms is presumably dictated by the relative densities of CD58 and the ligand on the target cell surface. In physiological settings, it is more likely that CD45 exclusion is primarily driven by the CD2/CD58 pair as the density of CD58 on the target cell surface is likely to exceed that of the cognate pMHC molecules. There might be a few notable exceptions, for instance, some non-pMHC TAAs such as HER2 are highly expressed by cancer cells (up to ~100 molecules per μm^2) and CD58 is often downregulated by tumours[34,36,352,407]. Under such circumstances, the interactions of a bispecific-bound TAA with the TCR/CD3 complex could be the dominant form of adhesion within cellular contacts.

7.1.3 Geometrical requirements of CD8 recruitment

Conventional interactions between pMHC class I molecules and $\alpha\beta$TCRs lead to the recruitment of CD8 co-receptors to form a ternary pMHC/TCR/CD3/CD8 complex. The capacity of the CD8 co-receptor to augment T-cell responses is restricted to pMHC/TCR/CD3 complexes whose spatial arrangement maintains the CD8 binding site, located at the α3 domain of MHC-I, within ~14 nm from the T-cell surface[57,357]. This principle is illustrated by TCRs which bind to pMHC with a reversed docking polarity, whereby the α3 domain is positioned ~5 nm further away from the T-cell membrane, effectively preventing CD8 recruitment[57,357].

Therefore, CD8 can be likened to a piece of a jigsaw puzzle that interlocks solely with a pMHC/TCR/CD3 complex of a prescribed shape. Notably, results consistent with CD8 recruitment were only obtained for the N-terminal, and not C-terminal ImmTACs, suggesting that the N-terminal variants mediate the formation of a pMHC/ImmTAC/TCR/CD3 complex which minimally deviates from the native complex in terms of its geometry. These findings are supported by prior observations that N-terminal ImmTACs preferentially stimulate $CD8^+$ T cells over $CD4^+$ T cells in co-cultures of PBMCs with ImmTAC-labelled $GP100^+$ melanoma cell lines[331]. Whilst bispecifics engaging non-pMHC TAAs were shown to promote tolerogenic responses that negatively impact clinical outcomes, the favourable activation of $CD8^+$ T cells by N-terminal ImmTACs may limit such an effect[408–410]. Moreover, CD8 recruitment to the ImmTAC-bound TCR/CD3 complex partly explains the ~1000-fold difference between the potency of ImmTACs and bispecifics targeting non-pMHC antigens such as blinatumomab (CD19-BiTE)[298,299,411]. Co-opting CD8 signalling increases antigen sensitivity by stabilising the primed TCR/pMHC complex[105,107,118]. In consequence, the lower affinity TCR/pMHC interactions display a greater dependence on CD8 recruitment[62,112]. In experiments in Chapter 4, through modifications of the CD8 binding site, a similar relationship was found to apply to the interactions of N-terminal ImmTACs and the TCR/CD3 complex. Ablation of the CD8 binding site had a greater impact on the potency of low-affinity ImmTACs whereas the high-affinity ImmTAC (N-HI) showed limited dependence on CD8 recruitment for T-cell activation.

7.2 Interactions of T cells with genuine cellular surfaces

This thesis provides the first description of the entire T cell/target cell 'interaction cycle' in a cellular system. In Chapters 5 and 6 the interactions of primary $CD8^+$ T cells with U-2 OS cells were visualized from the formation of the first CCs through signalling and assembly of an early immune synapse. The main

aspects of these processes will be discussed with a focus on the mechanisms leading to the stabilisation of microvilli on the target cell surface, their subsequent scanning behaviour, and remodelling of the cellular interface upon TCR triggering culminating in the formation of synapse-like structures.

7.2.1 How are the microvilli stabilised on the cancer cell surface?

Once T cells have settled on the U-2 OS cell monolayer they have likely engaged in active probing of the local environment through the oscillatory motion of the microvilli attempting to contact the target cells[137,168,197,201,412]. This motion was visualized by Jenkins et al. as T-cell microvilli approaching the SLB surface within a distance of <0.2 μm without forming detectable CCs[137]. At this point, the T-cell behaviour is likely to be agnostic of the molecular composition of the target cell surface. Still, as the microvillus approaches the target cell surface, it will face physical resistance from the glycocalyx barrier. The probability of a microvillus penetrating the glycocalyx layer of the U-2 OS cells to form a first CC was highly dependent on the presence of ICAM-1. With ICAM-1 on the U-2 OS cell surface, the first CD58-demarcated CC formed within seconds from a T cell settling on the U-2 OS cell monolayer, but in its absence, T cells appeared to be gliding across the surface of the monolayer on a timescale of minutes before forming detectable CCs. But, how do the CD2/CD58 and LFA-1/ICAM-1 adhesion pairs cooperate to stabilise the microvilli?

The SMLM and SEM studies of the resting T-cell surface showed that microvillar tips contain over 90% of total CD2 but less than 5% of total LFA-1[169,175,176]. Furthermore, it has been shown that LFA-1 is excluded from CCs, thus initially the CD2/CD58 pair is likely to have a dominant role in stabilising the very first interaction[137,143,413]. Jenkins et al. found that immediately following the accumulation of CD2/CD58 at the CC, it becomes surrounded by a ring of LFA-1/ICAM-1. Similar LFA-1/ICAM-1-based structures were reported to form around TCR microclusters, likely corresponding to CCs[413,414]. In the present

study, ICAM-1 expressed by U-2 OS cells was not labelled, hence to verify the mechanism of microvillar stabilisation, follow-up experiments ought to be conducted using target cells expressing a fluorescent ICAM-1 fusion protein.

7.2.2 How do T cells scan the target cell surface?

In the presence of the TCR ligand, the scanning stage was short-lived with calcium flux occurring shortly after CC formation. The experiments in the absence of ImmTAC provided insight into the T cell-target cell interactions during prolonged 'scanning', a better reflection of the T-cell behaviour in a lymph node or in a tumour where it engages multiple cells in rapid succession[415,416]. In the absence of ICAM-1, the morphology of the T cell did not change significantly throughout the interactions with an invariable low T-cell footprint (~6 μm^2 at t = 3 min) and sustained oscillatory motion of the microvilli forming sparse, transient CC (<10 at t = 3 min). When ICAM-1-presenting target cells were used, T cells spread over the U-2 OS cell surface forming numerous CCs (>20 at t = 3 min) and achieving a footprint (~45 μm^2 at t = 3 min) almost as large as the ligand-exposed T cells (~50 μm^2 at t = 3 min). However, the persistence of CCs remained relatively low, consistent with a continuous re-adsorption and projection of microvilli from the T-cell body[168]. Similarly, Jenkins et al. found that the removal of ICAM-1 from non-agonistic SLBs drastically reduces the footprint of primary $CD8^+$ T cells, but in that study, it was CD58, not ICAM-1, that determined the number of CCs formed at the interface of primary $CD8^+$ T cell with the SLB[137]. The glycocalyx layer on the SLB used by Jenkins et al. is ~10-fold shorter than that of the U-2 OS cells. Therefore, it could be speculated that as the thickness of the glycocalyx increases, T cells become increasingly reliant on the higher-affinity and more accessible integrin-based adhesion to anchor the microvilli and engage CD58[137].

The T-cell spreading on ICAM-1-presenting U-2 OS cell surface in the absence of TCR signalling is a somewhat unexpected observation, as conventionally, prior antigenic stimulation is required to activate LFA-1/ICAM-1-mediated adhesion[123,129,417]. This regulatory mechanism of LFA-1, known as 'inside-out'

signalling, dictates that in the absence of a TCR ligand, ICAM-1 should have a limited effect on the T cell/target cell interactions. Despite the spreading behaviour, co-culture assays of T cells with CD58LO+ICAM-1 U-2 OS cells indicated no T-cell activation without ImmTAC. These results are supported by studies showing that resting T cells have basal levels of active LFA-1 allowing for some adhesion to occur without complete immobilisation on the target cell surface[124,128]. Lacouture et al. found that this basal state could be underpinned by a significant proportion of LFA-1 (38%) adopting the open conformation on ICAM-1-presenting surfaces in the absence of TCR ligands[128].

7.2.3 Effects of signalling on the T cell/U-2 OS cell interface

Strikingly, the presence of ICAM-1 rather than the TCR ligand on the U-2 OS cell surface was the primary determinant of T-cell behaviour. The notable exception was the area of individual CCs which increased by 50-70% following calcium flux. For instance, the average CC area for T cells interacting with ICAM-1-presenting U-2 OS cells with and without the TCR ligand were 0.178 and 0.116 μm^2, respectively. This could be explained by an improved stabilisation of the microvilli which led to increased CD58 accumulation in the CCs or their dilation. The following mechanisms could explain this effect. First, the proportion of LFA-1 in the open conformation likely increased in response to TCR stimulation allowing traction forces to be exerted by the actin cytoskeleton on the integrins[124,129,417]. Second, the additional stabilisation could be provided by the delayed accumulation of the ternary pMHC/ImmTAC/TCR/CD3 complex in the CCs, which, compared to the CD2/CD58 complex, would have an exaggerated role in stabilising the CC due to its supraphysiological affinity. Furthermore, TCR triggering would allow for the pMHC/ImmTAC/TCR/CD3 interaction to be reinforced through binding of the CD8-bound Lck to the phosphorylated ITAMs, thus forming a quaternary complex[105–107].

T-cell spreading in response to antigen is considered to be required for the amplification of TCR signalling through sustained recruitment of downstream signalling proteins such as ZAP70, LAT and SLP-76 into the CCs[137,168,195–197]. Consistent with these observations, following TCR triggering, TCR/CD3 complex accumulation and ZAP70 recruitment to the CCs were detected during the spreading burst.

7.2.4 Formation of synapse-like structures at the T cell/cancer cell interface

Imaging studies of the effector $CD8^+$ T cell-target cell conjugates suggest that the final stage of the interaction involves contraction of the T-cell footprint, accompanied by a centripetal migration of the CCs to form a monofocal immune synapse[137,205,210]. In the prototypical $CD8^+$ T-cell synapse, the centre of the interface flattens, giving rise to a cSMAC, where the TCR signalling is terminated and the secretory domain is assembled.[137,194,195,205,210]. It was reported that CD2/CD58 accumulates in the cSMAC along with the TCR[137,203]. In the present study, T-cell behaviour reminiscent of immune synapse formation was only seen on ICAM-1-presenting cell surfaces with the T-cell agonist present. The contraction was accompanied by a reduction in the number of CC (<20 CC/cell at t = 25 min) with the remaining CC concentrating in the centre of the interface. The CC did not coalesce into a cSMAC and instead adopted a multifocal organisation previously observed at the interfaces of naïve $CD8^+$ T cells and DCs or Th2-polarised $CD4^+$ T cells and fibroblasts[214,215]. Interestingly, the morphology of the CCs, equivalent to the individual foci, was unperturbed by this process, retaining the ~500 nm diameter. This finding is consistent with previous reports on the T cell/DC multifocal synapse, where the width of the foci ranged from 160 to 470 nm[215].

Recently, it was reported that the CD2/CD58 pair is arranged into ring-like corollas at the edge of the synapse, where the signalling of co-stimulatory and inhibitory receptors is sustained[208]. However, the CD2/CD58 corollas were absent from the T cell/U-2 OS cell interfaces. It is possible that formation of

such late-stage structures is dependent on the composition of the target cell surface[213]. Demetriou et al. predominantly observed corolla formation at high CD58 densities, upwards of 100 molecules/μm^2 – 16-fold times the density of CD58 on the imaging U-2 OS cell lines[208]. Similarly, the formation of an extensive close contact such as the cSMAC could be hindered by the thick glycocalyx of cancer cells, favouring the multifocal organisation at the synapse.

7.3 Mechanisms of TCR triggering

The question of how the binding of ligands to the TCR/CD3 complex is transduced to initiate phosphorylation i.e. 'TCR triggering' is subject to ongoing debate. Two models are currently favourably viewed in light of the most recent evidence – the KS model and the mechanotransduction model. This thesis is well-positioned to assess the former, and therefore, its findings will be primarily discussed in the context of the KS model.

7.3.1 CD45 exclusion from close contacts

The KS model posits that as the CCs form at the interface of two cells, the CD45 exclusion therein shifts the local balance of kinase-phosphatase activity to favour TCR phosphorylation[255,385]. TIRFM imaging of T cells on APC surrogates enabled the exclusion of CD45 from CCs to be reliably observed, albeit the reported exclusion values range from as low as 10% to 80%[137,194,256,258,365,418]. The ~40% exclusion reported by Jenkins et al. is likely the most accurate of these estimates owing to the use of an advanced SLB system[137]. However, the results produced in the T cell/SLB systems are not consistent with findings by Krummel and colleagues who observed no CD45 segregation at the microvillar contacts formed at the interface of T cell/APC conjugates[168].

As reported in Chapter 5, the imaging of live T cells on U-2 OS cell monolayers using eWM and eSPIM microscopy did not reveal significant CD45 exclusion from the CCs. Similarly, no substantial CD45 segregation from CCs was observed using the 3D-SIM imaging of cryofixed T cell/U-2 OS cell conjugates in Chapter

6. CD45 exclusion was only detected when an instrument with a superior optical sectioning capacity was used. Removal of the out-of-focus fluorescence signal allowed the CD45 exclusion to be measured, placing it at ~10% on average with several bright CCs displaying exclusion values up to ~25%. The low CD45 segregation was apparently sufficient to drive TCR phosphorylation as ZAP70 was readily recruited to the CCs.

Considering the variability of the CD45 exclusion values generated through different types of measurements, it is imperative to evaluate whether the 10% exclusion is an artefact of the methodology of the present study. It is plausible that the measurable CD45 exclusion is a function of the instrument's optical sectioning capacity and resolution, i.e., 3D SMLM would yield higher exclusion values than those obtained through SDCM imaging. However, should the 10% exclusion reflect the genuine events at cell/cell surfaces, the latest mathematical models should be reparametrised accordingly[256,259]. As per the model formulated by Fernandes et al., the reduced ratio of net kinase activity between the contact and non-contact areas would improve antigen discrimination, at the expense of antigen sensitivity and the speed of antigen recognition[256]. If the updated model fails to account for the rapid T-cell responses at low ligand densities, other assumptions underpinning the KS model would need to be reexamined.

The KS model posits that CD45 segregation alone can drive TCR phosphorylation, implying that *de novo* Lck activation in the CCs is not required. However, it does not explicitly rule out this possibility[260]. Bulk FRET and immunofluorescence data indicate that the amount of active Lck does not change following TCR triggering[77,79]. Yet, recent findings suggest that the proportion of active Lck might increase in response to TCR stimulation[78]. It is conceivable that a reduction in CD45 activity could favour selective dephosphorylation of the inhibitory Y505 of Lck, but not the activating Y394, thereby increasing the Lck trans-phosphorylation rates within the CCs. This hypothesis is supported by studies showing that CD45 has a mostly negative effect on Lck activity, especially at high phosphatase levels[76,90,92,419]. Thus, the small shift in the phosphatase

activity may initiate a local self-amplifying phosphorylation cycle. The important caveat, as highlighted by Davis and van der Merwe, is that rapid diffusion of the free Lck through the CCs could impede such a mechanism[260]. Recently, it was shown that Lck is confined within the microvillar tips likely through its association with co-receptors or CD2. Therefore, there is a population of slow-diffusing kinase that could be responsive to the local changes in the phosphate levels[169]. Genetically-encoded FRET Lck sensors, akin to those used by Philipsen et al., could be incorporated into the T cell/U-2 OS cell system to inspect the Lck activation state within the CCs[78]. This approach would enable the ratio of local kinase/phosphatase activity in the CCs to be calculated and evaluated using quantitative methods.

7.3.2 Close-contact size

The size of the CCs needs to be constrained as CD45 exclusion over a large area of the T-cell membrane leads to non-specific activation[86,137,255,366]. According to the mathematical models of TCR triggering, individual CC should be less than 500 nm in diameter to ensure efficient antigen discrimination[256,259]. Imaging studies of T cells in systems relying on APC surrogates, consistently indicate that the diameter of CCs is within a 400-500 nm range[137,168,194,198]. In agreement with these findings, the present study indicates that the initial CCs (t = 0) formed by T cells on all types of U-2 OS cell surfaces had an average diameter of ~420 nm (area of ~0.137 μm^2). Following TCR triggering, the CC size marginally increased, likely due to secondary stabilising effects (discussed in section 7.2.3), but the average diameter did not exceed 560 nm.

The sizes of CCs measured using live-cell imaging stand in contrast to the dimensions of microvilli on resting $CD8^+$ T cells defined by the SEM images (diameter of ~80 nm) and putative contact areas visualised by FIB-SEM (~200 nm across). This disparate data can be reconciled in several ways. First, the light-diffraction limit increases the apparent size of objects at submicron scales. Thus, in reality, the CCs are likely smaller than implied by the live-cell microscopy

data presented in Chapter 5. Second, the processing of samples for both types of EM imaging may distort the specimen. Finally, it could be speculated that the accumulation of adhesive interactions at the microvillar tip may lead to its dilation and flattening against the target cell surface. Razvag et al. showed that indeed the CCs might expand over time[370]. These factors pose a challenge to the faithful estimation of the CC dimensions, but these issues might at least be partially tackled by 3D SMLM methods affording spatial resolution that is better matched to the dimensions of microvilli.

The mathematical models indicate the formation of CCs exceeding a diameter of 700 nm (area of 0.385 μm^2) would lead to the loss of antigen discrimination[256]. Consistent with these predictions, supraphysiological densities of CD2/CD58 adhesion on SLBs were shown to lead to the formation of abnormally large CCs and T-cell activation in the absence of cognate pMHC[86,137]. In Chapter 4, it was shown that the overexpression of CD58 on the U-2 OS cell surface leads to the activation of T cells in the absence of TCR ligand. Moreover, the CC formed at the interface of T cells and CD58-overexpressing target cells had an average area of 0.920 μm^2 exceeding the previously proposed 0.385 μm^2 threshold[256]. The increase in the size of CCs upon CD58 overexpression can be explained by the mechano-adhesive function of the CD2/CD58 pair. Additionally, recruitment of Lck to the cytoplasmic domain of CD2 could further contribute to the increased phosphorylation rates of the TCR/CD3 complex in the enlarged CCs[139,140,145–147,420,421]

Similar to the overexpression of CD58, strengthening the CD8$\alpha\beta$/HLA-A2 interaction has also led to T-cell activation in the absence of the TCR ligand. By switching the GP100-MHC from the WT (K_D = 137 μM) to the A2-K^B (K_D = 11 μM) variant, the affinity of the interaction was increased by ~13-fold. With an affinity similar to that of the CD2/CD58 binding (K_D = ~20 μM) and CD2/CD58-like dimensions, the complex of CD8$\alpha\beta$ with the A2-K^B variant increased the pool of small adhesion molecules. It is likely that similarly to CD58 overexpression, this resulted in a considerable CC dilation. Given the

association of the CD8α chain with Lck, increased enrichment of CD8 within the CC could further increase the local kinase activity[98,99]. These results are in line with the findings reported by Wooldridge et al., who showed that $CD8^+$ T cells can mount cytotoxic responses against target cells expressing A2-K^B molecules in the absence of a cognate peptide[422].

Taken together, these results indicate that the components of the antigen recognition apparatus have evolved into a delicate network of interactions optimised for rapid yet sensitive identification of non-self. How exactly these perturbations of CD58 and CD8 alter the architecture of the cellular interface could be investigated through a series of CLEM experiments similar to those presented in Chapter 6.

7.3.3 Insights into other models of TCR triggering

The mechanotransduction and allosteric models of TCR triggering invoke the location of the ligand binding site or even conformational changes within the ligand itself as determinants of signalling outcomes[249,253,423]. The binding sites of the UCHT1 scFv and pMHC molecules on the TCR/CD3 complex are located far apart and the two ligands are structurally distinct. According to the mechanotransduction model, synthetic ligands of this type might not be able to recapitulate the signalling properties of native ligands. Nonetheless, binding of ImmTACs to the TCR/CD3 complex resulted in ZAP70 recruitment, calcium flux, upregulation of surface activation markers, and ultimately target cell killing[316,331]. Also, *bona fide* single ImmTAC molecules can trigger the T cell (Appendix 1). It is conceivable that the UCHT-1 epitope could be uniquely positioned allowing the conformational changes to be induced via an alternative allosteric mechanism. However, this notion is inconsistent with findings reported by Wilhelm et al. showing that Fab-based ligands binding to various epitopes on the murine TCR/CD3 complex can elicit pMHC-like signalling as long as the physiological dimensions are maintained[355].

Finally, implicit in the mechanotransduction models is that antigens are discriminated based on their ability to form slip or catch bonds with the TCR[251,252].

However, recent findings by Pettmann et al. challenge this assumption[288]. Rather than improving antigen discrimination as proposed by the mechanotransduction model, forces seem to have the opposite effect. Interestingly, CD2/CD58- and LFA-1/ICAM-1-mediated adhesion was shown to favour discrimination by shielding the TCR/CD3 complex from external forces[288]. As established in this thesis, the microvillar CCs are stabilised by the accumulation of CD2/CD58 pair and the larger cellular interface by LFA-1/ICAM-1 pair. Therefore, given the ubiquitous expression of CD58 and ICAM-1 across tissues, it is likely that the involvement of forces in TCR triggering is limited to enable effective discrimination of antigens.

7.4 Concluding remarks

The central aim of this thesis was to identify the mechanisms of TCR triggering and antigen recognition at native cellular interfaces. To this end, a cancer cell was adopted as a model cellular surface and a bispecific molecule, used for cancer immunotherapy, was repurposed as a universal T-cell agonist. First, the determinants of an effective bispecific-based therapy were examined. It was established that the affinity of the bispecific/TCR/CD3 interaction should be engineered to surpass the physiological levels, but not beyond a threshold that impedes serial triggering. To efficiently activate T cells, bispecifics should preserve the native architecture of the pMHC/TCR/CD3 complex to leverage the co-receptor signalling, maintain compatibility with the CD2/CD58 adhesion pair and ensure efficient CD45 exclusion. These requirements can be met by the design of compact bispecific molecules. Second, it was shown that the adhesion molecules shape cellular interactions. The initial microvillar CCs were stabilised by the CD2/CD58 pair, but effective scanning of the target cell required the participation of the LFA-1/ICAM-1 pair. The CCs were measured to be 460 nm in diameter and were shown to be the site of TCR triggering. Engineered enlargement of CCs through CD58 overexpression led to spurious T-cell activation. In the future, modifications of the adhesion system in therapeutic T cells should be considered to further emulate the features of LFA-1/ICAM-1 while preserving

the physiological levels of CD2/CD58 adhesion. Finally, the role of CD45 in the TCR triggering mechanism was investigated. In support of the KS model, imaging data suggested that CD45 was excluded from the CCs, but the measured levels of CD45 exclusion were unexpectedly low. 3D SMLM techniques will be essential to definitively resolve this question. Taken together, this is the first indication that TCR signalling is initiated at size-constrained cellular contacts depleted of CD45.

References

1. Kaufmann, S. H. Immunology's Coming of Age. *Frontiers in Immunology* **10,** 684 (2019).
2. Delorme, E. J. & Alexander, P. Treatment of primary fibrosarcoma in the rat with immune lymphocytes. *Lancet (London, England)* **2,** 117–120 (1964).
3. Klein, G, Sjorgen, H., Klein, E & Hellstrom, K. Demonstration of resistance against methylcholanthrene-induced sarcomas in the primary autochthonous host. *Cancer research* **20,** 1561–1572 (1960).
4. Rosenberg, S. A. *et al.* Use of Tumor-Infiltrating Lymphocytes and Interleukin-2 in the Immunotherapy of Patients with Metastatic Melanoma. *New England Journal of Medicine* **319,** 1676–1680 (1988).
5. Flajnik, M. F. & Kasahara, M. Origin and evolution of the adaptive immune system: genetic events and selective pressures. *Nature Reviews Genetics 2010 11:1* **11,** 47–59 (2009).
6. Takeuchi, O. & Akira, S. Pattern Recognition Receptors and Inflammation. *Cell* **140,** 805–820 (2010).
7. Holers, V. M. Complement and its receptors: New insights into human disease. *Annual Review of Immunology* **32,** 433–459 (2014).
8. Pamcer, Z. *et al.* Somatic diversification of variable lymphocyte receptors in the agnathan sea lamprey. *Nature 2004 430:6996* **430,** 174–180 (2004).
9. Ottinger, E. A., Botfield, M. C. & Shoelson, S. E. Tandem SH2 domains confer high specificity in tyrosine kinase signaling. *Journal of Biological Chemistry* **273,** 729–735 (1998).
10. Pui, J. C. *et al.* Notch1 Expression in Early Lymphopoiesis Influences B versus T Lineage Determination. *Immunity* **11,** 299–308 (1999).
11. Rothenberg, E. V. Transcriptional drivers of the T-cell lineage program. *Current Opinion in Immunology* **24,** 132–138 (2012).
12. Klein, L., Kyewski, B., Allen, P. M. & Hogquist, K. A. Positive and negative selection of the T cell repertoire: what thymocytes see (and don't see). *Nature Reviews Immunology* **14,** 377–391 (2014).
13. Saint-Ruf, C. *et al.* Analysis and Expression of a Cloned Pre-T Cell Receptor Gene. *Science* **266,** 1208–1212 (1994).
14. Hardardottir, F., Baron, J. L. & Janeway, C. A. T cells with two functional antigen-specific receptors. *Proceedings of the National Academy of Sciences* **92,** 354–358 (1995).
15. Hogquist, K. A. *et al.* Identification of a Naturally Occurring Ligand for Thymic Positive Selection. *Immunity* **6,** 389–399 (1997).

16. Kisielow, P., Teh, H. S., Blüthmann, H. & Von Boehmer, H. Positive selection of antigen-specific T cells in thymus by restricting MHC molecules. *Nature 1988 335:6192* **335,** 730–733 (1988).

17. Singer, A., Adoro, S. & Park, J. H. Lineage fate and intense debate: myths, models and mechanisms of CD4- versus CD8-lineage choice. *Nature Reviews Immunology 2008 8:10* **8,** 788–801 (2008).

18. Anderson, M. S. & Su, M. A. Aire and T cell development. *Current Opinion in Immunology* **23,** 198–206 (2011).

19. Jordan, M. S. *et al.* Thymic selection of CD4+CD25+ regulatory T cells induced by an agonist self-peptide. *Nature Immunology 2001 2:4* **2,** 301–306 (2001).

20. Matloubian, M. *et al.* Lymphocyte egress from thymus and peripheral lymphoid organs is dependent on S1P receptor 1. *Nature 2004 427:6972* **427,** 355–360 (2004).

21. Hunter, M. C., Teijeira, A. & Halin, C. T cell trafficking through lymphatic vessels. *Frontiers in Immunology* **7,** 236060 (2016).

22. Gowans, J. L. The recirculation of lymphocytes from blood to lymph in the rat. *The Journal of Physiology* **146,** 54 (1959).

23. Gowans, J. L. The Effect of the Continuous Re-infusion of Lymph and Lymphocytes on the Output of Lymphocytes from the Thoracic Duct of Unanaesthetized Rats. *British Journal of Experimental Pathology* **38,** 67 (1957).

24. Girard, J. P., Moussion, C. & Förster, R. HEVs, lymphatics and homeostatic immune cell trafficking in lymph nodes. *Nature Reviews Immunology* **12,** 762–773 (2012).

25. Debes, G. F. *et al.* Chemokine receptor CCR7 required for T lymphocyte exit from peripheral tissues. *Nature Immunology* **6,** 889–894 (2005).

26. Schwab, S. R. *et al.* Immunology: Lymphocyte sequestration through S1P lyase inhibition and disruption of S1P gradients. *Science* **309,** 1735–1739 (2005).

27. Lo, C. G., Xu, Y., Proia, R. L. & Cyster, J. G. Cyclical modulation of sphingosine-1-phosphate receptor 1 surface expression during lymphocyte recirculation and relationship to lymphoid organ transit. *Journal of Experimental Medicine* **201,** 291–301 (2005).

28. Shiow, L. R. *et al.* CD69 acts downstream of interferon-α/β to inhibit S1P1 and lymphocyte egress from lymphoid organs. *Nature* **440,** 540–544 (2006).

29. Chen, D. S. & Mellman, I. Oncology meets immunology: The cancer-immunity cycle. *Immunity* **39,** 1–10 (2013).

30. Tran, E. *et al.* Cancer immunotherapy based on mutation-specific CD4+ T cells in a patient with epithelial cancer. *Science* **344,** 641–645 (2014).

31. Bos, R. & Sherman, L. A. CD4+ T-cell help in the tumor milieu is required for recruitment and cytolytic function of CD8+ T lymphocytes. *Cancer Research* **70,** 8368–8377 (2010).

32. Ghasempour, S. & Freeman, S. A. The glycocalyx and immune evasion in cancer. *The FEBS Journal* **290,** 55–65 (2023).

33. Patel, S. J. *et al.* Identification of essential genes for cancer immunotherapy. *Nature* **548,** 537–542 (2017).

34. Majzner, R. G. *et al.* CD58 Aberrations Limit Durable Responses to CD19 CAR in Large B Cell Lymphoma Patients Treated with Axicabtagene Ciloleucel but Can be Overcome through Novel CAR Engineering. *Blood* **136,** 53–54 (2020).

35. Maeurer, M. J. *et al.* Tumor escape from immune recognition: loss of HLA-A2 melanoma cell surface expression is associated with a complex rearrangement of the short arm of chromosome 6. *Clinical Cancer Research* **2,** 641–52 (1996).

36. Challa-Malladi, M. *et al.* Combined Genetic Inactivation of β2-Microglobulin and CD58 Reveals Frequent Escape from Immune Recognition in Diffuse Large B Cell Lymphoma. *Cancer Cell* **20,** 728–740 (2011).

37. Blum, J. S., Wearsch, P. A. & Cresswell, P. Pathways of Antigen Processing. *Annual review of immunology* **31,** 443 (2013).

38. Kelly, A. *et al.* Assembly and function of the two ABC transporter proteins encoded in the human major histocompatibility complex. *Nature* **355,** 641–644 (1992).

39. Powis, S. J. *et al.* Restoration of antigen presentation to the mutant cell line RMA-S by an MHC-linked transporter. *Nature* **354,** 528–531 (1991).

40. Trowsdale, J. *et al.* Sequences encoded in the class II region of the MHC related to the 'ABC' superfamily of transporters. *Nature* **348,** 741–744 (1990).

41. Hammer, G. E., Gonzalez, F., Champsaur, M., Cado, D. & Shastri, N. The aminopeptidase ERAAP shapes the peptide repertoire displayed by major histocompatibility complex class I molecules. *Nature Immunology* **7,** 103–112 (2005).

42. Grandea, A. G. & Van Kaer, L. Tapasin: an ER chaperone that controls MHC class I assembly with peptide. *Trends in Immunology* **22,** 194–199 (2001).

43. Colbert, J. D., Cruz, F. M. & Rock, K. L. Cross-presentation of exogenous antigens on MHC I molecules. *Current Opinion in Immunology* **64,** 1–8 (2020).

44. Rock, K. L., Gamble, S. & Rothstein, L. Presentation of Exogenous Antigen with Class I Major Histocompatibility Complex Molecules. *Science* **249,** 918–921 (1990).

45. Kovacsovics-Bankowski, M., Clark, K., Benacerraf, B. & Rock, K. L. Efficient major histocompatibility complex class I presentation of exogenous antigen upon phagocytosis by macrophages. *Proceedings of the National Academy of Sciences* **90,** 4942–4946 (1993).

46. Wolfers, J. *et al.* Tumor-derived exosomes are a source of shared tumor rejection antigens for CTL cross-priming. *Nature Medicine* **7,** 297–303 (2001).

47. Joffre, O. P., Segura, E., Savina, A. & Amigorena, S. Cross-presentation by dendritic cells. *Nature Reviews Immunology* **12,** 557–569 (2012).

48. Kovacsovics-Bankowski, M. & Rock, K. L. A Phagosome-to-Cytosol Pathway for Exogenous Antigens Presented on MHC Class I Molecules. *Science* **267,** 243–246 (1995).

49. Shen, L., Sigal, L. J., Boes, M. & Rock, K. L. Important role of cathepsin S in generating peptides for TAP-independent MHC class I crosspresentation in vivo. *Immunity* **21,** 155–165 (2004).

50. Palmowski, M. J. *et al.* Role of Immunoproteasomes in Cross-Presentation. *The Journal of Immunology* **177,** 983–990 (2006).

51. Marks, M. S., Blum, J. S. & Cresswell, P. Invariant chain trimers are sequestered in the rough endoplasmic reticulum in the absence of association with HLA class II antigens. *Journal of Cell Biology* **111,** 839–855 (1990).

52. Roche, P. A., Marks, M. S. & Cresswell, P. J. Formation of a nine-subunit complex by HLA class II glycoproteins and the invariant chain. *Nature* **354,** 392–394 (1991).

53. Sette, A. *et al.* Invariant Chain Peptides in Most HLA-DR Molecules of an Antigen-Processing Mutant. *Science* **258,** 1801–1804 (1992).

54. Hiltbold, E. M. & Roche, P. A. Trafficking of MHC class II molecules in the late secretory pathway. *Current Opinion in Immunology* **14,** 30–35 (2002).

55. Zarutskie, J. A. *et al.* The kinetic basis of peptide exchange catalysis by HLA-DM. *Proceedings of the National Academy of Sciences of the United States of America* **98,** 12450–12455 (2001).

56. Dong, D. *et al.* Structural basis of assembly of the human T cell receptor–CD3 complex. *Nature* **573,** 546–552 (2019).

57. Sušac, L. *et al.* Structure of a fully assembled tumor-specific T cell receptor ligated by pMHC. *Cell* **185,** 3201–3213 (2022).

58. Reth, M. & Alarcon B Wileman, C. H. Antigen receptor tail clue. *Nature* **338,** 383–384 (1989).

59. Huang, J. *et al.* A Single Peptide-Major Histocompatibility Complex Ligand Triggers Digital Cytokine Secretion in CD4+ T Cells. *Immunity* **39,** 846–857 (2013).

60. Sykulev, Y., Joo, M., Vturina, I., Tsomides, T. J. & Eisen, H. N. Evidence that a Single Peptide–MHC Complex on a Target Cell Can Elicit a Cytolytic T Cell Response. *Immunity* **4,** 565–571 (1996).

61. Irvine, D. J., Purbhoo, M. A., Krogsgaard, M. & Davis, M. M. Direct observation of ligand recognition by T cells. *Nature* **419,** 845–849 (2002).

62. Purbhoo, M. A., Irvine, D. J., Huppa, J. B. & Davis, M. M. T cell killing does not require the formation of a stable mature immunological synapse. *Nature Immunology* **5,** 524–530 (2004).

63. Schamel, W. W. *et al.* Coexistence of multivalent and monovalent TCRs explains high sensitivity and wide range of response. *Journal of Experimental Medicine* **202,** 493–503 (2005).

64. Kumar, R. *et al.* Increased Sensitivity of Antigen-Experienced T Cells through the Enrichment of Oligomeric T Cell Receptor Complexes. *Immunity* **35,** 375–387 (2011).

65. Brameshuber, M. *et al.* Monomeric TCRs drive T cell antigen recognition. *Nature Immunology* **19,** 487–496 (2018).

66. James, J. R. *et al.* Single-molecule level analysis of the subunit composition of the T cell receptor on live T cells. *Proceedings of the National Academy of the United States of America* **104,** 17662–17667 (2007).

67. Notti, R. Q. *et al.* The resting and ligand-bound states of the membrane-embedded human T-cell receptor-CD3 complex. *bioRxiv* (2023).

68. Saotome, K. *et al.* Structural analysis of cancer-relevant TCR-CD3 and peptide-MHC complexes by cryoEM. *Nature Communications 2023 14:1* **14,** 1–12 (2023).

69. Rossy, J., Williamson, D. J. & Gaus, K. How does the kinase Lck phosphorylate the T cell receptor? Spatial organization as a regulatory mechanism. *Frontiers in Immunology* **3,** 167 (2012).

70. Paige, L. A., Nadler, M. J., Harrison, M. L., Cassady, J. M. & Geahlen, R. L. Reversible palmitoylation of the protein-tyrosine kinase p56lck. *Journal of Biological Chemistry* **268,** 8669–8674 (1993).

71. Koegl, M., Zlatkine, P., Ley, S. C., Courtneidge, S. A. & Magee, A. I. Palmitoylation of multiple Src-family kinases at a homologous N-terminal motif. *Biochemical Journal* **303,** 749–753 (1994).

72. Turner, J. M. *et al.* Interaction of the unique N-terminal region of tyrosine kinase p56lck with cytoplasmic domains of CD4 and CD8 is mediated by cysteine motifs. *Cell* **60,** 755–765 (1990).

73. Binder, C. *et al.* CD2 Immunobiology. *Frontiers in Immunology* **11,** 533081 (2020).

74. Boggon, T. J. & Eck, M. J. Structure and regulation of Src family kinases. *Oncogene 2004 23:48* **23,** 7918–7927 (2004).

75. Yamaguchi, H. & Hendrickson, W. A. Structural basis for activation of human lymphocyte kinase Lck upon tyrosine phosphorylation. *Nature* **384,** 484–489 (1996).

76. Oro, U. D. & Ashwell, J. D. Cutting Edge: The CD45 Tyrosine Phosphatase Is an Inhibitor of Lck Activity in Thymocytes. *The Journal of Immunology* **162,** 1879–1883 (1999).

77. Nika, K. *et al.* Constitutively active lck kinase in T cells drives antigen receptor signal transduction. *Immunity* **32,** 766–777 (2010).

78. Philipsen, L. *et al.* De novo phosphorylation and conformational opening of the tyrosine kinase Lck act in concert to initiate T cell receptor signaling. *Science Signaling* **10,** 1–14 (2017).

79. Paster, W. *et al.* Genetically Encoded Förster Resonance Energy Transfer Sensors for the Conformation of the Src Family Kinase Lck. *The Journal of Immunology* **182,** 2160–2167 (2009).

80. Stirnweiss, A. *et al.* T cell activation results in conformational changes in the Src family kinase Lck to induce its activation. *Science Signaling* **6,** 1–11 (2013).

81. McNeill, L. *et al.* CD45 isoforms in T cell signalling and development. *Immunology Letters* **92,** 125–134 (2004).

82. Ogilvy, S. *et al.* Either of the CD45RB and CD45RO Isoforms Are Effective in Restoring T Cell, But Not B Cell, Development and Function in CD45-Null Mice. *The Journal of Immunology* **171,** 1792–1800 (2003).

83. Kozieradzki, I *et al.* T cell development in mice expressing splice variants of the protein tyrosine phosphatase CD45. *The Journal of Immunology* **158,** 3130–3139 (1997).

84. Zamoyska, R. Why Is There so Much CD45 on T Cells? *Immunity* **27,** 421–423 (2007).

85. McCall, M. N., Shotton, D. M. & Barclay, A. N. Expression of soluble isoforms of rat CD45. Analysis by electron microscopy and use in epitope mapping of anti-CD45R monoclonal antibodies. *Immunology* **76,** 310 (1992).

86. Chang, V. T. *et al.* Initiation of T cell signaling by CD45 segregation at 'close contacts'. *Nature Immunology* **17,** 574–582 (2016).

87. Carbone, C. B. *et al.* In vitro reconstitution of T cell receptor-mediated segregation of the CD45 phosphatase. *Proceedings of the National Academy of Sciences of the United States of America* **114,** E9338–E9345 (2017).

88. Hui, E. & Vale, R. D. In vitro membrane reconstitution of the T-cell receptor proximal signaling network. *Nature Structural and Molecular Biology* **21,** 133–142 (2014).

89. Pingel, J. T. & Thomas, M. L. Evidence That the Leukocyte-Common Antigen Is Required for Antigen-Induced T Lymphocyte Proliferation. *Cell* **59,** 1055–1065 (1999).

90. McNeill, L. *et al.* The Differential Regulation of Lck Kinase Phosphorylation Sites by CD45 Is Critical for T Cell Receptor Signaling Responses. *Immunity* **27,** 425–437 (2007).

91. Wallace, V. A. *et al.* Alterations in the level of CD45 surface expression affect the outcome of thymic selection. *The Journal of Immunology* **158,** 3205–3214 (1997).

92. Secrist, P., Ann Burns, L., Karnitzs, L., Koretzky, G. A. & Abraham, R. T. Stimulatory Effects of the Protein Tyrosine Phosphatase Inhibitor, Pervanadate, on T-cell Activation Events*. *Journal of Biological Chemistry* **268,** 5886–5893 (1993).

93. Leahy, D. J. A structural view of CD4 and CD8. *The FASEB Journal* **9,** 17–25 (1995).

94. Li, Y., Yin, Y. & Mariuzza, R. A. Structural and biophysical insights into the role of CD4 and CD8 in T cell activation. *Frontiers in Immunology* **4,** 55589 (2013).

95. Moody, A. M. *et al.* Developmentally regulated glycosylation of the CD8$\alpha\beta$ coreceptor stalk modulates ligand binding. *Cell* **107,** 501–512 (2001).

96. Rudd, P. M., Elliott, T., Cresswell, P., Wilson, I. A. & Dwek, R. A. Glycosylation and the immune system. *Science* **291,** 2370–2376 (2001).

97. Kim, P. W., Sun, Z. Y. J., Blacklow, S. C., Wagner, G. & Eck, M. J. A zinc clasp structure tethers Lck to T cell coreceptors CD4 and CD8. *Science* **301,** 1725–1728 (2003).

98. Veillette, A., Bookman, M. A., Horak, E. M. & Bolen, J. B. The CD4 and CD8 T cell surface antigens are associated with the internal membrane tyrosine-protein kinase p56lck. *Cell* **55,** 301–308 (1988).

99. Barber, E. K., Dasgupta, J. D., Schlossman, S. F., Trevillyan, J. M. & Rudd, C. E. The CD4 and CD8 antigens are coupled to a protein-tyrosine kinase (p56lck) that phosphorylates the CD3 complex. *Proceedings of the National Academy of Sciences* **86,** 3277–3281 (1989).

100. Leishman, A. J. *et al.* T cell responses modulated through interaction between CD8$\alpha\alpha$ and the nonclassical MHC class I molecule, TL. *Science* **294,** 1936–1939 (2001).

101. Wyer, J. R. *et al.* T cell receptor and coreceptor CD8$\alpha\alpha$ bind peptide-MHC independently and with distinct kinetics. *Immunity* **10,** 219–225 (1999).

102. Jönsson, P., Southcombe, J. H., Mafalda, A., Huo, J. & Fernandes, R. A. Remarkably low affinity of CD4/peptide-major histocompatibility complex class II protein interactions. **113** (2016).

103. Doyle, C. & Strominger, J. L. Interaction between CD4 and class II MHC molecules mediates cell adhesion. *Nature* **330,** 256–259 (1987).

104. Norment, A. M., Salter, R. D., Parham, P., Engelhard, V. H. & Littman, D. R. Cell-cell adhesion mediated by CD8 and MHC class I molecules. *Nature* **336,** 79–81 (1988).

105. Xu, H. & Littman, D. R. A Kinase-Independent Function of Lck in Potentiating Antigen-Specific T Cell Activation. *Cell* **74,** 633–643 (1993).

106. O'Rourke, A. M., Rogers, J. & Mescher, M. F. Activated CD8 binding to class I protein mediated by the T-cell receptor results in signalling. *Nature 1990 346:6280* **346,** 187–189 (1990).

107. Jiang, N. *et al.* Two-Stage Cooperative T Cell Receptor-Peptide Major Histocompatibility Complex-CD8 Trimolecular Interactions Amplify Antigen Discrimination. *Immunity* **34,** 13–23 (2011).

108. Van der Merwe, P. A. & Cordoba, S. P. Late Arrival: Recruiting Coreceptors to the T Cell Receptor Complex. *Immunity* **34,** 1–3 (2011).

109. Casas, J. *et al.* Ligand-engaged TCR is triggered by Lck not associated with CD8 coreceptor. *Nature Communications* **5,** 1–11 (2014).

110. Stepanek, O. *et al.* Coreceptor Scanning by the T Cell Receptor Provides a Mechanism for T Cell Tolerance. *Cell* **159,** 333–345 (2014).

111. Mørch, A. M. *et al.* The kinase occupancy of T cell coreceptors reconsidered. *Proceedings of the National Academy of Sciences* **119,** e2213538119 (2022).

112. Holler, P. D. & Kranz, D. M. Quantitative analysis of the contribution of TCR/pepMHC affinity and CD8 to T cell activation. *Immunity* **18,** 255–264 (2003).

113. Wang, H. *et al.* ZAP-70: an essential kinase in T-cell signaling. *Cold Spring Harbor perspectives in biology* **2,** a002279 (2010).

114. Isakov, N. *et al.* ZAP-70 binding specificity to T cell receptor tyrosine-based activation motifs: the tandem SH2 domains of ZAP-70 bind distinct tyrosine-based activation motifs with varying affinity. *Journal of Experimental Medicine* **181,** 375–380 (1995).

115. Goyette, J. *et al.* Dephosphorylation accelerates the dissociation of ZAP70 from the T cell receptor. *Proceedings of the National Academy of Sciences of the United States of America* **119,** e2116815119 (2022).

116. Katz, Z. B., Novotná, L., Blount, A. & Lillemeier, B. F. A cycle of Zap70 kinase activation and release from the TCR amplifies and disperses antigenic stimuli. *Nature Immunology* **18,** 86–95 (2016).

117. Huse, M. The T-cell-receptor signaling network. *Journal of Cell Science* **122,** 1269–1273 (2009).

118. Mørch, A. M., Bálint, Santos, A. M., Davis, S. J. & Dustin, M. L. *Coreceptors and TCR Signaling – the Strong and the Weak of It* 2020.

119. Chakraborty, A. K. & Weiss, A. Insights into the initiation of TCR signaling. *Nature Immunology* **15,** 798–807 (2014).

120. Springer, T. A. & Dustin, M. L. Integrin inside-out signaling and the immunological synapse. *Current Opinion in Cell Biology* **24,** 107–115 (2012).

121. Takagi, J., Petre, B. M., Walz, T. & Springer, T. A. Global conformational earrangements in integrin extracellular domains in outside-in and inside-out signaling. *Cell* **110,** 599–611 (2002).

122. Constantin, G. *et al.* Chemokines Trigger Immediate $\beta 2$ Integrin Affinity and Mobility Changes: Differential Regulation and Roles in Lymphocyte Arrest under Flow. *Immunity* **13,** 759–769 (2000).

123. Walling, B. L. & Kim, M. LFA-1 in T cell migration and differentiation. *Frontiers in Immunology* **9,** 340974 (2018).

124. Schürpf, T. & Springer, T. A. Regulation of integrin affinity on cell surfaces. *EMBO Journal* **30,** 4712–4727 (2011).

125. Chen, X. *et al.* Requirement of open headpiece conformation for activation of leukocyte integrin $\alpha X \beta 2$. *Proceedings of the National Academy of Sciences of the United States of America* **107,** 14727–14732 (2010).

126. Shamri, R. *et al.* Lymphocyte arrest requires instantaneous induction of an extended LFA-1 conformation mediated by endothelium-bound chemokines. *Nature Immunology* **6,** 497–506 (2005).

127. Stanley, P. *et al.* Intermediate-affinity LFA-1 binds α-actinin-1 to control migration at the leading edge of the T cell. *The EMBO Journal* **27,** 62 (2008).

128. Lacouture, C. *et al.* LFA-1 nanoclusters integrate TCR stimulation strength to tune T-cell cytotoxic activity. *Nature Communications* **15,** 1–14 (2024).

129. Dustin, M. L. & Springer, T. A. T-cell receptor cross-linking transiently stimulates adhesiveness through LFA-1. *Nature* **341,** 619–624 (1989).

130. Dustin, M. L. Adhesive bond dynamics in contacts between t lymphocytes and glass- supported planar bilayers reconstituted with the immunoglobulin-related adhesion molecule CD58. *Journal of Biological Chemistry* **272,** 15782–15788 (1997).

131. Ye, F. *et al.* Recreation of the terminal events in physiological integrin activation. *Journal of Cell Biology* **188,** 157–173 (2010).

132. Ganpule, G, Knorr, R, Miller, J. M., Carron, C. P. & Dustin, M. L. Low affinity of cell surface lymphocyte function-associated antigen-1 (LFA-1) generates selectivity for cell-cell interactions. *The Journal of Immunology* **159,** 2685–2692 (1997).

133. Shimaoka, M. *et al.* Reversibly locking a protein fold in an active conformation with a disulfide bond: Integrin αL I domains with high affinity and antagonist activity in vivo. *Proceedings of the National Academy of Sciences of the United States of America* **98,** 6009–6014 (2001).

134. Bachmann, M. F. *et al.* Distinct Roles for LFA-1 and CD28 during Activation of Naive T Cells: Adhesion versus Costimulation. *Immunity* **7,** 549–557 (1997).

135. Dustin, M. L., Ferguson, L. M., Chan, P. Y., Springer, T. A. & Golan, D. E. Visualization of CD2 interaction with LFA-3 and determination of the two-dimensional dissociation constant for adhesion receptors in a contact area. *Journal of Cell Biology* **132,** 465–474 (1996).

136. Van der Merwe, P. A. *et al.* Human Cell-Adhesion Molecule CD2 Binds CD58 (LFA-3) with a Very Low Affinity and an Extremely Fast Dissociation Rate but Does Not Bind CD48 or CD59. *Biochemistry* **33,** 4945–4954 (1994).

137. Jenkins, E. *et al.* Antigen discrimination by T cells relies on size-constrained microvillar contact. *Nature Communications* **14,** 1–21 (2023).

138. Bachmann, M. F., Barner, M. & Kopf, M. Cd2 Sets Quantitative Thresholds in T Cell Activation. *Journal of Experimental Medicine* **190,** 1383–1392 (1999).

139. Bell, G. M., Fargnoli, J., Bolen, J. B., Kish, L. & Imboden, J. B. The SH3 domain of p56lck binds to proline-rich sequences in the cytoplasmic domain of CD2. *Journal of Experimental Medicine* **183,** 169–178 (1996).

140. Carmo, A. M., Mason, D. W. & Beyers, A. D. Physical association of the cytoplasmic domain of CD2 with the tyrosine kinases p56lck and p59fyn. *European Journal of Immunology* **23,** 2196–2201 (1993).

141. Hutchingst, N. J., Clarkson, N., Chalkley, R., Barclay, A. N. & Brown, M. H. Linking the T cell surface protein CD2 to the actin-capping protein CAPZ via CMS and CIN85. *Journal of Biological Chemistry* **278,** 22396–22403 (2003).

142. Kirsch, K. H., Georgescu, M. M., Ishimaru, S. & Hanafusa, H. CMS: An adapter molecule involved in cytoskeletal rearrangements. *Proceedings of the National Academy of Sciences of the United States of America* **96,** 6211–6216 (1999).

143. Dustin, M. L. *et al.* A Novel Adaptor Protein Orchestrates Receptor Patterning and Cytoskeletal Polarity in T-Cell Contacts. *Cell* **94,** 667–677 (1998).

144. Tibaldi, E. V. & Reinherz, E. L. CD2BP3, CIN85 and the structurally related adaptor protein CMS bind to the same CD2 cytoplasmic segment, but elicit divergent functional activities. *International Immunology* **15,** 313–329 (2003).

145. Steeg, C., Von Bonin, A., Mittrücker, H. W., Malissen, B. & Fleischer, B. CD2-mediated signaling in T cells lacking the ζ-chain-specific immune receptor tyrosine-based activation (ITAM) motif. *European Journal of Immunology* **27,** 2233–2238 (1997).

146. Beyers, A. D., Barclay, A. N., Law, D. A., He, Q. & Williams, A. F. Activation of T lymphocytes via monoclonal antibodies against rat cell surface antigens with particular reference to CD2 antigen. *Immunological Reviews* **111,** 59–77 (1989).

147. Skånland, S. S., Moltu, K., Berge, T., Aandahl, E. M. & Taskén, K. T-cell co-stimulation through the CD2 and CD28 co-receptors induces distinct signalling responses. *Biochemical Journal* **460,** 399–410 (2014).

148. Zhao, J. *et al.* CD2AP Links Cortactin and Capping Protein at the Cell Periphery To Facilitate Formation of Lamellipodia. *Molecular and Cellular Biology* **33,** 38–47 (2013).

149. Kuo, J. C. H., Gandhi, J. G., Zia, R. N. & Paszek, M. J. Physical biology of the cancer cell glycocalyx. *Nature Physics* **14,** 658–669 (2018).

150. Ardman, B., Sikorski, M. A. & Staunton, D. E. CD43 interferes with T-lymphocyte adhesion. *Proceedings of the National Academy of Sciences of the United States of America* **89,** 5001–5005 (1992).

151. Paszek, M. J. *et al.* The cancer glycocalyx mechanically primes integrin-mediated growth and survival. *Nature* **511,** 319–325 (2014).

152. Dushek, O., Goyette, J. & van der Merwe, P. A. Non-catalytic tyrosine-phosphorylated receptors. *Immunological Reviews* **250,** 258–276 (2012).

153. Haas, Q. *et al.* Siglec-9 Regulates an Effector Memory CD8th T-cell Subset That Congregates in the Melanoma Tumor Microenvironment. *Cancer Immunology Research* **7,** 707–718 (2019).

154. Freeman, S. A. *et al.* Transmembrane Pickets Connect Cyto- and Pericellular Skeletons Forming Barriers to Receptor Engagement. *Cell* **172,** 305–317 (2018).

155. Nabi, I. R., Shankar, J. & Dennis, J. W. The galectin lattice at a glance. *Journal of Cell Science* **128,** 2213–2219 (2015).

156. Beatson, R. *et al.* Cancer-associated hypersialylated MUC1 drives the differentiation of human monocytes into macrophages with a pathogenic phenotype. *Communications Biology 2020 3:1* **3,** 1–15 (2020).

157. Beatson, R. *et al.* The mucin MUC1 modulates the tumor immunological microenvironment through engagement of the lectin Siglec-9. *Nature Immunology* **17,** 1273–1281 (2016).

158. Hudak, J. E., Canham, S. M. & Bertozzi, C. R. Glycocalyx engineering reveals a Siglec-based mechanism for NK cell immunoevasion. *Nature Chemical Biology* **10,** 69–75 (2013).

159. Gubbels, J. A. *et al.* MUC16 provides immune protection by inhibiting synapse formation between NK and ovarian tumor cells. *Molecular Cancer* **9,** 1–14 (2010).

160. Okamoto, T. *et al.* Core2 O-glycan-expressing prostate cancer cells are resistant to NK cell immunity. *Molecular Medicine Reports* **7,** 359–364 (2013).

161. Madsen, C. B. *et al.* Glycan Elongation Beyond the Mucin Associated Tn Antigen Protects Tumor Cells from Immune-Mediated Killing. *PLoS ONE* **8** (2013).

162. Jung, Y. *et al.* Three-dimensional localization of T-cell receptors in relation to microvilli using a combination of superresolution microscopies. *Proceedings of the National Academy of Sciences of the United States of America* **113,** E5916–E5924 (2016).

163. Majstoravich, S. *et al.* Lymphocyte microvilli are dynamic, actin-dependent structures that do not require Wiskott-Aldrich syndrome protein (WASp) for their morphology. *Blood* **104,** 1396–1403 (2004).

164. Kim, H. R. & Jun, C. D. T Cell Microvilli: Sensors or Senders? *Frontiers in immunology* **10,** 1753 (2019).

165. Sage, P. T. *et al.* Antigen Recognition Is Facilitated by Invadosome-like Protrusions Formed by Memory/Effector T Cells. *The Journal of Immunology* **188,** 3686–3699 (2012).

166. Ueda, H., Morphew, M. K., McIntosh, J. R. & Davis, M. M. CD4 + T-cell synapses involve multiple distinct stages. *Proceedings of the National Academy of Sciences of the United States of America* **108,** 17099–17104 (2011).

167. Jenkins, M. R. *et al.* Distinct structural and catalytic roles for Zap70 in formation of the immunological synapse in CTL. *eLife* **2014** (2014).

168. Cai, E. *et al.* Visualizing dynamic microvillar search and stabilization during ligand detection by T cells. *Science* **356** (2017).

169. Ghosh, S. *et al.* ERM-Dependent Assembly of T Cell Receptor Signaling and Co-stimulatory Molecules on Microvilli prior to Activation. *Cell Reports* **30,** 3434–3447 (2020).

170. Weinbaum, S., Tarbell, J. M. & Damiano, E. R. The structure and function of the endothelial glycocalyx layer. *Annual Review of Biomedical Engineering* **9,** 121–167 (2007).

171. Hu, K. H. & Butte, M. J. T cell activation requires force generation. *Journal of Cell Biology* **213,** 535–542 (2016).

172. Yi, J. C. & Samelson, L. E. Microvilli set the stage for T-cell activation. *Proceedings of the National Academy of Sciences of the United States of America* **113,** 11061–11062 (2016).

173. Rossboth, B. *et al.* TCRs are randomly distributed on the plasma membrane of resting antigen-experienced T cells. *Nature Immunology* **19,** 821–827 (2018).

174. Jung, Y., Wen, L., Altman, A. & Ley, K. CD45 pre-exclusion from the tips of T cell microvilli prior to antigen recognition. *Nature Communications* **12,** 1–16 (2021).

175. Ghosh, S. *et al.* CCR7 signalosomes are preassembled on tips of lymphocyte microvilli in proximity to LFA-1. *Biophysical Journal* **120,** 4002–4012 (2021).

176. Berlin, C. *et al.* α4 integrins mediate lymphocyte attachment and rolling under physiologic flow. *Cell* **80,** 413–422 (1995).

177. Von Andrian, U. H., Hasslen, S. R., Nelson, R. D., Erlandsen, S. L. & Butcher, E. C. A central role for microvillous receptor presentation in leukocyte adhesion under flow. *Cell* **82,** 989–999 (1995).

178. Sengupta, P. *et al.* A lipid-based partitioning mechanism for selective incorporation of proteins into membranes of HIV particles. *Nature Cell Biology* **21,** 452–461 (2019).

179. Fehon, R. G., McClatchey, A. I. & Bretscher, A. Organizing the cell cortex: the role of ERM proteins. *Nature Reviews Molecular Cell Biology* **11,** 276–287 (2010).

180. Shaffer, M. H. *et al.* Ezrin and Moesin Function Together to Promote T Cell Activation. *The Journal of Immunology* **182,** 1021–1032 (2009).

181. Straus, D. B. & Weiss, A. The CD3 chains of the T cell antigen receptor associate with the ZAP-70 tyrosine kinase and are tyrosine phosphorylated after receptor stimulation. *Journal of Experimental Medicine* **178,** 1523–1530 (1993).

182. Samelson, L. E. Signal transduction mediated by the T cell antigen receptor: The role of adapter proteins. *Annual Review of Immunology* **20,** 371–394 (2002).

183. Zhang, W., Sloan-Lancaster, J., Kitchen, J., Trible, R. P. & Samelson, L. E. LAT: The ZAP-70 tyrosine kinase substrate that links T cell receptor to cellular activation. *Cell* **92,** 83–92 (1998).

184. Koretzky, G. A., Abtahian, F. & Silverman, M. A. SLP76 and SLP65: complex regulation of signalling in lymphocytes and beyond. *Nature Reviews Immunology* **6,** 67–78 (2006).

185. Tousley, A. M. *et al.* Co-opting signalling molecules enables logic-gated control of CAR T cells. *Nature 2023* **615,** 507–516 (2023).

186. Liu, S. K. & McGlade, C. J. Gads is a novel SH2 and SH3 domain-containing adaptor protein that binds to tyrosine-phosphorylated Shc. *Oncogene* **17,** 3073–3082 (1998).

187. Cahalan, M. D. & Chandy, K. G. The functional network of ion channels in T lymphocytes. *Immunological Reviews* **231,** 59–87 (2009).

188. June, C. H., Ledbetter, J. A., Gillespie, M. M., Lindsten, T. & Thompson, C. B. T-Cell Proliferation Involving the CD28 Pathway Is Associated witH Cyclosporine-Resistant Interleukin 2 Gene Expression. *Molecular and Cellular Biology* **7,** 4472–4481 (1987).

189. Azuma, M. *et al.* B70 antigen is a second ligand for CTLA-4 and CD28. *Nature* **366,** 76–79 (1993).

190. Mueller, D. L., Jenkins, M. K. & Schwartz, R. H. Clonal expansion versus functional clonal inactivation: a costimulatory signalling pathway determines the outcome of T cell antigen receptor occupancy. *Annual review of immunology* **7,** 445–480 (1989).

191. Schwartz, R. H. T CELL ANERGY *. *Annu. Rev. Immunol* **21,** 305–339 (2003).

192. Qureshi, O. S. *et al.* Trans-endocytosis of CD80 and CD86: A molecular basis for the cell-extrinsic function of CTLA-4. *Science* **332,** 600–603 (2011).

193. Sheppard, K. A. *et al.* PD-1 inhibits T-cell receptor induced phosphorylation of the ZAP70/CD3ζ signalosome and downstream signaling to PKCθ. *FEBS Letters* **574,** 37–41 (2004).

194. Varma, R., Campi, G., Yokosuka, T., Saito, T. & Dustin, M. L. T Cell Receptor-Proximal Signals Are Sustained in Peripheral Microclusters and Terminated in the Central Supramolecular Activation Cluster. *Immunity* **25,** 117–127 (2006).

195. Yokosuka, T. *et al.* Newly generated T cell receptor microclusters initiate and sustain T cell activation by recruitment of Zap70 and SLP-76. *Nature Immunology* **6,** 1253–1262 (2005).

196. Campi, G., Varma, R. & Dustin, M. L. Actin and agonist MHC-peptide complex-dependent T cell receptor microclusters as scaffolds for signaling. *Journal of Experimental Medicine* **202,** 1031–1036 (2005).

197. Bunnell, S. C. *et al.* T cell receptor ligation induces the formation of dynamically regulated signaling assemblies. *Journal of Cell Biology* **158,** 1263–1275 (2002).

198. Brodovitch, A., Bongrand, P. & Pierres, A. T Lymphocytes Sense Antigens within Seconds and Make a Decision within One Minute. *The Journal of Immunology* **191,** 2064–2071 (2013).

199. Yokosuka, T. *et al.* Programmed cell death 1 forms negative costimulatory microclusters that directly inhibit T cell receptor signaling by recruiting phosphatase SHP2. *The Journal of experimental medicine* **209,** 1201–17 (2012).

200. Yokosuka, T. *et al.* Spatiotemporal Regulation of T Cell Costimulation by TCR-CD28 Microclusters and Protein Kinase C q Translocation. *Immunity* **29,** 589–601 (2008).

201. Bunnell, S. C., Kapoor, V., Trible, R. P., Zhang, W. & Samelson, L. E. Dynamic Actin Polymerization Drives T Cell Receptor-Induced Spreading: A Role for the Signal Transduction Adaptor LAT. *Immunity* **14,** 315–329 (2001).

202. Monks, C. R., Freiberg, B. A., Kupfer, H., Sciaky, N. & Kupfer, A. Three-dimensional segregation of supramolecular activation clusters in T cells. *Nature* **395,** 82–86 (1998).

203. Grakoui, A. *et al.* The immunological synapse: A molecular machine controlling T cell activation. *Science* **285,** 221–227 (1999).

204. Leupin, O., Zaru, R., Laroche, T., Müller, S. & Valitutti, S. Exclusion of CD45 from the T-cell receptor signaling area in antigen-stimulated T lymphocytes. *Current Biology* **10,** 277–280 (2000).

205. Potter, T., Grebe, K., Freiberg, B. & Kupfer, A. Formation of supramolecular activation clusters on fresh ex vivo CD8+ T cells after engagement of the T cell antigen receptor and CD8 by antigen-presenting cells. *Proceedings of the National Academy of Sciences of the United States of America* **98,** 12624–12629 (2001).

206. Johnson, K. G., Bromley, S. K., Dustin, M. L. & Thomas, M. L. A supramolecular basis for CD45 tyrosine phosphatase regulation in sustained T cell activation. *Proceedings of the National Academy of Sciences of the United States of America* **97,** 10138–10143 (2000).

207. Freiberg, B. A. *et al.* Staging and resetting T cell activation in SMACs. *Nature Immunology* **3,** 911–917 (2002).

208. Demetriou, P. *et al.* A dynamic CD2-rich compartment at the outer edge of the immunological synapse boosts and integrates signals. *Nature Immunology* **21,** 1232–1243 (2020).

209. Huppa, J. B., Gleimer, M., Sumen, C. & Davis, M. M. Continuous T cell receptor signaling required for synapse maintenance and full effector potential. *Nature Immunology* **4,** 749–755 (2003).

210. Stinchcombe, J. C., Bossi, G., Booth, S. & Griffiths, G. M. The immunological synapse of CTL contains a secretory domain and membrane bridges. *Immunity* **15,** 751–761 (2001).

211. Stinchcombe, J. C., Majorovits, E., Bossi, G., Fuller, S. & Griffiths, G. M. Centrosome polarization delivers secretory granules to the immunological synapse. *Nature* **443,** 462–465 (2006).

212. Beal, A. M. *et al.* Protein Kinase Cθ Regulates Stability of the Peripheral Adhesion Ring Junction and Contributes to the Sensitivity of Target Cell Lysis by CTL. *The Journal of Immunology* **181,** 4815–4824 (2008).

213. Thauland, T. J. & Parker, D. C. Diversity in immunological synapse structure. *Immunology* **131,** 466–472 (2010).

214. Thauland, T. J., Koguchi, Y., Wetzel, S. A., Dustin, M. L. & Parker, D. C. Th1 and Th2 Cells Form Morphologically Distinct Immunological Synapses 1. *The Journal of Immunology* **181,** 393–399 (2008).

215. Brossard, C. *et al.* Multifocal structure of the T cell – dendritic cell synapse. *European Journal of Immunology* **35,** 1741–1753 (2005).

216. Bromley, S. K., Peterson, D. A., Gunn, M. D. & Dustin, M. L. Cutting Edge: Hierarchy of Chemokine Receptor and TCR Signals Regulating T Cell Migration and Proliferation. *The Journal of Immunology* **165,** 15–19 (2000).

217. Woolf, E. *et al.* Lymph node chemokines promote sustained T lymphocyte motility without triggering stable integrin adhesiveness in the absence of shear forces. *Nature Immunology* **8,** 1076–1085 (2007).

218. Okada, T. & Cyster, J. G. CC Chemokine Receptor 7 Contributes to Gi-Dependent T Cell Motility in the Lymph Node. *The Journal of Immunology* **178,** 2973–2978 (2007).

219. Worbs, T., Mempel, T. R., Bölter, J., Von Andrian, U. H. & Förster, R. CCR7 ligands stimulate the intranodal motility of T lymphocytes in vivo. *Journal of Experimental Medicine* **204,** 489–495 (2007).

220. Gunzer, M. *et al.* Antigen Presentation in Extracellular Matrix: Interactions of T Cells with Dendritic Cells Are Dynamic, Short Lived, and Sequential. *Immunity* **13,** 323–332 (2000).

221. Dustin, M. L. T-cell activation through immunological synapses and kinapses. *Immunological Reviews* **221,** 77–89 (2008).

222. Sims, T. N. *et al.* Opposing Effects of PKCθ and WASp on Symmetry Breaking and Relocation of the Immunological Synapse. *Cell* **129,** 773–785 (2007).

223. Mayya, V. *et al.* Durable Interactions of T Cells with T Cell Receptor Stimuli in the Absence of a Stable Immunological Synapse. *Cell Reports* **22,** 340–349 (2018).

224. Mariuzza, R. A., Agnihotri, P. & Orban, J. The structural basis of T-cell receptor (TCR) activation: An enduring enigma. *Journal of Biological Chemistry* **295,** 914–925 (2020).

225. Van der Merwe, P. A. & Dushek, O. Mechanisms for T cell receptor triggering. *Nature Reviews Immunology* **11,** 47–55 (2011).

226. Krogsgaard, M. *et al.* Agonist/endogenous peptide–MHC heterodimers drive T cell activation and sensitivity. *Nature 2005 434:7030* **434,** 238–243 (2005).

227. Juang, J. *et al.* Peptide-MHC heterodimers show that thymic positive selection requires a more restricted set of self-peptides than negative selection. *Journal of Experimental Medicine* **207,** 1223–1234 (2010).

228. Locksley, R. M., Reiner, S. L., Hatam, F., Littman, D. R. & Killeen, N. Helper T cells without CD4: Control of leishmaniasis in CD4-deficient mice. *Science* **261,** 1448–1451 (1993).

229. Schilham, M. W. *et al.* Alloreactive cytotoxic T cells can develop and function in mice lacking both CD4 and CD8. *European Journal of Immunology* **23,** 1299–1304 (1993).

230. Stone, J. D. & Stern, L. J. CD8 T cells, like CD4 T cells, are triggered by multivalent engagement of TCRs by MHC-peptide ligands but not by monovalent engagement. *Journal of immunology* **176,** 1498–1505 (2006).

231. Meuer, S. C. *et al.* Evidence for the T3-associated 90K heterodimer as the T-cell antigen receptor. *Nature* **303,** 808–810 (1983).

232. Kaye, J., Porcelli, S., Tite, J., Jones, B. & Janeway, C. A. Both a monoclonal antibody and antisera specific for determinants unique to individual cloned helper T cell lines can substitute for antigen and antigen-presenting cells in the activation of T cells. *Journal of Experimental Medicine* **158,** 836–856 (1983).

233. Boniface, J. J. *et al.* Initiation of Signal Transduction through the T Cell Receptor Requires the Multivalent Engagement of Peptide/MHC Ligands. *Immunity* **9,** 459–466 (1998).

234. Sykulev, Y., Joo, M., Vturina, I., Tsomides, T. J. & Eisen, H. N. Evidence that a single peptide-MHC complex on a target cell can elicit a cytolytic T cell response. *Immunity* **4,** 565–571 (1996).

235. Bentley, G. A., Boulot, G, Karjalainen, K & Mariuzza, R. A. Crystal Structure of the β Chain of a T Cell Antigen Receptor. *Science* **267,** 1984–1987 (1995).

236. Wang, J. H. *et al.* Atomic structure of an $\alpha\beta$ T cell receptor (TCR) heterodimer in complex with an anti-TCR Fab fragment derived from a mitogenic antibody. *The EMBO Journal* **17,** 10–26 (1998).

237. Ghendler, Y., Smolyar, A., Chang, H. C. & Reinherz, E. L. One of the CD3ϵ Subunits within a T Cell Receptor Complex Lies in Close Proximity to the Cβ FG Loop. *Journal of Experimental Medicine* **187,** 1529–1536 (1998).

238. Natarajan, K. *et al.* An allosteric site in the T-cell receptor Cβ domain plays a critical signalling role. *Nature Communications* **8,** 1–14 (2017).

239. Rangarajan, S. *et al.* Peptide–MHC (pMHC) binding to a human antiviral T cell receptor induces long-range allosteric communication between pMHC- and CD3-binding sites. *Journal of Biological Chemistry* **293,** 15991–16005 (2018).

240. Degermann, S., Sollami, G. & Karjalainen, K. T Cell Receptor β Chain Lacking the Large Solvent-exposed Cβ FG Loop Supports Normal α/β T Cell Development and Function in Transgenic Mice. *The Journal of Experimental Medicine* **189,** 1679 (1999).

241. Touma, M. *et al.* The TCR Cβ FG Loop Regulates $\alpha\beta$ T Cell Development. *The Journal of Immunology* **176,** 6812–6823 (2006).

242. Aivazian, D. & Stern, L. J. Phosphorylation of T cell receptor ζ is regulated by a lipid dependent folding transition. *Nature Structural Biology* **7,** 1023–1026 (2000).

243. Gagnon, E., Schubert, D. A., Gordo, S., Chu, H. H. & Wucherpfennig, K. W. Local changes in lipid environment of TCR microclusters regulate membrane binding by the CD3ϵ cytoplasmic domain. *Journal of Experimental Medicine* **209,** 2423–2439 (2012).

244. Zhang, H., Cordoba, S. P., Dushek, O. & Van Der Merwe, P. A. Basic residues in the T-cell receptor ζ cytoplasmic domain mediate membrane association and modulate signaling. *Proceedings of the National Academy of Sciences of the United States of America* **108,** 19323–19328 (2011).

245. Xu, C. *et al.* Regulation of T Cell Receptor Activation by Dynamic Membrane Binding of the CD3ϵ Cytoplasmic Tyrosine-Based Motif. *Cell* **135,** 702–713 (2008).

246. Fernandes, R. A. *et al.* What Controls T Cell Receptor Phosphorylation? *Cell* **142,** 668–669 (2010).

247. DeFord-Watts, L. M. *et al.* The CD3 ζ Subunit Contains a Phosphoinositide-Binding Motif That Is Required for the Stable Accumulation of TCR–CD3 Complex at the Immunological Synapse. *The Journal of Immunology* **186,** 6839–6847 (2011).

248. DeFord-Watts, L. M. *et al.* The Cytoplasmic Tail of the T Cell Receptor CD3 ϵ Subunit Contains a Phospholipid-Binding Motif that Regulates T Cell Functions. *The Journal of Immunology* **183,** 1055–1064 (2009).

249. Kim, S. T. *et al.* The $\alpha\beta$ T cell receptor is an anisotropic mechanosensor. *Journal of Biological Chemistry* **284,** 31028–31037 (2009).

250. Li, Y.-C. *et al.* Cutting Edge: Mechanical Forces Acting on T Cells Immobilized via the TCR Complex Can Trigger TCR Signaling. *The Journal of Immunology* **184,** 5959–5963 (2010).

251. Sibener, L. V. *et al.* Isolation of a Structural Mechanism for Uncoupling T Cell Receptor Signaling from Peptide-MHC Binding. *Cell* **174,** 672–687 (2018).

252. Liu, B., Chen, W., Evavold, B. D. & Zhu, C. Accumulation of dynamic catch bonds between TCR and agonist peptide-MHC triggers T cell signaling. *Cell* **157,** 357–368 (2014).

253. Das, D. K. *et al.* Force-dependent transition in the T-cell receptor β-subunit allosterically regulates peptide discrimination and pMHC bond lifetime. *Proceedings of the National Academy of Sciences of the United States of America* **112,** 1517–1522 (2015).

254. Wu, P. *et al.* Mechano-regulation of Peptide-MHC Class I Conformations Determines TCR Antigen Recognition. *Molecular Cell* **73,** 1015–1027 (2019).

255. Davis, S. J. & Merwe, P. A. V. D. The kinetic-segregation model: TCR triggering and beyond. *Nature Immunology* **7,** 803–809 (2006).

256. Fernandes, R. A. *et al.* A cell topography-based mechanism for ligand discrimination by the T cell receptor. *Proceedings of the National Academy of Sciences of the United States of America* **116,** 14002–14010 (2019).

257. Aleksic, M. *et al.* Dependence of T Cell Antigen Recognition on T Cell Receptor-Peptide MHC Confinement Time. *Immunity* **32,** 163–174 (2010).

258. Chen, K. Y. *et al.* Trapping or slowing the diffusion of T cell receptors at close contacts initiates T cell signaling. *Proceedings of the National Academy of Sciences* **118,** e2024250118 (2021).

259. Burroughs, N. J., Lazic, Z. & Van Der Merwe, P. A. Ligand detection and discrimination by spatial relocalization: A kinase-phosphatase segregation model of TCR activation. *Biophysical Journal* **91,** 1619–1629 (2006).

260. Davis, S. J. & van der Merwe, P. A. Lck and the nature of the T cell receptor trigger. *Trends in Immunology* **32,** 1–5 (2011).

261. Cordoba, S.-P. *et al.* The large ectodomains of CD45 and CD148 regulate their segregation from and inhibition of ligated T-cell receptor. *Blood* **121,** 4295–4302 (2013).

262. Irles, C. *et al.* CD45 ectodomain controls interaction with GEMs and Lck activity for optimal TCR signaling. *Nature Immunology* **4,** 189–197 (2002).

263. Al-Aghbar, M. A., Chu, Y.-S., Chen, B.-M. & Roffler, S. R. High-Affinity Ligands Can Trigger T Cell Receptor Signaling Without CD45 Segregation. *Frontiers in Immunology* **9,** 713 (2018).

264. Chen, B. M. *et al.* The affinity of elongated membrane-tethered ligands determines potency of T cell receptor triggering. *Frontiers in Immunology* **8,** 793 (2017).

265. Li, F. *et al.* Ligand-induced segregation from large cell-surface phosphatases is a critical step in $\gamma\delta$ TCR triggering. *bioRxiv* (2023).

266. He, X., Woodford-Thomas, T. A., Johnson, K. G., Shah, D. D. & Thomas, M. L. Targeting of CD45 protein tyrosine phosphatase activity to lipid microdomains on the T cell surface inhibits TCR signaling. *European Journal of Immunology* **32,** 2578–2687 (2002).

267. Choudhuri, K., Wiseman, D., Brown, M. H., Gould, K. & Van Der Merwe, P. A. T-cell receptor triggering is critically dependent on the dimensions of its peptide-MHC ligand. *Nature* **436,** 578–582 (2005).

268. Choudhuri, K. *et al.* Peptide-Major Histocompatibility Complex Dimensions Control Proximal Kinase-Phosphatase Balance during T Cell Activation. *Journal of Biological Chemistry* **284,** 26096–26105 (2009).

269. Wild, M. K. *et al.* Dependence of T Cell Antigen Recognition on the Dimensions of an Accessory Receptor–Ligand Complex. *Journal of Experimental Medicine* **190,** 31–42 (1999).

270. James, J. R. & Vale, R. D. Biophysical mechanism of T-cell receptor triggering in a reconstituted system. *Nature* **487,** 64–69 (2012).

271. Lippert, A. H. *et al.* Soft Polydimethylsiloxane-Supported Lipid Bilayers for Studying T Cell Interactions. *Biophysical Journal* **120,** 35–45 (2021).

272. Pettmann, J., Santos, A. M., Dushek, O. & Davis, S. J. Membrane Ultrastructure and T Cell Activation. *Frontiers in Immunology* **9,** 2152 (2018).

273. Purbhoo, M. A. *et al.* The Human CD8 Coreceptor Effects Cytotoxic T Cell Activation and Antigen Sensitivity Primarily by Mediating Complete Phosphorylation of the T Cell Receptor η Chain. *Journal of Biological Chemistry* **276,** 32786–32792 (2001).

274. Lin, J. J. Y. *et al.* Mapping the stochastic sequence of individual ligand-receptor binding events to cellular activation: T cells act on the rare events. *Science signaling* **12,** eaat8715 (2019).

275. Altan-Bonnet, G. & Germain, R. N. Modeling T Cell Antigen Discrimination Based on Feedback Control of Digital ERK Responses. *PLOS Biology* **3,** e356 (2005).

276. Lyons, D. S. *et al.* A TCR binds to antagonist ligands with lower affinities and faster dissociation rates than to agonists. *Immunity* **5,** 53–61 (1996).

277. Evavold, B. D. & Allen, P. M. Separation of IL-4 Production from Th Cell Proliferation by an Altered T Cell Receptor Ligand. *Science* **252,** 1308–1310 (1991).

278. Valitutti, S., Miller, S., Cella, M., Padovan, E. & Lanzavecchia, A. Serial triggering of many T-cell receptors by a few peptide–MHC complexes. *Nature* **375,** 148–151 (1995).

279. Siller-Farfán, J. A. & Dushek, O. Molecular mechanisms of T cell sensitivity to antigen. *Immunological Reviews* **285,** 194–205 (2018).

280. Lever, M., Maini, P. K., Van Der Merwe, P. A. & Dushek, O. Phenotypic models of T cell activation. *Nature Reviews Immunology* **14,** 619–629 (2014).

281. Lever, M. *et al.* Architecture of a minimal signaling pathway explains the T-cell response to a 1 million-fold variation in antigen affinity and dose. *Proceedings of the National Academy of Sciences of the United States of America* **113,** E6630–E6638 (2016).

282. Irving, M. *et al.* Interplay between T Cell Receptor Binding Kinetics and the Level of Cognate Peptide Presented by Major Histocompatibility Complexes Governs CD8+ T Cell Responsiveness. *Journal of Biological Chemistry* **287,** 23068–23078 (2012).

283. Mckeithan, T. W. Kinetic proofreading in T-cell receptor signal transduction. *Proceedings of the National Academy of the United States of America* **92,** 5042–5046 (1995).

284. Pettmann, J. *et al.* The discriminatory power of the T cell receptor. *eLife* **10,** 1–45 (2021).

285. James, J. R. Tuning ITAM multiplicity on T cell receptors can control potency and selectivity to ligand density. *Science Signaling* **11,** 1088 (2018).

286. Love, P. E. & Hayes, S. M. ITAM-mediated signaling by the T-cell antigen receptor. *Cold Spring Harbor perspectives in biology* **2,** a002485 (2010).

287. Alam, S. M. *et al.* Qualitative and quantitative differences in T cell receptor binding of agonist and antagonist ligands. *Immunity* **10,** 227–237 (1999).

288. Pettmann, J. *et al.* Mechanical forces impair antigen discrimination by reducing differences in T-cell receptor/peptide-MHC off-rates. *EMBO journal* (2022).

289. Robert, P. *et al.* Kinetics and mechanics of two-dimensional interactions between T cell receptors and different activating ligands. *Biophysical Journal* **102,** 248–257 (2012).

290. Rosenberg, S. A. & Restifo, N. P. Adoptive cell transfer as personalized immunotherapy for human cancer. *Science* **348,** 62–68 (2015).

291. Clynes, R. A. & Desjarlais, J. R. Redirected T Cell Cytotoxicity in Cancer Therapy. *Annual Review of Medicine* **70,** 437–450 (2019).

292. Leko, V. & Rosenberg, S. A. Identifying and Targeting Human Tumor Antigens for T Cell-Based Immunotherapy of Solid Tumors (2020).

293. Kawakami, Y. *et al.* Identification of the immunodominant peptides of the MART-1 human melanoma antigen recognized by the majority of HLA-A2-restricted tumor infiltrating lymphocytes. *Journal of Experimental Medicine* **180,** 347–352 (1994).

294. Kawakami, Y. *et al.* Identification of a human melanoma antigen recognized by tumor-infiltrating lymphocytes associated with in vivo tumor rejection. *Proceedings of the National Academy of Sciences* **91,** 6458–6462 (1994).

295. Fisk, B., Blevins, T. L., Wharton, J. T. & Ioannides, C. G. Identification of an immunodominant peptide of HER-2/neu protooncogene recognized by ovarian tumor-specific cytotoxic T lymphocyte lines. *Journal of Experimental Medicine* **181,** 2109–2117 (1995).

296. Schumacher, T. N. & Schreiber, R. D. Neoantigens in cancer immunotherapy. *Science* **348,** 69–74 (2015).

297. Prior, I. A., Lewis, P. D. & Mattos, C. A Comprehensive Survey of Ras Mutations in Cancer. *Cancer Research* **72,** 2457–2467 (2012).

298. Hsiue, E. H. C. *et al.* Targeting a neoantigen derived from a common TP53 mutation. *Science* **371** (2021).

299. Douglass, J. *et al.* Bispecific antibodies targeting mutant RAS neoantigens. *Science immunology* **6,** 5515 (2021).

300. Rosenberg, S. A., Spiess, P. & Lafreniere, R. A New Approach to the Adoptive Immunotherapy of Cancer with Tumor-Infiltrating Lymphocytes. *Science* **233,** 1318–1321 (1986).

301. Muul, L. M., Spiess, P. J., Director, E. P. & Rosenberg, S. A. Identification of specific cytolytic immune responses against autologous tumor in humans bearing malignant melanoma. *The Journal of Immunology* **138,** 989–995 (1987).

302. Kotowski, M. & Sharma, S. CRISPR-based editing techniques for genetic manipulation of primary T cells. *Methods and Protocols* **3,** 1–27 (2020).

303. Riviere, I., Gallardo, H. F., Hagani, A. B. & Sadelain, M. Retroviral-mediated gene transfer in primary murine and human T-lymphocytes. *Applied Biochemistry and Biotechnology - Part B Molecular Biotechnology* **15,** 133–142 (2000).

304. Eyquem, J. *et al.* Targeting a CAR to the TRAC locus with CRISPR/Cas9 enhances tumour rejection. *Nature* **543,** 113–117 (2017).

305. Gross, G., Waks, T. & Eshhar, Z. Expression of immunoglobulin-T-cell receptor chimeric molecules as functional receptors with antibody-type specificity. *Proceedings of the National Academy of Sciences* **86,** 10024–10028 (1989).

306. Jackson, H. J., Rafiq, S. & Brentjens, R. J. Driving CAR T-cells forward. *Nature Reviews Clinical Oncology* **13,** 370–383 (2016).

307. Mansilla-Soto, J. *et al.* HLA-independent T cell receptors for targeting tumors with low antigen density. *Nature Medicine* **28,** 345–352 (2022).

308. Baeuerle, P. A. *et al.* Synthetic TRuC receptors engaging the complete T cell receptor for potent anti-tumor response. *Nature Communications* **10,** 1–12 (2019).

309. Liu, Y. *et al.* Chimeric STAR receptors using TCR machinery mediate robust responses against solid tumors. *Science Translational Medicine* **13,** 5191 (2021).

310. Seung, E. *et al.* A trispecific antibody targeting HER2 and T cells inhibits breast cancer growth via CD4 cells. *Nature* **603,** 328–334 (2022).

311. Quezada, S. A. *et al.* Tumor-reactive CD4+ T cells develop cytotoxic activity and eradicate large established melanoma after transfer into lymphopenic hosts. *Journal of Experimental Medicine* **207,** 637–650 (2010).

312. Speiser, D. E., Chijioke, O., Schaeuble, K. & Münz, C. CD4+ T cells in cancer. *Nature Cancer* **4,** 317–329 (2023).

313. Fenis, A., Demaria, O., Gauthier, L., Vivier, E. & Narni-Mancinelli, E. New immune cell engagers for cancer immunotherapy. *Nature Reviews Immunology,* 1–16 (2024).

314. Moore, P. A. *et al.* Application of dual affinity retargeting molecules to achieve optimal redirected T-cell killing of B-cell lymphoma. *Blood* **117,** 4542–4551 (2011).

315. Topp, M. S. *et al.* Targeted therapy with the T-cell-engaging antibody blinatumomab of chemotherapy-refractory minimal residual disease in B-lineage acute lymphoblastic leukemia patients results in high response rate and prolonged leukemia-free survival. *Journal of clinical oncology* **29,** 2493–2498 (2011).

316. Nathan, P. *et al.* Overall Survival Benefit with Tebentafusp in Metastatic Uveal Melanoma. *New England Journal of Medicine* **385,** 1196–1206 (2021).

317. Wu, L. *et al.* Trispecific antibodies enhance the therapeutic efficacy of tumor-directed T cells through T cell receptor co-stimulation. *Nature Cancer* **1,** 86–98 (2019).

318. Patel, A. *et al.* Using CombiCells, a platform for titration and combinatorial display of cell surface ligands, to study T-cell antigen sensitivity modulation by accessory receptors. *The EMBO journal* **43,** 132–150 (2024).

319. Bufi, N. *et al.* Human Primary Immune Cells Exhibit Distinct Mechanical Properties that Are Modified by Inflammation. *Biophysical journal* **108,** 2181–2190 (2015).

320. Fisher, P. J., Bulur, P. A., Vuk-Pavlovic, S., Prendergast, F. G. & Dietz, A. B. Dendritic cell microvilli: A novel membrane structure associated with the multifocal synapse and T-cell clustering. *Blood* **112,** 5037–5045 (2008).

321. Groves, J. T. & Dustin, M. L. Supported planar bilayers in studies on immune cell adhesion and communication. *Journal of Immunological Methods* **278,** 19–32 (2003).

322. Chan, P. Y. *et al.* Influence of receptor lateral mobility on adhesion strengthening between membranes containing LFA-3 and CD2. *Journal of Cell Biology* **115,** 245–255 (1991).

323. Tözeren, A. *et al.* Micromanipulation of adhesion of a Jurkat cell to a planar bilayer membrane containing lymphocyte function-associated antigen 3 molecules. *Journal of Cell Biology* **116,** 997–1006 (1992).

324. Geijtenbeek, T. B. *et al.* Identification of DC-SIGN, a novel dendritic cell-specific ICAM-3 receptor that supports primary immune responses. *Cell* **100,** 575–585 (2000).

325. Li, D. *et al.* Extended-resolution structured illumination imaging of endocytic and cytoskeletal dynamics. *Science* **349** (2015).

326. Hoffman, D. P. *et al.* Correlative three-dimensional super-resolution and block-face electron microscopy of whole vitreously frozen cells. *Science* **367** (2020).

327. Xu, C. S. *et al.* Enhanced FIB-SEM systems for large-volume 3D imaging. *eLife* **6** (2017).

328. Fraietta, J. A. *et al.* Disruption of TET2 promotes the therapeutic efficacy of CD19-targeted T cells. *Nature* **558,** 307–312 (2018).

329. Shah, N. N. & Fry, T. J. Mechanisms of resistance to CAR T cell therapy. *Nature Reviews Clinical Oncology* **16,** 372–385 (2019).

330. Deacy, A. M., Gan, S. K. E. & Derrick, J. P. Superantigen Recognition and Interactions: Functions, Mechanisms and Applications. *Frontiers in Immunology* **12,** 731845 (2021).

331. Liddy, N. *et al.* Monoclonal TCR-redirected tumor cell killing. *Nature Medicine* **18,** 980–987 (2012).

332. Li, Y. *et al.* Directed evolution of human T-cell receptors with picomolar affinities by phage display. *Nature Biotechnology* **23,** 349–354 (2005).

333. Boulter, J. M. *et al.* Stable, soluble T-cell receptor molecules for crystallization and therapeutics. *Protein Engineering, Design and Selection* **16,** 707–711 (2003).

334. Robertson, I. B. *et al.* Tuning the potency and selectivity of ImmTAC molecules by affinity modulation. *Clinical and Experimental Immunology* **215,** 105–119 (2024).

335. Parkhurst, M. R. *et al.* Improved induction of melanoma-reactive CTL with peptides from the melanoma antigen gp100 modified at HLA-A*0201-binding residues. *The Journal of Immunology* **157,** 2539–2548 (1996).

336. Hansen, T. H., Connolly, J. M., Gould, K. G. & Fremont, D. H. *Basic and translational applications of engineered MHC class I proteins* 2010.

337. Stone, J. D., Chervin, A. S. & Kranz, D. M. T-cell receptor binding affinities and kinetics: impact on T-cell activity and specificity. *Immunology* **126,** 165–176 (2009).

338. Purbhoo, M. A. *et al.* Quantifying and Imaging NY-ESO-1/LAGE-1-Derived Epitopes on Tumor Cells Using High Affinity T Cell Receptors. *The Journal of Immunology* **176,** 7308–7316 (2006).

339. Bossi, G. *et al.* Examining the presentation of tumor-associated antigens on peptide-pulsed T2 cells. *OncoImmunology* **2,** e26840 (2013).

340. Cole, D. K. *et al.* Hotspot autoimmune T cell receptor binding underlies pathogen and insulin peptide cross-reactivity. *The Journal of Clinical Investigation* **126,** 2191–2204 (2016).

341. Hattrup, C. L. & Gendler, S. J. Structure and Function of the Cell Surface (Tethered) Mucins. *Annual Review of Physiology* **70,** 431–457 (2008).

342. Johnson, L. A., Banerji, S., Lagerholm, B. C. & Jackson, D. G. Dendritic cell entry to lymphatic capillaries is orchestrated by CD44 and the hyaluronan glycocalyx. *Life Science Alliance* **4** (2021).

343. Möckl, L. *et al.* Quantitative Super-Resolution Microscopy of the Mammalian Glycocalyx. *Developmental Cell* **50,** 57–72 (2019).

344. Park, S. *et al.* Mucins form a nanoscale material barrier against immune cell attack. *bioRxiv,* 2022.01.28.478211 (2022).

345. Daly, S. *et al.* High-density volumetric super-resolution microscopy. *Nature Communications* **15,** 1–10 (2024).

346. Giles, J. R. *et al.* Human epigenetic and transcriptional T cell differentiation atlas for identifying functional T cell-specific enhancers. *Immunity* **55,** 557–574 (2022).

347. Restifo, N. P. & Gattinoni, L. Lineage relationship of effector and memory T cells. *Current Opinion in Immunology* **25,** 556–563 (2013).

348. Velasco Cárdenas, R. M. *et al.* Harnessing CD3 diversity to optimize CAR T cells. *Nature Immunology 2023 24:12* **24,** 2135–2149 (2023).

349. Burton, J. *et al.* Inefficient exploitation of accessory receptors reduces the sensitivity of chimeric antigen receptors. *Proceedings of the National Academy of Sciences of the United States of America* **120** (2023).

350. Poloni, C. *et al.* T-cell activation–induced marker assays in health and disease. *Immunology and Cell Biology* **101,** 491–503 (2023).

351. Lever, M. *et al.* Architecture of a minimal signaling pathway explains the T-cell response to a 1 million-fold variation in antigen affinity and dose. *Proceedings of the National Academy of Sciences* **113,** E6630–E6638 (2016).

352. Staufer, O. *et al.* Solution structure and synaptic analyses reveal molecular mechanisms of bispecific T cell engagers. *bioRxiv* (2023).

353. Bakalar, M. H. *et al.* Size-Dependent Segregation Controls Macrophage Phagocytosis of Antibody-Opsonized Targets. *Cell* **174,** 131–142 (2018).

354. Huhn, A. *et al.* The molecular reach of antibodies determines their SARS-CoV-2 neutralisation potency. *bioRxiv* (2023).

355. Wilhelm, K. B. *et al.* Height, but not binding epitope, affects the potency of synthetic TCR agonists. *Biophysical Journal* **120,** 3869–3880 (2021).

356. Xiao, Q. *et al.* Size-dependent activation of CAR-T cells. *Science immunology* **7,** eabl3995 (2022).

357. Zareie, P. *et al.* Canonical T cell receptor docking on peptide-MHC is essential for T cell signaling. *Science* **372** (2021).

358. Schmid, E. M. *et al.* Size-dependent protein segregation at membrane interfaces. *Nature Physics* **12,** 704–711 (2016).

359. Sasada, T. & Reinherz, E. L. A Critical Role for CD2 in Both Thymic Selection Events and Mature T Cell Function. *The Journal of Immunology* **166,** 2394–2403 (2001).

360. Wooldridge, L. *et al.* Interaction between the CD8 coreceptor and major histocompatibility complex class I stabilizes T cell receptor-antigen complexes at the cell surface. *Journal of Biological Chemistry* **280,** 27491–27501 (2005).

361. Choi, E. M., Palmowski, M., Chen, J. & Cerundolo, V. The use of chimeric A2Kb tetramers to monitor HLA A2 immune responses in HLA A2 transgenic mice. *Journal of Immunological Methods* **268,** 35–41 (2002).

362. Koretzky, G. A., Picus, J., Thomas, M. L. & Weiss, A. Tyrosine phosphatase CD45 is essential for coupling T-cell antigen receptor to the phosphatidyl inositol pathway. *Nature* **346,** 66–68 (1990).

363. Moingeon, P. *et al.* CD2-mediated adhesion facilitates T lymphocyte antigen recognition function. *Nature* **339,** 312–314 (1989).

364. Cai, Z. *et al.* Requirements for Peptide-induced T Cell Receptor Downregulation on Naive CD8+ T Cells. *Journal of Experimental Medicine* **185,** 641–652 (1997).

365. Cai, H. *et al.* Full control of ligand positioning reveals spatial thresholds for T cell receptor triggering. *Nature Nanotechnology* **13,** 610–617 (2018).

366. Van Der Merwe, P. A., Davis, S. J., Shaw, A. S. & Dustin, M. L. Cytoskeletal polarization and redistribution of cell-surface molecules during T cell antigen recognition. *Seminars in Immunology* **12,** 5–21 (2000).

367. Beppler, C. *et al.* Hyperstabilization of T cell microvilli contacts by chimeric antigen receptors. *The Journal of cell biology* **222** (2023).

368. Stinchcombe, J. C. *et al.* Ectocytosis renders T cell receptor signaling self-limiting at the immune synapse. *Science* **380,** 818–823 (2023).

369. Razvag, Y. *et al.* T Cell Activation through Isolated Tight Contacts. *Cell Reports* **29,** 3506–3521 (2019).

370. Razvag, Y., Neve-Oz, Y., Sajman, J., Reches, M. & Sherman, E. Nanoscale kinetic segregation of TCR and CD45 in engaged microvilli facilitates early T cell activation. *Nature Communications* **9,** 1–17 (2018).

371. Gee, K. R. *et al.* Chemical and physiological characterization of fluo-4 Ca2+-indicator dyes. *Cell Calcium* **27,** 97–106 (2000).

372. Messmer, D., Messmer, B. & Chiorazzi, N. The global transcriptional maturation program and stimuli-specific gene expression profiles of human myeloid dendritic cells. *International Immunology* **15,** 491–503 (2003).

373. Galore-Haskel, G. *et al.* Histopathological expression analysis of intercellular adhesion molecule 1 (ICAM-1) along development and progression of human melanoma. *Oncotarget* **8,** 99580–99586 (2017).

374. Natali, P. *et al.* Differential Expression of Intercellular Adhesion Molecule 1 in Primary and Metastatic Melanoma Lesions1. *Cancer Research* **50,** 1271–1278 (1990).

375. Johnson, J. P., Stade, B. G., Holzmann, B., Schwable, W. & Riethmuller, G. De novo expression of intercellular-adhesion molecule 1 in melanoma correlates with increased risk of metastasis. *Proceedings of the National Academy of Sciences* **86,** 641–644 (1989).

376. Cassioli, C. *et al.* Increasing LFA-1 Expression Enhances Immune Synapse Architecture and T Cell Receptor Signaling in Jurkat E6.1 Cells. *Frontiers in Cell and Developmental Biology* **9,** 673446 (2021).

377. Stevens, A. J. *et al.* Programming multicellular assembly with synthetic cell adhesion molecules. *Nature* **614,** 144–152 (2022).

378. Trebak, M. & Kinet, J. P. Calcium signalling in T cells. *Nature Reviews Immunology* **19,** 154–169 (2019).

379. Dransfield, I., Cabañas, C., Craig, A. & Hogg, N. Divalent cation regulation of the function of the leukocyte integrin LFA-1. *Journal of Cell Biology* **116,** 219–226 (1992).

380. Lee, J. O., Rieu, P., Arnaout, M. A. & Liddington, R. Crystal structure of the A domain from the a subunit of integrin CR3 (CD11 b/CD18). *Cell* **80,** 631–638 (1995).

381. Baumgart, F., Schneider, M. & Schütz, G. J. How t cells do the "search for the needle in the haystack". *Frontiers in Physics* **7,** 427884 (2019).

382. Montoya, M. C. *et al.* Role of ICAM-3 in the initial interaction of T lymphocytes and APCs. *Nature Immunology* **3,** 159–168 (2002).

383. De Fougerolles, A. R. & Springer, T. A. Intercellular adhesion molecule 3, a third adhesion counter-receptor for lymphocyte function-associated molecule 1 on resting lymphocytes. *Journal of Experimental Medicine* **175,** 185–190 (1992).

384. Starling, G. C. *et al.* Intercellular adhesion molecule-3 is the predominant co-stimulatory ligand for leukocyte function antigen-1 on human blood dendritic cells. *European Journal of Immunology* **25,** 2528–2532 (1995).

385. Davis, S. J. & Van Der Merwe, P. A. The structure and ligand interactions of CD2: implications for T-cell function. *Immunology Today* **17,** 177–187 (1996).

386. Du, Y. *et al.* Membrane-anchored DNA nanojunctions enable closer antigen-presenting cell–T-cell contact in elevated T-cell receptor triggering. *Nature Nanotechnology* **18,** 818–827 (2023).

387. Carr, A. R. *et al.* Three-Dimensional Super-Resolution in Eukaryotic Cells Using the Double-Helix Point Spread Function. *Biophysical Journal* **112,** 1444–1454 (2017).

388. Pavani, S. R. P. *et al.* Three-dimensional, single-molecule fluorescence imaging beyond the diffraction limit by using a double-helix point spread function. *Proceedings of the National Academy of Sciences of the United States of America* **106,** 2995–2999 (2009).

389. Thompson, M. A., Lew, M. D., Badieirostami, M. & Moerner, W. E. Localizing and tracking single nanoscale emitters in three dimensions with high spatiotemporal resolution using a double-helix point spread function. *Nano Letters* **10,** 211–218 (2010).

390. Ritter, A. T. *et al.* ESCRT-mediated membrane repair protects tumor-derived cells against T cell attack. *Science* **376,** 377–382 (2022).

391. Choudhuri, K. *et al.* Polarized release of T-cell-receptor-enriched microvesicles at the immunological synapse. *Nature* **507,** 118–123 (2014).

392. Kuball, J. *et al.* Increasing functional avidity of TCR-redirected T cells by removing defined N-glycosylation sites in the TCR constant domain. *Journal of Experimental Medicine* **206,** 463–475 (2009).

393. Stork, R. *et al.* N-Glycosylation as Novel Strategy to Improve Pharmacokinetic Properties of Bispecific Single-chain Diabodies. *Journal of Biological Chemistry* **283,** 7804–7812 (2008).

394. Stinchcombe, J. C. *et al.* Ectocytosis renders T cell receptor signaling self-limiting at the immune synapse. *Science* **380,** 818–823 (2023).

395. Kopek, B. G., Shtengel, G., Xu, C. S., Clayton, D. A. & Hess, H. F. Correlative 3D superresolution fluorescence and electron microscopy reveal the relationship of mitochondrial nucleoids to membranes. *Proceedings of the National Academy of Sciences of the United States of America* **109,** 6136–6141 (2012).

396. Hell, S. W. *et al.* The 2015 super-resolution microscopy roadmap. *Journal of Physics D: Applied Physics* **48** (2015).

397. Martell, J. D., Deerinck, T. J., Lam, S. S., Ellisman, M. H. & Ting, A. Y. Electron microscopy using the genetically encoded APEX2 tag in cultured mammalian cells. *Nature Protocols 2017 12:9* **12,** 1792–1816 (2017).

398. Lam, S. S. *et al.* Directed evolution of APEX2 for electron microscopy and proximity labeling. *Nature Methods* **12,** 51–54 (2014).

399. Shu, X. *et al.* A Genetically Encoded Tag for Correlated Light and Electron Microscopy of Intact Cells, Tissues, and Organisms. *PLOS Biology* **9,** e1001041 (2011).

400. Martell, J. D. *et al.* Engineered ascorbate peroxidase as a genetically encoded reporter for electron microscopy. *Nature Biotechnology 2012 30:11* **30,** 1143–1148 (2012).

401. Lin, J. J. *et al.* Membrane Association Transforms an Inert Anti-TCRβ Fab' Ligand into a Potent T Cell Receptor Agonist. *Biophysical Journal* **118,** 2879–2893 (2020).

402. Vissa, A., Wilhelm, K. B., Stinger, B. & Groves, J. T. Building an affinity panel of synthetic polyclonal T-cell receptor ligands that mimic native peptide-MHC. *Biophysical Journal* **122,** 509a (2023).

403. Stinger, B., Vissa, A., Wilhelm, K. B. & Groves, J. T. Synthetic T cell receptor ligands that mimic native pMHC ligand binding kinetics. *Biophysical Journal* **123,** 102a (2024).

404. Dushek, O. *et al.* Antigen potency and maximal efficacy reveal a mechanism of efficient T cell activation. *Science Signaling* **4** (2011).

405. Bluemel, C. *et al.* Epitope distance to the target cell membrane and antigen size determine the potency of T cell-mediated lysis by BiTE antibodies specific for a large melanoma surface antigen. *Cancer Immunology, Immunotherapy 2010 59:8* **59,** 1197–1209 (2010).

406. Li, J. *et al.* Membrane-Proximal Epitope Facilitates Efficient T Cell Synapse Formation by Anti-FcRH5/CD3 and Is a Requirement for Myeloma Cell Killing. *Cancer Cell* **31,** 383–395 (2017).

407. Boero, S. *et al.* Analysis of in vitro ADCC and clinical response to trastuzumab: Possible relevance of FcγRIIIA/FcγRIIA gene polymorphisms and HER-2 expression levels on breast cancer cell lines. *Journal of Translational Medicine* **13,** 1–14 (2015).

408. Duell, J. *et al.* Frequency of regulatory T cells determines the outcome of the T-cell-engaging antibody blinatumomab in patients with B-precursor ALL. *Leukemia 2017 31:10* **31,** 2181–2190 (2017).

409. Tanaka, A. & Sakaguchi, S. Regulatory T cells in cancer immunotherapy. *Cell Research 2017 27:1* **27,** 109–118 (2016).

410. Casey, M. *et al.* Regulatory T cells hamper the efficacy of T-cell-engaging bispecific antibody therapy. *Haematologica* **109,** 787–798 (2024).

411. Lowe, K. L. *et al.* Novel TCR-based biologics: mobilising T cells to warm 'cold' tumours. *Cancer Treatment Reviews* **77,** 35–43 (2019).

412. Brodovitch, A. *et al.* T lymphocytes need less than 3 min to discriminate between peptide MHCs with similar TCR-binding parameters. *European Journal of Immunology* **45,** 1635–1642 (2015).

413. Kaizuka, Y., Douglass, A. D., Varma, R., Dustin, M. L. & Vale, R. D. Mechanisms for segregating T cell receptor and adhesion molecules during immunological synapse formation in Jurkat T cells. *Proceedings of the National Academy of Sciences of the United States of America* **104,** 20296–20301 (2007).

414. Hashimoto-Tane, A. *et al.* Micro-adhesion rings surrounding TCR microclusters are essential for T cell activation. *Journal of Experimental Medicine* **213,** 1609–1625 (2016).

415. Deguine, J., Breart, B., Lemaître, F., Di Santo, J. P. & Bousso, P. Intravital Imaging Reveals Distinct Dynamics for Natural Killer and CD8+ T Cells during Tumor Regression. *Immunity* **33,** 632–644 (2010).

416. Bousso, P. & Robey, E. Dynamics of CD8+ T cell priming by dendritic cells in intact lymph nodes. *Nature Immunology* **4,** 579–585 (2003).

417. Dustin, M. L., Bromley, S. K., Kan, Z., Peterson, D. A. & Unanue, E. R. Antigen receptor engagement delivers a stop signal to migrating T lymphocytes. *Proceedings of the National Academy of Sciences of the United States of America* **94,** 3909–3913 (1997).

418. Crites, T. J. *et al.* TCR Microclusters Pre-Exist and Contain Molecules Necessary for TCR Signal Transduction. *The Journal of Immunology* **193,** 56–67 (2014).

419. Wong, N. K. Y., Lai, J. C. Y., Birkenhead, D., Shaw, A. S. & Johnson, P. CD45 Down-Regulates Lck-Mediated CD44 Signaling and Modulates Actin Rearrangement in T Cells. *The Journal of Immunology* **181,** 7033–7043 (2008).

420. Nunes, R. J. *et al.* Protein Interactions between CD2 and Lck Are Required for the Lipid Raft Distribution of CD2. *The Journal of Immunology* **180,** 988–997 (2008).

421. Samelson, L. E., Fletcher, M. C., Ledbetter, J. A. & June, C. H. Activation of tyrosine phosphorylation in human T cells via the CD2 pathway. Regulation by the CD45 tyrosine phosphatase. *The Journal of Immunology* **145,** 2448–2454 (1990).

422. Wooldridge, L. *et al.* MHC Class I Molecules with Superenhanced CD8 Binding Properties Bypass the Requirement for Cognate TCR Recognition and Nonspecifically Activate CTLs. *The Journal of Immunology* **184,** 3357–3366 (2010).

423. Choi, H. K. *et al.* Catch bond models may explain how force amplifies TCR signaling and antigen discrimination. *Nature Communications* **14,** 1–20 (2023).

Appendices

A
Appendix 1

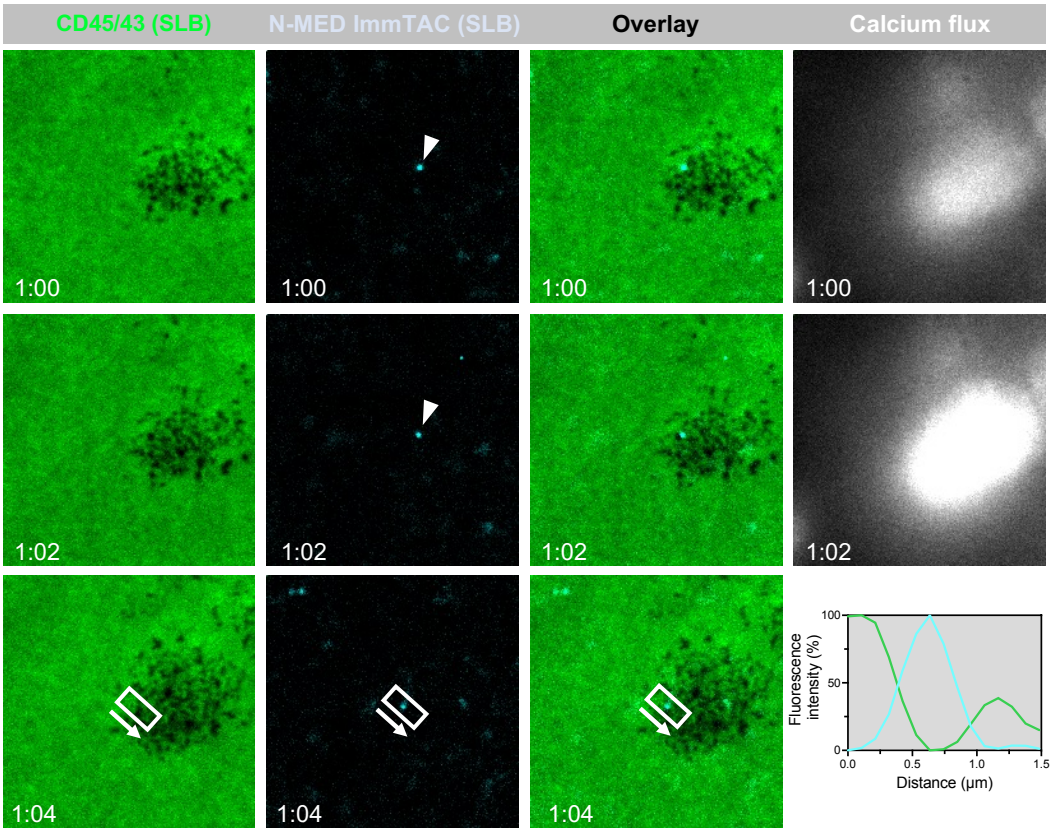


Figure A.1: Primary CD8$^+$ T cells can activate in response to a *bona fide* single ImmTAC. Total internal reflection microscopy of primary CD8$^+$ T cells on supported-lipid bilayers (SLB). SLB was prepared according to Jenkins et al. to contain CD58, CD45, CD43, ICAM-1, and GP100-HLA-A2 complex[137]. The SLB was incubated with 30 pM N-MED ImmTAC for 10 min to generate the 1 N-MED ImmTAC/GP100-MHC 'ligand unit' per µm^2. ImmTAC was stoichiometrically labelled with SiR. CD45 and CD43 acting as model glycocalyx were labelled with AF555. The black 'holes' in the SLB glycocalyx (CD43/CD45) fluorescence correspond to close contacts between the SLB and T-cell microvilli. T cells were labelled with a calcium indicator Fluo-4 AM. TIRFM images were taken at long exposure times (800 ms) to 'blur' the rapidly diffusing ImmTAC molecules and capture those stably bound to the TCR/CD3 complex. Images show a single ImmTAC within the close contact followed by a near-immediate (2 s) calcium flux. The line profile shows the position of the ImmTAC molecule within the close contact. TIRFM imaging was performed by Daniel Heraghty.